

**Expanding the Centrifugal Microfluidic Toolbox through Enhanced Functionality
and Advanced Unit Operations**

Michael Shane Woolf
Midlothian, Virginia

A.A.S. Physical Therapy Assisting, Tidewater Community College, 1996
B.S. Biology/Secondary Education Minor, James Madison University, 2007
M.S. Forensic Science, Virginia Commonwealth University, 2016

A Dissertation presented to the Graduate Faculty of the University of Virginia in
Candidacy for the Degree of Doctor of Philosophy

Department of Chemistry
University of Virginia
July 2021

Acknowledgments

For me, the path to UVA and the Landers Lab has been circuitous and, at times, downright frustrating. I never imagined finishing a dissertation so many years after high school graduation. This decades-long journey has been filled with unexpected redirects, unforeseen kinks, hiccups, and crushing disappointments. To be perfectly frank, I am often in disbelief that I am here at all. Fortunately, I have not made this journey alone and am profoundly grateful to many people that played roles, great and small, along the way.

I would be remiss if I didn't recognize the long line of educators and mentors with generous hearts, immense patience, and a knack for helping me find confidence and a brighter future: Dave Evans, Sgt. George Grace, Dr. Dan Norvell (formerly Lt. Dan), Dr. Scott Lewis, Dr. Conley K. McMullen, Annetta Haddox, and Dr. Baneshwar Singh. Each of you, in your unique way, allowed me to grow as a student, as a researcher, and as a person. Thank you.

Dr. Michelle Peace, thank you for your ongoing support, encouragement, mentorship, and friendship. Your steadfast belief in me continues to be invaluable.

Dr. Joan Bienvenue, thank you for sharing the story of your career path and your journey to success. That humble seminar at VCU was most unexpected and truly serendipitous. Thank you for your time and for formally introducing me to Dr. Landers. Without that introduction, none of this would have been possible.

Dr. James Landers, you took a chance on 'the old guy' and I can only hope that my work product has made it all worthwhile. You have provided the unique, interdisciplinary environment and the team of peers that have pushed me to think and to grow. Thank you for allowing me to explore. And thank you for never pigeonholing me as merely a biologist or as a forensic scientist.

For their guidance and particular contributions to the research in this dissertation (in no particular order), I recognize Dr. Dan Nelson, Dr. Shannon Krauss, Dr. Brandon Thompson, Dr. Charlie Clark, Leah Dignan, Aeren Nauman, Hannah Lewis, Kevyn Hadley, Rachel Moffett, Sabrina Kim, Natalie Collins, and Maura Charette. To Hannah, Leah, and Aeren I wish to express my deep gratitude. Hannah, you will always be my 'second favorite undergrad.' Thank you for your hard work and dedication. Leah, your encouragement, insights, support, and friendship are beyond value. Aeren, without your engineering expertise, much of this work would have never come to fruition. Thank you all.

Dedication

For my wife, Sherri L. Woolf. You believed in me when I didn't believe in myself. Thanks for walking with me, around the world, and back again.

In loving memory of my father, Charles L. Woolf. I didn't have childhood heroes. But I did have a kick-ass Dad. Thanks for teaching me the value of hard work and persistence. I finally made it, Pop. Wish you were here to help me celebrate.

“Hard work beats talent when talent doesn't work hard.”

-Tim Notke

Abstract

Detection and analysis of biochemical markers is essential in many disciplines. The projects described in this dissertation were focused on the development of centrifugal microfluidic approaches to address unmet needs and technology gaps in the forensic, biomedical, and National Defense and Security communities. Conventional laboratory instrumentation currently used for these purposes is often expensive, non-portable, and dictates labor-intensive and time-consuming benchtop protocols conducted by highly trained personnel. These limitations can be overcome through advancements in and lab-on-a-disc (LoaD) microfluidic technologies that allow for integration and automation of numerous unit operations within a cost-effective, compact, and portable platform amenable to use by nontechnical personnel. Among these, rotationally driven microfluidic platforms can be complete sample-to-answer, push-button micro total analysis systems (μ TAS) (e.g., narcotics and explosives detection) or they may simply automate a portion of a much larger process chain (e.g., dynamic solid phase extraction (dSPE) of nucleic acids or differential extraction (DE) of forensic sexual assault evidence).

The projects outlined in this dissertation were driven by clear unmet needs or technology gaps, with focus on adapting existing laboratory processes to LoaD platforms. The centrifugal differential extraction project (CDx) project was aimed at automating the manually intensive, time-consuming sample preparation workflow associated with analyzing sexual assault evidence samples, i.e., reducing analyst hands-on time and enhancing sperm fraction enrichment. Similarly, the centrifugal vertical flow project (cVF) aimed to develop a portable, field deployable device capable of supplanting existing paper-based lateral flow immunoassay technology with more sensitive, rapid pathogen detection while maintaining independence from central laboratories. Given the complex nature of both parent projects, a large portion of research exploration was

necessarily dedicated to describing, characterizing, and integrating novel or improved microfluidic unit operations that enhance on-disc functionality by expanding the ‘microfluidic toolbox.’

With regard to the CDx project, the central research goal was to design and develop a centrifugal microfluidic disc capable of performing, automating, and multiplexing a complete forensic DE sample preparation. Initial design and testing efforts towards that goal detailed in **Chapter 2** demonstrate that a full forensic differential extraction (DE) can be performed on a single microfluidic disc that provides for timed reagent release, temperature control for sequential enzymatic reactions, and fluidic fractionation that yields discrete sperm (SF), non-sperm (NSF), and waste fractions from sexual assault evidence samples. Optimization of flow control and microvalving strategies were major hurdles in the development of this microfluidic architecture. As such, **Chapter 3** is devoted to a detailed discussion of the development, characterization, and optimization of two microvalve closure methods, i.e., laser-based and contact heating closure strategies.

The driving motivator for the cVF project was to develop a disc-based system capable of outperforming existing lateral flow immunoassay (LFI) test strips; operational limitations of traditional LFI test strips include poor control over incubation times, reliance upon capillary flow, limited ability to process larger sample volumes, and dependence upon porous materials that rapidly saturate with fluid. During the cVF analysis, the three-dimensional flow path directs the fluid stream orthogonally through embedded nanoporous membranes that are permanently bonded to the disc substrates during the disc fabrication process. The work presented in **Chapter 4** describes visualization and characterization of on-disc flow and fluid drainage patterns, achieved largely through high-speed videography. These studies highlight critical observations impacting ongoing centrifugal vertical flow (cVF) experiments and efforts, including changes in drainage

profiles attributed to differing sample matrix composition and the loss of hydraulic pressure with changes in fluid column fill height during continued flow. The work presented in **Chapter 5** describes crucial pilot and proof-of-principal studies for on-disc pathogen detection via cVF sandwich-type immunocapture.

In large part, the future success the CDx and cVF parent projects hinges upon key microfluidic functionality, chiefly microvalving and on-disc flow through porous media. Understanding the advantages and limitations of these approaches will influence future decision-making and research objectives. Substantial work on the CDx and cVF parent projects remains, yet the exploratory and unit operation development studies outlined here bode well for the future of both ventures. Once fully developed, these rotationally-driven CDx system is poised to significantly impact the forensic science community by ameliorating persistent evidence backlogs, improving laboratory turnaround times, and enhancing sperm fraction enrichment. Likewise, the cVF project will provide enhanced pathogen detection capabilities by offering control over sample volume and incubation times and eliminating reliance upon capillary flow and wicking materials.

Table of Contents

Acknowledgments.....	ii
Dedication.....	iii
Abstract.....	iv
Table of Contents.....	vii
List of Figures.....	xi
List of Tables.....	xiv
List of Publications.....	xv
<hr/>	
Chapter 1. Introduction and Literature Review.....	1
<hr/>	
1.1 Introduction.....	1
1.1.1 Centrifugal Microfluidics.....	1
1.1.2 Unit Operations - Overview.....	2
1.1.3 Unit Operations - Microvalving.....	3
1.1.4 Unit Operations - Embedded Membranes.....	14
1.1.5 Description of Research Goals and Concluding Remarks.....	18
1.2 References.....	20
<hr/>	
Chapter 2. Towards an Affinity-Free, Centrifugal Microfluidic System for Rapid, Automated Forensic Differential Extraction.....	24
<hr/>	
2.1 Introduction.....	24
2.1.1 Forensic Sexual Assault Evidence: An Unmet Need.....	24
2.1.2 Forensic Differential Extraction (DE).....	25
2.1.3 Centrifugal Microfluidics.....	28
2.1.4 Disc Design and Fabrication.....	29
2.1.5 Preliminary Studies and the Impetus for Closable Valving.....	30
2.1.6 Redesigned On-Disc CDx Workflow and Laser-Based Valving Strategy.....	35
2.1.7 Enzymatic DE and the Swab-In Approach.....	38
2.2 Experimental.....	39
2.2.1 Disc Fabrication.....	39
2.2.2 Assessing Fluid Recovery and On-Disc Sample Chamber Position.....	42
2.2.3 Proof-of-Principle Dye Study.....	43
2.2.4 Assessing Removal of E-cell DNA from the CDx Architecture.....	44
	vii

2.2.5	Tracking Sperm Cell DNA within the CDx Architecture.....	45
2.3	Results and Discussion.....	46
2.3.1	Assessing Fluid Recovery from Absorbent Sample Cuttings.....	46
2.3.2	Proof-of-Principle Dye Study	48
2.3.3	Assessing Removal of Non-Sperm Cell DNA from the CDx Architecture...	50
2.3.4	Tracking Sperm Cell DNA within the CDx Architecture.....	51
2.4	Conclusions	54
2.5	References	57
<hr/>		
Chapter 3. Closable Microvalving Methods for Polymeric Centrifugal Microfluidic Devices....		62
3.1	Introduction	62
3.1.1	Microvalving on Centrifugal Microfluidic Discs	62
1.1.1	Valve Opening via Laser Irradiation	63
3.1.2	Valve Closure.....	65
3.2	Experimental	68
3.2.1	Microfluidic Disc Fabrication.....	68
3.2.2	Valve Opening	69
3.2.3	Contact Heating - Preliminary Feasibility Study.....	69
3.2.4	Contact Heating - Secondary Evaluation.....	71
3.2.5	Valve Closure - Preliminary Studies.....	72
3.2.6	Valve Closure - Automation Studies	74
3.2.7	Valve Closure - Optimization and Addressing Failure Modes.....	76
3.2.8	Data Analysis.....	76
3.3	Materials and Methods	78
3.3.1	PrTZAL System.....	78
3.4	Results and Discussion.....	79
3.4.1	Contact Heating Method	79
3.4.2	Laser-based Method - Preliminary Studies.....	82
3.4.3	Automated Target Channel Alignment Studies	85
3.4.4	Optimization of the Laser-based Method and Addressing Failure Modes	86
3.5	Summary and Conclusions.....	89
3.6	Acknowledgements	91
3.7	References	91

Chapter 4.	Characterization of a Centrifugal Microfluidic Vertical Flow Platform...	94
4.1	Introduction	94
4.1.1	Foundational Microfluidics and Fluid Flow	94
4.2	Experimental	99
4.2.1	Disc Fabrication	99
4.2.2	Microfluidic Layout and Flow Pattern.....	100
4.2.3	Centrifugally Driven Vertical Flow (proof-of-principle)	100
4.2.4	Characterization of On-Disc Vertical Flow	101
4.3	Results and Discussion.....	103
4.3.1	On-Disc Vertical Flow.....	103
	Effect of Membrane Pore Size and Rotational Frequency	106
	Effect of Sample Composition	111
4.3.2	Logical Extensions and Ongoing Efforts.....	115
4.4	Conclusions	117
4.5	Acknowledgments.....	119
4.6	References	120
Chapter 5.	Closable Microvalving Methods for Polymeric Centrifugal Microfluidic Devices..	123
5.1	Introduction	123
5.1.1	Lateral flow, Vertical flow, and Point-of-Care Diagnostics	123
5.2	Experimental Section	127
5.2.1	Image Capture, Processing, and Data Analysis	127
5.2.2	VFI Microfluidic Disc Fabrication	129
5.2.3	On-disc, Vertical Flow, Immunocapture – proof of principle	130
5.2.4	On-disc, Vertical Flow with Sandwich-type Immunocapture – proof of principle	131
5.2.5	Comparison of on-disc cVFI with traditional LFI – dilution series.....	132
5.3	Results and Discussion.....	132
5.3.1	Preliminary Studies – Centrifugally Assisted LFI.....	133
5.3.2	Transitioning to On-Disc Vertical Flow	135
5.3.3	On-Disc Immunocapture Studies – controls only, no antigen present.....	137
5.3.4	On-Disc Immunocapture Studies –antigen present.....	140
5.3.5	Comparison of on-disc cVFI with traditional LFI – dilution series.....	142

5.3.6	Visual Inspection	143
5.3.7	Grayscale Intensity Profiles	143
5.3.8	Grayscale Values – Evaluation of LFI test lines.....	144
5.3.9	Grayscale Values – Evaluation of cVFI test spots.....	145
5.3.10	HSB Analysis - Hue.....	146
5.3.11	HSB Analysis - Saturation.....	147
5.3.12	Ongoing Efforts to Optimize the Flow Pattern	149
5.4	Conclusions	150
5.5	Acknowledgements	151
5.6	References	152
<hr/>		
Chapter 6.	Final Remarks	156
<hr/>		
6.1	Conclusions	156
6.2	Ongoing Studies, Persistent Challenges, and Future Work	159
6.2.1	The CDx Project	159
6.2.2	The VFI Project.....	168
6.3	Summation	180
6.4	References	180

List of Figures

Figure 1-1. A centrifugal microfluidic disc with a well-defined fluid volume (red) in a straight microchannel.....	2
Figure 1-2. Passive, frequency-dependent microvalving strategies: (a) capillary, (b) hydrophobic, (c) burstable seal, (d) capillary siphon, (e) overflow siphon, and (f) pneumatic siphon valve.....	5
Figure 1-3. Integrated elastomeric components for microdevice flow control.....	6
Figure 1-4. Schematic views of two-layer, frequency-independent, elastomeric, polydimethylsiloxane (PDMS) microfluidic valves.....	7
Figure 1-5. Different approaches to frequency-independent wax-based microvalving.....	8
Figure 1-6. A section of the microfluidic disc.....	10
Figure 1-7. Modified laser-based valve opening via patterning of xerographic toner.....	11
Figure 1-8. Schematic diagram showing the opening of an insertable polyethylene terephthalate (bPeT) piece.....	13
Figure 1-9. Magnified view of a single-use, closable ethylene vinyl acetate (EVA) valve.....	15
Figure 1-11. Schematic illustrations of conventional dead-end flow filtration and on-disc filtration.....	16
Figure 1-12. A centrifugal microfluidic approach to enhanced flow control for lateral flow strips.....	17
Figure 2-1. Stepwise workflow associated with the traditional DE of sexual assault evidence..	27
Figure 2-2. Schematic of the proposed microfluidic architecture.....	31
Figure 2-3. Histogram analysis to assess the effective elution of multiple, discrete fractions. ...	33
Figure 2-4. Image analysis to assess the removal of dye from the swab chamber.	35
Figure 2-5. Actuation of an optically addressable, sacrificial laser valve and closure of a previously open microfluidic channel.	36
Figure 2-6. Schematic overview of the model CDx disc and workflow based on traditional DE.....	38
Figure 2-7. Exploded view (bottom) and schematic overview (top) of the putative five-layer (2-fluidic layer) microfluidic disc with integrated closable valving.	41
Figure 2-8. Fluid recovery from ¼ cotton swab cuttings and fluid recovery workflow (A-D)..	47
Figure 2-9. Image analysis to assess the removal of concentrated dye from the sample chamber and CDx architecture.	50
Figure 2-10. A prototype CDx disc and DNA quantification data from on-disc extractions.	51
Figure 2-11. Evaluation of sperm cell DNA retention and recovery.....	52
Figure 3-1. Laser-actuated valve opening.....	64
Figure 3-2. Changes in Z-height alter the apparent size and shape of the laser spot on the disc surface.....	67

Figure 3-3. Working principle of laser irradiated, closable microchannels.....	68
Figure 3-4. Schematic diagram and photographs of the gantry platform for bringing the heating element into contact with the disc.....	71
Figure 3-5. Overview of the microfluidic disc and the sequence of valving/fluidic events.	75
Figure 3-6. Schematic diagrams of the PrTZAL platform and automated target channel alignment.....	76
Figure 3-7. Main effect plots of the selected generalized linear models from preliminary contact heating data.	81
Figure 3-8. Evaluation of valve closure via the contact heating method over a wider stylus temperature range.....	82
Figure 3-9. Initial evaluation of three primary variables (power, height, and time) and the effects on valve closure success (MANUAL SYSTEM).	84
Figure 3-10. Distribution plots for the evaluation of three key variables (power, height, and material type) and the effects on valve closure success (AUTOMATED SYSTEM).....	85
Figure 3-11. Evaluation of laser-actuated valve closure on the fully automated PrTZAL system.	88
Figure 4-1. Design and assembly of a VF disc.	98
Figure 4-2. On-disc microfluidic layout and vertical flow pattern.	101
Figure 4-3. Proof-of-principle dye studies to demonstrate feasibility of disc-based vertical flow through porous membranes.....	104
Figure 4-4. Exponential decay curves depicting the remaining fluid column height in the sample chamber (Δr) as a function of elapsed time.	108
Figure 4-5. Predicted changes in hydraulic pressure head (kPa) as a function of changing fluid column height (Δr).....	109
Figure 4-6. Semi-log transformation of drainage data for BioRAD 0.2 μm pore size membrane cut-outs when experiencing differing rotational frequencies.....	110
Figure 4-7. Exponential decay curves depicting the remaining fluid column height in the sample chamber (Δr) as a function of elapsed time.	112
Figure 4-8. Semi-log plots of the $\log_{10}\Delta r$ as a function of elapsed time. The slopes of these semi-log plots represent decay constants (k) for the draining fluid column.....	113
Figure 4-9. Changes in decay constant with differing sample composition and decreasing rotational frequency.	115
Figure 4-10. On-disc whole blood sample preparation.	116
Figure 4-11. On-disc flowthrough of large volume body fluid samples (human serum).	116
Figure 4-12. On-disc flowthrough of large volume body fluid samples (human urine).	117
Figure 5-1. Schematic comparison between lateral and vertical flow immunoassays.....	125
Figure 5-2. Overview of AOI generation via digital image cropping and color space conversion.	128

Figure 5-3. Overview of ROI generation via color thresholding and image masking.....	128
Figure 5-4. Scanned image of a fully assembled cVF disc (top view) and a close-up detailing a single cVFI testing domain.	130
Figure 5-5. Initial efforts to perform on-disc centrifugally assisted LFI.	134
Figure 5-6. Preliminary evaluation of on-disc VF immunocapture of Ebola VLP and <i>Y. pestis</i> YPF1 antigens.	136
Figure 5-7. Proof-of-Principle for on-disc cVFI immunocapture using a mouse IgG and goat anti-mouse antibody pair.	139
Figure 5-8. Proof-of-principle evaluation of an on-disc, sandwich-type, VFI for the detection of Ebola and <i>Y. pestis</i>	142
Figure 5-9. Detection of Zaire Ebola virus-like particles (VLP) using the LFI prototype system. A 10X eVLP dilution series (10 to 0.001 $\mu\text{g}/\text{ml}$) was prepared in chase buffer (n = 1 ea).	143
Figure 5-10. Detection of Zaire Ebola virus-like particles (VLP) using the cVFI prototype system.	144
Figure 5-11. Detection of Zaire Ebola virus-like particles (VLP) using the LFI prototype system.	149
Figure 6-1. Schematic overview of modifications to the CDx sample chamber vertex and outlet channel (top view).....	160
Figure 6-2. On-disc bead tracking studies.	162
Figure 6-3. Multidimensional orthographic projection of the proposed 3D printed sample chamber.	164
Figure 6-4. Schematic overview of the CDx disc and the integrated TCDE workflow.	167
Figure 6-5. Pilot study results attempting to extend on-disc assay sensitivity beyond 1 $\text{ng}/\mu\text{l}$	169
Figure 6-6. Image analysis of on-disc cVFI color responses at low eVLP concentrations (n= 3 ea at 1.0 and 0.1 $\text{ng}/\mu\text{l}$, n = 1 ea for positive and negative controls).....	170
Figure 6-7. Schematic top view of three cVFI disc designs and isometric projections of two 7-layer cVF microfluidic architectures.	172
Figure 6-8. Visualizing on-disc pressure sensitive adhesive (PSA) failures.	174
Figure 6-9. Meso-scale liquid handling and flow through.....	176
Figure 6-10. Schematic overview of the current fluorescence detection system.	177
Figure 6-11. Autofluorescence and photobleaching response curves for three different PeT films (n = 4 ea).	178
Figure 6-12. Autofluorescence and photobleaching response curves for different unbacked nitrocellulose membranes and unbacked, hydrophobic PVDF.....	179

List of Tables

Table 3-1. Laser diode settings and closure conditions for all laser-based closure experiments. 73

Table 4-1. Universal® Laser System settings for VF disc fabrication and PeT coverlet rastering.
..... 100

Table 4-2. Constituents and concentrations of artificial blood plasma body fluid simulant..... 102

Table 4-3. Constituents and concentrations of artificial urine body fluid simulant..... 102

Table 6-1. Critical features and optimal working temperatures for each of the enzyme components used in the TCDE process..... 166

List of Publications and Manuscripts in Preparation

The research described in this dissertation resulted in, or contributed to, the following publications:

1. Krauss, S. T.; Woolf, M. S.; Hadley, K. C.; Collins, N. M.; Nauman, A. Q.; Landers, J. P., Centrifugal microfluidic devices using low-volume reagent storage and inward fluid displacement for presumptive drug detection. *Sensors and Actuators B: Chemical* 2019, 284, 704-710.
2. Clark, C. P.; Farmehini, V.; Spiers, L.; Woolf, M. S.; Swami, N. S.; Landers, J. P., Real time electronic feedback for improved acoustic trapping of micron-scale particles. *Micromachines (Basel)* 2019, 10 (7), 489.
3. Clark, C. P. and Woolf, M. S.[†]; Karstens, S. L.; Lewis, H. M.; Nauman, A. Q.; Landers, J. P., Closable Valves and Channels for Polymeric Microfluidic Devices. *Micromachines (Basel)* 2020, 11 (7), 627. († CPC and MSW contributed equally to this work.)
4. Woolf, M. S.; Dignan, L. M.; Lewis, H. M.; Nauman, A. Q.; Tomley, C. J.; Landers, J., Optically-Controlled Closable Microvalves for Polymeric Centrifugal Microfluidic Devices. *Lab on a Chip* 2020, (20), 1426 - 1440.
5. Woolf, M. S.; Dignan, L. M.; Scott, A. T.; Landers, J. P., Digital postprocessing and image segmentation for objective analysis of colorimetric reactions. *Nature Protocols* 2020, 1-21.
6. Dignan, L. M.; Woolf, M. S.; Tomley, C. J.; Nauman, A. Q.; Landers, J. P., Multiplexed Centrifugal Microfluidic System for Dynamic Solid-Phase Purification of Polynucleic Acids Direct from Buccal Swabs. *Analytical Chemistry* 2021.
7. Woolf, M.S.; Dignan, L.M.; Karas, S.M.; Lewis, H.M.; Hadley, K.C.; Nauman, A.Q.; Geise, G.M.; Landers, J.P., Characterization of a Centrifugal Microfluidic Orthogonal Flow Platform. *Microfluidics and Nanofluidics* 2021, In preparation.
8. Woolf, M.S.; Dignan, L.M.; Karas, S.M.; Lewis, H.M.; Kim, S.N.; Geise, G.M.; DeMers, H.L.; Hau, D.; Gates-Hollingsworth, M.A.; AuCoin, D.P.; Landers, J.P., A Centrifugal Microfluidic Approach to Rapid Biothreat Detection via Vertical Flow Immunocapture. *Talanta* 2021, In preparation.
9. Woolf, M.S.; Hadley, K.C.; Moffett, R.P.; Landers, J.P., Towards an Affinity-Free, Centrifugal Microfluidic System for Rapid, Automated Forensic Differential Extraction. *Forensic Science International* 2021, In preparation.

Chapter 1 . Introduction and Literature Review

1.1 Introduction

1.1.1 *Centrifugal Microfluidics*

Microfluidic devices, such as micro total analysis systems (μ TAS)^{1, 2} and lab-on-a-CD platforms,³⁻⁶ offer attractive, unconventional approaches to standard sample preparation and analysis techniques.⁷ Self-contained, single-use, centrifugally-driven devices directly address many limitations associated with traditional, benchtop laboratory methods. As such, they are ideal candidates for the miniaturization and automation of clinical and forensic applications. These rotational devices offer immediate benefits that include *reduction of* (1) sample size and reagent volumes, (2) the number of sample handling and transfer steps, (3) cross-contamination, (4) potential sample loss, (5) processing time, (6), external hardware requirements, (7) hands-on time, and (8) user exposure to potentially dangerous samples. The centrifugal discs proposed in **Chapters 2-5**, much like the rotationally-driven bioanalytical disc described by Anderson et al. in August of 1969,⁸ exploit pseudo-gravitational forces to move fluids within the microfluidic architecture (**Figure 1-1**) without external intervention.

The exploitation of centrifugal force as the primary force driving fluid movement within a microfluidic architecture permits pulse-free fluid displacement and ultimately reduces instrument size and cost; by eliminating the need for peripheral hardware such as pneumatic and hydraulic syringe pumps.^{3, 4} In a rotational frame of reference, a liquid body with density ρ , spinning at a frequency ω , and positioned at a distance r from the center of rotation (CoR) will experience a centrifugal force,

$$f_{\omega} = \rho r \omega^2 \quad \text{Eq. 1}$$

a Coriolis force,

$$f_c = -2\rho\omega v \quad \text{Eq. 2}$$

and an Euler force.

$$f_E = \rho r \frac{d\omega}{dt} \quad \text{Eq. 3}$$

Key variables impacting the velocity of the fluid within the microchannel also include fluid viscosity (η), the average distance of the fluid plug (\bar{r}) from the center of rotation (CoR), and the radial extent of the fluid between the inner and outer menisci (Δr) (**Figure 1-1**). The influence of these forces on disc design in the *CDx* and *cVF* projects is discussed in subsequent chapters. Additionally, the relationship between these forces and the consequent approaches regarding flow control, microvalving, and embedded membranes are detailed.

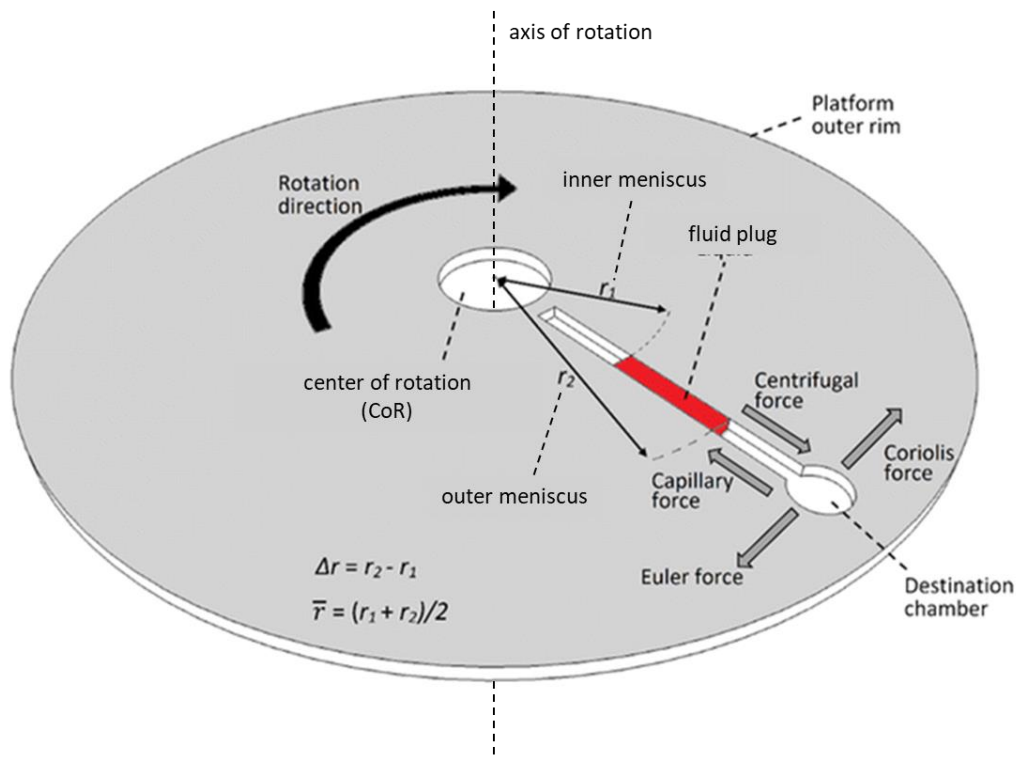


Figure 1-1. A centrifugal microfluidic disc with a well-defined fluid volume (red) in a straight microchannel. The microchannel is in the plane of the disc (xy plane) and is oriented perpendicular to the axis of rotation (z-axis). In this example, disc rotation is clockwise. Resultant forces acting on the fluid body are labeled with grey arrows, e.g., centrifugal force is radially outward from the center of rotation. In contrast, the Coriolis force is opposite the direction of rotation. Adapted with permission from [7].

1.1.2 Unit Operations - Overview

The adaptation of sample preparation and detection methods to a microfluidic device requires careful consideration of the requisite procedural steps to form a process chain. A process

chain is defined as a series of successive events or steps, and each discrete occurrence in the chain is referred to as a unit operation. For example, in mathematics, the quadratic equation can be viewed as an exemplary process chain, in which the order of each arithmetic unit operation occurs is dictated by order of precedence, i.e., working left-to-right, the order of arithmetic unit operations is parentheses, exponents, multiplication/division, addition/subtraction. Unit operations are not unique to mathematics and span multiple disciplines, including food processing, engineering, chemistry, and microfluidics. In microfluidics, the list of unit operations includes liquid transport (pumping, flow switching, and inward radial displacement), metering, aliquoting (sample splitting), centrifugation, separation, reagent storage, and reconstitution, washing, filtration, mixing, heating (incubation), and valving.^{9,10} Subsequent sections within this introductory chapter contextualize **Chapters 2-3** and **Chapters 4-5** by offering a concise review of the relevant unit operations, that is, microvalving strategies and embedded membranes, respectively.

1.1.3 *Unit Operations - Microvalving*

From a practical perspective, a microfluidic valve is defined as a device or method for regulating unidirectional fluid or gas movement within a microfluidic architecture. Judicious valve integration facilitates a wide array of additional unit operations in the microscale regime and serves as the linchpin of successful timed reagent release, mixing, metering, and flow switching. The indispensability of microvalving is evidenced by the fact that the number of valving events required for successful on-disc integration of a multistep analysis often approximates or exceeds the sum of steps prescribed by the equivalent benchtop protocol.¹¹ Nominally, microvalves must be 1) biocompatible with fluid samples, reagents, and downstream processes, 2) resistant to leakage and failure upon disc rotation, and 3) minimize fluid loss due to changes in surface retention or dead volume.^{11,12} Although additional classifications have been described, much of

the published literature related to microfluidics partitions microvalves into two wide-ranging categories; *passive* and *active* valves. Consequently, discussion hereafter is limited to these two valve states - valves in the *open* state permit flow, while valves in the *closed* state prevent flow.

Passive Valving Approaches

Capillary,¹³⁻¹⁶ check, siphon,¹⁷⁻¹⁹ and hydrophobic valves^{16, 20-22} are well documented and play essential roles in many microfluidic applications (**Figure 1-2**).^{3, 4, 23} With the exception of check valves, these valving strategies rely on the delicate interplay between capillary and rotationally-generated forces for actuation. Additionally, capillary, siphon, and hydrophobic valves are breached via single-use (sacrificial) opening events. In some respects, the *passive* moniker is fitting as each of these valves begins in the closed state and will resist fluid flow below specific rotational frequencies; no additional manipulation or actuation is required for the valve to remain closed. However, the term *passive valve* is a misnomer when viewed in the context of valve opening events. For valve opening to occur, these approaches all require increased hydraulic pressure at the fluid-valve interface, i.e., valve wetting and opening only occur at or above a particular *burst frequency*. As such, these valving strategies might be described more aptly as *frequency-dependent* or *rpm-dependent*.¹¹ Beyond valving semantics, these frequency-dependent approaches all suffer from one or more operational limitations.

First, as discussed, frequency-dependent valves function as single-use sacrificial valves that transition from closed-to-open states. None, except for check valves, are capable of sealing (resealing) microfeatures; thus, these valving strategies cannot be used to close previously opened microchannels and valves, isolate downstream liquid volumes, nor

prevent backflow. Second, all are sensitive to perturbation and failure under high pressure.

For instance, experiments outlined in **Chapter 2** demonstrate that high rotational

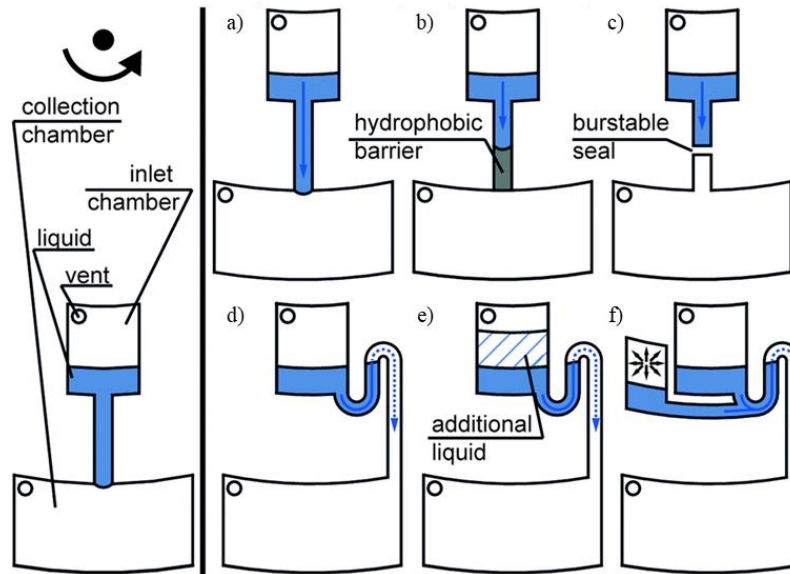


Figure 1-2. Passive, frequency-dependent microvalving strategies: (a) capillary, (b) hydrophobic, (c) burstable seal, (d) capillary siphon, (e) overflow siphon, and (f) pneumatic siphon valve. Adapted with permission from [12].

frequencies are needed for fluid recovery from absorbent sample cuttings. In the instance described, the first high-frequency fluid recovery step occurs very early in the CDx microfluidic process chain, precluding the implementation of serial siphon,¹⁷ capillary,⁹ or hydrophobic²¹ valving strategies that require progressive low-to-high frequency spin protocols. Third, with the exception of capillary valves, none act upon existing disc materials or architectural microfeatures; all require additional materials and components (e.g., printed xerographic toner, embedded elastomeric layers or structures, etc.), added microfluidic design complexity (e.g., siphon structures, capillary constrictions, elastomeric boss structures with corresponding valving ports and vias, etc.), or supplementary fabrication steps (e.g., surface treatments, xerographic toner printing/patterning, embedding elastomeric materials, etc.). Further, the integration of hydrophobic surface treatments, such as xerographic toner, raises questions about valve biocompatibility with

liquid samples. Finally, elastomeric check valves offer truly reversible, multi-use valving. However, these frequency-dependent valves have proven quite challenging to integrate into existing fabrication pipelines for disc-like centrifugal formats (**Figure 1-3**). To date, the successful integration of elastomeric check valves into discs fabricated via the print cut laminate (PCL) approach has not been reported.²⁴

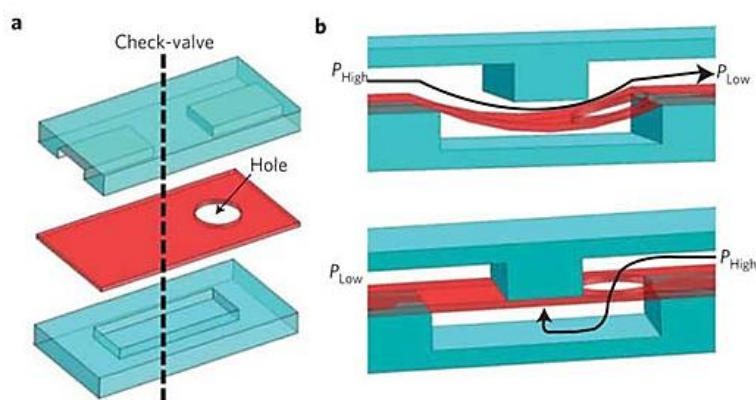


Figure 1-3. Integrated elastomeric components for microdevice flow control. (A) A three-layer exploded view of an elastomeric check valve. (B) Cross-sectional schematic of the check-valve in the open and closed states. Adapted with permission from [25].

Active Valving Approaches

Active microvalves require additional means of actuation, independent of the disc's rotational frequency. Three core valving approaches in alternative microfluidic systems are discussed here to provide context for later discussions in **Chapters 2** and **4**, including frequency-independent elastomeric, phase-change wax, and laser-based valve opening. Frequency-independent, elastomeric diaphragms, such as Quake^{26, 27} and Mathies^{28, 29} valves, provide true reversible valving capabilities. These elastomeric diaphragms exploit the flexibility of polydimethylsiloxane (PDMS) membranes to selectively obstruct fluid flow. Each valve is comprised of two primary layers - one fluidic (flow channels) and one pneumatic with a flexible, intervening membrane (control channels) (**Figure 1-4**).^{26, 27} Actuation and suppression of external

pumps permit precise, complex, and dynamic microfluidic control. However, these frequency-independent, elastomeric valving systems are not readily amendable to rotational microfluidics, thereby increasing architectural design complexity and adding substantial time to the fabrication process. Unavoidably, this valving strategy also requires an extensive, external, pneumatic control system (e.g., external valves, control lines, pumps, etc.), ultimately impacting the overall intricacy, size, and manufacturing cost of the supporting instrumentation.

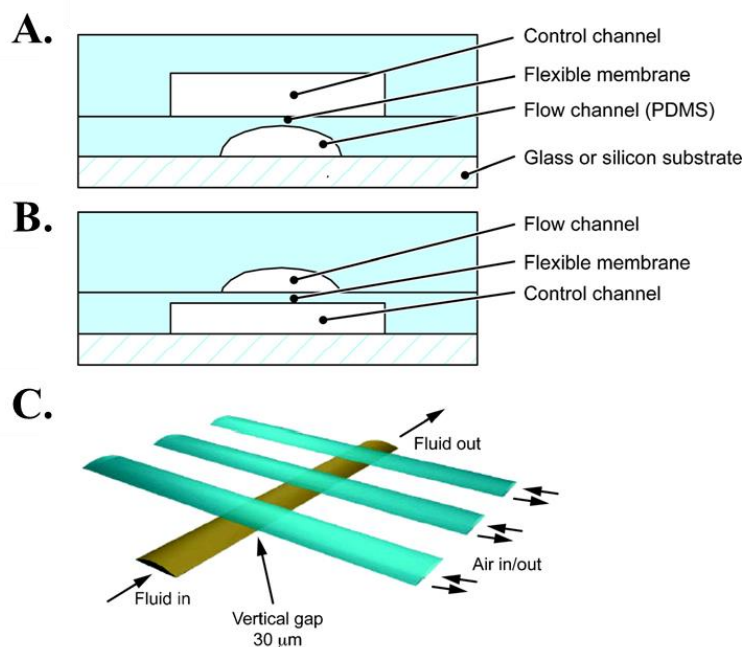


Figure 1-4. Schematic views of two-layer, frequency-independent, elastomeric, polydimethylsiloxane (PDMS) microfluidic valves. (A) An elastomeric push-down valve is formed where the flow channel is positioned orthogonal to the pneumatic control channel directly above. (B) Alternatively, a push-up valve forms where a control channel lies orthogonal to and below the flow channel. (C) Schematic of a linear peristaltic pump using three membrane valves in a series. Adapted with permission from [27].

Phase-change wax valves rely on the incorporation of meltable, paraffin-based substances to provide single-use or, in some instances, reversible valve operation. Early examples of these valves required pneumatic/vacuum systems, integrated microheaters, or large external heating sources for full functionality (Figure 1-5A-C).^{30, 31} More recent iterations of this wax-based approach utilize laser irradiation and paraffin-based ferrofluids to facilitate valve actuation,

effectively supplanting microheaters, minimizing peripheral hardware, and simplifying operational control (**Figure 1-5D and E**).³² These phase-change wax-based approaches offer vigorous on-disc fluidic control. However, each phase-change valving strategy requires either the incorporation of wax or dictates increased fabrication complexity to the disc or the supporting hardware.

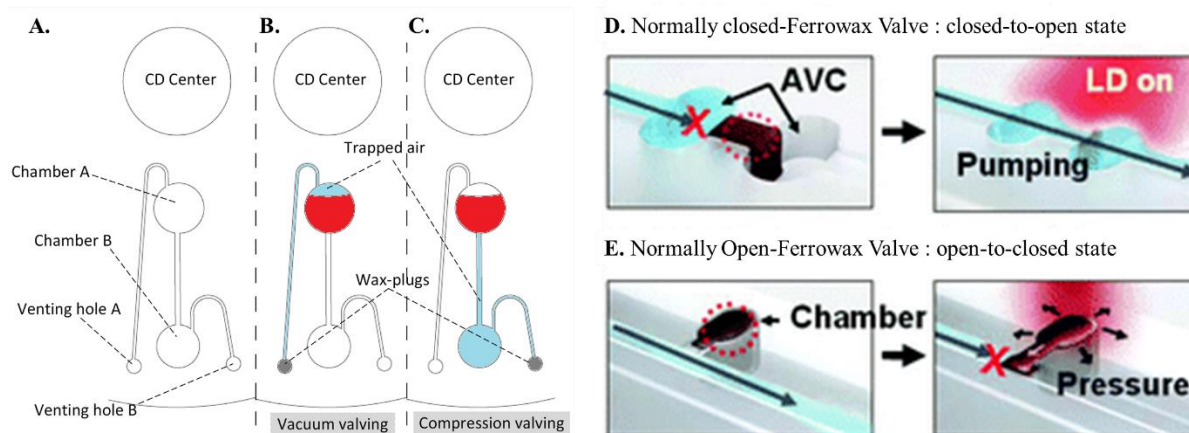


Figure 1-5. Different approaches to frequency-independent wax-based microvalving. (A) General design for testing vacuum/compression valving approaches with overviews of (B) vacuum valving (C) and compression valving setups. (D and E) Schematic diagrams depicting the operation of laser irradiated ferrowax microvalves. (D) In the normally closed version of the valve, wax is housed between two assistant valve chambers (AVCs). Irradiated nanoparticles within the paraffin wax plug transfer heat energy to the surrounding wax, resulting in accelerated wax melting and flow. As designed, the wax plug resolidifies and is trapped in the downstream AVC. (E) The ferrowax AVC chamber is located adjacent to the main channel for the normally open version of the valve. Upon irradiation, the ferrowax melts and expands into the main channel, solidifying and blocking the channel. Adapted with permission from [30] and [32].

Minimally, heat-activated wax valves require the incorporation of a phase-change medium (e.g., wax) into the microfluidic architecture, which presents challenges to, or precludes, disc fabrication methods that require heat bonding of layers. To this point, successful integration of wax-based valves within PCL fabricated discs has not yet been reported. Adding wax to PCL fabricated discs pre-lamination results in premature valve actuation and ultimate disc/assay failure, while adding wax to discs post-lamination adds considerable time and complexity to the fabrication process chain. Further, wax valving materials are often in direct contact with liquid samples and reagents during actuation (e.g., heating and liquefaction); this raises concern

regarding sample contamination, the intermingling of phase-change materials, and biocompatibility. Finally, depending on the approach, phase-change wax valving dictates added architectural design complexity (e.g., AVC chambers, holding reservoirs for wax materials, added venting or chambers for vacuum/compression generation, etc.), compels additional external controls and components (heating elements, temperature sensing elements, mixing structures), and entails microarchitectures that occupy significant on-disc space (e.g., large on-disc footprint in the xy plane). Overall, the conditions and constraints for wax valving make it an impractical and unattractive option for flow control on PCL fabricated discs.

Single-use, laser-irradiated valves offer a simple, easily implemented approach to valve opening.^{33, 34} These destructible valves function well regardless of fluidic pressure or rotational frequency. Laser-actuated valves require minimal microfluidic architectural modification, have a negligible on-disc footprint, and are compatible with existing disc materials and microfeatures. Peripheral hardware requirements are nominal and entail little more than a laser diode or other means of electromagnetic irradiation. The earliest description of on-disc laser-based valve opening can be found in a patent filed by Zuccheli and Van de Vyver in 2004 (**Figure 1-6**).³³ In that patent, the inventors described a three-layer microfluidic disc comprised of two component layers (substrate layers) separated by an intervening material layer (perforation layer) with ‘*selected adsorptive properties.*’

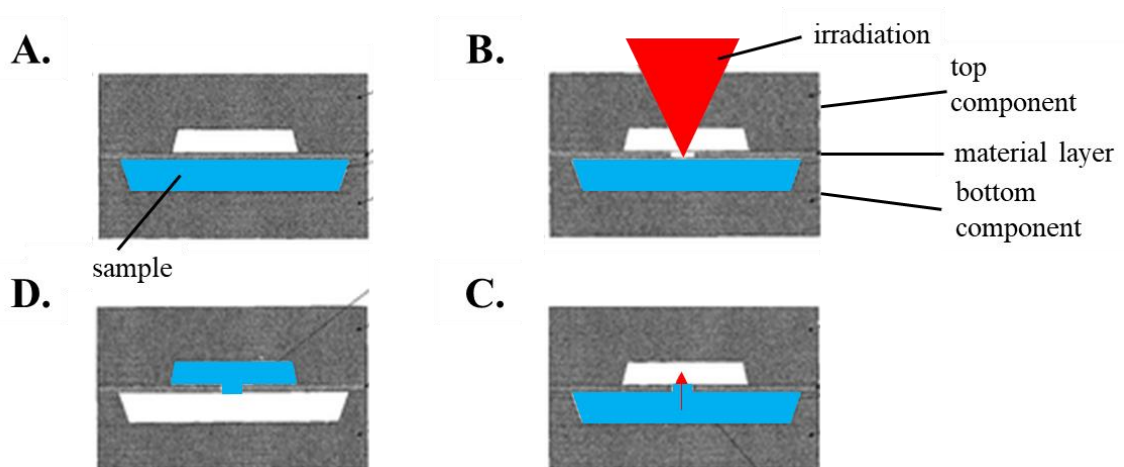


Figure 1-6. A section of the microfluidic disc. (A and B) Microfluidic components within each top and bottom component are separated by a material layer. The bottom microfluidic component contains a fluid or sample, and the material layer is perforated by electromagnetic radiation. (C and D) The sample moves from the bottom microfluidic chamber to the top via centrifugal forces. Adapted from [33].

As described, each valve is irreversible and begins in a closed state. Before actuation, an intact material layer (perforation layer) prevents flow and communication between fluidic channels in the adjacent substrate layers (**Figure 1-6A**). A focusing system is used to minimize spot size and concentrate irradiation energy at the surface of the material layer, causing localized heating of the material layer and subsequent perforation formation (**Figure 1-6B** and **C**). Perforation at the irradiation site permits fluid transport between previously unconnected fluidic channels in the neighboring substrate layers (**Figure 1-6C** and **D**). Adaptations of this laser-based valve opening approach include patterning clear polyethylene terephthalate (PeT) films with black (high optical density) xerographic toner from an off-the-shelf office laser printer (**Figure 1-7**).³⁴ As described by the authors, patterning the transparent films with small, targeted spots eliminates the need for an entire surface or layer of absorbing material. This targeted patterning reduces the impact of irradiation on the surrounding materials, minimizes the need for laser spot accuracy, and presents the possibility of valve opening via scanning during active disc rotation. The Landers Lab has published numerous papers using this valve opening method.

Briefly, toner patches were printed onto transparent PeT films (Film Source, Inc. Maryland Heights, MO, USA or CG5000, 3M, Maplewood, Minnesota, USA) using a LaserJet 4000 (HP, Palo Alto, CA, USA). Two printer passes resulted in a toner thickness of $\sim 12 \mu\text{m}$. Valves were opened via laser irradiation for 2 seconds with a 700 mW, 638 nm laser diode (Thorlabs, Inc., Newton, NJ) located 2 cm above the disc surface.

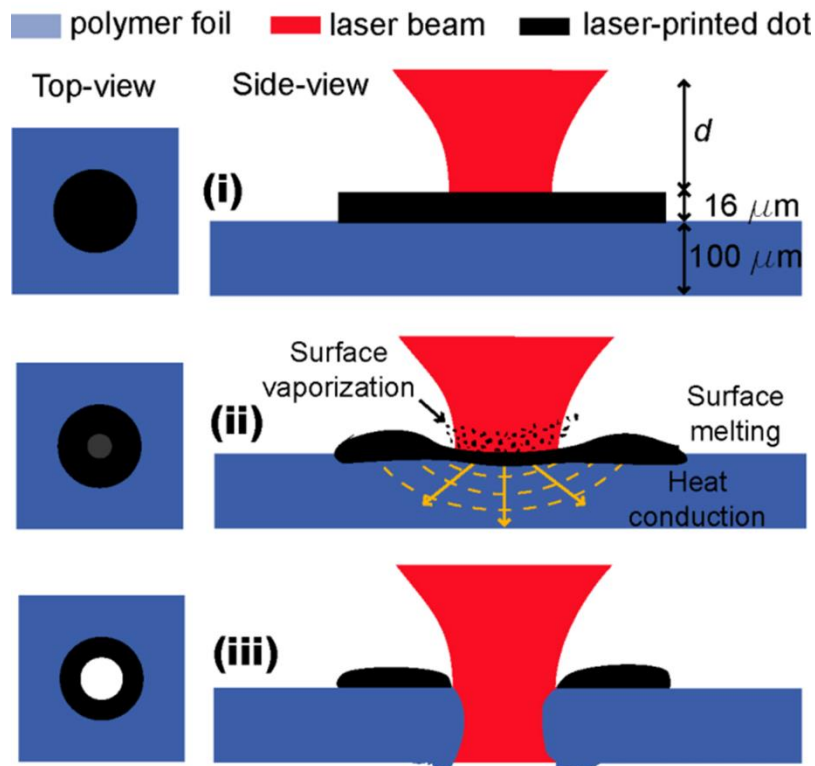


Figure 1-7. Modified laser-based valve opening via patterning of xerographic toner. (i) Toner patches are irradiated with a focused laser. (ii) Sustained irradiation induces localized heating, melting, and evaporation. (iii) Under optimized conditions, a perforation is produced at the point of irradiation. Adapted with permission from [34].

Despite those successes, printed toner valving presented a unique set of challenges. Superficially, patterning transparent PeT films with xerographic toner seems trivial; from experience, the opposite is more frequently true. Toner valve failure modes include poor alignment of the irradiation source with the targeted spot and rapid heating and vaporization of the toner before perforation formation. Poor alignment of the irradiation source and target spot can be due to inadequate tolerances of the homing, sensing, and orientation

system or inconsistency in the toner printing process. For example, previous work in the Landers Lab showed that two passes through a laser printer were required to achieve sufficient toner density on the PeT film surface. Sources of variability during this double printing step included poor alignment of the PeT film in the feed tray, variability in feed mechanism, and thermal shrinkage of the PeT film. Qualitatively, printed toner density varied with toner cartridge fill level, age of the printer and cartridge, and toner manufacturer. Further, changes in toner composition were frequently implicated as a possible source of valving failure, i.e., lot-to-lot variation, item discontinuation, and item unavailability from suppliers. Issues related to premature vaporization of the toner were partially remedied by depositing toner on both sides of the PeT film; however, this required four total passes through the printer, which induced further thermal shrinkage and created additional challenges related to the alignment of the top and bottom patches. Although not discussed in published literature, printer toner surfaces raise concerns regarding sample contamination; for example, concentrated acids, chloroform, and other organic solvents can induce toner dissolution or resuspension. Additionally, biocompatibility could be compromised, e.g., iron oxide, a common component of xerographic toners, is a known PCR and other nucleic acid assay inhibitor.

In the Landers Lab, challenges related to toner solvation and intermingling were addressed by minimizing toner-solvent exposure time and/or replacing toner with black PeT monolayers (bPeT) (**Chapter 3**) or insertable bPeT cut-outs (not published). Other groups have shown that black polyethylene pieces can be inserted into polycarbonate discs to engender valve opening and flow control; slight disc rotation during valve irradiation induced elongated perforations (**Figure 1-8**).³⁵

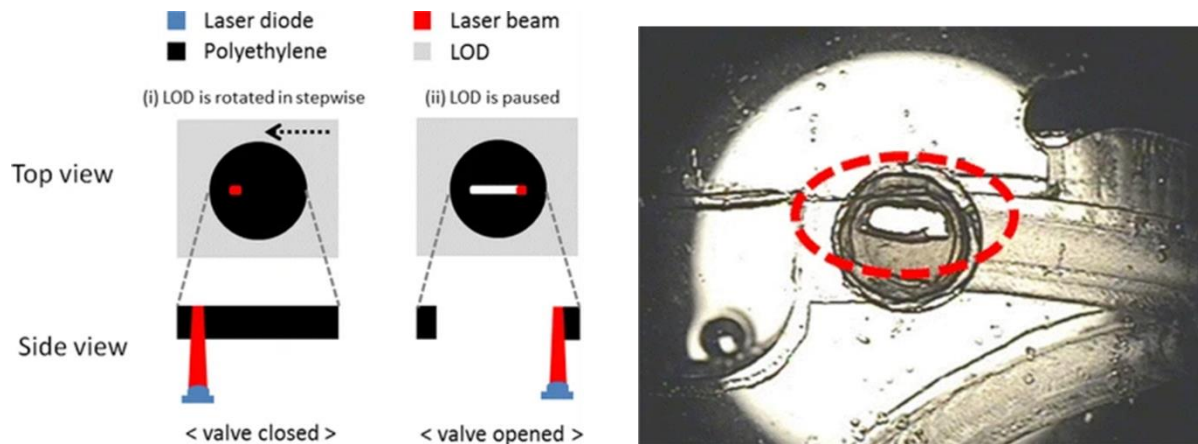


Figure 1-8. Schematic diagram showing the opening of an insertable polyethylene terephthalate (bPeT) piece (*left*). A combination of focused laser irradiation with disc rotation creates an elongated perforation in the embedded bPeT material (*photograph-right*). Adapted with permission from [35].

Single-shot laser valves offer a simple, easy-to-implement approach to valve opening.³³⁻³⁵ These destructible valves function well regardless of fluidic pressure or rotational frequency. Yet, despite these benefits, they offer no resolution to the problem of microfeature sealing and closure, which are often required for accurate fluidic control in complex or highly multiplexed microsystems. Microvalves that can be closed on-demand provide a way to seal chambers during heating or incubation steps, allow for precise metering without backflow of reagents due to wicking, and prevent cross-contamination and crosstalk between reservoirs or elution steps. In **Chapter 3**, I describe two methods for microchannel closure. The studies presented in that chapter coincided with work from another group published in September 2018.³⁶ In that system, laser-based valving was facilitated by integrating ethylene vinyl acetate (EVA) thermoplastic pieces into the middle layer of a polycarbonate disc. Valve (microchannel) closure is prompted when the EVA material near a channel inlet (**Figure 1-9a**) was heated with a laser module for 10 seconds. Then, the downstream microchannel was blocked and sealed with melted EVA (**Figure 1-9b**) during a subsequent disc spin step.

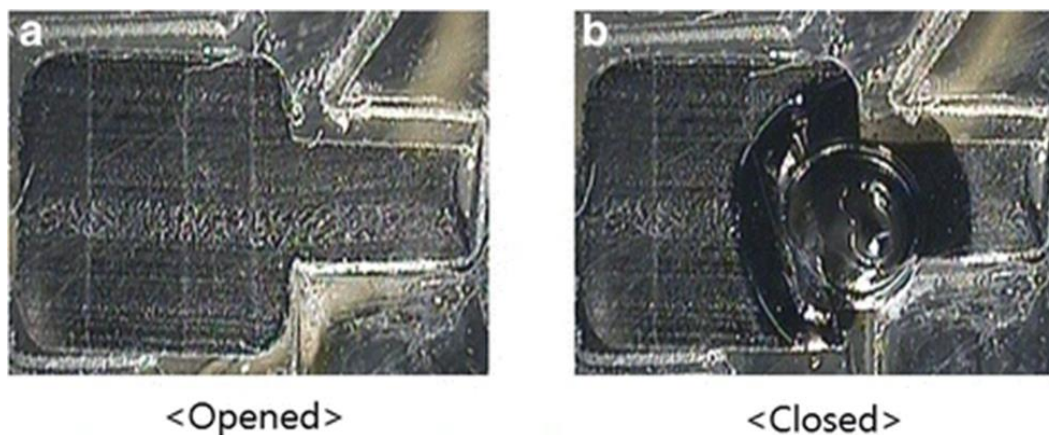


Figure 1-9. Magnified view of a single-use, closable ethylene vinyl acetate (EVA) valve. (A) Fluid can flow freely through an otherwise open channel located within the top layers of the disc. (B) Microchannel closure is induced via laser irradiation and melting of the underlying EVA material. Adapted with permission from [36].

1.1.4 Unit Operations - Embedded Membranes

Porous membranes are central to many macroscale applications spanning a range of disciplines.³⁷ Embedding porous membranes into centrifugal discs extends functionality and adds several unique unit operations to the ‘*microfluidic toolbox*.’ This section is intended to help contextualize **Chapters 4** and **5** by offering a succinct appraisal of the relevant literature pertaining to on-disc integration of embedded membranes. To date, the preponderance of on-disc, membrane-based applications have focused on filtration and separation of particulates from fluid samples.³⁸⁻⁴⁰ As described, each of these membrane-based techniques shares a similar on-disc fluid flow path and differ primarily in how the membranous material is integrated into the fully assembled disc.

In 2013, Karle et al. demonstrated on-disc filtration and pre-concentration of bacteria from environmental water samples (**Figure 1-10A**). In that publication, thin, microporous polycarbonate film material (polycarbonate track etch filter material, 0.2 μm pore size) was embedded within milled PMMA discs. Permanently heat bonding the filters to the PMMA substrate before final disc assembly and lamination ensured that the microfluidic architecture was sealed, creating a distinctive, leak-free flow path. Templeton et al. later affirmed the utility of this approach by describing an on-disc system to remove sediment from environmental water samples

that enabled downstream, on-disc analysis of the permeate fraction (**Figure 1-10B**). In those studies, glass microfiber and cellulosic membrane cut-outs (4.5 mm radius) were permanently sealed into milled polycarbonate discs and each filter was solvent bonded to a polycarbonate disc layer (acetone and manual pressure) before final disc assembly and sealing (intervening double-sided adhesive layers).

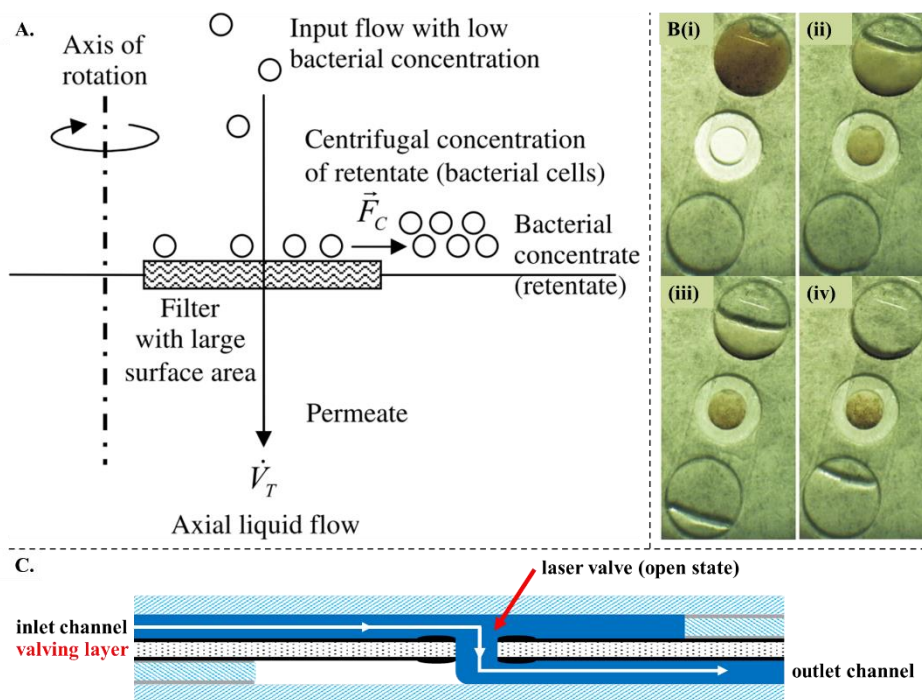


Figure 1-10. Leak-free on-disc orthogonal through embedded membranes. **(A)** Schematic illustration of orthogonal (axial) flow of fluid permeates with concomitant particle (bacteria) removal via continuous centrifugation. **(B)** Demonstration of on-disc orthogonal flow filtration for sediment removal from environmental water samples. **(C)** Three-dimensional microchannel flow stream that includes two 90° turns and a portion of the flow paths perpendicular to the plane of the disc. Adapted with permission from [38, 39, 41].

In the previous sections, irradiation of an optically dense valving layer creates a permanent connection between fluidic channels, i.e., single-use, laser-based valve opening events permit fluid communication between previously disconnected channels (**Figure 1-10C**). Flow through the inlet channel is outward from the center of rotation. At the newly formed perforation, the fluid stream turns 90° , and the flow path is directed orthogonally (relative to the xy plane, the plane of the disc) through the hole. The fluid stream again turns 90° and proceeds, unincumbered, through the outlet

channel. With embedded membranes, the three-dimensional flow path through the filtration system is only slightly different. Briefly, the porous media is inserted into the middle layer of the disc and directly into this flow path. The flow stream is directed orthogonally through the membrane at the fluid-membrane interface (**Figure 1-10A**). Membrane fouling (clogging of pores with particulate, cells, or other substances) is prevented by continuously removing particles (e.g., bacteria, sediment, blood cells, etc.) from the filter at the fluid-filter interface. For example, bacteria, which are excluded by the filter, continue to experience the centrifugal field (\vec{F}_C); ongoing exposure to the centrifugal forces compels unremitting outward radial displacement of particles, forming an enriched bacterial retentate or compact sediment pellet (**Figure 1-10A and B**, respectively). Lenz et al. used the term *cross-flow* to describe this ongoing outward radial displacement of particles (**Figure 1-11**).⁴⁰

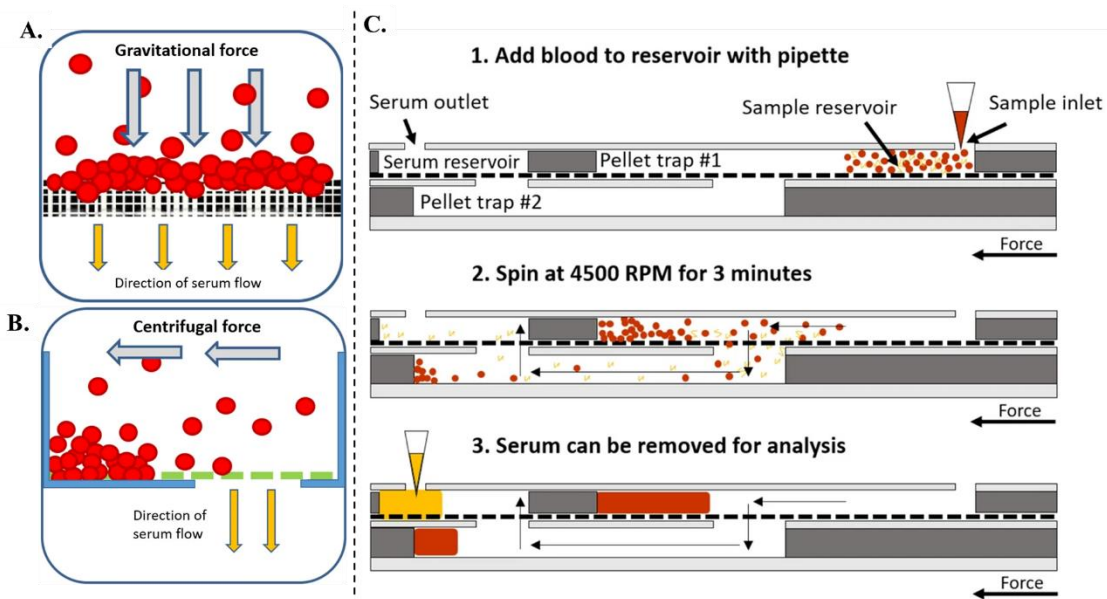


Figure 1-11. Schematic illustrations of conventional (A) dead-end flow filtration and (B) on-disc filtration. (C1) The initial flow stream is radially outward from the center of rotation. (C2) As hydraulic pressure increases, serum passes through the embedded membrane, while most red blood cells are diverted via filter exclusion and *cross-flow* into the pellet trap. (C3) Red blood cells that escaped the first filtration step are captured in a second downstream pellet trap. Adapted with permission from [40].

Collectively, these publications show clear proof-of-principle for on-disc flowthrough of embedded porous media. However, none of these approaches utilize implanted nanoporous membranes for anything other than filtration. On the contrary, Kainz et al. described a rotationally driven microfluidic system for enhanced flow control for lateral flow strips (**Figure 1-12**).⁴² Unlike the embedded membrane strategies described above, the three-dimensional flow path employed here does not involve 90 ° turns or orthogonal flow through the membrane. Rather, the porous membrane, inlet, and outlet are aligned radially and in the same *xy plane*, positioning the membrane directly in the flow stream and creating a parallel (lateral) flow path (**Figure 1-12**). Ideally, the flow path would carry all of the fluid sample into and through the membrane, i.e., flow rate to the membrane (Q_{ch}) equal to the flow rate through the membrane (Q_m) (**Figure 1-12B**).

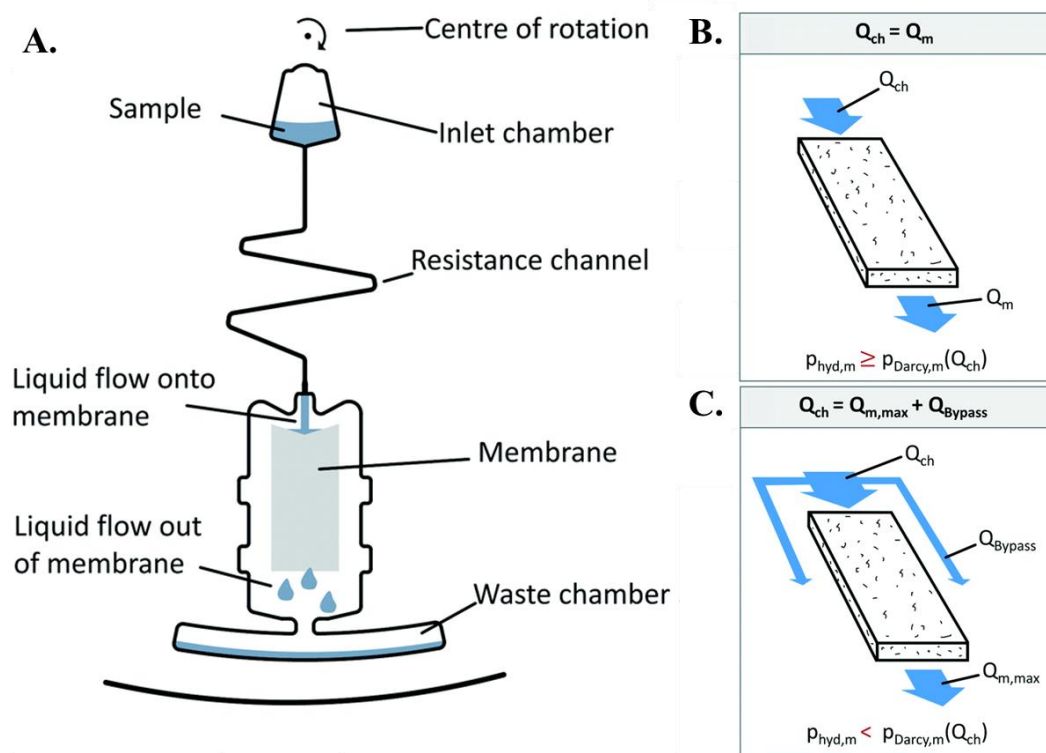


Figure 1-12. A centrifugal microfluidic approach to enhanced flow control for lateral flow strips. (A) Schematic illustration of the microfluidic architecture. The porous membrane is inserted into the disc directly in the flow path. (B) When flow rate to the membrane (Q_{ch}) equals flow rate through the membrane (Q_m), all fluid flow is directed through the membrane. (C) When $Q_{ch} > Q_{m,max}$, undesirable bypass flow occurs. Adapted with permission from [42].

However, unlike the previously discussed strategies for membrane integration, this on-disc approach did not bond the porous material directly to the disc. Thus, there was no creation of a leak-free membrane-disc seal. Accordingly, undesirable bypass flow could occur when there was insufficient centrifugal pressure on the liquid column within the porous medium to ensure complete liquid transfer through the membrane; that is, the flow rate to the membrane (Q_{ch}) exceeds the upper limit for possible flow through the membrane ($Q_{m,max}$) (**Figure 1-12C**). Summarized plainly, this report demonstrated effective on-disc immunocapture and antigen detection via sandwich-type immunoassay and gold nanoparticle detection; on-disc flow was adjustable and controlled entirely through centrifugal force. No other absorbent pads (wicking or otherwise) were needed. As described, this approach did not account for membrane swelling, changes in sample matrix composition, loss of hydraulic pressure due to changes in sample chamber filling height, and relied heavily upon the delicate interplay between Q_{ch} , Q_m , and $Q_{m,max}$.

1.1.5 *Description of Research Goals and Concluding Remarks*

This dissertation focuses on the development of two centrifugal microfluidic systems that address distinct unmet needs and technology gaps in forensic and biomedical sciences. These include methods for centrifugal differential extraction (*CDx*) from forensic cellular mixtures and vertical flow immunoassay (*cVFI*) systems for biomedical applications. Once fully developed, these rotationally-driven systems are poised to impact the target disciplines significantly. In large part, the future success of these parent projects hinges upon key microfluidic functionality, chiefly microvalving and on-disc flow through porous media. Understanding the advantages and limitations of these existing techniques provides some insight into the decision-making and

research objectives. Accordingly, this introductory chapter provides the requisite context for the research directions outlined in the coming chapters.

With regard to the *CDx* project, the overarching research goal was to design and develop a centrifugal microfluidic architecture capable of performing and automating a complete forensic differential extraction sample preparation, i.e., preferential cellular lysis. Initial design and testing efforts towards that goal are detailed in **Chapter 2**. Optimization of flow control and microvalving strategies were major hurdles in the development of the *CDx* architecture. Without exception, the valving approaches described in this chapter are not amenable to the PCL disc fabrication approach. As such, two novel approaches to valve closing were explored, described, and characterized. The contact heating and laser-based methods for closing microvalve on polymeric microfluidic discs are described in **Chapter 3**.

The driving motivator for the *cVFI* project was to develop an on-disc system capable of outperforming existing lateral flow immunoassay (LFI) test strips. As currently designed, the *cVF* disc includes embedded nanoporous membranes that are permanently bonded to the disc substrates during the disc fabrication process. Accordingly, the three-dimensional flow path directs the flow stream orthogonally through the membrane.

The goal of the studies presented in **Chapter 4** was to characterize on-disc flow through insertable membranes, emphasizing the impact of changing fluid filling height, sample composition, and dynamic adjustments to cellulosic membranes during prolonged periods of fluid exposure. Finally, the research objective for the studies detailed in **Chapter 5** was twofold - to demonstrate on-disc immunocapture via sandwich-type assay and provide an initial assessment of on-disc assay performance.

In short, the following chapters highlight key challenges and findings in the development of the two parent projects (*CDx* and *cVFI*), as well as detailed insights regarding closable valving and on-disc vertical flow through porous media. **Chapter 6** provides added discussion of ongoing efforts, persistent challenges, and future directions for each project.

1.2 References

1. Reyes, D. R.; Iossifidis, D.; Auroux, P.-A.; Manz, A., Micro total analysis systems. 1. Introduction, theory, and technology. *Analytical chemistry* **2002**, *74* (12), 2623-2636.
2. Manz, A.; Graber, N.; Widmer, H. á., Miniaturized total chemical analysis systems: a novel concept for chemical sensing. *Sensors and actuators B: Chemical* **1990**, *1* (1-6), 244-248.
3. Ducrée, J.; Haeberle, S.; Lutz, S.; Pausch, S.; Von Stetten, F.; Zengerle, R., The centrifugal microfluidic Bio-Disk platform. *Journal of Micromechanics and Microengineering* **2007**, *17* (7), S103.
4. Gorkin, R.; Park, J.; Siegrist, J.; Amasia, M.; Lee, B. S.; Park, J.-M.; Kim, J.; Kim, H.; Madou, M.; Cho, Y.-K., Centrifugal microfluidics for biomedical applications. *Lab on a Chip* **2010**, *10* (14), 1758-1773.
5. Madou, M.; Zoval, J.; Jia, G.; Kido, H.; Kim, J.; Kim, N., Lab on a CD. *Annu. Rev. Biomed. Eng.* **2006**, *8*, 601-628.
6. Lai, S.; Wang, S.; Luo, J.; Lee, L. J.; Yang, S.-T.; Madou, M. J., Design of a compact disk-like microfluidic platform for enzyme-linked immunosorbent assay. *Analytical chemistry* **2004**, *76* (7), 1832-1837.
7. Al-Faqheri, W.; Thio, T. H. G.; Qasaimeh, M. A.; Dietzel, A.; Madou, M., Particle/cell separation on microfluidic platforms based on centrifugation effect: a review. *Microfluidics and Nanofluidics* **2017**, *21* (6), 1-23.
8. Anderson, N. G., The development of automated systems for clinical and research use. *Clinica Chimica Acta* **1969**, *25* (2), 321-330.
9. Madou, M. J.; Kellogg, G. J. In *LabCD: a centrifuge-based microfluidic platform for diagnostics*, Systems and Technologies for Clinical Diagnostics and Drug Discovery, International Society for Optics and Photonics: 1998; pp 80-93.
10. Duffy, D. C.; Gillis, H. L.; Lin, J.; Sheppard, N. F.; Kellogg, G. J., Microfabricated Centrifugal Microfluidic Systems: Characterization and Multiple Enzymatic Assays. *Analytical Chemistry* **1999**, *71* (20), 4669-4678.
11. Abi-Samra, K.; Hanson, R.; Madou, M.; Gorkin III, R. A., Infrared controlled waxes for liquid handling and storage on a CD-microfluidic platform. *Lab on a Chip* **2011**, *11* (4), 723-726.
12. Strohmeier, O.; Keller, M.; Schwemmer, F.; Zehnle, S.; Mark, D.; von Stetten, F.; Zengerle, R.; Paust, N., Centrifugal microfluidic platforms: advanced unit operations and applications. *Chemical Society Reviews* **2015**, *44* (17), 6187-6229.

13. Zhang, C.; Xing, D.; Li, Y., Micropumps, microvalves, and micromixers within PCR microfluidic chips: Advances and trends. *Biotechnology Advances* **2007**, *25* (5), 483-514.
14. Glière, A.; Delattre, C., Modeling and fabrication of capillary stop valves for planar microfluidic systems. *Sensors and Actuators A: Physical* **2006**, *130*, 601-608.
15. Maria, M. S.; Rakesh, P.; Chandra, T.; Sen, A., Capillary flow-driven microfluidic device with wettability gradient and sedimentation effects for blood plasma separation. *Scientific reports* **2017**, *7*, 43457.
16. Tsougeni, K.; Papageorgiou, D.; Tserepi, A.; Gogolides, E., “Smart” polymeric microfluidics fabricated by plasma processing: controlled wetting, capillary filling and hydrophobic valving. *Lab on a Chip* **2010**, *10* (4), 462-469.
17. Siegrist, J.; Gorkin, R.; Clime, L.; Roy, E.; Peytavi, R.; Kido, H.; Bergeron, M.; Veres, T.; Madou, M., Serial siphon valving for centrifugal microfluidic platforms. *Microfluidics and nanofluidics* **2010**, *9* (1), 55-63.
18. Steigert, J.; Brenner, T.; Grumann, M.; Riegger, L.; Lutz, S.; Zengerle, R.; Ducrée, J., Integrated siphon-based metering and sedimentation of whole blood on a hydrophilic lab-on-a-disk. *Biomedical microdevices* **2007**, *9* (5), 675-679.
19. Gorkin, R.; Soroori, S.; Southard, W.; Clime, L.; Veres, T.; Kido, H.; Kulinsky, L.; Madou, M., Suction-enhanced siphon valves for centrifugal microfluidic platforms. *Microfluidics and Nanofluidics* **2012**, *12* (1), 345-354.
20. Feng, Y.; Zhou, Z.; Ye, X.; Xiong, J., Passive valves based on hydrophobic microfluidics. *Sensors and Actuators A: Physical* **2003**, *108* (1-3), 138-143.
21. Ouyang, Y.; Wang, S.; Li, J.; Riehl, P. S.; Begley, M.; Landers, J. P., Rapid patterning of ‘tunable’ hydrophobic valves on disposable microchips by laser printer lithography. *Lab on a Chip* **2013**, *13* (9), 1762-1771.
22. Thompson, B. L.; Ouyang, Y.; Duarte, G. R.; Carrilho, E.; Krauss, S. T.; Landers, J. P., Inexpensive, rapid prototyping of microfluidic devices using overhead transparencies and a laser print, cut and laminate fabrication method. *Nature protocols* **2015**, *10* (6), 875-86.
23. Mark, D.; Haeberle, S.; Roth, G.; Von Stetten, F.; Zengerle, R., Microfluidic lab-on-a-chip platforms: requirements, characteristics and applications. In *Microfluidics based microsystems*, Springer: 2010; pp 305-376.
24. Thompson, B. L.; Ouyang, Y.; Duarte, G. R.; Carrilho, E.; Krauss, S. T.; Landers, J. P., Inexpensive, rapid prototyping of microfluidic devices using overhead transparencies and a laser print, cut and laminate fabrication method. *Nature protocols* **2015**, *10* (6), 875.
25. Mosadegh, B.; Kuo, C.-H.; Tung, Y.-C.; Torisawa, Y.-s.; Bersano-Begey, T.; Tavana, H.; Takayama, S., Integrated elastomeric components for autonomous regulation of sequential and oscillatory flow switching in microfluidic devices. *Nature physics* **2010**, *6* (6), 433-437.
26. Thorsen, T.; Maerkl, S. J.; Quake, S. R., Microfluidic large-scale integration. *Science* **2002**, *298* (5593), 580-584.
27. Melin, J.; Quake, S. R., Microfluidic large-scale integration: the evolution of design rules for biological automation. *Annu. Rev. Biophys. Biomol. Struct.* **2007**, *36*, 213-231.

28. Grover, W. H.; Ivester, R. H.; Jensen, E. C.; Mathies, R. A., Development and multiplexed control of latching pneumatic valves using microfluidic logical structures. *Lab on a Chip* **2006**, *6* (5), 623-631.
29. Zhang, W.; Lin, S.; Wang, C.; Hu, J.; Li, C.; Zhuang, Z.; Zhou, Y.; Mathies, R. A.; Yang, C. J., PMMA/PDMS valves and pumps for disposable microfluidics. *Lab on a Chip* **2009**, *9* (21), 3088-3094.
30. Al-Faqheri, W.; Ibrahim, F.; Thio, T. H. G.; Moebius, J.; Joseph, K.; Arof, H.; Madou, M., Vacuum/compression valving (VCV) using paraffin-wax on a centrifugal microfluidic CD platform. *PloS one* **2013**, *8* (3), e58523.
31. Oh, K. W.; Namkoong, K.; Chinsung, P., A phase change microvalve using a meltable magnetic material: Ferro-Wax. *Micro Total Analysis Systems* **2005**, *1*, 554-556.
32. Park, J.-M.; Cho, Y.-K.; Lee, B.-S.; Lee, J.-G.; Ko, C., Multifunctional microvalves control by optical illumination on nanoheaters and its application in centrifugal microfluidic devices. *Lab on a Chip* **2007**, *7* (5), 557-564.
33. Zucchelli, P.; Van de Vyver, B., Devices and methods for programmable microscale manipulation of fluids. Google Patents: 2006.
34. Garcia-Cordero, J. L.; Kurzbuch, D.; Benito-Lopez, F.; Diamond, D.; Lee, L. P.; Ricco, A. J., Optically addressable single-use microfluidic valves by laser printer lithography. *Lab on a Chip* **2010**, *10* (20), 2680-2687.
35. Choi, M.-S.; Yoo, J.-C., Automated centrifugal-microfluidic platform for DNA purification using laser burst valve and coriolis effect. *Applied biochemistry and biotechnology* **2015**, *175* (8), 3778-3787.
36. Ko, J.; Yoo, J.-C., Loop-mediated isothermal amplification using a lab-on-a-disc device with thin-film phase change material. *Applied biochemistry and biotechnology* **2018**, *186* (1), 54-65.
37. Adiga, S. P.; Jin, C.; Curtiss, L. A.; Monteiro-Riviere, N. A.; Narayan, R. J., Nanoporous membranes for medical and biological applications. *Wiley Interdisciplinary Reviews: Nanomedicine and Nanobiotechnology* **2009**, *1* (5), 568-581.
38. Karle, M.; Wöhrle, J.; von Stetten, F.; Zengerle, R.; Mark, D. In *Axial centrifugal filtration—a novel approach for rapid bacterial concentration from a large volume*, 2013 Transducers & Eurosensors XXVII: The 17th International Conference on Solid-State Sensors, Actuators and Microsystems (TRANSDUCERS & EUROSensors XXVII), IEEE: 2013; pp 1235-1238.
39. Templeton, E. J.; Salin, E. D., A novel filtration method integrated on centrifugal microfluidic devices. *Microfluidics and nanofluidics* **2014**, *17* (1), 245-251.
40. Lenz, K. D.; Jakhar, S.; Chen, J. W.; Anderson, A. S.; Purcell, D. C.; Ishak, M. O.; Harris, J. F.; Akhadov, L. E.; Kubicek-Sutherland, J. Z.; Nath, P., A centrifugal microfluidic cross-flow filtration platform to separate serum from whole blood for the detection of amphiphilic biomarkers. *Scientific reports* **2021**, *11* (1), 1-8.

41. Woolf, M. S.; Dignan, L. M.; Lewis, H. M.; Nauman, A. Q.; Tomley, C. J.; Landers, J., Optically-Controlled Closable Microvalves for Polymeric Centrifugal Microfluidic Devices. *Lab on a Chip* **2020**, (20), 1426 - 1440.
42. Kainz, D. M.; Früh, S. M.; Hutzenlaub, T.; Zengerle, R.; Paust, N., Flow control for lateral flow strips with centrifugal microfluidics. *Lab on a Chip* **2019**, 19 (16), 2718-2727.

Chapter 2 . Towards an Affinity-Free, Centrifugal Microfluidic System for Rapid, Automated Forensic Differential Extraction

2.1 Introduction

2.1.1 Forensic Sexual Assault Evidence: An Unmet Need

In the United States, rape¹ is historically the third most common violent crime, with roughly 90,000 cases reported annually (1996-2015).¹ In these cases, timely processing of sexual assault evidence collection kits (SAECKs) is a crucial step in ensuring the expedient identification, judicious prosecution, and ultimately, removal of sexual predators from the populace. However, backlogs of evidence and slow SAECK turnaround times persist due, in part, to an ever-growing demand for forensic DNA services and the unique nature of SAECK DNA evidence.^{2, 3} Despite ongoing technological advancements, new case submissions continue to eclipse laboratory testing capacities.⁴ This supply-demand gap is further exacerbated by the time-consuming, labor-intensive serological screening and sample preparation required for downstream DNA analysis. In particular, forensic practitioners must evaluate a variety of biological samples on an assortment of substrates from each SAECK and any remaining evidence associated with the case, including clothing from the alleged perpetrator and from the scene of the incident. DNA evidence originating from SAECKs specifically, may include oral rinses, intimate swabs obtained from the victim (e.g., vaginal-cervical, anal, etc.), and fabric cuttings (e.g., clothing, bedding, etc.). These items must be individually screened at the discretion of the forensic scientist for the existence of probative bodily

¹ Many agencies and organizations define rape and sexual assault differently. For the purposes of this manuscript, the term rape refers to the revised definition of rape released by the U.S. Attorney General in 2013. Explicitly, rape is, “*The penetration, no matter how slight, of the vagina or anus with any body part or object, or oral penetration by a sex organ of another person, without the consent of the victim.*” Accordingly, the statistics reported herein do not include instances of victimization that are encompassed by definitions of rape and sexual assault employed elsewhere, e.g., threatened rape, threatened attacks, unwanted contact, grabbing, fondling, etc. (Morgan, R. E.; Kena, G., Criminal victimization, 2018. Bureau of Justice Statistics 2019, 845.)

fluids to provide the investigation with context and inform best practices for downstream sample preparation.

While a full discussion of backlog types and causes is beyond the scope of this paper, it is important to note that herein we utilize the *National Institute of Justice* (NIJ) definition for casework backlogs, which describes a backlogged case as one that remains untested >30 days after submission to the laboratory;² recent reports from publicly-funded U.S. forensic laboratories indicated that the typical SAECK backlog exceeds 11,000.^{5,6} As recently as 2008, the *U.S. Bureau of Justice Statistics* estimated that a 73% increase in the number of DNA analysts was required to realize a true 30-day turnaround time and eliminate end-of-year backlogs.⁷ Since many State and local jurisdictions are struggling to recruit, hire, and retain qualified forensic staff, it is unlikely that the addition of more analysts will solve this problem.⁸ Alternatively, the inclusion of automated, cost-efficient technology^{9, 10} with decreased labor requirements^{11, 12} and enhanced throughput is a more attainable solution for eliminating the backlog.^{13, 14}

2.1.2 Forensic Differential Extraction (DE)

With few exceptions, SAECK samples are collected from the victim and thus comprised of unbalanced cellular mixtures, primarily consisting of large numbers of the victim's epithelial cells (e-cells) and the alleged offender's sperm. Comparatively large proportions of the victim's genetic material can confound offender identification by producing complicated DNA mixture profiles or, in a worst-case scenario, completely masking the alleged perpetrator's DNA profile. To alleviate this problem, a supplementary sample preparation procedure known as differential extraction (DE) is performed prior to downstream genetic analysis. Forensic DE is a multistep

² The NIJ distinguishes casework backlogs from convicted offender/arrestee and historical backlogs. The term historical backlog refers to cases that were never submitted to crime labs for evaluation. (Nelson, M., Making sense of DNA backlogs: myths vs. reality. National Institute of Justice, Office of Justice Programs, US Department of Justice 2010.)

preferential cellular lysis process that generates two critical extracts or fractions, namely the sperm fraction (SF) and non-sperm fraction (NSF). Herein, the term ‘non-sperm’ is used to describe a lysate (NSF) comprised of large quantities of e-cell DNA from the victim and non-sperm DNA from the alleged perpetrator (e.g., e-cell, spermatocyte, etc.); this extract may also contain DNA from blood, bacteria, and yeast.¹⁵ The goal of DE is to yield a final SF extract enriched with sperm cell DNA from the alleged perpetrator and devoid of non-sperm cell DNA from the victim. Ideally, DE enriches the SF to such an extent that downstream genetic analysis produces a full, single-source profile of the sperm cell DNA, thus precluding complex mixture profile interpretation and deconvolution.

Conventional or traditional DE approaches are rooted in the method first described by Gill et al. in 1985 and later modified by Yoshida et al. in 1995.^{16, 17} (**Figure 2-1**). Explicitly, a sample (e.g., cotton swab, fabric cutting, etc.) is initially exposed to a digestion cocktail that utilizes chemical and enzymatic activity (e.g., sodium dodecyl sulfate (SDS) and proteinase K (ProK)) to preferentially rupture all non-sperm cells and solubilize non-sperm cell DNA, while leaving sperm cells and sperm nuclei intact.^{14,15} An ensuing high-speed centrifugation step is used to release the liquid from the evidence substrate and to pellet sperm cells in the bottom of the collection tube. The substrate is then removed for the remainder of the DE process, and the liquid supernatant, which constitutes the NSF, is separated. The sperm cells and sperm nuclei comprising the pellet, formed during the previous centrifugation, are reserved for further sample processing, i.e., to remove residual non-sperm cell DNA, cellular debris, and potential PCR inhibitors, via several wash and centrifugation steps (often 2-3). Finally, to yield a final fraction (SF) enriched with sperm cell DNA, sperm cell DNA is liberated with a cocktail of reagents including a surfactant, a proteinase enzyme, and a reducing agent (e.g., SDS, ProK, and dithiothreitol (DTT)). Obtaining a

full, single-source male DNA profile from this DE process is most often dependent on the extent to which sperm cells are released from the evidence substrate, during the initial centrifugation, and how efficiently the sperm cells are separated from non-sperm cells (e.g., e-cells).¹⁸⁻²¹

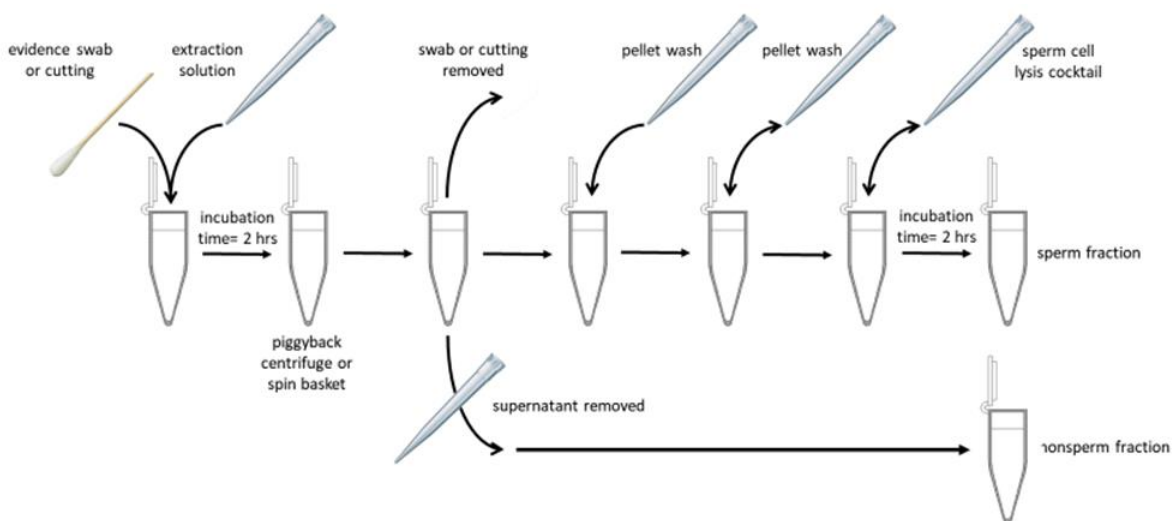


Figure 2-1. Stepwise workflow associated with the traditional DE of sexual assault evidence. Workflow based on 2017 published VDFS procedures manual. In total, this process requires no less than 4 hours of incubation time, multiple manual pipetting steps, one complete tube transfer, and at least three centrifugations of ≥ 5 minutes at 10,000 rpm.

While conventional DE is often effective and universally used, it has contributed to slow laboratory turnaround times due, at least in part, to a manually intensive workflow, propensity for poor sperm cell DNA recovery, and frequent failure to adequately eliminate non-sperm cell DNA.^{9, 16, 22} Recent forensic literature and anecdotal reporting suggest that simple water/buffer washes of the sperm pellet are inadequate for the removal of extraneous e-cell DNA, especially in instances where large proportions of e-cells dominate the initial cell mixture. However, with few exceptions, conventional DE has changed little since its inception.^{2, 15, 23, 24}

To decrease the manual labor requirements of DE, some crime laboratories have adopted mechanized robotic platforms to partially automate the process. Despite the reported reduction in hands-on-time, mechanized platforms deliver no substantial differences in chemistry, execution of

the procedure, or enhancement of sperm cell DNA recovery efficiency.^{2, 23, 24} Moreover, implementation of these robotic platforms requires substantial financial investment and specialized examiner training, thus precluding their universal use. We believe that significant, affordable, and accessible improvement of the DE process will require a combination of changes to both chemistry and technical execution of the automation process.

Microfluidic devices, such as micro total analysis systems (μ TAS)^{16,17} and lab-on-a-CD platforms,¹⁸⁻²¹ offer an attractive, unconventional approach to standard DE sample preparation. Recent μ TAS innovations and focused research efforts have borne commercial instruments capable of producing a single-source DNA profile within two hours (RapidHIT®, IntegenX, Pleasanton CA).²² These instruments will undoubtedly grant some relief of the growing analytical burden, caused in part by swelling state legislative requirements for expanding offender and/or arrestee profiling,^{2, 25} However, these rapid DNA systems are restricted to processing samples which do not require DE or downstream DNA quantification (e.g., reference samples, convicted offender, and arrestee samples) and, therefore, fail to address the specific needs of the forensic science community pertaining to the slow turnaround times of backlogged SAECKs.²⁴⁻²⁶

Unlike other robotic approaches to the DE conundrum, the single-use putative devices described herein focus purely on self-contained microfluidics and enzymes. To realize complete, on-disc automation of the DE workflow, the proposed **centrifugal differential extraction (CDx)** disc and instrument must minimally provide for: (i) timed reagent release, (ii) temperature control for novel, sequential enzymatic reactions, and (iii) fractionation that yields discrete sperm (SF), non-sperm (NSF), and waste fractions from SAECKs.

2.1.3 *Centrifugal Microfluidics*

The self-contained, single-use, **CDx** disc is ideal for differential extraction and provides benefits that include reduction of (1) sample size and reagent volumes, (2) the number of manual sample handling and transfer steps, (3) cross-contamination risk, (4) potential sample loss, and (5) processing time.²⁷⁻³¹ The cornerstone of this microfluidic approach is the exploitation of rotational forces as the primary driving force. Much like the rotationally-driven bioanalytical disc originally described by Anderson et al. in 1969, the **CDx** device exploits the pseudo-gravitational centrifugal force to move fluids within the microfluidic architecture,²⁶ which inherently brings reduced instrument size and cost by removing the need for peripheral hardware (e.g., tubing, pneumatic and hydraulic syringe pumps, etc.), thus avoiding the need for large, clunky, and costly robotic platforms for automation.^{2, 18, 19, 23, 27}

2.1.4 *Disc Design and Fabrication*

The architectural design of a centrifugal microfluidic device defines its functionality, and dictates the number, type, and sequence of unit operations.¹⁶ In this case, the prototype **CDx** disc mirrors a conventional DE workflow (**Figure 2-1** and **Figure 2-2**) with features that mimic a pipettor, mixing/metering device, fractionator, and a centrifuge.²⁸⁻³⁰ In the current form, each **CDx** disc consists of four identical domains that are individually capable of processing a single evidence cutting via step-wise e-cell lysis, three intermediate wash steps, and a final sperm cell lysis in parallel. To integrate these unit operations, we leverage the well-established print-cut-laminate (PCL) method of disc fabrication, which has been used for rapid prototyping and testing of complex microfluidic architectures that are capable of cell lysis, dynamic solid phase DNA extraction, and PCR amplification.³⁰⁻³³ Further, by leveraging common office equipment and inexpensive plastic materials, the PCL method simplifies device prototyping and reduces the materials cost for each disc to roughly \$1 USD.³⁴ A typical PCL disc, like the **CDx** described

herein, consists of 5 laminated layers with two primary fluidic layers and an optically dense middle layer that facilitates laser-based valving (**Figure 2-2**).

2.1.5 *Preliminary Studies and the Impetus for Closable Valving*

During the initial design stages of the *CDx* fluidic architecture, it was necessary to explore and assess the partitioning of multiple fluid volumes from a single sample chamber. Brenner et al. proposed a frequency-dependent method for flow switching in a symmetrical, inverted y-shaped channel that facilitated the preferential filling of two distinct recovery reservoirs.³⁵ That approach to flow switching provided valuable insights into how the Coriolis force impacts on-disc fluid flow and how two discrete liquid fractions might be produced from a common inlet channel. The critical frequency (ω^*) required to achieve this flow switch occurs when the Coriolis force (f_C) becomes dominant over the centrifugal force (f_ω); these conditions arise at approximately 4,000 rpm. At that time, no spin system in the Landers Lab could reliably sustain these rotational frequencies. I hypothesized that timed sacrificial laser valve opening combined with microchannel asymmetry might provide a workable alternative solution to the challenge of eluting multiple liquid fractions. In large part, my original approach to designing the elution architecture was to adjust channel tilt angle relative to the radial axis and by manipulating resistance to flow, thereby modulating the overall channel discharge (Q).³⁶ In this original design, three key nodes in the channel architecture ensured that newly formed fractions did not mix with previously eluted fluid volumes (**Figure 2-2**).

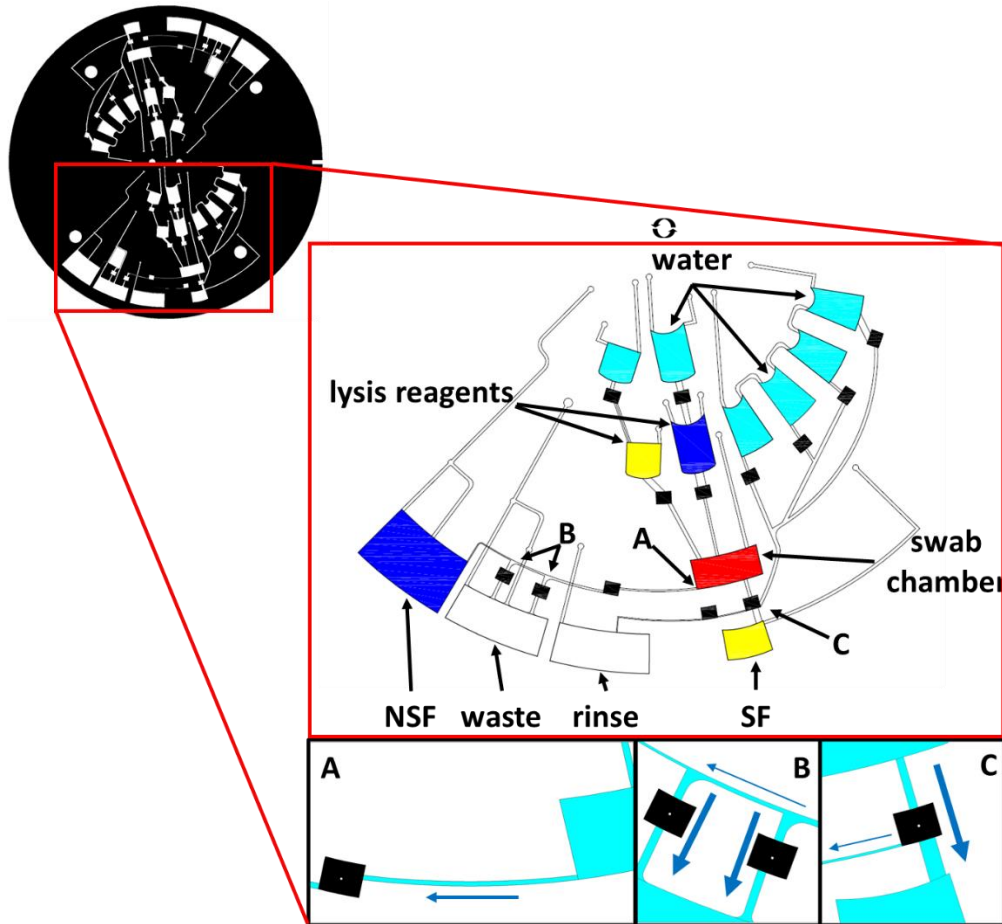


Figure 2-2. Schematic of the proposed microfluidic architecture. The 350 μm wide channel opening at node (A) serves as the primary transport channel to the NSF and waste reservoirs but also functions as a capillary burst valve. Actuation of laser valves at node (B) combined with two stepwise channel constrictions (250 and 150 μm respectively) facilitate preferential filling of the waste reservoir. Sacrifice of the laser valve at node (C) permits elution of the final SF volume. Arrows in panel A-C denote the direction of preferential filling.

This approach required timed release, mixing, incubation, and elution of distinct fluid volumes. As planned, the first sequence of unit operations entailed the initial lysis reagent release, incubation, and elution into the non-sperm fraction recovery reservoir (NSF). During that process, the first laser valve downstream of the swab chamber (Node A) served two functions. In the closed state, node A permitted the arrest of fluid volumes within the swab chamber following upstream reagent release and centrifugation. In the open state, the valve at node A permitted unfettered access to the downstream NSF reservoir (**Figure 2-2 A**). A critical feature of this design was the timed release, arrest, mixing, and incubation of different fluid volumes within the sample chamber.

Once opened, the valve at node A presented a potential hindrance to this sequential process and, if not considered could thwart efforts towards the successful isolation of multiple additional fractions. The tilt angle (90°) and constriction (350 μm) at node A (i.e., transport channel to NSF and waste reservoirs) were designed to address this concern; I hypothesized that increasing the resistance to flow at this node might be sufficient to permit the release, arrest, mixing, and incubation of subsequent reagents volumes within the central sample chamber. Essentially, the constriction at node A functions as a capillary valve with a burst frequency similar to those described by Ouyang et al., i.e., a 500 μm wide channel in a single PeT layer of the device (132 μm deep) exhibits a burst frequency of approximately 500 rpm.³⁷

Access to the intermediate waste reservoir was realized by sacrificing two previously closed laser valves at node B and increasing rotational frequency to 3,000 rpm (**Figure 2-2B**). To achieve preferential filling of the waste chamber while preventing unwanted flow into the open NSF reservoir, manipulation of resistance to flow at node B was required. The two variables influencing hydraulic resistance to flow (R_h) at that node are channel length l and channel radius r .³⁸ Mathematically, this is expressed as

$$R_h = \frac{\Delta p}{Q} = \frac{8\eta l}{\pi r^4} \quad \text{Eq. 4}$$

where Q is the discharge in $m^3 \cdot s^{-1}$ and Δp is the change in pressure.³⁸ Thus, I hypothesized that reducing the radius of the NSF transport channel by 1/2 relative to the waste channels would yield 16-fold increase in resistance to flow; the difference in channel tilt angle (90°) was intended to maximize the effect of centrifugal forces on the waste reservoir channels.

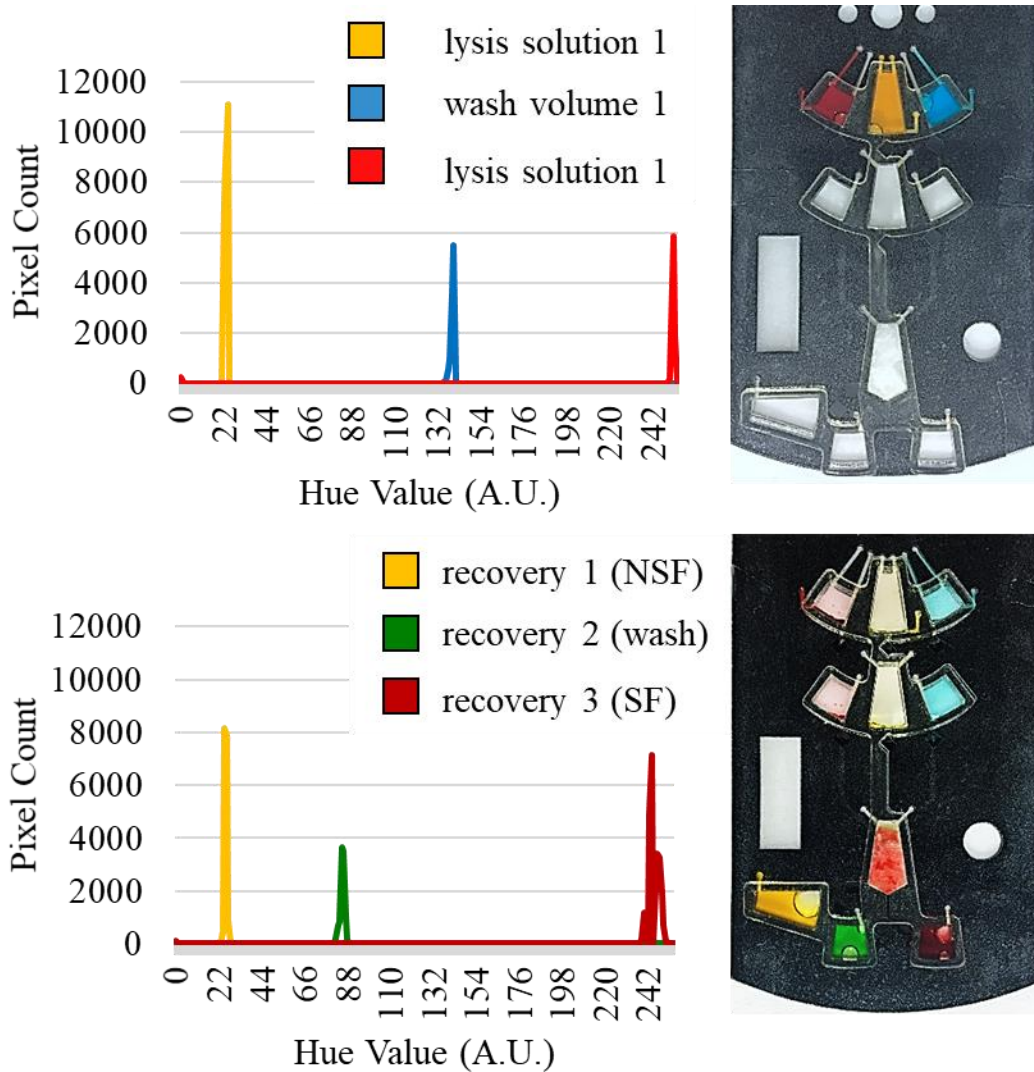


Figure 2-3. Histogram analysis to assess the effective elution of multiple, discrete fractions. A clean $\frac{1}{2}$ swab cutting was present in the swab chamber for these studies. Fractions were eluted at 2,000 rpm. To obtain hue values and pixel count data, JPEG images of the chip were cropped and analyzed in ImageJ.

To evaluate the preferential diversion of fluid within that architecture, yellow, blue, and red food dyes were used to represent the epithelial lysis, wash, and sperm cell lysis reagents, respectively (**Figure 2-3**). Each dye volume was sequentially released to and eluted from the swab chamber. Histogram analysis revealed distinct, untainted red and yellow peaks pre- and post-elution, indicating that the elution of two or three distinct fractions was possible with the aforementioned strategy. Similar dye studies were employed to ensure that previously eluted volumes do not reenter the channel architecture or the swab chamber.

In the context of forensic SAECKs, these initial studies demonstrated that it is possible to recover distinct fractions from a single sample chamber. However, it was unclear if this approach could sufficiently remove non-sperm cell DNA prior to sperm cell lysis and elution of the critical SF component. Here, as with traditional DE, the removal of residual non-sperm cell DNA is critical as the presence of the victim's DNA in the final extract can generate a mixed STR profile. As such, additional dye studies were used to assess the removal of dye from the swab chamber during the washing/cleanup steps. Briefly, 100 μ l of 5 mM blue erioglaucine dye was added to the epithelial lysis reagent chamber and eluted into the NSF reservoir (**Figure 2-4**). Water was used to wash the swab chamber prior to introduction of the sperm lysis mimic. Complete elimination of blue dye from the final SF volume would indicate a successful trial. Dye experiments with as many as six 100 μ l washes suggested little improvement after three washes (data not shown). Multiple smaller washes (6 x 50 μ l) revealed no improvement and provided more potential failure points at laser valves and preferential fluid diversion nodes. These studies also revealed that small volumes of the concentrated blue dye (~2 μ l) remained trapped on or near the terminal laser patch during the washing process, leading to trace amounts of blue dye in the final fraction and suggesting a potential for trapping DNA during on-disc SAECK extraction. That finding prompted the addition of a supplementary rinsing step to remove residual dye from final laser patch.

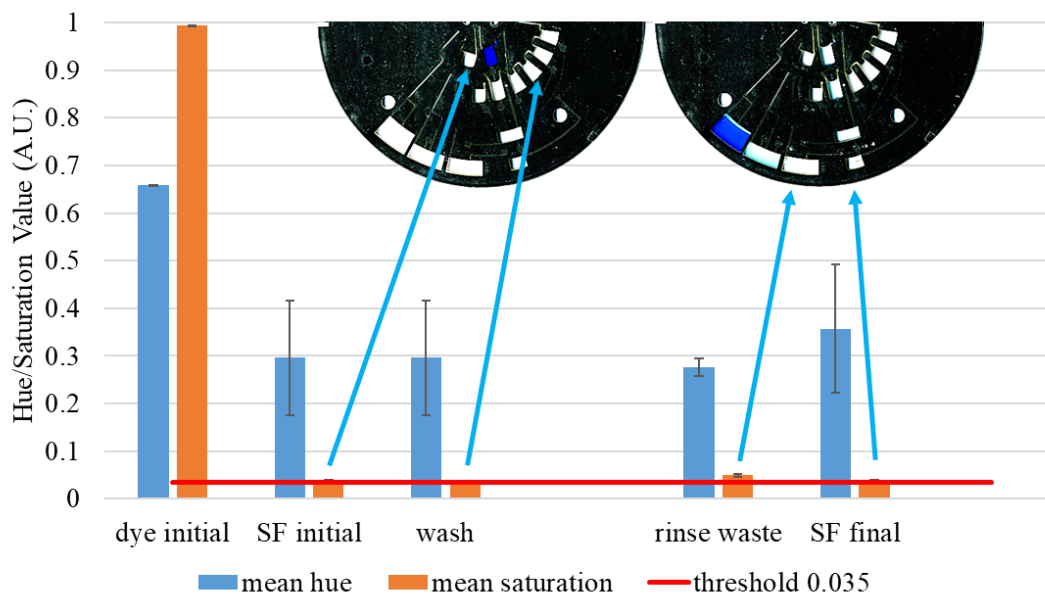


Figure 2-4. Image analysis to assess the removal of dye from the swab chamber. Hue and saturation were measured for each key component prior to testing (n=4 each). Blue dye corresponded to the initial epithelial lysis solution, while water was used for the washes and SF reagent volume (dye, SF initial, and wash). Red line corresponds to the baseline/background saturation value of the initial water volumes. Three 100 μ l washes satisfactorily remove 100 μ l of 2.5 mM erioglaucine. However, hue alone is insufficient for that assessment as it becomes more variable at lower concentrations. At very low concentrations, saturation is a more reliable indicator of dye removal.

Rinsing the terminal laser valve at node C (**Figure 2-2 C**) with 50-100 μ l of water removed the bulk of the residual dye trapped in that channel (**Figure 2-4**); suggesting that it is possible to remove trapped DNA prior to elution of the critical SF volume. Despite the early promise of this approach, this mixed active-passive approach to flow control was sensitive to perturbation and susceptible to failure with changes in reagent composition. I believe that given sufficient time, and perhaps extensive computer flow modeling, it is possible to reliably isolate two or three fractions from a central sample chamber. However, the sensitivity of this method adds considerable design complexity when considering more than three fractions and ultimately forced a shift in my approach to on-disc valving.

2.1.6 Redesigned On-Disc CDx Workflow and Laser-Based Valving Strategy

As discussed above, integration of all essential unit operations requires exceptional flow control with precisely timed, stepwise reagent release, delivery, and recovery with intermittent

sequestration of multiple discrete fractions (i.e., SF, NSF, and waste). To achieve the absolute fluidic control needed for successful fractionation, the *CDx* elution architecture leverages and incorporates active laser-based valving methods for channel opening and closure.^{30, 34, 39 40} **Figure 2-5** provides an overview of laser-based valve opening and closing and a visual, photographic demonstration of channel closure (**Figure 2-5 G**).

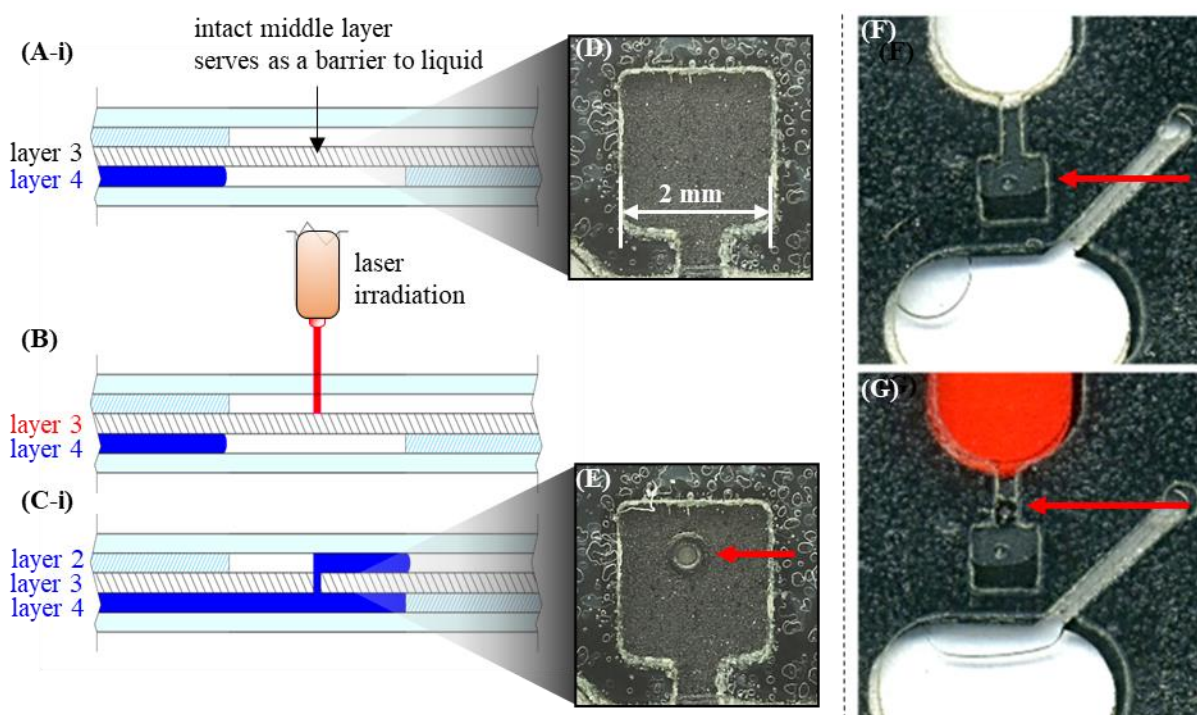


Figure 2-5. Actuation of an optically addressable, sacrificial laser valve (**A-E**) and closure (**F-G**) of a previously open microfluidic channel. (**A-i**) Passage of fluid is prevented by the intact middle layer (layer 3) that lies between two otherwise open channels. (**B**) Clear PET exhibits high transparency to light irradiation above 400 nm (>80% at 671 nm). Thus, light passes through the transparent top and bottom PET layers relatively unadulterated. Conversely, printed xerographic toner on the middle PET layer provides increased absorbance (>99%). In turn, conversion of light energy into thermal energy engenders rapid, localized heating that ablates an orifice at the irradiated spot (~80-100 μm) – effectively opening a microvalve between previously disconnected channels. (**C-i**) The orifice created by ablation of the plastic permits passage of the fluid stream as rotation is resumed.³⁸ (**D and E**) Photographic images of a 2x2 mm laser patch in the closed (**D**) and open (**E**) states. Photographic images of open (**F**) and closed (**G**) microfluidic architectures.

Sacrificial, ‘one-shot’ valve opening events provide stringent temporal reagent release, enable preferential fluid routing, and prevent premature fluid access to downstream chambers and channels (**Figure 2-5 A through C**).^{39, 41} In conjunction with these ablatable one-shot valve

openings, laser-based closable valves directly address issues surrounding undesirable fluid backflow and facilitate fractionation (**Figure 2-5 G**); in the absence of a closable valving event, capillary forces induce rapid wicking and fluidic backflow that lead to unfavorable mixing of sperm, waste, and non-sperm fractions.^{30, 36, 42, 43} This laser-based approach to microvalving is discussed at length in Chapter 2 and in our recently published Lab on a Chip article.³⁰

Exploitation of this new laser-based valve closing method allowed for simplification of the channel network connecting chambers on the *CDx* disc (**Figure 2-6**); all considerations regarding channel constriction and tilt angle were disregarded and all channel widths were fixed at 500 μm . The number of reagent and recovery chambers was expanded from three to five. **Figure 2-6** provides a schematic overview of a single processing domain and the associated on-disc workflow, inspired by the traditional DE approach; laser valve locations for a single *CDx* processing domain are also detailed in this figure. Once all reagents are loaded into chambers nearest the center of rotation (CoR) (**Figure 2-6 B**), the fluidic protocol for on-disc DE, comprised of five nearly identical unit operation sequences (**Figure 2-6 C through G**), is initiated. Unit operation sequence 1 (**Figure 2-6 C**) begins with a single valve opening event, which releases the non-sperm cell lysis cocktail (NSLC). To facilitate the release and elimination of non-sperm cell DNA, the NSLC is centrifugally driven into and incubated within the sample chamber. Opening a second downstream laser valve permits centrifugal elution of the lysate into a recovery chamber. Accordingly, a valve closure event marks the end of this unit operation sequence, i.e., a downstream microchannel is closed to isolate the lysate in the recovery chamber, forming the NSF (**Figure 2-5 G** and **Figure 2-6 C**, red-black arrow head). Operation sequences 2-4 correspond to three sequential water or buffer wash/rinse steps (**Figure 2-6 D, E, and F**). Sequence 5 constitutes the sperm lysis (SL) step (**Figure 2-6 G**). During sequence 5, the *Acrosolv*-based sperm lysis cocktail (reagent chamber 5)

is released, centrifugally driven into, and incubated within the swab chamber. The resultant lysate is eluted. A valve closure event isolates the eluate, forming final SF volume (**Figure 2-6 G**).

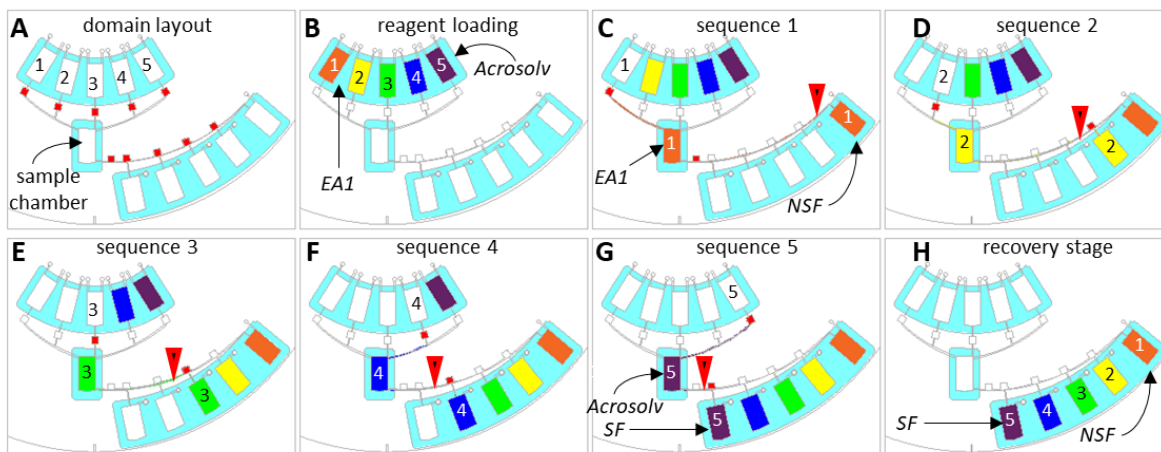


Figure 2-6. Schematic overview of the model CDx disc and workflow based on traditional DE. (A) Laser valves (red) provide strict flow control and timed release of reagents. (B) Reagents located near the center of rotation (CoR). (C) E-cell lysis and isolation of the NSF. (D) Wash 1 and isolation of the first waste fraction. (E) Wash 2 and isolation of the second waste fraction. (F) Wash 3 and isolation of the third waste fraction. (G) Sperm cell lysis and isolation of the final SF. (H) Complete on-disc forensic DE with discrete SF, waste (x3), and NSF. It should be noted, that using this design, the final sperm lysis reagent and sperm cell lysate will encounter no more than two laser valves and will have little or no contact with previously closed valves or their byproducts.

2.1.7 Enzymatic DE and the Swab-In Approach

To expedite the isolation of sperm cell DNA from SAECK samples, we employ state-of-the-art enzyme treatments and an on-disc workflow that forgoes the aggressive vortexing, reducing agents, and prolonged incubation times (>2 hrs) associated with conventional DE. The method described here diverges from the conventional method for differential cell lysis in three ways. First, the *CDx* treatment process relies on two key enzymes, the EA1 protease (available as *forensicGEM* and *prepGEM* from MicroGEM Corp., Hamilton, NZ) and *Acrosolv* (MicroGEM). Much like conventional forensic DE, the first and most important enzyme employed by this method is a proteolytic enzyme that preferentially lyses e-cells and other non-sperm cells present in the mixture. Unlike Pro K, EA1 does not require the assistance of concentrated ionic or anionic detergents, which are known to adversely affect downstream PCR assays. *Acrosolv*, a proprietary

mixture of proteases, is designed to release DNA from sperm nuclei without the need for reducing agents.^{15,44} Second, device architecture must be optimized for the removal of non-sperm cell DNA from the sample chamber to enable complete cell separation and lysis. Similar to the conventional DE method, the **CDx** workflow is designed to accomplish this task simply with water or buffer washes. Third, and finally, with this method, it is important to reproducibly dislodge unbound or loosely bound sperm cells from evidence cuttings without a reliance upon the aggressive vortexing and centrifugation steps required by the conventional method. Anecdotal reports suggest that this aggressive vortex-centrifugation approach fails to dislodge a significant proportion of the sperm cells.⁴⁵ The on-disc **CDx** technique employs a swab-in approach intended to exploit this natural tendency to maximize sperm cell DNA recovery by retaining unbound and loosely bound sperm cells and by lysing them directly from the cutting during the last enzymatic treatment step of the CDx workflow. Simply stated, unlike conventional DE, the swab-in approach retains and treats the cutting throughout the **CDx** workflow to improve yield.

2.2 Experimental

2.2.1 Disc Fabrication

Each **CDx** disc is a PCL device comprised of five layers of polyethylene terephthalate films (PeT) and polymethyl metacrylate accessory pieces (PMMA) (**Figure 2-7**).³⁴ Heat and pressure sensitive adhesives (HSA and PSA, respectively) are used to facilitate strong layer adhesion.^{30, 46} The outer layers (1 and 5) consist of a clear PeT film (101.6 μm , Film Source, Inc. Maryland Heights, MO, USA). The primary fluidic layers (2 and 4) consist of clear PeT film bound on both sides by HSA (50.8 μm , EL-7970-39, Adhesives Research, Inc. Glen Rock, PA, U.S.A.). Layer 3, a black PET monolayer (bPeT, 75 μm , Lumirror* X30, Toray Industries, Inc. Chuo-ku, Tokyo, Japan), functions as the laser valving medium. Prior to alignment and lamination, microfluidic

features (e.g., inlets, vents, and chamber voids) are cut into the appropriate layers via laser ablation (VLS3.50, Universal® Laser Systems, Scottsdale, AZ, U.S.A.). The laser ablated layers are aligned and lamination bonded at 180-200°C (13” UltraLam 250B, Akiles Products, Inc. Mira Loma, CA, U.S.A.). PMMA accessory pieces with associated PeT coverlets (1.5 mm thick, McMaster-Carr, Atlanta, GA) are used to add chamber depth and volume where needed; accessory pieces are attached to the top PeT layer of a laminated 5-layer disc with PSA (55.8 µm, ARcare 7876, Adhesives Research, Inc., U.S.A.).

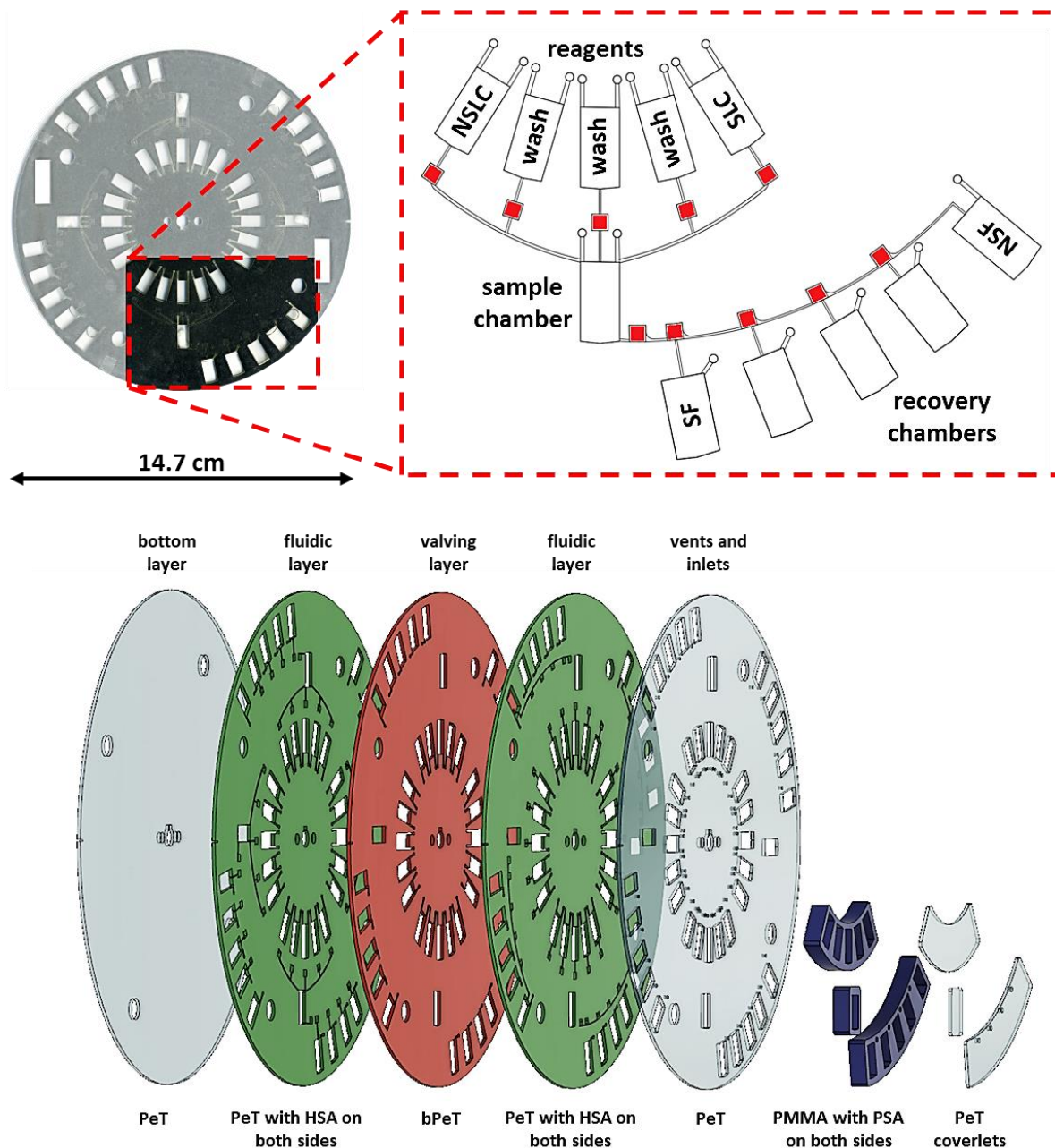


Figure 2-7. Exploded view (bottom) and schematic overview (top) of the putative five-layer (2-fluidic layer) microfluidic disc with integrated closable valving. Each device is designed to have five laminated layers of PeT transparency film. The base and top layers consist entirely of PeT while layers 2 & 4, as the primary microfluidic layers, are bound by adhesive (HSA) which is applied prior to device assembly. Layer 3 functions as the primary valving layer and is precoated with two layers of toner on each side. Microfluidic inlets, vents, and voids are cut into the appropriate layers via laser ablation (simple CO₂ laser). PMMA is used to add chamber depth and volume and is attached post-lamination with adhesive.

2.2.2 *Assessing Fluid Recovery and On-Disc Sample Chamber Position*

The fibrous tips of sterile 6" cotton swabs (Puritan Medical Products, Guilford, ME, U.S.A.) were cut away from the wooden shaft using a standard fine point blade (#11 X-ACTO®, Elmer's Products, Inc., High Point, NC) or a single-edge industrial razor blade (#9 carbon steel, VWR International, LLC., Radnor, PA, U.S.A.) Blades were pre-cleaned with 10% bleach and methanol. Each swab tip was sectioned lengthwise into four pieces of roughly equal size. Swab cuttings were placed into 0.2 ml polypropylene PCR microtubes and soaked in 100 µl of purified water at room temperature for 15 minutes. Fluid was recovered from each swab cutting via piggyback centrifugation; concisely, after incubation, the bottom of each PCR tube was punctured with a syringe needle, nested into a 0.65 ml tube, and subjected to a single centrifugation at 604 * g; where g is gravitational force equivalent (g-force) and the standard unit of acceleration due to gravity at the Earth's surface. Timed spinning intervals (n = 4 ea) included 5, 10, 15, 30, 45, 60, and 90 sec. To simulate subsequent washing of an SAECK sample in a swab-in protocol, each swab cutting was then transferred to a new PCR tube, soaked with an additional 55 µl of purified water, and piggyback centrifuged into an unused 0.65 ml tube. Recovered fluid volumes were calculated via conversion of eluted fluid mass (g) at 27°C. These findings were compared to a small sampling of on-disc recovery trials (n = 4 ea at 30 sec). For the on-disc studies, swab cuttings were sealed into chambers 6 cm from the CoR. Purified water was added to the sample chamber via an inlet vent (not shown). Rotational forces (3,000 rpm or 604 * g at 6 cm from CoR) were used to elute fluid from the sample chamber into a downstream graduated chamber (graduations in 10 µl increments).

2.2.3 *Proof-of-Principle Dye Study*

During the initial design and testing of the **CDx** architecture, a dye elution study was conducted. The red dye solution provided a visible means of evaluating laser-based valving success (e.g., partitioning of multiple, discrete fluid volumes from a single sample chamber) and was intended to mimic potential small molecule, PCR inhibitors that could adversely impact downstream DNA quantification and amplification, e.g., fabric dyes (denim), humic acid, heme, etc. Removal of the dye from the **CDx** architecture (prior to release and elution of the final wash volume) would suggest that small molecule PCR inhibitors can be removed from the **CDx** architecture with simple water or buffer washes. This proof-of-principle evaluation was performed using a small volume **CDx** prototype with no PMMA accessory pieces. Eliminating the PMMA pieces reduced disc thickness, enabling better imaging and subsequent analysis, but also reduced chamber volumes; sample chamber volume = 10 μ l and wash chamber volumes \cong 7.5 μ l. A 5 mM Allura red dye solution (CAS Number 25956-17-6, Sigma-Aldrich, St. Louis, MO, U.S.A.) was prepared in 1X Tris-EDTA buffer (TE pH = 7.5, Sigma-Aldrich). Aliquots of red dye and water were added to the appropriate reagent chambers; 10 μ l red dye was used to represent the EA1 lysate, whereas water (colorless) was used for all washes. On-disc fluidic workflow for this dye followed the process described in **Figure 2-6**. Briefly, the red dye was released from the sample reagent chamber nearer the CoR, centrifugally driven into and held within the sample chamber (30 sec), centrifugally eluted from the swab chamber, and isolated in a downstream recovery chamber with a single valve closure event. Each of the remaining wash volumes were sequentially released to, held within, and eluted from the sample chamber (n = 3 ea). Digital images of each device, captured with a Perfection V100 Photo desktop scanner (Seiko Epson, Suwa, Nagano, Japan), were cropped and analyzed with the Fiji distribution of ImageJ 2.0.0-rc-69/1.52p bundled with Java

1.8.0_172 (64-bit), <https://imagej.net/Fiji/Downloads>.⁴⁷⁻⁴⁹ For laser valve opening events laser patches were irradiated for 500 ms with diode output power and z-height = 500 mW and 15.00 mm, respectively. For laser valve closure events, target channels were irradiated for 2500 ms with diode output power and z-height = 600 mW and 27.00 mm, respectively.

2.2.4 *Assessing Removal of E-cell DNA from the CDx Architecture*

To conduct this non-sperm cell DNA removal study, a full volume **CDx** prototype disc, with PMMA accessory pieces, was fabricated (chamber volumes \cong 200 μ l). Buccal swabs (e-cells only) were collected from a single donor and dried at room temperature for \cong 48 hours prior to cutting and extraction. A pre-cleaned razor blade was used to remove and quarter the fibrous tip of each buccal swab. Individual cuttings were sealed into the swab chambers of the prototype disc (PeT coverlet attached after swab was inserted into the chamber). Each cutting was incubated, extracted, and washed on-disc per the microfluidic workflow outlined in **Figure 2-6** and in accordance with the recommended MicroGEM *prepGem* protocol, i.e., EA1 protease activity facilitated preferential e-cell lysis and each wash step consisted entirely of purified water (Extraction Conditions: 10 μ l of 10X orange buffer, 2 μ l *prepGEM*, water to 100 μ l, 52°C 5 min, 75°C 3 min). Laser valving afforded timed reagent release and fraction isolation. A custom, stand-alone thermoelectric heating system was used for on-disc incubation, i.e., an 8-core microcontroller (Propeller P8X32A-M44; Propeller Inc., Rockland, CA, U.S.A.) was used to regulate a **d**ual, **i**ntegrated **P**eltier **s**ystem (diPs) with independent T-type thermocouple feedback (Peltier CP08,127,05,L1,RT,W4.5, Laird Thermal Systems, Inc., Morrisville, NC, U.S.A.). Each of the resulting fractions were manually recovered from the disc. To facilitate this fraction retrieval, recovery chamber PeT coverlets were pierced with a clean syringe, permitting pipette tip insertion and manual fluid retrieval. A NanoDrop™ 3300 Fluorospectrometer (Thermo Fisher

Scientific, Waltham, MA) was used to quantify the DNA in each fraction with the PicoGreen® dsDNA assay (Thermo Fisher).

2.2.5 *Tracking Sperm Cell DNA within the CDx Architecture*

Sterile cotton swabs (Puritan) were spiked with 100 µl aliquots of neat semen from a single, anonymous male donor. Spiked swabs were dried at room temperature for \cong 48 hours prior to swab tip removal and quartering. Individual cuttings were sealed into the full-volume prototype disc. Each spiked sample cutting was treated per the workflow detailed in **Figure 2-6** and in accordance with the recommended MicroGEM *prepGEM* protocol. Again, the diPs platform provided thermoelectric heating and laser valving afforded timed reagent release and fraction isolation. Each resulting fraction was recovered from the disc.

Recovery fractions 1 through 4 (Fig. 3) were manually rationed into two roughly equal volumes. The first portion of each fraction received no additional treatment prior to DNA quantification, whereas the second portion was treated with *Acrosolv* per the manufacturers protocol. This secondary treatment of fractions, hereafter referred to as re-extraction, was intended to assess the extent of intact sperm cell loss from the swab chamber during the initial NSF elution and wash steps. Recovery fraction 5 (**Figure 2-6 H**) corresponded to the final SF volume and received no additional treatment prior to DNA quantification, i.e., this fraction already underwent *Acrosolv* treatment. As before, a NanoDrop™ 3300 Fluorospectrometer and the PicoGreen® dsDNA assay were used to quantify the DNA in each fraction (initially recovered and re-extracted).

2.3 Results and Discussion

The proposed CDx platform must minimally facilitate fluid recovery from absorbent evidence cuttings, provide for timed reagent release and fluidic fractionation, remove extraneous non-sperm cell DNA prior to elution of the final sperm fraction, and maximize retention and recovery of sperm cell DNA. The sections that follow provide proof-of-feasibility that each of these criteria can be met with a PCL fabricated disc. Specifically, on-disc fluid recovery from cotton swab cuttings is discussed in section **2.3.1**. Dye studies that highlight the effective integration of comprehensive laser-based valving are presented in section **2.3.2**. These dye studies showcase how thoughtful valving and architectural design can be used to facilitate removal of concentrated dye (contaminants) from the sample chamber and downstream architecture. Finally, sections **2.3.3** and **2.3.4** present findings that highlight how on-disc fractionation can be used to assess the microfluidic workflow and assay performance, i.e., evaluate each sequence in the on-disc process chain for potential refinement and improvement.

2.3.1 *Assessing Fluid Recovery from Absorbent Sample Cuttings*

To promote fluid recovery from the sample substrate (e.g., cotton swab or fabric cutting) and to pellet sperm cells, conventional, in-tube DE protocols call for several prolonged centrifugation steps (>5 min @ 10,000 rpm). Likewise, the on-disc **CDx** protocol exploits rotational forces to achieve fluid recovery from the sample. Challenges to on-disc fluid recovery include maximum disc dimensions (e.g., radius) and limits to rotational frequency. Given the direct relationship between angular frequency, on-disc chamber position, and centrifugo-hydraulic pressure, we hypothesized that a sample chamber positioned farther from the center of rotation and rotating at maximum frequency would facilitate enhanced lysate recovery. To elaborate, discs fabricated with our current PCL approach are slightly larger than a standard compact disc (120

mm diameter (\emptyset) and are limited only by the manufactured width of the heat sensitive adhesive ($\cong 140$ mm). Most centrifugal microfluidic systems operate at modest rotational frequencies of 10–50 Hz (600–3,000 rpm).³⁰ Thus, we calculated that the contents of a **CDx** sample chamber positioned at 6 cm from CoR (some space is required for downstream recovery chambers) and rotating at 3,000 rpm would experience $rcf \cong 604 * g$. By comparison, a microtube spinning at 10,000 rpm with a 6 cm rotor radius experiences $rcf \cong 6,708 * g$; a 10-fold decrease in applied g-force. This calculated reduction in applied g-force engendered some concern regarding diminished on-disc capacity for fluid recovery.

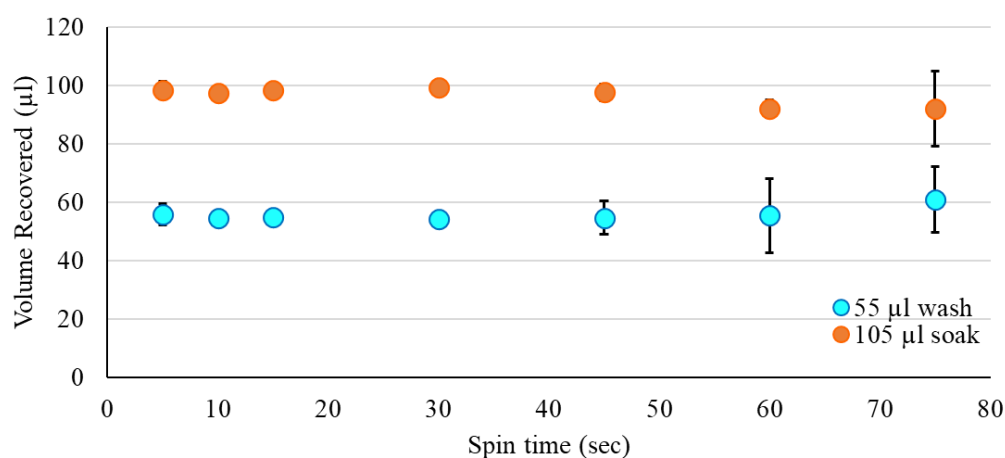


Figure 2-8. Fluid recovery from $\frac{1}{4}$ cotton swab cuttings and fluid recovery workflow (A-D). Fluid was recovered via piggyback centrifugation at $604 * g$ ($n=4$ for each data point). Fluid volume was calculated by conversion of mass measurements (g) at $27^{\circ}C$. Swab tips were removed the wooden shaft (A) and quartered (B). Swab cuttings were soaked in 100 μ l of purified water at room temperature for 15 minutes (orange data points). Fluid was recovered by piggyback centrifugation (C). Swab cuttings were then washed with an additional 50 μ l of purified water (blue data points). Fluid was recovered as above (D).

Reduced on-disc fluid recovery could impact reagent input volume requirements, efficiency of DNA removal during washing steps, and the ability to isolate individual liquid fractions. Prior to designing and testing the **CDx** disc, we performed preliminary studies to evaluate fluid recovery from cotton swab cuttings. Fluid was recovered from $\frac{1}{4}$ swab cuttings via piggyback centrifugation at $604 * g$ (**Figure 2-8**, $n = 4$ for each data point). Results of this in-tube study indicated that our initial concerns regarding fluid recovery at modest rotational frequencies

(3,000 rpm) were unwarranted. Fluid volume was calculated by conversion of mass measurements (grams) at 27°C. Fluid recovery following the initial 100 µl soak was >90% when spin time ≤ 30 sec (**Figure 2-8**, orange data points). Some increased variability in fluid recovery at time points ≥ 45 sec was noted, with a general trend towards lower recovery with longer spin times. Several sources of this increased data variation are possible. However, in this case, we believe this variation is best explained by differences in capillary retention forces between cotton swabs and/or cotton fibers that are pulled through the PCR tube outlet hole during the prolonged spin cycle; cotton fibers extending through the outlet hole could act as simple wicks, pulling fluid back into the swab cutting and preventing more complete recovery. These notions are supported by the data for the second 55 µl soaking event, whereby nearly 100% of the fluid was recovered when spin time < 30 sec (**Figure 2-8**, blue data points). When spin time ≥ 45 sec, fluid recovery ≥ 100%, suggesting that fluid retained during the initial soak-spin recovery step was recuperated during the second soak-spin cycle. On-disc recovery was comparable (not shown).

2.3.2 *Proof-of-Principle Dye Study*

Integration of the closable valving approach allows the **CDx** disc to behave very much like a centrifuge, while providing enhanced fractionation capability and facilitating independent evaluation and analysis of each eluate. Preliminary dye studies demonstrate these new capabilities and offer some insights into how small molecule contaminants behave in the **CDx** architecture (**Figure 2-9**). Inspection of the final **CDx** dye fractions indicated that washes 3 and 4 were visibly ‘clear’ with no perceivable traces of red dye. The legitimacy of this visual observation was evaluated via digital image analysis. Mean color values were digitally measured for each initial and final fluid volume, e.g., HSB, RGB, and L*a*b* values for each dye sample, water control, and recovered volume (n=3 each). Principle component analysis (PCA) indicated that color

difference between the fluid volumes is largely influenced by color saturation (HSB color space) and that the saturation component is a good summary of the total variance in the observed color differences. A paired t-test (p-value = 0.1437, $\alpha = 0.01$) indicated a failure to reject the null hypothesis (H_0 = equality of the means) between the mean saturation values of the initial water volumes and the final recovery fractions (R3 and R4). Stated another way, we cannot conclude that there is a statistically significant difference in the mean saturation values of the initial water volumes (controls) and the final recovery volumes that corresponded with water rinses 3 and 4. This return to baseline color saturation suggests the near-complete elimination of dye from the downstream **CDx** architecture prior to rinses 3 and 4 and provides objective and logical confirmation of the visual observations. This experiment demonstrates that with an inexpensive polymeric spin-disc, we can create sophisticated fraction isolation and collection architecture controlled and driven by a simple, cost-effective instrument. Further, this study hints that 1-2 water washes will be sufficient for the removal of excess cell-free DNA and cellular lysate from the **CDx** architecture.

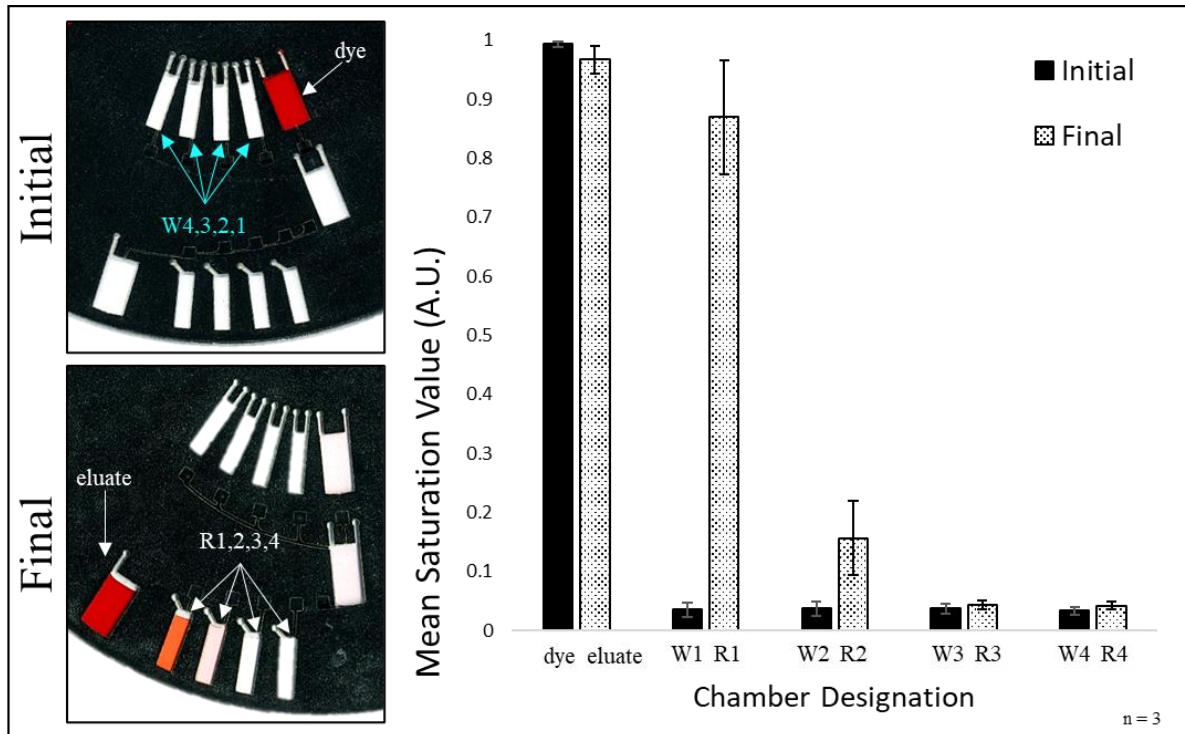


Figure 2-9. Image analysis to assess the removal of concentrated dye from the sample chamber and CDx architecture. (A) Reagents were loaded into chambers nearer the center of rotation. Images of each domain were digitally captured prior to on-disc processing, e.g., each ‘initial’ image included the dye sample and water controls (n=3 each). Initial water volumes were designated W1, 2, 3, and 4. (B) Images of each domain were captured after on-disc processing, e.g., each ‘final’ image included the elute and four recovered fractions – designated R1, 2, 3, and 4. (C) Mean saturation values for each of the initial reagent volumes compared to the equivalent recovered fraction. Error bars indicate ± 1 standard deviation.

2.3.3 Assessing Removal of Non-Sperm Cell DNA from the CDx Architecture

While dye testing is a widely accepted method for evaluating and developing microfluidic architectures,^{29, 50, 51} it is not necessarily representative of the behavior of cellular extracts with high concentrations of DNA, cellular debris (e.g., proteins, lipids, etc.), and anionic detergents that may possess different fluidic characteristics,^{36, 52} which is often the case when the contents of hundreds of thousands of cells are released into a sample solution.⁵³⁻⁵⁶ As such, the existing architecture was reevaluated with whole cell extracts, rather than concentrated dye solutions. The emphasis of this study was on the effective isolation of fractions and the removal of non-sperm cell DNA from the CDx architecture. DNA quantification on the NanoDrop 3300 fluorospectrometer (Thermo) indicated that the NSF and the first rinse volume (R1) contained the

preponderance of DNA in the recovered fractions (**Figure 2-10 B**). Low fluorescence signals were noted in the remaining fractions; however, the signals observed in R3 and the SF were outside the linear range of the standards curve for this PicoGreen® dsDNA assay (31.25 pg/μl at 46.27 RFU). This study suggested that simple washing removed residual DNA from the sample cutting and from the microfluidic architecture. Recovery fractions R2 and R3 contained little or no carryover DNA, which compared well with the results of the dye study (**Figure 2-9**), in which the saturation values of R2 and R3 were approaching baseline (pure water). Taken together, these results signify that one or more intermediate wash steps may be entirely unnecessary and can be removed in the future to streamline workflow. Regardless, fluorescence signal in the critically important final SF volume was in the range of background fluorescence.

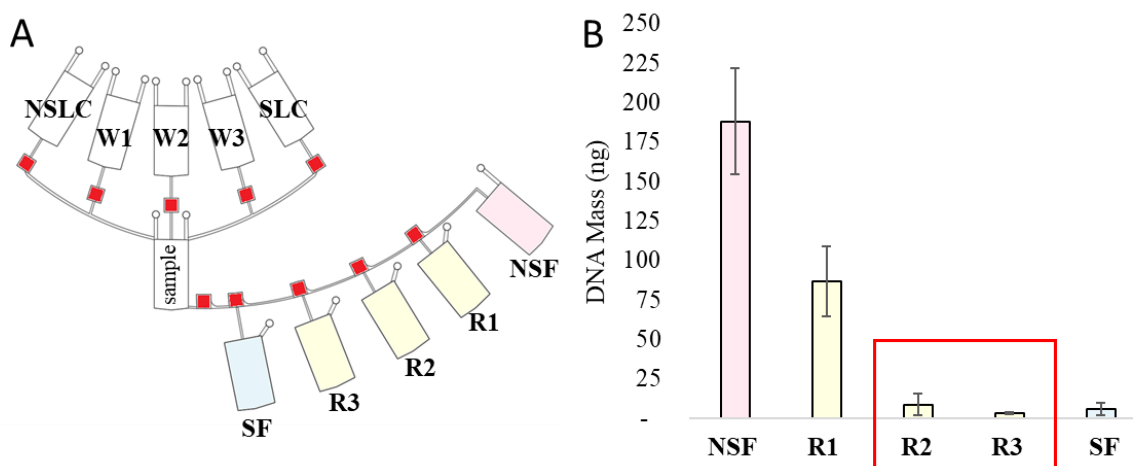


Figure 2-10. A prototype CDx disc and DNA quantification data from on-disc extractions. (A) Top view of a prototype CDx disc that was designed to automate the traditional Gill method of DE. (B) Buccal swabs were dried, cut, incubated, extracted, and washed on the prototype CDx disc (EA1 treatment only). DNA quantification values (PicoGreen™) for those buccal swabs are shown in the above bar plot Panel B. For a full breakdown of how fluids are moved from the upper chambers (nearer to the CoR) to the lower chambers (nearer the periphery of the disc) refer to **Figure 2-6**.

2.3.4 Tracking Sperm Cell DNA within the CDx Architecture

For this study, the non-sperm lysis cocktail (NSL) consisted entirely of MicroGEM *prepGEM* in Orange buffer (see above). DNA quantification of the initial lysate and recovered

wash volumes indicated that although male DNA was present in all four recovered volumes, the preponderance of this non-sperm male DNA was in the initial eluate, which would correspond to the NSF of an SAECK sample (**Figure 2-11 A**). Recovery fractions R2 and R3 contained little or no carryover DNA, which indicated that it may be possible to remove at least one of these intermediate wash steps without compromising downstream SF purity (**Figure 2-11 A**). The fluorescence signal observed in R3 was outside the linear range of the PicoGreen® dsDNA assay (observed = 31.25 pg/μl at 46.27 RFU; using 2 μl sample aliquots, linear range is from 1 ng/ml to 1000 ng/ml). The presence of male DNA in the initial lysate can be understood by considering that seminal fluid contains non-trivial numbers of male, non-sperm round cells (RCs), including cytoplasmic masses, neutrophils, leukocytes, developing spermatids, and male epithelial cells; unlike mature sperm cells, these male, non-sperm RC cells are susceptible to disruption and lysis via EA1 activity during the initial preferential lysis with *prepGEM*.^{15, 57} In this study, non-sperm RC DNA was considered residual and, as seen in the previous e-cell DNA elution study, is removed from the sample cutting and sample chamber during the washing cycles. In a mixed SAECK sample, this RC DNA would co-elute with e-cell DNA from the victim.

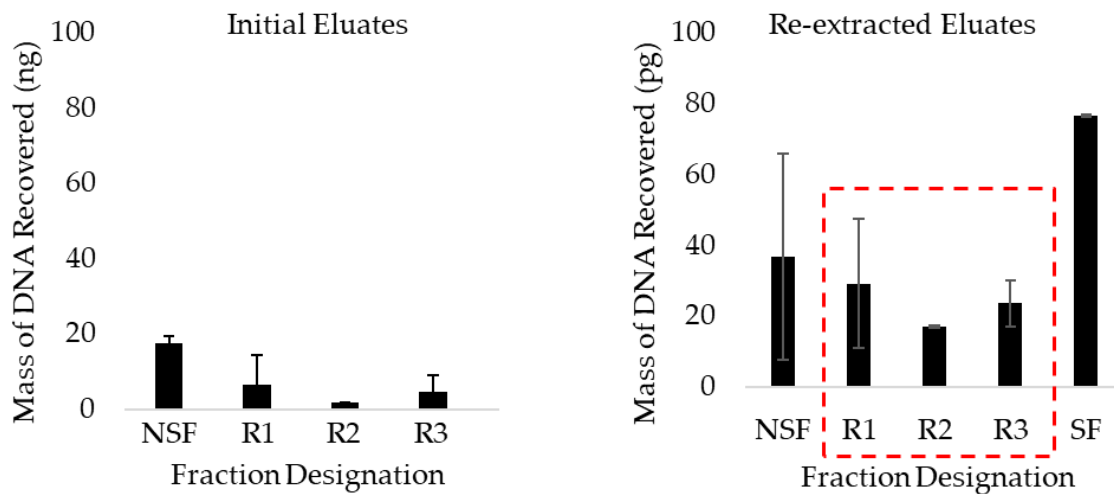


Figure 2-11. Evaluation of sperm cell DNA retention and recovery. Swabs were spiked with neat semen dilutions. Swab cuttings were incubated within a prototype CDx disc, extracted on-disc with *prepGEM* EA1, processed via the

CDx workflow, and recovery volumes were evaluated for the presence of dsDNA with the PicoGreen™ assay. (A) Following the initial treatment with EA1, some male DNA was present in all four recovered volumes. This DNA is likely from male, non-sperm round cells. (B) Treatment of these recovered volumes with Acrosolv (MicroGEM) revealed the presence of intact sperm cells and nuclei. A large portion of the male DNA was retained until elution of the final SF volume. Sample size (n=3). Error bars represent 1 standard deviation. Red box denotes sperm cell DNA that would be recovered with the final SF volume, if the wash steps were replaced with a nuclease treatment.

Re-extraction of the recovered volumes with *Acrosolv* provide clear evidence that DNA within sperm cells and sperm nuclei was not liberated until the final enzymatic treatment. To be clear, in an ideal DE, most of the intact sperm cells would be retained until the final SLC treatment and elution step. In this study, *Acrosolv* treatment induced a significant increase in DNA concentration in all recovered volumes (**Figure 2-11 B**); indicating that some intact sperm cells and nuclei were present in all fractions. These results are not overly surprising given that conventional DE relies entirely upon the extrication and recovery of unbound or loosely bound sperm cells. This preliminary assessment of the **CDx** workflow indicated that a large portion of the intact sperm cells and nuclei were retained on the sample cutting and within the sample chamber until the final *Acrosolv* treatment; the final sperm fraction (~42%, n = 3) of the male DNA (**Figure 2-11 B**). Conversely, roughly 60% of the sperm cells and nuclei were unbound or loosely bound and were dislodged during the opening steps of the **CDx** workflow; the initial NSF eluate, R1, R2, and R3 contained ~20, 16, 9, and 13% of the sperm cell DNA, respectively (n = 3 ea). This outcome is consistent with the notion that large proportions of the sperm cells remain on the sample cutting following the initial preferential lysis step and that non-trivial numbers of intact sperm cells and nuclei are lost during intermediate wash steps. Thus, keeping the swab in place (swab-in approach) and eliminating wash steps stand to significantly improve sperm cell DNA recovery.

These outcomes also support the assertion that sperm cells and nuclei are resistant to EA1 digestion and remain intact following the initial enzymatic treatment. The exact nature of the

protective mechanism that prevents simultaneous sperm and non-sperm lysis via EA1 digestion is uncertain. However, we hypothesize that this protection is due to 1) the dense proteinaceous matrix of the inner and outer acrosomal membranes (IAM and OAM) that surrounds and supports $\geq \frac{2}{3}$ of the condensed sperm cell nucleus,^{58, 59} 2) extensive disulfide cross-linking of proteins within the IAM and OAM,⁵⁸ 3) nuclear protamines that stabilize the condensed sperm cell DNA,^{60, 61} 4) a lack of EA1 cut sites within the IAM, OAM, and protamines,⁵⁷ or 5) a combination of these phenomena. Unlike *Acrosolv*, the EA1 enzyme lacks the substrate specificity needed to solubilize the sperm nucleus or to digest the acrosome in a timely manner.

Nevertheless, we believe that the presence of substantial sperm cell DNA in the final SF volume bodes well for the swab-in approach and provides preliminary support for the contention that the **CDx** disc can generate a highly enriched sperm fraction. I do not believe that the presence of intact sperm cells in the initial NSF or intermediate recovery volumes is unique to the **CDx** prototype disc or the associated workflow, but rather a common (albeit underreported) shortcoming of the DE process. Nevertheless, these results do expose an area of potential **CDx** design improvement regarding sperm cell retention and loss during early workflow steps.

2.4 Conclusions

We demonstrate clear proof-of-principle for a microfluidic approach capable of automating the conventional DE workflow with a total processing time of ≤ 15 min. To realize full, on-disc automation of the DE workflow, the proposed centrifugal differential extraction (**CDx**) platform must minimally provide for timed reagent release, temperature control for sequential enzymatic reactions, and fluidic fractionation that yields discrete sperm (SF), non-sperm (NSF), and waste fractions from SAECKs. These studies highlight the enhanced fractionation capabilities proffered by integrated laser valve opening and closing strategies and the plasticity of the PCL disc

fabrication method for addressing fluid handling, unit operation integration, other fluidics-related issues, and demonstrates that modest rotational frequencies ($\leq 3,000$ rpm) generate sufficient rotational forces to facilitate reasonable on-disc fluid recovery from sample cuttings ($\geq 90\%$ with $\frac{1}{4}$ cotton swab cuttings). Dye and buccal swab extraction studies established that small molecule (red dye) and non-sperm cell DNA are removed from the sample chamber prior to extraction and elution of the critical sperm fraction. Additional on-disc extraction studies reaffirmed the notion that *prepGEM* does not adversely impact sperm cell integrity, i.e., the EA1 enzyme lacks the substrate specificity needed to simultaneously rupture non-sperm and sperm cells.

Although some intact sperm cells and nuclei were found in all recovered fractions, we believe the redesigned sample chamber and modified outlet channel location offer a workable solution to this shortcoming. Further, we are aware that NanoDrop data is not optimal for forensic casework. However, this analytical approach offers gross insights into microfluidic behavior and provides a cost-effective alternative to expensive qPCR kits within the context of these developmental, proof-of-principle studies. In some ways, the NanoDrop data provided herein stands as a significant improvement in forensic research and development transparency. Most published DE studies focus on end-point results and whether downstream genetic profiles are single source; in most instances, the results of these conventional DE approaches are ‘good enough’ for casework but fail to methodically account for many potential sources of sperm cell DNA loss. We are unaware of any published DE studies that attempt to assess each step of the DE workflow systematically and quantitatively for potential sperm cell loss/retention. With that in mind, we are preparing further studies to evaluate and more accurately characterize the modified *CDx* microdevice, e.g., systematic analysis of each eluted fraction with the commercially available Quantifiler Trio kit (ThermoFisher).

We believe that on-disc sperm cell recovery can be improved in multiple ways. First, thoughtful microfluidic design changes can be used to enhance sperm retention within the sample chamber. In fact, we recently published work showcasing a sample chamber design for enhanced bead retention for dynamic solid phase extraction; in that manuscript, 100 % of the 6 μm beads are retained in the sample chamber.³³ Second, we are exploring options to replace intermediate wash steps with a single nuclease treatment; if successful, we believe this simplification of the workflow will improve overall sperm cell DNA recovery by as much as 40%. Finally, should it be necessary, the incorporation of an embedded filtration system can further aide sperm cell retention, e.g., a 3-5 μm pore size non-cellulosic membrane could function as a straining mechanism to retain sperm cells and nuclei while permitting outflow of solubilized cellular debris and extraneous non-sperm DNA during washing steps.^{62, 63}

Collectively, we believe that these findings stand as clear proof-of-principle for a prototype centrifugal microfluidic device capable of performing an all-inclusive conventional forensic DE. The systematic approach to *CDx* development described herein provides greater transparency regarding DE characterization, and once fully developed, will produce a device that provides multiple key advantages and improvements relative to current forensic DE methodology, including full automation, increased sperm cell DNA recovery via the swab-in approach, reduced processing time and cost, enclosed format, enriched sperm fractions with more favorable male : female DNA ratios, and fewer sperm fractions that generate complex DNA mixtures.

2.5 References

1. Crime in the United States 2015 - Uniform Crime Reporting (UCR) Program. <https://ucr.fbi.gov/crime-in-the-u.s/2015/crime-in-the-u.s.-2015> (accessed Nov 17, 2017).
2. Timken, M. D.; Klein, S. B.; Buoncristiani, M. R., Improving the efficacy of the standard DNA differential extraction method for sexual assault evidence. *Forensic science international: genetics* **2018**, *34*, 170-177.
3. Nelson, M., *Making sense of DNA backlogs: myths vs. reality*. National Institute of Justice, Office of Justice Programs, US Department of ...: 2010.
4. Hurst, L.; Lothridge, K., DNA Evidence and Offender Analysis Measurement: DNA Backlogs, Capacity and Funding. National Institute of Justice: Washington, D.C., 2010.
5. Durose, M. R.; Burch, A. M.; Walsh, K.; Tiry, E.; Statistics, B. o. J.; Justice, U. D. o.; Programs, O. o. J.; America, U. S. o., Publicly funded forensic crime laboratories: resources and services, 2014. *Impressions* **2016**, *50* (44), 40.
6. Burch, A. M.; Durose, M. R.; Walsh, K. A., Census of publicly funded forensic crime laboratories, 2009. *Washington, DC: US Department of Justice, Office of Justice Programs, Bureau of Justice Statistics. Retrieved April 2012*, 24, 2013.
7. Durose, M. R.; Walsh, K. A.; Burch, A. M., *Census of publicly funded forensic crime laboratories, 2005*. US Department of Justice, Office of Justice Programs, Bureau of Justice ...: 2008.
8. Ritter, N., The road ahead: Unanalyzed evidence in sexual assault cases. **2011**.
9. Butler, J., Chapter 2—DNA Extraction Methods. *Butler JM* **2012**, 29-47.
10. Forensic DNA Research and Development: Miniaturization and Automation. <https://nij.ojp.gov/topics/articles/forensic-dna-research-and-development>.
11. Sacco, L., The Violence Against Women Act: Overview, legislation, and federal funding (CRS Report No. R42499). 2015.
12. James, N., *DNA testing in criminal justice: Background, current law, grants, and issues*. Congressional Research Service: 2012.
13. Butler, J. M., *Forensic DNA Typing - 2nd Edition*. 2nd ed.; Academic Press: 2005.
14. Butler, J. M., The future of forensic DNA analysis. *Philosophical transactions of the royal society B: biological sciences* **2015**, *370* (1674), 20140252.
15. Cotton, R. W.; Fisher, M. B., Properties of sperm and seminal fluid, informed by research on reproduction and contraception. *Forensic Science International: Genetics* **2015**, *18*, 66-77.

16. Gill, P.; Jeffreys, A. J.; Werrett, D. J., Forensic application of DNA 'fingerprints'. *Nature* **1985**, *318* (6046), 577-579.
17. Yoshida, K.; Sekiguchi, K.; Mizuno, N.; Kasai, K.; Sakai, I.; Sato, H.; Seta, S., The modified method of two-step differential extraction of sperm and vaginal epithelial cell DNA from vaginal fluid mixed with semen. *Forensic science international* **1995**, *72* (1), 25-33.
18. Bruijns, B. B.; Tiggelaar, R. M.; Gardeniers, H., The extraction and recovery efficiency of pure DNA for different types of swabs. *Journal of forensic sciences* **2018**, *63* (5), 1492-1499.
19. Adamowicz, M. S.; Stasulli, D. M.; Sobestanovich, E. M.; Bille, T. W., Evaluation of methods to improve the extraction and recovery of DNA from cotton swabs for forensic analysis. *PLoS One* **2014**, *9* (12), e116351.
20. Lachica, E.; García-Ferrer, R., Study of semen stains by scanning electron microscopy. Influence of their ageing. *Forensic science international* **1998**, *91* (1), 35-40.
21. Brownlow, R. J.; Dagnall, K. E.; Ames, C. E., A comparison of DNA collection and retrieval from two swab types (cotton and nylon flocked swab) when processed using three QIAGEN extraction methods. *Journal of Forensic Sciences* **2012**, *57* (3), 713-717.
22. Forensic Biology Procedures Manual - Extraction of DNA. Biology Program Manager: Richmond, Virginia, U.S.A., 2020; pp 5-7.
23. Klein, S. B.; Buoncristiani, M. R., Evaluating the efficacy of DNA differential extraction methods for sexual assault evidence. *Forensic science international: genetics* **2017**, *29*, 109-117.
24. Timken, M. D.; Klein, S. B.; Kubala, S.; Scharnhorst, G.; Buoncristiani, M. R.; Miller, K. W., Automation of the standard DNA differential extraction on the Hamilton AutoLys STAR system: A proof-of-concept study. *Forensic Science International: Genetics* **2019**, *40*, 96-104.
25. Garvin, A. M.; Bottinelli, M.; Gola, M.; Conti, A.; Soldati, G., DNA Preparation from Sexual Assault Cases by Selective Degradation of Contaminating DNA from the Victim. *Journal of Forensic Sciences* **2009**, *54* (6), 1297-1303.
26. Anderson, N. G., The development of automated systems for clinical and research use. *Clinica Chimica Acta* **1969**, *25* (2), 321-330.
27. Timken, M. D.; Klein, S. B.; Buoncristiani, M. R., Improving the efficacy of the standard DNA differential extraction method for sexual assault evidence. *Forensic Sci Int Genet* **2018**, *34*, 170-177.
28. Thompson, B. L.; Ouyang, Y.; Duarte, G. R.; Carrilho, E.; Krauss, S. T.; Landers, J. P., Inexpensive, rapid prototyping of microfluidic devices using overhead transparencies and a laser print, cut and laminate fabrication method. *Nature protocols* **2015**, *10* (6), 875-86.

29. Krauss, S. T.; Remcho, T. P.; Lipes, S. M.; Aranda IV, R.; Maynard III, H. P.; Shukla, N.; Li, J.; Tontarski Jr, R. E.; Landers, J. P., Objective method for presumptive field-testing of illicit drug possession using centrifugal microdevices and smartphone analysis. *Analytical chemistry* **2016**, 88 (17), 8689-8697.
30. Woolf, M. S.; Dignan, L. M.; Lewis, H. M.; Nauman, A. Q.; Tomley, C. J.; Landers, J., Optically-Controlled Closable Microvalves for Polymeric Centrifugal Microfluidic Devices. *Lab on a Chip* **2020**, (20), 1426 - 1440.
31. DuVall, J. A.; Le Roux, D.; Tsuei, A.-C.; Thompson, B. L.; Birch, C.; Li, J.; Nelson, D. A.; Mills, D. L.; Ewing, M. M.; McLaren, R. S., A rotationally-driven polyethylene terephthalate microdevice with integrated reagent mixing for multiplexed PCR amplification of DNA. *Analytical methods* **2016**, 8 (40), 7331-7340.
32. Thompson, B. L.; Birch, C.; Li, J.; DuVall, J. A.; Le Roux, D.; Nelson, D. A.; Tsuei, A.-C.; Mills, D. L.; Krauss, S. T.; Root, B. E., Microfluidic enzymatic DNA extraction on a hybrid polyester-toner-PMMA device. *Analyst* **2016**, 141 (15), 4667-4675.
33. Dignan, L. M.; Woolf, M. S.; Tomley, C. J.; Nauman, A. Q.; Landers, J. P., Multiplexed Centrifugal Microfluidic System for Dynamic Solid-Phase Purification of Polynucleic Acids Direct from Buccal Swabs. *Analytical Chemistry* **2021**.
34. Thompson, B. L.; Ouyang, Y.; Duarte, G. R.; Carrilho, E.; Krauss, S. T.; Landers, J. P., Inexpensive, rapid prototyping of microfluidic devices using overhead transparencies and a laser print, cut and laminate fabrication method. *Nature protocols* **2015**, 10 (6), 875.
35. Brenner, T.; Glatzel, T.; Zengerle, R.; Ducrée, J., Frequency-dependent transversal flow control in centrifugal microfluidics. *Lab on a Chip* **2005**, 5 (2), 146-150.
36. Ducrée, J.; Haeberle, S.; Lutz, S.; Pausch, S.; Von Stetten, F.; Zengerle, R., The centrifugal microfluidic Bio-Disk platform. *Journal of Micromechanics and Microengineering* **2007**, 17 (7), S103.
37. Ouyang, Y.; Wang, S.; Li, J.; Riehl, P. S.; Begley, M.; Landers, J. P., Rapid patterning of 'tunable' hydrophobic valves on disposable microchips by laser printer lithography. *Lab on a Chip* **2013**, 13 (9), 1762-1771.
38. Flow in Tubes. <https://courses.lumenlearning.com/boundless-physics/chapter/flow-in-tubes/> (accessed Nov 17, 2017).
39. Garcia-Cordero, J. L.; Kurzbuch, D.; Benito-Lopez, F.; Diamond, D.; Lee, L. P.; Ricco, A. J., Optically addressable single-use microfluidic valves by laser printer lithography. *Lab on a Chip* **2010**, 10 (20), 2680-2687.
40. Zucchelli, P.; Van de Vyver, B., Devices and methods for programmable microscale manipulation of fluids. Google Patents: 2006.
41. Le Roux, D.; Thompson, B. L.; DuVall, J. A.; Nelson, D. A.; Birch, C.; Mills, D. L.; Scott, A. T.; Root, B. E.; Landers, J. P., A Fully-Integrated Microfluidic Disc for Swab-STR

Profiling in 40 min on a Portable 10 lb Instrument. *Science Translational Medicine In Preparation*.

42. Liu, S.; Li, S.; Liu, J., Jurin's law revisited: Exact meniscus shape and column height. *The European Physical Journal E* **2018**, *41* (3), 46.

43. Sandeep, A.; Saleem, K.; Akhil, V.; Harneet, K.; Parveen, L., Microfluidic mechanics and applications: a review. *Журнал нано-та електронної фізики* **2013**, (5, № 4 (2)), 04047 (12)-04048.

44. Yakoo, M. N. The development and optimization of a direct lysis differential extraction method. Boston University, 2017.

45. Voorhees, J. C.; Ferrance, J. P.; Landers, J. P., Enhanced elution of sperm from cotton swabs via enzymatic digestion for rape kit analysis. *Journal of forensic sciences* **2006**, *51* (3), 574-579.

46. Birch, C.; DuVall, J. A.; Le Roux, D.; Thompson, B. L.; Tsuei, A.-C.; Li, J.; Nelson, D. A.; Mills, D. L.; Landers, J. P.; Root, B. E., Rapid Fabrication of Electrophoretic Microfluidic Devices from Polyester, Adhesives and Gold Leaf. *Micromachines (Basel)* **2017**, *8* (1), 17.

47. Rueden, C. T.; Schindelin, J.; Hiner, M. C.; DeZonia, B. E.; Walter, A. E.; Arena, E. T.; Eliceiri, K. W., ImageJ2: ImageJ for the next generation of scientific image data. *BMC bioinformatics* **2017**, *18* (1), 529.

48. Schindelin, J.; Arganda-Carreras, I.; Frise, E.; Kaynig, V.; Longair, M.; Pietzsch, T.; Preibisch, S.; Rueden, C.; Saalfeld, S.; Schmid, B.; Tinevez, J.-Y.; White, D. J.; Hartenstein, V.; Eliceiri, K.; Tomancak, P.; Cardona, A., Fiji: an open-source platform for biological-image analysis. *Nature Methods* **2012**, *9*, 676.

49. Schneider, C. A.; Rasband, W. S.; Eliceiri, K. W., NIH Image to ImageJ: 25 years of image analysis. *Nature methods* **2012**, *9* (7), 671-675.

50. Chu, M.; Nguyen, T.; Lee, E.; Morival, J.; Khine, M., Plasma free reversible and irreversible microfluidic bonding. *Lab on a Chip* **2017**, *17* (2), 267-273.

51. Han, L.; Zi, X.; Garmire, L. X.; Wu, Y.; Weissman, S. M.; Pan, X.; Fan, R., Co-detection and sequencing of genes and transcripts from the same single cells facilitated by a microfluidics platform. *Scientific reports* **2014**, *4*, 6485.

52. Gorkin, R.; Park, J.; Siegrist, J.; Amasia, M.; Lee, B. S.; Park, J.-M.; Kim, J.; Kim, H.; Madou, M.; Cho, Y.-K., Centrifugal microfluidics for biomedical applications. *Lab on a Chip* **2010**, *10* (14), 1758-1773.

53. Clark, C. P.; Farmehini, V.; Spiers, L.; Woolf, M. S.; Swami, N. S.; Landers, J. P., Real time electronic feedback for improved acoustic trapping of micron-scale particles. *Micromachines (Basel)* **2019**, *10* (7), 489.

54. Shimmons, B. W.; Svrcek, W.; Zajic, J., Cell concentration control by viscosity. *Biotechnology and Bioengineering* **1976**, *18* (12), 1793-1805.
55. Perley, C. R.; Swartz, J. R.; Cooney, C. L., Measurement of cell mass concentration with a continuous-flow viscometer. *Biotechnology and Bioengineering* **1979**, *21* (3), 519-523.
56. Newton, J. M.; Schofield, D.; Vlahopoulou, J.; Zhou, Y., Detecting cell lysis using viscosity monitoring in *E. coli* fermentation to prevent product loss. *Biotechnology progress* **2016**, *32* (4), 1069-1076.
57. Moss, D.; Harbison, S.-A.; Saul, D., An easily automated, closed-tube forensic DNA extraction procedure using a thermostable proteinase. *International journal of legal medicine* **2003**, *117* (6), 340-349.
58. Ito, C.; Toshimori, K., Acrosome markers of human sperm. *Anatomical science international* **2016**, *91* (2), 128-142.
59. Fléchon, J.-E., The acrosome of eutherian mammals. *Cell and tissue research* **2016**, *363* (1), 147-157.
60. Biegeleisen, K., The probable structure of the protamine–DNA complex. *Journal of theoretical biology* **2006**, *241* (3), 533-540.
61. Balhorn, R., The protamine family of sperm nuclear proteins. *Genome biology* **2007**, *8* (9), 227.
62. Karle, M.; Wöhrle, J.; von Stetten, F.; Zengerle, R.; Mark, D. In *Axial centrifugal filtration—a novel approach for rapid bacterial concentration from a large volume*, 2013 Transducers & Euroensors XXVII: The 17th International Conference on Solid-State Sensors, Actuators and Microsystems (TRANSDUCERS & EUROSENSORS XXVII), IEEE: 2013; pp 1235-1238.
63. Lenz, K. D.; Jakhar, S.; Chen, J. W.; Anderson, A. S.; Purcell, D. C.; Ishak, M. O.; Harris, J. F.; Akhadov, L. E.; Kubicek-Sutherland, J. Z.; Nath, P., A centrifugal microfluidic cross-flow filtration platform to separate serum from whole blood for the detection of amphiphilic biomarkers. *Scientific reports* **2021**, *11* (1), 1-8.

Chapter 3 . Closable Microvalving Methods for Polymeric Centrifugal Microfluidic Devices

3.1 Introduction

3.1.1 *Microvalving on Centrifugal Microfluidic Discs*

Effective valving is essential for fluidic control on the microscale. The selected valving method factors heavily into the potential for large scale manufacture and commercialization of microfluidic devices.^{1, 2} Valving strategies dictate and limit fabrication methodology, impact architectural complexity, and prescribe the type and extent of required supporting peripheral hardware. Inevitably, those same variables dictate the ability to translate from prototype to commercial product and largescale manufacture.^{1, 2} With little exception, many of the valving methods described in the literature suffer from operational limitations or are not amenable to rapid, low-cost fabrication.

Passive valving approaches such as capillary, check, siphon, and hydrophobic valving, complicate the microfluidic design and tend to fail when high fluidic pressures are required early in the analytical process.³⁻⁹ For example, many clinical and forensic protocols require an initial recovery of fluid from various sample collection materials. Adequate fluid recovery often requires high rotational frequencies (higher *g forces, where *g is the conventional value of gravitational acceleration at the Earth's surface), to facilitate sufficient fluid release from the absorbent material (e.g., cotton swab or fabric cutting). These high frequencies can perturb passive valving strategies that progress from low rotational frequencies (low fluidic pressure) in the early steps to higher rotational frequencies (higher fluidic pressure) in the latter stages.¹⁰⁻¹² Tape, torque-actuated, expandable foam, chloroform dissolution, phase-change wax valves, and elastomeric diaphragms are attractive alternatives; that offer greater reliability when higher fluidic pressures are needed early in the analytical process.¹³⁻²⁰ However, these approaches add

architectural complexity and are generally time-consuming and labor intensive to operate; making subsequent automation impractical. Manufacturing costs also rise in relation to increased fabrication complexity, extra supplementary materials, and requisite peripheral hardware.

Herein, we propose and describe two novel methods for improved valve and channel closure that leverage the low-cost print-cut-laminate (PCL) method of fabrication described by Thompson et al.^{2, 9} and complement the simple, laser-based technique for valve opening presented by Cordero et al.^{2, 9} We have achieved active valve opening and closure with inexpensive polyester materials and little more than a heating element or laser diode. A perfunctory scan of the literature suggests that multi-actuation valving may not always be necessary; rather, for many multi-step assays, valves only need be opened and closed once. The contact and non-contact methods of valving described here are straightforward and effective, offering a viable alternative path to single use microvalving. Importantly, both approaches are amenable to automation and low-cost fabrication methods; enabling complex assays that require higher rotational frequencies.

1.1.1 Valve Opening via Laser Irradiation

Previously published work demonstrated that centrifugal microfluidic discs can be constructed using low-cost, commercial ‘off-the-shelf’ materials, common office equipment (i.e., laminators, laser printers, and laser etchers), according to the “print-cut-laminate” (PCL) fabrication method.⁹ Robust fluidic control is achieved on these discs through laser-actuated valve opening (**Figure 3-1**). This valving strategy relies on optically dense regions within the middle layers of the laminated, polymeric discs, i.e., black polyethylene terephthalate (bPeT) or laser-printed xerographic toner.

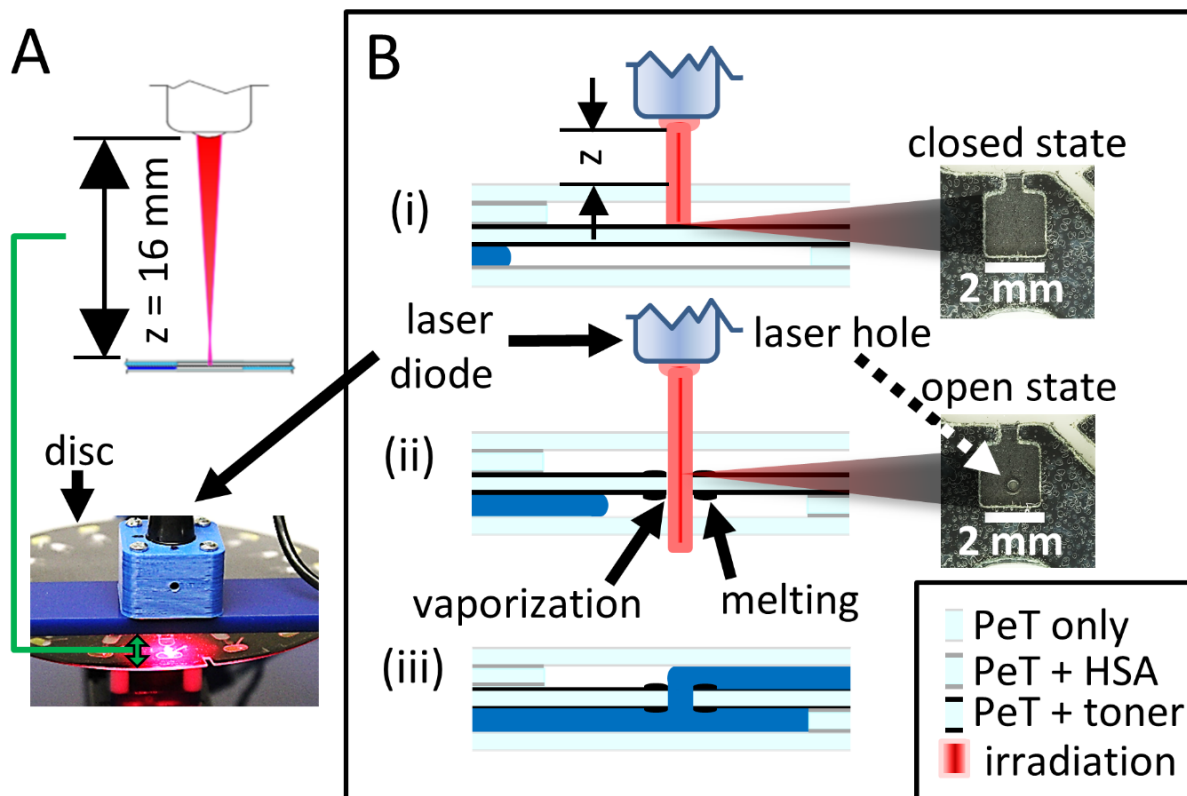


Figure 3-1. Laser-actuated valve opening. (A) Garcia-Cordero et al. described a method for opening normally closed valves by focusing a laser on an optically dense valving layer. (B-i) Briefly, laser light passes through the transparent outer layers of a microfluidic disc and strikes an optically dense middle layer (printed xerographic toner or a black PeT monolayer). (B-ii) The conversion of light energy to thermal energy induces a rapid rise in surface temperature and subsequent ablation or melting of the underlying material. (B-iii) The newly formed hole permits fluid flow between previously unconnected channels. Adapted with permission from Woolf et al., *Lab on a Chip*, 2020.

Each microfluidic disc is comprised of alternating layers of PeT and heat sensitive adhesive (HSA) (Fig 1B). Clear PeT layers exhibit high transparency to light irradiation above 400 nm ($>80\%$ at 671 nm).² Light passes through the transparent outer layers relatively unattenuated (**Figure 3-1 B-i**). Conversely, the optically dense material in the middle layer (xerographic toner or bPeT) exhibits high absorbance ($>99\%$).² In turn, absorption and conversion of light energy into thermal energy engenders rapid, localized heating that melts or ablates an orifice at the irradiated spot (~ 80 - 100 μm); effectively opening a microvalve between previously unconnected channels (**Figure 3-1 B-ii**). Disc rotation may then drive fluid through the newly opened microvalve, into formerly inaccessible channels or chambers (**Figure 3-1 B-iii**). To open a laser valve,

surface temperatures of the middle bPeT valving layer must reach or exceed the vaporization point of PeT ($T_v \sim 300^\circ\text{C}$), resulting in thermal degradation and perforating the layer at the point of focused irradiation. Equation (1) estimates the surface temperature (T) generated by divergent cones of radiation.²¹

$$T_{gaussian} = \frac{2P}{\pi^2 r K} + T_{amb}$$

Eq. 5

This localized heating phenomenon is governed by the power output of the laser (P), the thermal conductivity (K) of the incident material, ambient temperature (T_{amb}), and the radius of the illuminated spot (r) on the disc surface (Eq. 1).²¹ Fabry Perot laser diodes, like those used during this investigation, exhibit a Gaussian intensity distribution and a roughly ovoid cross-section (**Figure 3-1 B**).²²

3.1.2 Valve Closure

Herein we propose and describe two methods for valve and channel closure. First, we explore the pinpoint application of heat and pressure as a means for creating physical barriers between previously connected microfluidic chambers. Much like the spot-welding techniques used in automotive manufacturing or the heat-sealing methods used in the food industry, our approach uses a heated, rod-like pin to melt and irreversibly join plastic monolayers. We demonstrate that the application of direct heat and pressure over a polymeric microchannel or fluidic via causes the underlying plastic films to rapidly soften, melt, intermingle, and (upon cooling) reharden to form permanent welds.

Second, non-contact, transmission laser welding of plastics is well described, and is commonly used for joining polymeric films and to attach electronic components.²³ We demonstrate that non-contact, transmission laser welding can be used to rapidly create physical barriers that block channels, preventing or diverting fluid flow. Moreover, by employing the

same laser diode used for valve opening, the integration of multi-use valves becomes facile, yet requires no additional external hardware or increases in device fabrication complexity. Advantages of laser welding include easy automation, reduced manufacturing and labor costs, and the ability to bond materials of differing composition.²³ Given that transmission laser welding is capable of joining materials of different character, we hypothesized that it might be possible to adapt the method to permanently seal 100 x 500 μm microchannels on polymeric microfluidic devices.

As described by Moskvitin et. al, successful bonding of plastics is typically achieved only when three criteria are met: (1) target components reach melting temperature while avoiding thermal degradation, achieving a viscous-fluid state that retains the mechanical properties of the parent polymer; (2) there is intimate contact and pressure between the bonding surfaces for molecular mixing and bond formation; and (3) holding and cooling times are sufficient for material intermingling and weld development.²³ We hypothesized that manipulation of diode power output and z-height, relative to the surface of a microfluidic device, could result in slower more diffuse heating. This would result in the eventual collapse of overlaying, incident material, ultimately leading to bonding and irreversible “welding” of the layers surrounding a microchannel (HSA, PeT, bPeT, etc.). As with valve opening, laser radiation passes through the clear, outer PeT layer(s) of the microfluidic disc (transmission layer) and is absorbed by the adjacent, optically dense, inner valving layer. Absorption of the light energy generates a significant, localized change in temperature resulting in rapid heat transfer to, and melting of, the surrounding materials, including the neighbouring transparent layers. Upon cooling, this laser welding process should produce permanent bonds between the fused materials, effectively sealing a previously open microchannel (**Figure 3-3**). **Equation (1)** indicates that both the surface temperature, and the energy required to engender melting,

are proportional to laser diode power output but inversely proportional to spot size (radius), it is expected that as spot size increases, surface temperature at the interface of the valving and transmission layers would decrease.

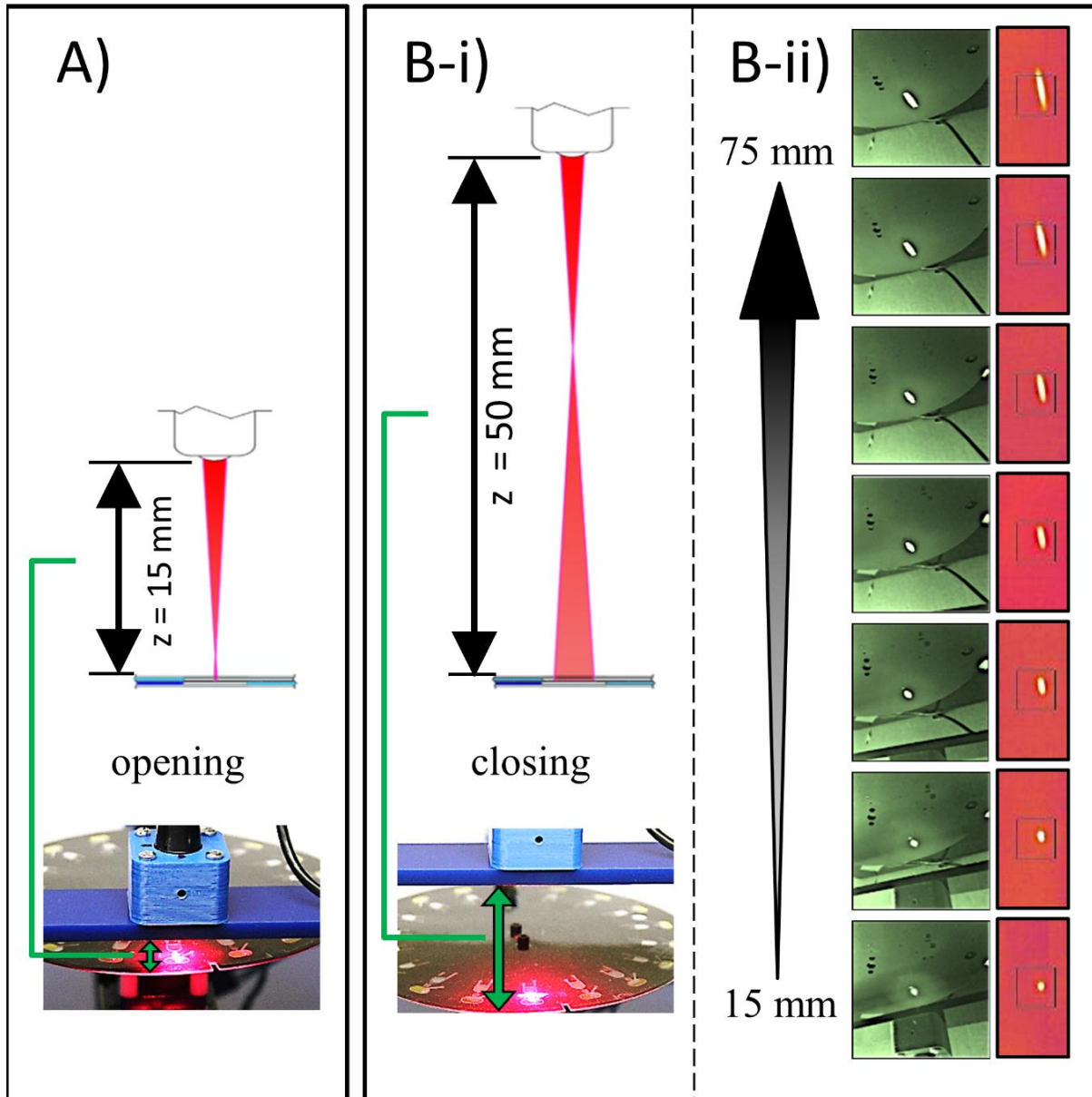


Figure 3-2. Changes in Z-height alter the apparent size and shape of the laser spot on the disc surface. (A) Focused light from a laser positioned 15 mm from the disc surface is used to open a microfluidic valve. (B i) Increasing the z-height of the laser increases the apparent size of the laser spot on the disc and reveals the ovoid/rectangular shape. (B ii) Visible light and thermal images of laser spots across a range of z-heights (15 to 75 mm). Single frame, visible light images were pulled from a slow-motion video capture (240 fps, iPhone 6S). For better visualization of the spots each frame was digitally recolored post-capture (R= 0, G=128, B=0, 50% transparency). Thermal images were acquired with a FLIR i50 infrared camera (140x140 pixels). Adapted with permission from Woolf et al., Lab on a Chip, 2020.

In **Chapter 1**, I described how integration of active valving methods can serve as the linchpin for complex centrifugal microfluidic systems (e.g., **CDx**) and demonstrated that the laser-based approach can be used to reliably supplant passive and manually actuated flow control methods described elsewhere.²⁴⁻²⁶ In this chapter, I describe the development and optimization of the of the contact and non-contact valve closure methods.

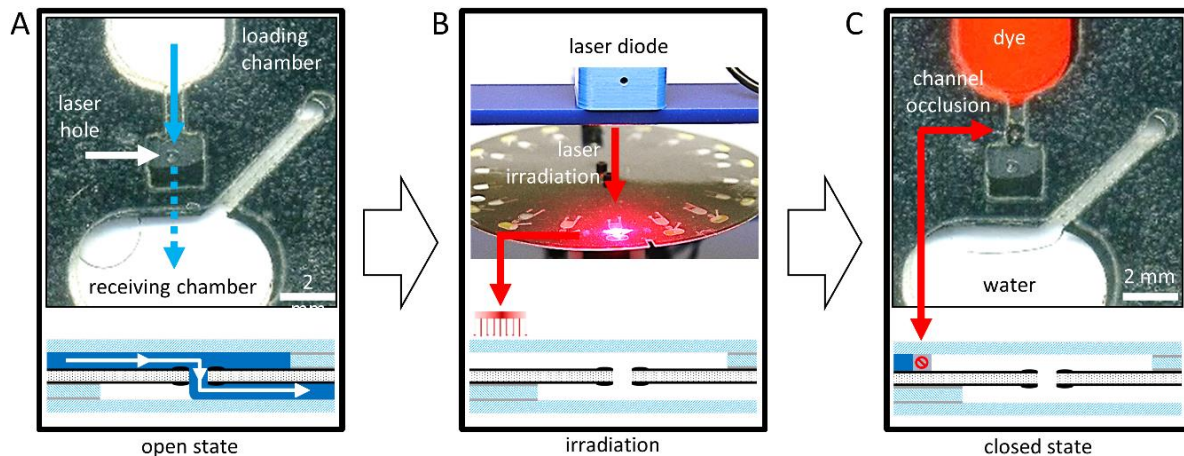


Figure 3-3. Working principle of laser irradiated, closable microchannels. (A) Normally closed valves consisting of a printed xerographic toner or a black PeT layer were opened with a 638 nm red laser (500 mW 0.5 sec 16 mm Z-height). (B) Increasing the Z-height of the laser increases the area of irradiation. (C) Irradiating a larger area permits the melting of the underlying material, subsequently closing the microfluidic channel and preventing fluid flow. Closeup images were acquired with a Canon Rebel T1i EOS 500D 15.1 MP DSLR camera body and Canon MP-E 65mm f/2.8 1-5x Macro lens at approximately 2x magnification. Adapted with permission from Woolf et al., *Lab on a Chip*, 2020.

3.2 Experimental

3.2.1 Microfluidic Disc Fabrication

The microfluidic devices for closable valve (CV) characterization were constructed using the aforementioned PCL fabrication method.^{9, 27} Each microfluidic disc was comprised of five 101.6 μm , polyethylene terephthalate (PeT) films (Film Source, Inc. Maryland Heights, MO, USA). A 50.8 μm heat sensitive adhesive (HSA) was used to facilitate strong layer adhesion (EL-7970-39, Adhesives Research, Inc. Glen Rock, PA, USA).²⁷ Layers 2 and 4 served as the primary fluidics layers, whereas the third (middle) layer functioned as a valving layer and prevented fluid passage between

otherwise open channels in layers 2 and 4. To enable laser-based valving, each middle layer consisted entirely of unaltered 75 μm bPeT (Lumirror* X30, Toray Industries, Inc. Chuo-ku, Tokyo, Japan) or clear PeT coated with xerographic toner (two 6 μm coats on each side). Prior to lamination, the microfluidic architecture was ablated into each layer using a CO₂ laser cutter (VLS3.50, Universal® Laser Systems, Scottsdale, AZ, USA). The five base layers were heat bonded with an office laminator at ~175-190°C (UltraLam 250B, Akiles Products, Inc. Mira Loma, CA, USA). When greater volumes were required, polymethyl methacrylate (PMMA) accessory pieces, also fabricated via laser ablation, were used to provide increased chamber depth. The PMMA pieces were affixed to the five-layer base disc with 55.8 μm pressure sensitive adhesive (PSA) (ARcare 7876, Adhesives Research, Inc.).

3.2.2 *Valve Opening*

Normally closed valves consisting of laser-printed xerographic toner or bPeT were opened with a 700 mW, 638 nm laser diode (L638P700M, Thorlabs, Inc. Newton, NJ, USA) (**Figure 3-2 A**).² The diode was positioned 16 mm above the disc surface and was focused with a collimation tube containing a single aspherical lens element (LTN330-A, Thorlabs, Inc.). All valving patches were irradiated for 500 ms at 500 mW. Prior to attempting valve closure, successful valve opening was confirmed by passing 10 μl water or food dye (5 drops per 15 ml) through the valve and into a receiving chamber. Disc rotation provided the centrifugal force required to move the fluid (**Figure 3-3 A**).

3.2.3 *Contact Heating - Preliminary Feasibility Study*

Preliminary evaluation of this closure method involved a sample set of 181 valves that were previously opened via laser irradiation. To confirm valve opening, water (10 μl) was loaded into a chamber nearer the center of rotation (CoR), centrifugally driven through the

open valve (1,000 rpm for 3 s) and collected in a downstream receiving chamber. For these preliminary experiments, heat and pressure were manually applied to the opened valves using a soldering stylus (FX-8801, HAKKO Corp. Naniwa-ku, Osaka, Japan) with an adjustable 70 W power supply (FX-888D-23BY, Hakko) (**Figure 3-4 A**). The conical stylus tip (T18-B, Hakko) was modified such that the end was flat with diameter $\phi = 1.5$ mm. Stylus temperature ranged from 100-180 °C. Stylus temperature was calibrated and verified with a Fluke 54 II B 60 HZ dual input thermometer and a T-type thermocouple (Fluke Corp. Everett, WA, USA). A 1.5 mm thick 6061 aluminum alloy plate placed below the disc, served as a heat sink. Contact time and applied pressure (manual) varied from 10-30 s and 110-965 psi, respectively (**Figure 3-4 D**). During this preliminary evaluation, all valve closures were challenged by loading 10 μ l of colored dye into the upstream chamber and exposing to a single 5 s spin at 2,000 rpm (approx. 245*g). Successful valve closures were defined as a closure that remained leak-free with no apparent fluid seepage or outflow.

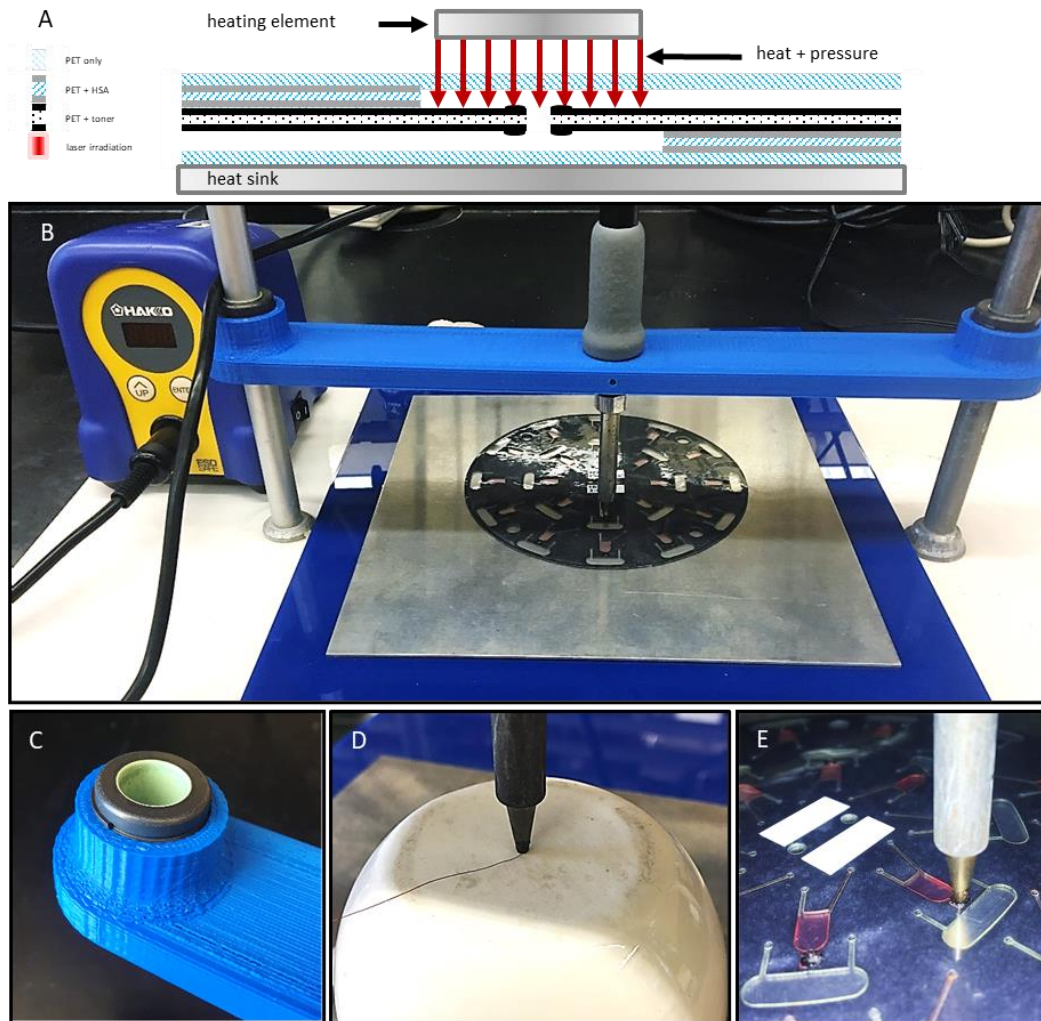


Figure 3-4. Schematic diagram and photographs of the gantry platform for bringing the heating element into contact with the disc. (A) Schematic diagram of the contact heating approach. (B) A gantry arm was 3D printed, outfitted with two self-aligning linear sleeve bearings (C), and suspended between two standard laboratory support stands. The soldering stylus was inserted into the gantry arm, held in place with set screws, and connected to the adjustable power supply. (D) Calibration of stylus temperature with a digital thermometer and a T-type thermocouple. (E) Closeup photograph of the soldering stylus in contact with a previously opened laser valve (2 x 2 mm). Adapted with permission from Woolf et al., *Lab on a Chip*, 2020.

3.2.4 Contact Heating - Secondary Evaluation

To better understand the effects of, and the relationship between, the three key predictor variables (time, temperature, and pressure), a second series of experiments was conducted. Briefly, to ensure uniform contact with the 2 mm x 2 mm laser patches, a custom gantry arm was 3D printed, outfitted with two, self-aligning linear sleeve bearings (McMaster-Carr, Elmhurst, IL, USA), and suspended between two standard laboratory ring stands (**Figure 3-4 B and C**). The soldering stylus was inserted into the gantry arm and held in place with two set

screws. The same adjustable 70 W power supply (FX-888D-23BY, Hakko) and modified conical stylus tip (T18-B, Hakko) were utilized. This gantry arm setup was used to evaluate an additional 180 valve closures (10 discs, n = 18 valves per disc). As before, water was passed through the previously opened valves to confirm successful opening. Valves closures were attempted at 18 different temperatures, ranging from 100-270 °C (n = 10 each). Contact time and applied pressure were held constant at 3 s and 336 ± 75 psi, respectively.

During this second set of experiments, all valve closures were challenged by loading 10 μ l of dye into the upstream chamber (**Figure 3-4 E**) and exposing to three sequential 5 s spins at 2,000, 3,000, and 4,000 rpm (approx. 245, 555, and 985*g). Successful valve closures were defined as a closure with no apparent fluid loss (leak free) after the 985*g spin. Gradual or partial leaks were recorded as complete failures at the earliest indication of dye ingress into the downstream chamber and/or fluid egress from the loading chamber. Thus, a valve closure was deemed successful only if the weld remained leak-free through the 985*g spin step.

3.2.5 *Valve Closure - Preliminary Studies*

Preliminary evaluation of this laser-based closure method involved 374 attempted valve closures (330 toner-HSA and 44 bPeT) across seven irradiation times, six power outputs, and six z-heights (**Table 3-1 A**). On these PCL fabricated devices, the cross-sectional microchannel profile is rectangular. Channel depth (D) is determined by the thickness of the PeT (approx. 100 μ m), while channel width (W) typically varies between 80-500 μ m. Preliminary experiments (data not shown) suggested greater difficulty closing channels with larger dimensions (wider), like those found on the dSPE device²⁵ (W = 400 μ m) and the CDx disc (W= 450 μ m). As such, all microchannel dimensions for the characterization and optimization studies were fixed at 100 μ m * 460 μ m (D*W) (**Fig. 3B** and **C**). All attempted valves closures were located 54.2 mm from the CoR, and top irradiated. Specifically, 264 channels were in

layer 2 (shallow) and 110 channels were in layer 4 (deep). During this preliminary evaluation, all channels were manually aligned with the laser diode using a 0.1 s laser flash at 500 mW for visual orientation. A mechatronic platform was constructed to perform automated z-height adjustments.

Table 3-1. Laser diode settings and closure conditions for all laser-based closure experiments. (A) Laser diode setting ranges for all laser-based valving experiments. (B) Disc material type and valve closure conditions for supplemental experiments that followed the preliminary statistical modelling (*manual alignment of the target channel and laser diode*). (C) Disc type and valve closure conditions for the optimization studies using the automated PrTZAL system. THSA = toner-HSA, PeT = polyethylene terephthalate, bPeT = black polyethylene terephthalate

A.				
		power (mW)	height (mm)	time (s)
range (manual)		200-700	25-30	1-4
range (automation)		200-700	20-30	2.5
increment size		100	1	0.5
B.				
disc type	n =	power (mW)	height (mm)	time (s)
THSA	199	700	26	3.0
THSA	48	700	27	3.0
bPeT	76	500	25	2.5
C.				
disc type	n =	power (mW)	height (mm)	time (s)
5-layer bPeT	90	600	27	2.5
6-layer bPeT	118	700	28	4.0

Following irradiation, the integrity of each attempted valve closure was challenged and evaluated for fluid loss. The entire opening, closure, and challenge workflow is detailed in **Figure 3-5**. A survey of publications related to centrifugal microfluidics suggests that most spin systems operate at modest rotational frequencies, commonly between 10-50 Hz (600-3,000 rpm).^{4, 10, 15, 28-31} Given that most centrifugal microfluidic platforms are no larger than a standard compact disc (120 mm \varnothing), most valves will experience a relative centrifugal force (rcf) ≤ 605 *g. As such, these attempted valve closures were challenged by loading 10 μ l dye into the upstream chamber and exposing the closure to four sequential 5 s spins (rcf = 61, 242, 545, and 970 *g) (**Figure 3-5C**). It should be noted that throughout these and subsequent dye

studies, slow or partial leaks were recorded as failures. Thus, a valve closure was deemed successful only if the weld remained leak-free through the 970 *g spin. To be precise, a failure was recorded at the earliest indication of dye ingress into the receiving chamber (any visible color change) and/or fluid egress from the loading chamber (any visible change in the height of the fluid column therein).

3.2.6 *Valve Closure - Automation Studies*

Based upon the preliminary studies, we set out to understand the effects of, and relationship between, two key predictor variables: power output and z-height, in order to identify optimal closure conditions for bPeT and toner-HSA (THSA) discs. For these studies, the mechatronic system was reconfigured to perform automated alignment of the target channel, as well as automated z-height adjustments- hereafter referred to as the PrTZAL (**p**ower, **t**ime, and **z**-height **a**djustable **l**aser) system (**Figure 3-6**). Other methods for channel alignment exist; however, those approaches frequently require laser-induced fluorescence or innate opto-signature detection of the channel.³² From an engineering perspective, our approach is a simpler, low-cost solution for target channel alignment. The PrTZAL system is detailed in the materials and methods section.

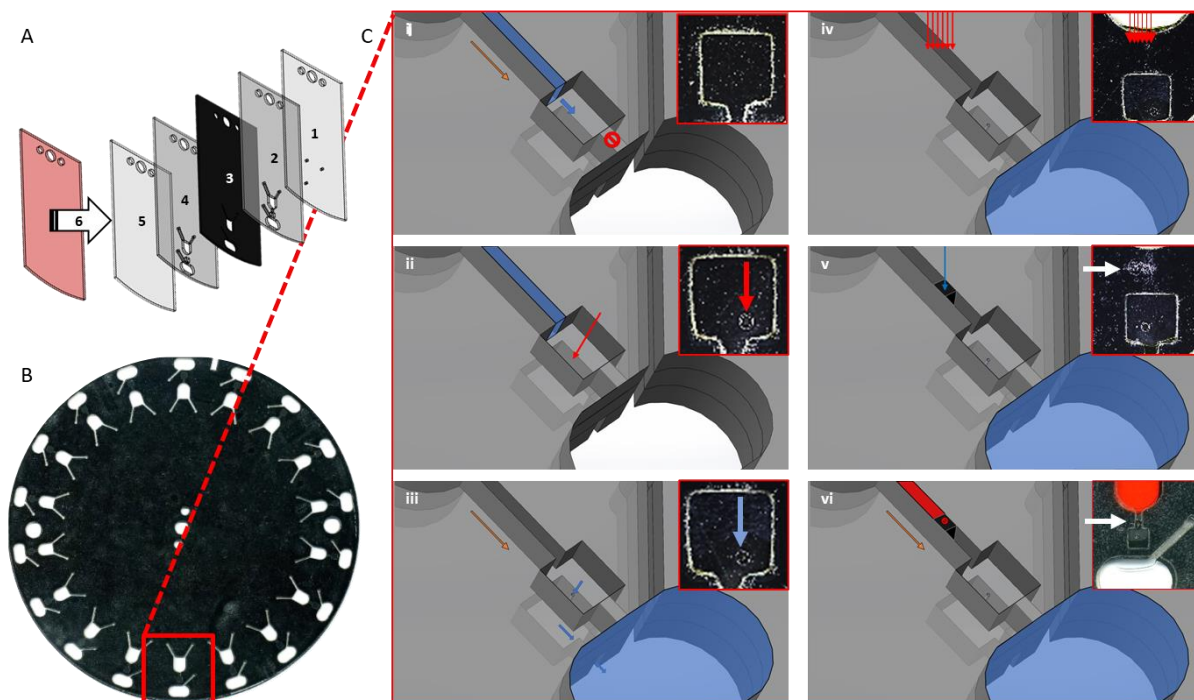


Figure 3-5. Overview of the microfluidic disc and the sequence of valving/fluidic events. (A) Exploded view of a model test chip. Each disc is fabricated using the PCL method and consists of 5 or 6 laminated layers. (B) A fully assembled microfluidic disc. (C) Closeup photographs of a single, representative test domain. (C-i) 10 μl of water or colored dye is added to the loading chamber, and the disc is spun to demonstrate integrity of the valve in the closed state. (C-ii) The optically dense valving patch (2x2 mm) is opened via laser irradiation (red arrow). (C-iii) The chip is spun and fluid moves into the receiving chamber, effectively demonstrating that the valve is now open. (C-iv & v) The 460 μm wide microchannel is irradiated and closed. To demonstrate that the laser valve is closed, 10 μl of dye is added to the loading chamber and the chip is spun at 500 rpm. (C-vi) The valve closure is subjected to repeated spin cycles with increasing g (up to 970 g). Closeup images were acquired with a Canon Rebel T1i EOS 500D 15.1 MP DSLR camera body and Canon MP-E 65mm f/2.8 1-5x Macro lens at approximately 2x magnification. Adapted with permission from Woolf et al., Lab on a Chip, 2020.

This evaluation involved 544 attempted valve closures ($n_{\text{bPeT}} = 264$ and $n_{\text{THSA}} = 280$) across a matrix of six power outputs and eleven z-heights (**Table 3-1 A**). Of note, the collimation tube used to focus the laser light does not have any temperature regulation capability. Poor heat dissipation while operating at high power output can cause elevated internal diode temperature, lower observed optical output power during prolonged irradiation times, diode degradation, and shortened diode lifetime. Thus, to avoid undue heat stress on the laser diode, irradiation time was held constant at 2.5 sec. All valves were 100 μm * 460 μm (D*W), located 54.2 mm from the CoR, and top irradiated during attempted valve closure. Each attempted closure was challenged as previously described. Fourteen candidate logistic

regression models were generated using power, z-height, and material type as predictor variables.

3.2.7 Valve Closure - Optimization and Addressing Failure Modes

Five bPeT-HSA discs were fabricated using the five-layer PCL method and 90 valve closures were evaluated (**Table 3-1 C**). Seven additional six-layer, bPeT-HSA discs were fabricated, and 118 valve closures were evaluated (**Table 3-1 C**): an extra layer of HSA and clear PeT were added to the bottom of each disc. All valves were $100\ \mu\text{m} \times 460\ \mu\text{m}$ (D*W), located 54.2 mm from the CoR, and top irradiated during attempted valve closure. Each attempted closure was challenged as previously described.

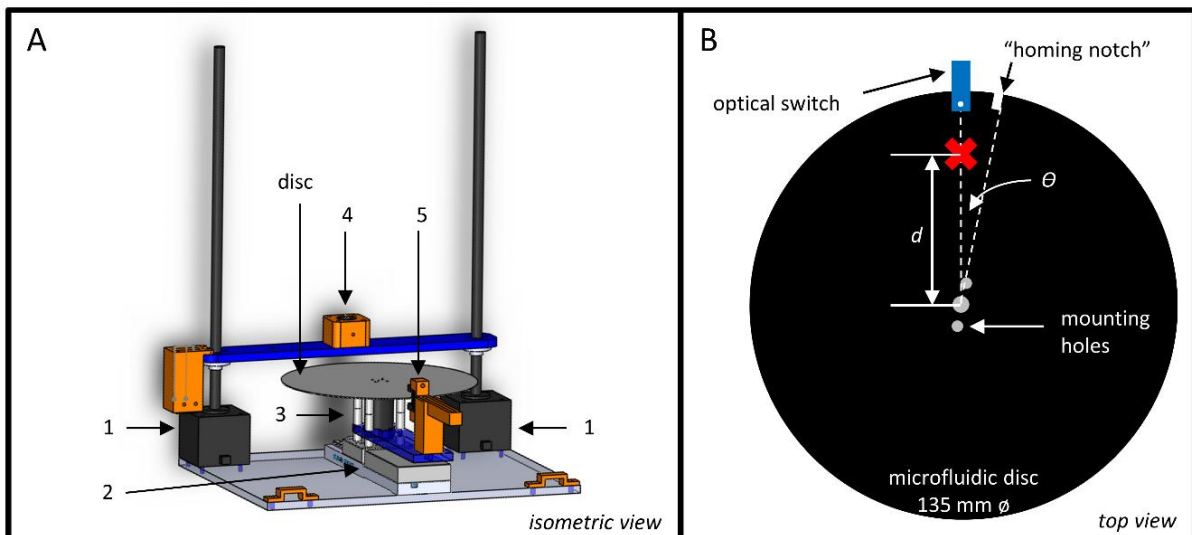


Figure 3-6. Schematic diagrams of the (A) PrTZAL platform and (B) automated target channel alignment. Major components of the PrTZAL system included (A1) two stepper motors for vertical translation of the diode, (A2) a horizontal translation stage, (A3) a DC micromotor for disc rotation, (A4) a laser diode with focusing optics, and (A5) a photo-interrupting optical switch. A 32-bit multi-processing chip controlled and regulated the system (not shown). (B) The laser diode was aligned with each target location (red “X”) by predefining the distance from the center of rotation (d) and the angle of rotation (θ) relative to a “homing notch” or optical break ($\theta = 0$). Adapted with permission from Woolf et al., Lab on a Chip, 2020.

3.2.8 Data Analysis

Logistic regression is a predictive analysis method suitable for modelling binary outcome data, i.e., success-failure, yes-no, 0-1, etc. Logistic regression yields a mathematical model that measures the effect of, and relationship between, one or more

explanatory variables and the binary dependent variable. This approach can be used to estimate the probability of valve or channel closure given certain independent variables (e.g., pressure, time, and temperature) and interactions between the variables. Logistic regression models were fashioned using the generalized linear model (*glm*) function in R version 3.6.1 (2019-07-05). The relative quality of the statistical models was assessed using the Bayesian information criterion (BIC) and Akaike information criterion (AIC).³³ BIC and AIC differences were calculated as

$$\Delta AIC_i = AIC_i - AIC_{min}$$

Eq. 6

and/or

$$\Delta BIC_i = BIC_i - BIC_{min}$$

Eq. 7

where AIC_i is the *AIC* for the *i*th model and AIC_{min} is the *AIC* of the lowest scoring (minimum) model and where BIC_i is the *BIC* for the *i*th model and BIC_{min} is the *BIC* of the lowest scoring (minimum) model. Models with lower AIC values were considered better fits for these data. Models with $\Delta BIC_i \leq 10$ were considered for further analysis (explained below).³³⁻³⁸ Candidate model(s) with $\Delta BIC_i \geq 10$ have essentially no statistical support and were omitted from further analysis. Statistical significance for each main effect (power, z-height, and material type) as well as the two-way and three-way interaction terms between them was determined via one-way ANOVA.³⁹

It should be noted that the purpose of this modelling was not to generate a single, predictive model but rather to better understand the impact of each explanatory variable on the probability of successful channel closure. Alas, this type of regression analysis employs a logistic function to estimate probabilities and produces coefficients that are

on the log-odds or logit scale.⁴⁰ Without a simple means of interpretation, ascertaining how each explanatory variable, coefficient, or interaction term impacts the probability of successful channel closure is, at best, difficult. Graphical displays, like marginal effects plots, help with visualization and provide a more intuitive means for understanding complex *glm*, their main effects, and the interaction terms. Accordingly, marginal effects plots were generated using the *effects* package in R and featured herein.³⁴⁻³⁶

The described statistical evaluation, combined with anecdotal observations made during the preliminary testing, provided the basis for a supplementary experiment in which an additional 323 valve closures were attempted; to appraise the utility of the chosen model, a battery of irradiation conditions (predicted to result in the highest rate of channel closure success) were attempted (**Table 3-1 B**).

3.3 Materials and Methods

3.3.1 PrTZAL System

The PrTZAL mechatronic system (**Figure 3-6 A**) was configured to perform automated z-height adjustment of the laser diode as well as alignment of the laser diode and target channel (**Figure 3-6 B**). A 700 mW 638 nm laser diode was used for all valve openings and closures. (L638P700M, Thorlabs, Inc. Newton, NJ, USA) (**Figure 3-6 A-4**). For valve opening events, the diode was positioned 16 mm above the disc surface and was focused with a collimation tube containing a single aspherical lens element (LTN330-A, Thorlabs, Inc.).

Targeted microchannels were identified and located using two variables: distance from center of rotation (d) and angle of rotation (θ) relative to a predefined homing position (**Figure 3-6 B**). A motorized translational stage (MTS50-Z8, Thorlabs), photo-interrupting optical switch (TT Electronics/Optek Technology, Woking, UK), and brushless DC micromotor

afforded the necessary horizontal and rotational adjustments to align the laser diode with each predefined target location; the horizontal and rotational resolutions are 0.04 mm and 0.2°, respectively. Z-height adjustments of the laser diode were driven by two stepper motors with a resolution of 0.04 mm (Pololu Robotics and Electronics, Las Vegas, NV, USA). A 32-bit multi-processing microcontroller regulated all PrTZAL functions (Propeller P8X32A-M44; Propeller Inc., Rockland, CA, USA).

3.4 Results and Discussion

The sections that follow detail two methods for permanently obstructing microfeatures (valve closure). Both methods are amenable to PCL disc fabrication with polymeric materials, and both can be automated. Generalized liner modeling (logistic regression) is used to evaluate each approach. Section **3.4.1** discusses how application of heat and pressure can be used to collapse and seal microchannels or previously opened laser-valves. While promising, this method requires two distinct modes of actuation for valve opening and closure, i.e., laser opening and contact heating closure. Preliminary studies (not presented) indicated that closing an open laser valve hole via more diffuse laser irradiation was unlikely, perhaps due to the coefficient of linear thermal expansion and a lack of external forces to bring softened materials into intimate proximity. However, sections **3.4.2** through **3.4.4** present findings that showcase how the same laser that was used to perforate a polymeric barrier layer (valve opening) can be used to collapse and seal a microchannel (valve closure). Section **3.4.2** illustrates microchannel collapse and occlusion via laser irradiation, section **3.4.3** discusses improved robustness and success rate via automated target channel alignment, and section **3.4.4** details optimization of the laser-based method by addressing failure modes and adding reinforcing material layers.

3.4.1 *Contact Heating Method*

By investigating contact heating as a means of channel closure, we sought to ameliorate two potential concerns associated with the expandable foam and chloroform redeposition valve closure methods (described elsewhere),²⁰ namely the need for any additional reagents and to circumvent the need for prolonged curing and evaporation. For these preliminary contact heating experiments, eight candidate logistic regression models were created using three key predictor variables: pressure, time, and temperature (main effects). The core *summary()* function in R returns the Wald z-statistic and the associated p-values for each term in the *glm*. These values for the highest quality statistical model suggested that all three predictor variables were statistically significant at $\alpha = 0.05$ ($z = 2.218, 1.999, 3.838$; $p\text{-value} = 0.026585, 0.045645, 0.000124$ for temperature, contact time, and applied pressure, respectively). Results from this initial experiment suggested that increasing contact time and pressure had positive effects on the probability of successful valve closure, while increasing temperature exhibited a negative effect on the probability of successful valve closure (**Figure 3-7**). When testing the null hypothesis that there is no interaction between stylus temperature and contact time, I rejected the null hypothesis at $\alpha = 0.05$; this modelling indicated a significant two-way interaction between temperature and time, although this interaction was not overwhelmingly significant at $\alpha = 0.05$, $z = -2.004$ and $p = 0.045039$. Collectively, these preliminary findings indicated that it is possible to close previously opened laser valves at lower stylus temperatures, but increased pressure and heating time were required. Thus, I surmised that the apparent negative effect of temperature on the probability of successful valve closure was at least partially due to the two-way interaction between stylus temperature and contact time. As such, I hypothesized that evaluating stylus temperature as the sole predictor variable, while holding contact time and applied pressure constant, would reveal more optimal closure conditions with a tighter, more favorable confidence intervals.

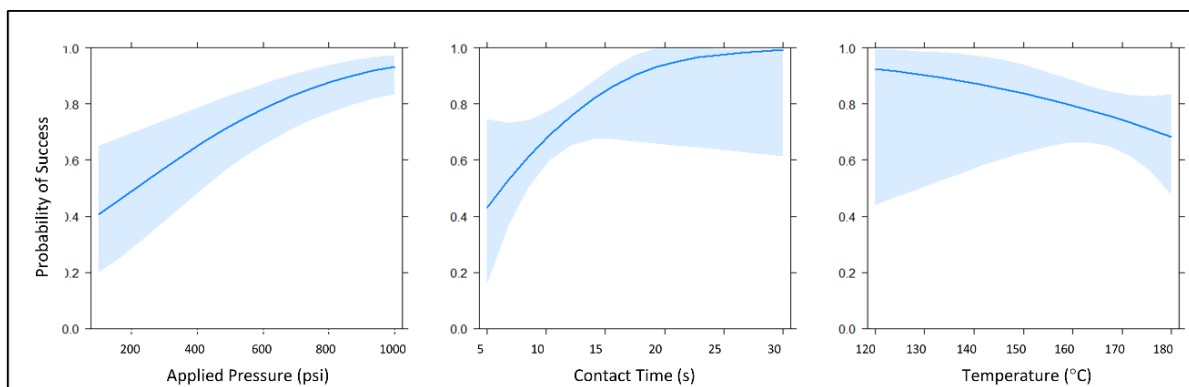


Figure 3-7. Main effect plots of the selected generalized linear models from preliminary contact heating data. The main effects for this model were the continuous predictor variables of: applied pressure, contact time, and temperature (power + height + time). Each of these marginal effects plots reflects the probability of successful channel closure when the other predictor variables are held constant at their respective means. Light blue traces indicate a 95% confidence interval for each probability plot. Adapted with permission from Woolf et al., Lab on a Chip, 2020.

During the secondary set of experiments, pressure and contact time were held constant (3 s and 336 ± 75 psi, respectively) while temperature varied (100 °C to 270 °C, $n = 10$ each). Therefore, temperature served as the sole predictor variable and a single candidate regression model was created. A sharp increase in the number of successful channel closures was noted, as the stylus temperature exceeded 230 °C (**Figure 3-8 A and B**). When the stylus temperature reached the melt temperature of PeT (250 °C), 93.2% of valve closures ($n = 73$) remained leak-free to 4,000 rpm (982.3 *g). This finding is significant given that most spin systems operate at modest rotational frequencies of 600-3,000 RPM (10-50 Hz)^{4, 10, 15, 28-31} and that most centrifugal microfluidic discs are no larger than a standard compact disc (120 mm \varnothing), i.e., most valves will experience a relative centrifugal force (rcf) ≤ 605 *g. Using temperature as the sole predictor variable for this data set, a single candidate generalized linear model was created. It was therefore confirmed that temperature was a statistically significant main effect term at $\alpha = 0.05$ ($p = 6.12 \times 10^{-10}$).

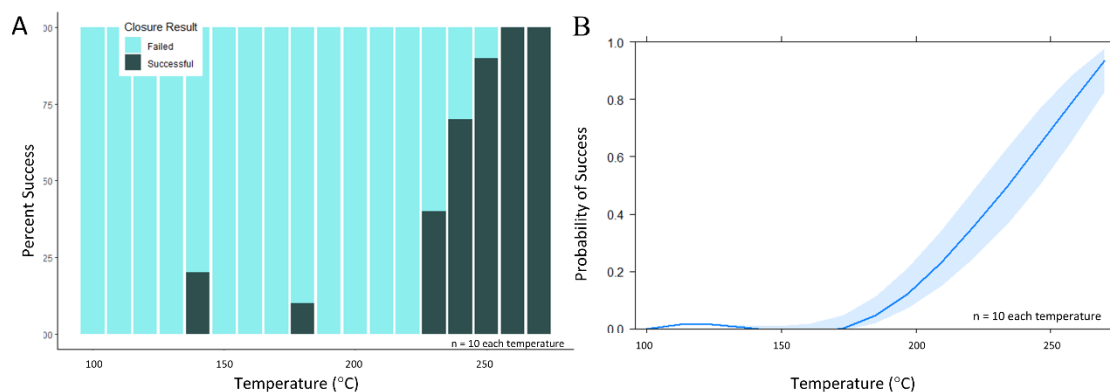


Figure 3-8. Evaluation of valve closure via the contact heating method over a wider stylus temperature range. (A) When pressure and time were held constant (336 ± 75 psi and 3 s respectively) and as stylus temperature exceeded 230°C , a sharp increase in channel closure success was noted. (B) This same data represented in a main effects plot, which suggests a rapid increase in the probability of successful closure as stylus temperature increases from 200 to 270°C . Adapted with permission from Woolf et al., Lab on a Chip, 2020.

Contact heating offers a straightforward approach to microfeature closure that is flexible and customizable, allowing the user to tune applied pressure as well as heating element temperature and dwell time. This strategy for closing valves is a striking alternative to other active valve closure methods (e.g., elastomeric diaphragms, ferrowax systems, polyurethane foam, etc.) for three key reasons. This versatile approach acts on existing microfeatures and requires no: 1) additional fabrication steps, 2) changes to microfluidic architecture, or 3) supplementary chemical reagents (e.g., waxes, foaming agents, solvents). From an engineering perspective, integration of the requisite heating element is rather simple, requiring little more than a retractable heating element. Alternatively, it is conceivable that a microheater could be applied locally to the device and/or valve, effectively minimizing engineering complexity by eliminating the need for a retractable heating element.

3.4.2 Laser-based Method - Preliminary Studies

Small, high-power output laser diodes have been used to open valves within polymeric, microfluidic architectures. The microscopic cross-section of these diodes is rectangular, producing a divergent, elliptically shaped cone of emitted light.²² This near-rectangular, ovoid profile of the laser spot was more pronounced and clearly visible with

increasing z-height (**Figure 3-2 B-ii**). In the context of these studies, this elongated profile was advantageous, producing irradiated regions that spanned the width of the channel without unnecessarily impacting the upstream or downstream architecture. Initial characterization of the laser spot suggested that positioning the laser diode ≥ 25 mm z-height would generate an ovoid spot sufficient to span the 460 μm wide channel (**Figure 3-2 B-i**). For this laser-based valve closure study, thirty-nine candidate logistic regression models were generated using five key predictor variables (main effects), including: irradiation time, laser power output, z-height, valving layer material type, channel depth, and the term interactions (R v.3.5.1, RStudio v.1.1.456).^{37, 38} Of the thirty-nine candidate *glm*, six had $\Delta BIC_i \leq 7$, suggesting similar trade-offs between model fit and complexity. Two-way ANOVA model analysis indicated no statistically significant difference between five of these models. These five models agreed that power, time, and z-height were individually statistically significant ($\alpha = 0.001$). Interestingly, material type effect was significant at level 0.01, while channel position (layer 2 v. layer 4) was not significant in any model; suggesting that bPeT discs performed better than THSA discs and channel depth had no impact on the outcome of attempted valve closure.

As shown in **Figure 3-9**, marginal effect plots of these non-linear relationships reflect the probability of successful channel closure (y-axis) as predicted by a single variable (x-axis) when the other predictor variables are held constant at their respective means. For example, with increasing power output from 400 to 600 mW, a sudden change in slope is observed, suggesting a rapid transition from near certainty of failure to near certainty of success. Likewise, as irradiation time increased from 2.0 to 3.0 s, a sharp positive effect on the outcome was observed. Conversely, as the distance between the laser diode and disc surface increased,

it was clear that there was a sharp decline in the probability of successful channel closure between 26 to 29 mm. The predicted probabilities of success for material type indicated a higher probability of successful channel closure when bPeT was used in the valving layer.

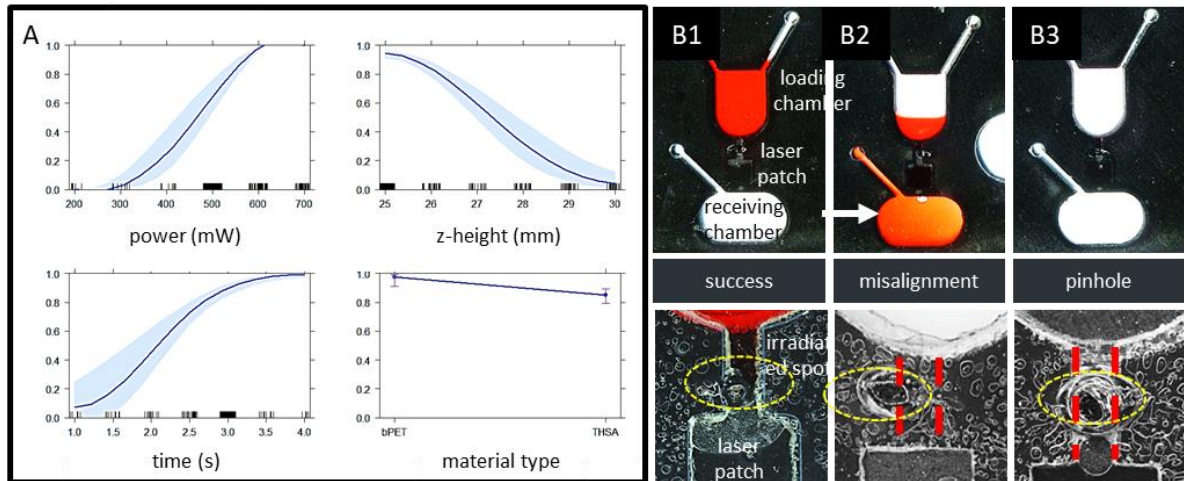


Figure 3-9. Initial evaluation of three primary variables (power, height, and time) and the effects on valve closure success (MANUAL SYSTEM). (A) Generalized linear modelling of binary response data with continuous predictors (power + height + time + type). (B) Photographs of the observed failure modes. (B1) Successful channel closure. (B2) Misalignment of the laser with the target channel resulted in a failed closure with visible mixing of fluids in the receiving chamber (white arrow). (B2) Pinhole formation at the point of irradiation resulted in a loss of material integrity with characteristic fluid escape from the disc with no apparent mixing in the receiving chamber. Dashed red lines indicate channel edges. Dashed yellow ovals indicate the location of irradiation. Adapted with permission from Woolf et al., Lab on a Chip, 2020.

Following that evaluation, we attempted to close an additional 323 valves using three sets of closure conditions. Despite the challenges associated with manual alignment, these proof-of-concept trials achieved modest, yet reasonable success rates (>90%). From this appraisal, three failure modes were identified: pinhole formation, incomplete channel closure, and misalignment (**Figure 3-9 B**). Infrequently, pinhole formation, due to material failure (i.e., an opening in the translucent PeT capping layer) at the point of closure, resulted in the loss of fluids from the disc. However, the most frequent failure mode was incomplete channel closure, with laser power and irradiation time being the most important parameters. This finding was consistent with the effects modelling, and simply suggested that those irradiation conditions were insufficient for complete channel occlusion. However, microscopic examination of failed

closures also revealed challenges with poor manual orientation of the laser spot relative to the target channel. This suggests that automated diode alignment was an absolute necessity for comprehensive and objective evaluation of this approach, and essential to improved success rates.

3.4.3 Automated Target Channel Alignment Studies

With automated target channel alignment, and a constant irradiation time of 2.5 s, a clear pattern began to emerge from the data. No failures were observed when diode power output was $\geq 500 \text{ mW}$ and height was $\geq 25 \text{ mm}$ (**Figure 3-10**). Two logistic regression models emerged as potential fits for these data with $\Delta BIC_i \leq 6$. A one-way ANOVA indicated no statistically significant difference between these two models ($p\text{-value} = 0.2981$; $\alpha = 0.05$). Both models indicated a statistically significant two-way interaction between power and z-height, leading to a rejection of the null hypothesis at a significance level of $\alpha = 0.001$ ($z = 6.473$ and 6.476 , $p\text{-value} = 9.58e^{-11}$ and $9.41e^{-11}$). Interestingly, material type was not statistically significant despite its inclusion as a stand-alone main effect in model 10. Unlike the preliminary evaluation, bPeT discs did not significantly outperform THSA discs, suggesting that the originally observed differences in performance were due to poor manual alignment of the target channel.

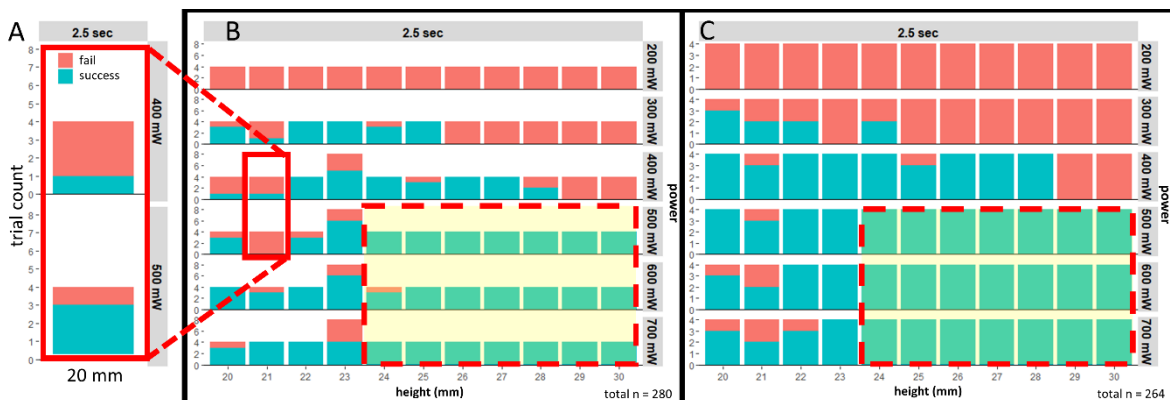


Figure 3-10. Distribution plots for the evaluation of three key variables (power, height, and material type) and the effects on valve closure success (AUTOMATED SYSTEM). Two material types were evaluated: (A) Exemplary distribution plots showing the number of successful closures under two sets of irradiation conditions.

The y-axis represents the number of trials (count) at each set of conditions. Explanation: top plot = 1 of 4 successes at 400 mW, 20 mm, 2.5 s and bottom plot = 3 of 4 successes at 500 mW, 20 mm, and 2.5 s. (B) A total of 280 trials were performed on Toner-HSA (THSA) discs and (C) 260 trials were performed on black PeT-HSA (bPeT) discs. Time was held constant at 2.5 s for all trials. Tinted, yellow boxes indicate regions within the data where no failed valving attempts were observed. Adapted with permission from Woolf et al., Lab on a Chip, 2020.

Visualization of the marginal effects models supported the notion that laser diode power output has a significant positive effect on the outcome of the attempted channel closure (**Figure 3-11 A-i**). Furthermore, contrary to the preliminary modelling, the effect was more pronounced as z-height increased from 24 to 30 mm (**Figure 3-11 A-ii**). This makes intuitive sense: as spot size increases, light energy is dispersed over a larger area, avoiding unnecessary thermal degradation and allowing more effective heat transfer, melting, and intermingling of the incident materials, ultimately leading to more successful valve closures.

3.4.4 *Optimization of the Laser-based Method and Addressing Failure Modes*

After automation of target channel alignment, 3 of 90 (3.3%) attempted valve closures failed on 5-layer bPeT-HSA discs at or before $970 * g$. The diode power output, z-height, and irradiation time were held constant at 600 mW, 27 mm, and 2.5 s, respectively. Without exception, valves that failed with $rcf \leq 970 * g$ appeared to be misaligned, resulting in partial occlusion of the channel and subsequent dye leakage through the open portion into the recovery chamber with increasing rcf and spin time.

However, it is known that hastening the laser welding process can increase stress in the irradiated region. Excessive heating induces breaks in the polymeric molecular structure, significantly increasing porosity while decreasing tensile strength.^{23, 41, 42} The presence of oxygen and water during the melting process can augment this degradation process, further weakening the polymeric film via thermooxidative and hydrolytic decomposition.^{42, 43} We suspected that failed closures, due to pinhole formation, were stress-induced mechanical failures that resulted directly from physical degradation. As such, we expected an increased

likelihood of observing this failure mode with repeated exposures to increasing rotational forces. To further test the robustness of these successful closures, each attempted closure was exposed to rotational forces beyond those experienced under normal operating conditions. i.e., in excess of $970 * g$. Rising hydraulic pressure due to increased rotational forces produced eleven additional weld failures (24%) with partial or total fluid loss at the point of irradiation (**Figure 3-11 B**).

The marginal effects plots indicated a higher probability of success with increased diode power output, z-height, and irradiation time. We hypothesized that increased laser residence time and power output would enhance melting and bond formation at the point of irradiation, while a larger spot size would minimize thermal degradation, thereby reducing the total number of pinhole-type mechanical failures. A small sample set of valves were tested (n=8) at 700 mW, 28 mm and 4.0 s, with little change in success rate and similar patterns of failure observed across the range of rcf (data not shown). This suggested that pinhole formation at the site of irradiation was most likely due to excessive thermal degradation rather than insufficient melting or dwell time.

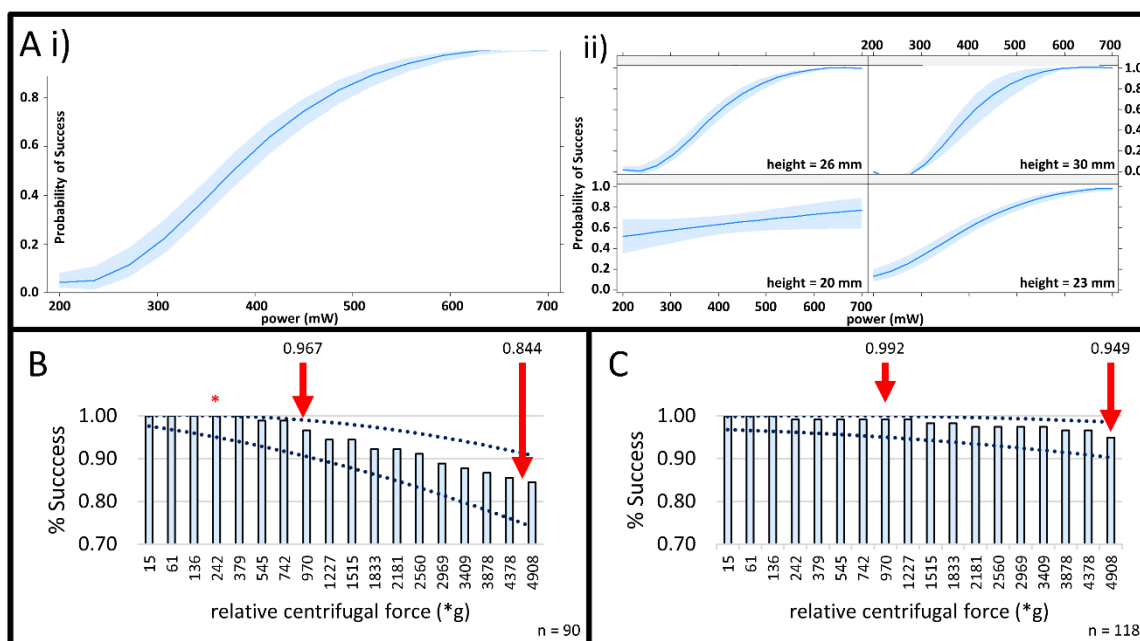


Figure 3-11. Evaluation of laser-actuated valve closure on the fully automated PrTZAL system. (A) Generalized linear modeling of binary response data with continuous predictors (power + height + type). Channel position was not included as a variable in the model. (A-i) The predicted probabilities of successful channel closure where diode power output ranges from 200 to 700 mW in 100 mW increments. For this plot, the coefficients for z-height and material type were held constant at the estimated mean values. (A-ii) Four representative z-height * power interaction effects plots. The shape and slope of the lines and the confidence bands change with increasing z-height. Specifically, a sharper transition from near certainty of failure to near certainty of success is observed between 400 and 600 mW when z-height exceeds 26 mm. (B) Success rate testing on 5-layer bPeT discs (n = 90). Irradiation conditions were held constant at 600 mW, 27 mm, and 2.5 s. (C) Success rate testing on 6-layer bPeT discs (n = 118). Irradiation conditions were held constant at 700 mW, 28 mm, and 4.0 s. Vertical bars indicate observed success rates (% success) after sequential exposures to increasing pseudo-gravitational forces (*g). Darker blue traces indicate a 95% binomial proportion confidence interval (CI) for the probability of successful channel closure under each set of experimental conditions. Adapted with permission from Woolf et al., Lab on a Chip, 2020.

Finally, a third method to address pinhole failures was attempted by way of an additional (6th) reinforcing layer of HSA-PeT, which was laminated to the bottom of each test disc. In a typical 5-layer disc, each target channel is surrounded on three sides by substantial amounts of adhesive and PeT (**Figure 3-5 A**). The 4th, outermost side is constrained by a single, 100 μm layer of PeT that serves as the floor of the channel. The new reinforcing layer provides additional bulk material that should improve heat dissipation while reducing thermal and physical stress on the thin, outer PeT layer (**Figure 3-5 A**). When the reinforcing layer of material was added, and the diode power output, z-height, and irradiation time were increased to 700 mW, 28 mm, and 4.0 s, 1 out of 118 attempted valve closures failed with $rcf \leq 970 *$

g (0.8%). As before, the valve that failed at $379 * g$ appeared to be misaligned relative to the target channel, with complete escape of fluid into the recovery chamber. An additional 5 valve closures failed at an $rcf > 970 * g$ (5.1%) (**Figure 3-11 C**).

3.5 Summary and Conclusions

I have explored and characterized two novel approaches to sealing valves and channels within laminated, polymeric microfluidic devices. These methods for permanently sealing microfluidic channels provide simple solutions to the recognized challenge of closable valving on centrifugal microfluidic devices. As reported here, both methods are rapid (<10 s) and robust within the normal rotational frequency range of centrifugal microfluidic devices. Proof-of-concept dye studies confirmed that an open channel can be closed using a heating stylus or via diffuse, high power irradiation with a laser diode. For the contact heating method, when pressure and contact time were held constant, a sharp increase in the number of successful channel closures was noted as stylus temperature exceeded 230 °C, approaching the melt temperature of PeT ($T_M = 250$ °C) (**Figure 3-8 A and B**). To date, we have demonstrated $>93\%$ success ($n = 73$) when $rcf \leq 982 * g$. Specifically, on 6-layer discs with microchannels ≤ 500 μm wide we expect the true success rate for this method to fall between 95.4 and 99.9% (95% binomial proportion CI) with closure conditions of 700 mW, 28.0 mm, and 4.0 s. For the laser-based approach, the highest quality statistical model (as determined by the BIC_{min}) established that, when irradiation time was held constant, a statistically significant two-way interaction exists between diode power output and z-height (significance level 0.001). A sharp increase in the probability of successful channel closure was noted with z-height ≥ 26.0 mm and power output ≥ 600 mW. To date, we have demonstrated $>99\%$ success under typical operational conditions ($rcf \leq 605 * g$). Specifically, on 6-layer discs with microchannels ≤ 500 μm wide we

expect the true success rate for the laser-based method to fall between 95.4 and 99.9% (95% binomial proportion CI): closure conditions = 700 mW, 28.00 mm, and 4.0 s.

The ability to inexpensively open and close valves imparts phenomenal functionality to a system, while circumventing complicated passive architectural designs and the pump/solenoid hardware that increase complexity and manufacturing costs. While the scope of this chapter is limited to PCL fabricated polymeric, centrifugal microfluidic devices (consisting of PeT, bPeT or xerographic toner, and HSA) we suspect that these methods will prove useful on a broad range of microdevices that contain, or are comprised of, other polymeric materials (e.g. PMMA, PDMS, COC, etc.).⁴⁴ By avoiding the need for external pneumatic pumping, nanoheaters, and laser diodes, these newly described procedures complement existing active valve opening and fabrication techniques by offering versatile, relatively inexpensive alternatives to expandable foam, chloroform dissolution, elastomeric diaphragms, phase-change wax systems. This effectively expands the valving options in the existing microfluidic toolbox.

When contemplating valving methods for integration and application, careful consideration of valve actuation conditions, limitations, and location relative to assay reaction and recovery chambers is warranted. It is possible that heat dissipation during prolonged irradiation or with larger stylus/spot sizes could adversely impact sensitive biological or chemical assays. Accordingly, one of the driving motivations for the optimization studies was identifying closure conditions that minimized the negative impact on the surrounding microfluidic features. As a whole, this body of work indicates that heat generation and dissipation during closure is localized with little impact on the surrounding architecture. Material deformation with the contact heating method was governed largely by the footprint of

the heating stylus tip (shape and dimensions). No deformation of adjacent chambers or valves was observed with the laser irradiation method (**Figure 3-9**).

Subsequent chapters describe how integration of the laser-based valving approach affords flow control that was heretofore unrealized, providing the capability to take multiple different solutions, centrifugally direct them through a central extraction chamber (either individually or mixed), then separate the eluate/desorbed material from that chamber into multiple, discrete, isolated fractions. Much like the optically addressable laser valves described by Garcia-Cordero et al., we anticipate that this laser-based closable valving approach can be modified for use with other fluidic systems i.e., multilevel, capillary-flow-based, or pressure driven.

3.6 Acknowledgements

I wish to thank Clay Ford at the UVa Library: Research Data Services and Data Analytics Center for the expert advice regarding data modelling and analysis.

3.7 References

1. H. Becker, *Lab on a Chip*, 2009, **9**, 2759-2762.
2. J. L. Garcia-Cordero, D. Kurzbuch, F. Benito-Lopez, D. Diamond, L. P. Lee and A. J. Ricco, *Lab on a Chip*, 2010, **10**, 2680-2687.
3. K. Tsougeni, D. Papageorgiou, A. Tserepi and E. Gogolides, *Lab on a Chip*, 2010, **10**, 462-469.
4. J. Siegrist, R. Gorkin, L. Clime, E. Roy, R. Peytavi, H. Kido, M. Bergeron, T. Veres and M. Madou, *Microfluidics and nanofluidics*, 2010, **9**, 55-63.
5. J. Steigert, T. Brenner, M. Grumann, L. Riegger, S. Lutz, R. Zengerle and J. Ducle'e, *Biomedical microdevices*, 2007, **9**, 675-679.
6. R. Gorkin, S. Soroori, W. Southard, L. Clime, T. Veres, H. Kido, L. Kulinsky and M. Madou, *Microfluidics and Nanofluidics*, 2012, **12**, 345-354.
7. Y. Feng, Z. Zhou, X. Ye and J. Xiong, *Sensors and Actuators A: Physical*, 2003, **108**, 138-143.

8. Y. Ouyang, S. Wang, J. Li, P. S. Riehl, M. Begley and J. P. Landers, *Lab on a Chip*, 2013, **13**, 1762-1771.
9. B. L. Thompson, Y. Ouyang, G. R. Duarte, E. Carrilho, S. T. Krauss and J. P. Landers, *Nature protocols*, 2015, **10**, 875-886.
10. R. Gorkin, J. Park, J. Siegrist, M. Amasia, B. S. Lee, J.-M. Park, J. Kim, H. Kim, M. Madou and Y.-K. Cho, *Lab on a Chip*, 2010, **10**, 1758-1773.
11. O. Strohmeier, M. Keller, F. Schwemmer, S. Zehnle, D. Mark, F. von Stetten, R. Zengerle and N. Paust, *Chemical Society Reviews*, 2015, **44**, 6187-6229.
12. I. H. A. Badr, R. D. Johnson, M. J. Madou and L. G. Bachas, *Analytical Chemistry*, 2002, **74**, 5569-5575.
13. T. Thorsen, S. J. Maerkl and S. R. Quake, *Science*, 2002, **298**, 580-584.
14. J. Melin and S. R. Quake, *Annu. Rev. Biophys. Biomol. Struct.*, 2007, **36**, 213-231.
15. J.-M. Park, Y.-K. Cho, B.-S. Lee, J.-G. Lee and C. Ko, *Lab on a Chip*, 2007, **7**, 557-564.
16. K. W. Oh, *Bio Lab, Samsung Advanced Institute of Technology*, 2005, 554-556.
17. W. H. Grover, R. H. Ivester, E. C. Jensen and R. A. Mathies, *Lab on a Chip*, 2006, **6**, 623-631.
18. W. Zhang, S. Lin, C. Wang, J. Hu, C. Li, Z. Zhuang, Y. Zhou, R. A. Mathies and C. J. Yang, *Lab on a Chip*, 2009, **9**, 3088-3094.
19. M. A. Unger, H.-P. Chou, T. Thorsen, A. Scherer and S. R. Quake, *Science*, 2000, **288**, 113-116.
20. C. P. Clark, M. S. Woolf, S. L. Karstens, H. M. Lewis, A. Q. Nauman and J. P. Landers, *Micromachines (Basel)*, 2020, **11**, 627.
21. R. Crafer and P. J. Oakley, *Laser processing in manufacturing*, Springer, 2013.
22. Physics Fundamentals: Laser Diode Characteristics, <https://www.sukhamburg.com/download/fundamentals-laserdiodes.pdf>.
23. G. V. Moskvitin, A. N. Polyakov and E. M. Birger, *Welding International*, 2013, **27**, 725-734.
24. K. Jackson, J. Borba, M. Meija, D. Mills, D. Haverstick, K. Olson, R. Aranda, G. Garner, E. Carrilho and J. Landers, *Analytica chimica acta*, 2016, **937**, 1-10.
25. L. M. Dignan, M. S. Woolf, C. J. Tomley, A. Q. Nauman and J. P. Landers, *Analytical Chemistry*, 2021.

26. M. S. Woolf, L. M. Dignan, H. M. Lewis, A. Q. Nauman, C. J. Tomley and J. Landers, *Lab on a Chip*, 2020, 1426 - 1440.
27. C. Birch, J. A. DuVall, D. Le Roux, B. L. Thompson, A.-C. Tsuei, J. Li, D. A. Nelson, D. L. Mills, J. P. Landers and B. E. Root, *Micromachines (Basel)*, 2017, **8**, 17.
28. D. C. Duffy, H. L. Gillis, J. Lin, N. F. Sheppard and G. J. Kellogg, *Analytical Chemistry*, 1999, **71**, 4669-4678.
29. D. Mark, P. Weber, S. Lutz, M. Focke, R. Zengerle and F. von Stetten, *Microfluidics and Nanofluidics*, 2011, **10**, 1279-1288.
30. J. Ducrée, S. Haerberle, S. Lutz, S. Pausch, F. Von Stetten and R. Zengerle, *Journal of Micromechanics and Microengineering*, 2007, **17**, S103.
31. D. Mark, T. Metz, S. Haerberle, S. Lutz, J. Ducrée, R. Zengerle and F. von Stetten, *Lab on a Chip*, 2009, **9**, 3599-3603.
32. A. Scott, D. Mills, C. Birch, S. Panesar, J. Li, D. Nelson, M. Starteva, A. Khim, B. Root and J. P. Landers, *Lab on a Chip*, 2019.
33. Y. Sakamoto, M. Ishiguro and G. Kitagawa, *Dordrecht, The Netherlands: D. Reidel*, 1986, **81**.
34. J. Fox and S. Weisberg, *Journal*, 2019, **3rd**.
35. J. Fox and S. Weisberg, *Journal of Statistical Software*, 2018, **87**, 1-27.
36. J. Fox and S. Weisberg, *Journal of Statistical Software*, 2003, **8**, 1-27.
37. R Core Team, *Journal*, 2018.
38. RStudio Team, *Journal*, 2018.
39. J. J. Dziak, D. L. Coffman, S. T. Lanza, R. Li and L. S. Jermin, *bioRxiv*, 2019, 449751.
40. F. E. Harrell Jr, *Regression modeling strategies: with applications to linear models, logistic and ordinal regression, and survival analysis*, Springer, 2015.
41. B. G. Girija, R. R. N. Sailaja and G. Madras, *Polymer Degradation and Stability*, 2005, **90**, 147-153.
42. S. Venkatachalam, S. G. Nayak, J. V. Labde, P. R. Gharal, K. Rao and A. K. Kelkar, in *Polyester*, InTech India, 2012, pp. 75-98.
43. F. Awaja and D. Pavel, *European Polymer Journal*, 2005, **41**, 1453-1477.
44. C.-W. Tsao, *Micromachines (Basel)*, 2016, **7**, 225.

Chapter 4 . Characterization of a Centrifugal Microfluidic Vertical Flow Platform

4.1 Introduction

4.1.1 Foundational Microfluidics and Fluid Flow

Over the last decade, there has been increased interest in porous membranes embedded within centrifugal total analysis systems (μ TAS)^{1, 2} and lab-on-a-CD platforms;³⁻⁶ this interest is largely centered on two primary membrane functions – centrifugally-assisted lateral flow immunoassays (LFI)⁷ and in-line filtration of environmental water samples, e.g., sediment and bacteria.^{8, 9}

Microfluidic platforms offer attractive, unconventional approaches that address many limitations associated with existing standard sample handling and laboratory-based analytical systems.¹⁰ For example, most conventional filtration systems are tethered to centralized laboratories, requiring large-scale benchtop equipment and precluding deployment to the point of collection. In contrast, most existing LFIs and stacked, non-pressure-driven vertical flow immunoassay (VFI) systems can be utilized at the point of care (POC). Still, these platforms rely entirely upon capillary action to drive fluid flow, which introduces a unique set of limitations.¹¹ Mathematically, two classical models describe capillary-driven fluid transport through porous matrices, like LFI test strips. First, the Lucas-Washburn equation defines the distance traversed by the fluid front (l) under capillary pressure as

$$l(t) = \sqrt{\frac{\gamma r \cos\theta}{2\eta} t}$$

Eq. 8

where γ is the surface tension at the liquid-air interface, r is the effective pore size (radius) of the porous medium (e.g., membrane), θ is the contact angle between the fluid and said porous medium, η is fluid viscosity, and t is time.¹²⁻¹⁴ Second, Darcy's law describes the volumetric capillary flow rate as

$$Q = \frac{\kappa WH}{\eta L} \Delta P$$

Eq. 9

where κ is the permeability, WH is the membrane cross-sectional area, L is the membrane length, and ΔP is the pressure change across the porous membrane material.^{12, 13} Both models dictate that flow rate and total sample transit time in the capillary flow regime are governed by membrane pore size and fluid viscosity. Thus, to achieve realistic assay run times, capillary-based systems (e.g., conventional LFI systems and non-pressure driven VFI systems) are limited to porous media with larger pore sizes and use with fluid samples that are not particularly viscous.¹¹

Further, assay sample volume is often restricted by LFI test cartridge and absorbent wicking pads that rapidly saturate.^{15, 16} Constraining sample volume limits assay performance in two ways. First, many biofluids and environmental samples exhibit low target concentrations, necessitating analysis of a larger sample volume (possibly on the order of milliliters) to achieve a positive test response.^{9, 17} Second, viscous samples (e.g., blood and sputum) may require dilution to prevent membrane clogging/fouling and to facilitate timely movement through a cellulosic matrix. Thus, sample volume constraints limit assay sensitivity, especially for viscous, low titer biofluids and dilute environmental samples.^{9, 17, 18}

In contrast, the microfluidic platform described here (**Figure 4-1**), like the centrifugally-driven bioanalytical disc described by Anderson et al. in 1969,¹⁹ exploits a rotating disc to generate pseudo-gravitational centrifugal forces (f_ω), defined as

$$f_\omega = \rho r \omega^2$$

Eq. 10

where a liquid body with mass density (ρ), spinning at a frequency (ω), and positioned at a distance (r) from the center of rotation (CoR), experiences an apparent outward force. In turn, these centrifugal forces generate hydraulic pressure heads (Δp_ω) and corresponding parabolic flow profiles with mean fluid velocities (\bar{v}) given as

$$\Delta p_\omega = \rho \bar{r} \Delta r \omega^2$$

Eq. 11

and

$$\bar{v} = \frac{D_h^2 \rho \omega^2 \bar{r} \Delta r}{32 \eta L}$$

Eq. 12

where D_h is the hydraulic diameter of the channel and \bar{r} and Δr are the average distance of the fluid plug from the CoR and the radial extent of the fluid plug, respectively (Fig. 2).^{3,4} Utilization of centrifugal force as the primary driving force to move fluids within a microfluidic architecture permits reduction of instrument size and cost. The use of this force eliminates the need for peripheral hardware such as pneumatic syringe pumps and the associated tubing networks while providing precise flow control not possible via passive capillary forces.^{3,4} With the well-researched and defined characteristics of centrifugally driven flow along with the growing body

of published literature related to vertical flow immunocapture,¹⁷ we have begun investigating and characterizing how embedded membranes might be coupled with on-disc centrifugally-driven microfluidic vertical flow.

For example, to overcome limitations associated with capillary-driven flow, Kainz et. al proposed an on-disc, centrifugally assisted LFI system (cLFI) that clearly demonstrated flow regulation through embedded membranes (parallel or lateral flow) via microdevice rotation. The cLFI used an architecture where the sample chamber and membrane were placed at radially distant positions from one another.⁷ Placing the membrane and sample loading chamber farther apart allowed for a longer inlet channel that, in turn, minimized changes in hydraulic pressure and flow rate (< 9%).⁷ This cLFI system, however, was prone to a phenomenon referred to as ‘bypass flow,’ which is undesirable fluid flow over and around the membrane. Accordingly, a mathematical ‘design factor’ to avoid fluid bypass was derived. In contrast, Karle et al. and Templeton et al. embedded membranes that were bound to a disc, thereby reducing or eliminating bypass flow.^{8, 9} Templeton et al. further demonstrated that insoluble fine particulates and sediments impact flow through embedded membranes but did not describe the impact of other solutes in the liquid samples.⁸

Here, we report preliminary findings related to our print-cut-laminate (PCL) approach to on-disc orthogonal flow (OF) through embedded, nanoporous membranes (**Figure 4-1**).²⁰ Collectively, the microfluidic equations described above provide the foundation for these studies and indicate that, within a confined microfluidic frame of reference and under the influence of a rotational field, centrifugal pumping is impacted by the physical properties of the fluid(s), the radial location of the fluid chambers, channel geometry and orientation, and the rotational frequency of the disc. We empirically characterize and elaborate upon some of the more salient

talking points underscored in existing publications, including the impact of sample composition on flow,⁸ fluid bypass,⁷ membrane-disc fusion,^{8, 9} total time to complete fluid drainage,⁸ and variations in hydraulic pressure head.⁷

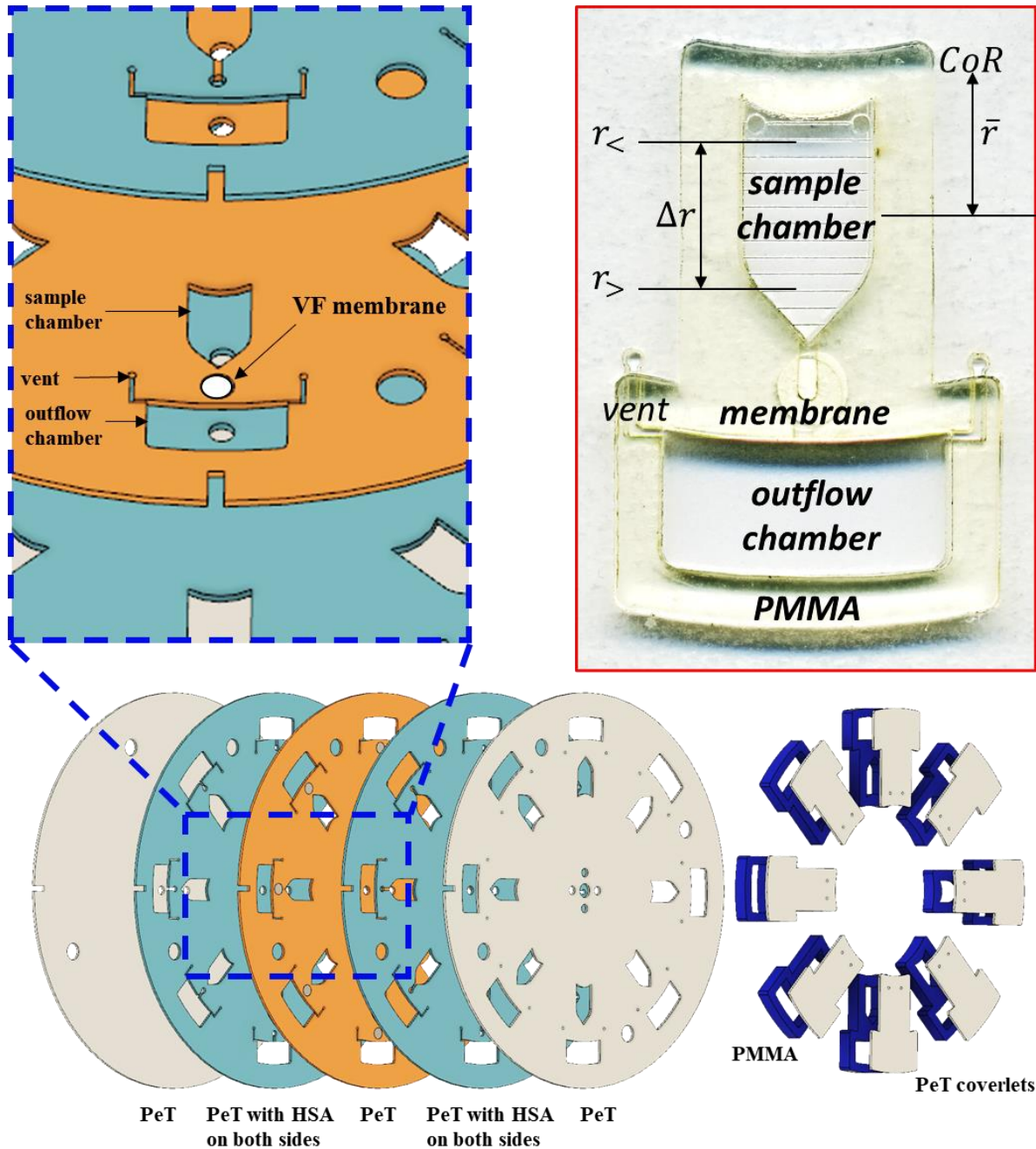


Figure 4-1. Design and assembly of a VF disc. (A) Schematic overview of a six-layer (5 + 1) microfluidic disc design comprised of one polymethyl methacrylate (PMMA) layer and five polyethylene terephthalate (PET) layers. Layers 2 and 4 serve as the primary fluidic layers. Layer 3 functions as a ‘flowthrough’ or ‘via’ layer. (B) Circular cut-outs (4- or 5- mm \varnothing) of porous membranes were placed into cut-out recesses in layer 3. Upon lamination, HSA coated layers 2 and 4 bond to the membrane, anchoring it in place. (C) A photograph of a single fully assembled cVF test domain.

4.2 Experimental

4.2.1 Disc Fabrication

Each centrifugal VF (cVF) disc was constructed via the PCL fabrication method.^{21, 22} Each 5-layer disc consisted of alternating sheets of polyethylene terephthalate film (PeT, 101.6 μm thickness, Film Source, Inc. Maryland Heights, MO, USA) and heat-sensitive adhesive (HSA, 50.8 μm thickness, EL-7970-39, Adhesives Research, Inc. Glen Rock, PA, USA).²² Disc layers, microfluidic architecture, and accessory pieces were designed in AutoCAD® 2019 (Autodesk Inc., San Rafael, CA, USA).

The microfluidic architecture was ablated into the appropriate layers with a 50 W CO₂ laser engraving system (VLS3.50, Universal® Laser Systems, Scottsdale, AZ, USA) (**Table 4-1**). Layers 2 and 4 served as the primary fluidic layers, layers 1 and 5 acted as capping layers, and the PeT layer 3 functioned as the ‘flowthrough’ or ‘via’ layer. A disposable biopsy punch was used to obtain circular cut-outs (4 or 5 mm \varnothing) of the porous membranes (Nitrocellulose Membrane, Precut, 0.2 μm pore size, BioRad, Hercules, CA, USA) and polyvinylidene difluoride (Immuno-Blot PVDF, 0.2 μm pore size, BioRad). Membrane cut-outs were placed into laser ablated voids located in layer 3. All disc layers were aligned, and heat bonded via a double pass-through of an office laminator (~175-190°C) (UltraLam 250B, Akiles Products, Inc. Mira Loma, CA, USA).

Polymethyl methacrylate (PMMA, 1.5 cm, McMaster-Carr, Elmhurst, IL, USA) accessory pieces provided additional chamber depth and volume. For the high-speed video studies, horizontal, linear graduations were rastered into the PeT coverlets of each sample loading chamber (**Figure 4-1**). Post-lamination, the PMMA accessory pieces and the concomitant PeT coverlets were bonded to the 5-layer disc (**Figure 4-1**) with pressure-sensitive adhesive (PSA, 55.8 μm

thickness, ARcare 7876, Adhesives Research, Inc.). To ensure consistent PSA adhesive bonding, fully assembled cVF discs were pressed under a 10 lb. load for ≥ 1 hr.

Table 4-1. Universal® Laser System settings for VF disc fabrication and PeT coverlet rastering.

Layer	Material	Cut Type	VLS Power	VLS Speed
1, 3, 5	PeT	Vector	12 %	10 %
2 and 4	HSA-PeT-HSA	Vector	18%	10%
accessory coverlet	PMMA	Vector	45 %	5 %
coverlet	PeT	Vector	12 %	10 %
coverlet etching	PeT	Raster	7 %	100 %

4.2.2 Microfluidic Layout and Flow Pattern

Each microfluidic disc consisted of multiple testing domains arranged radially around the disc's CoR. Each domain comprised a sample loading chamber located nearer the CoR, a porous membrane embedded within the middle layer of the disc, and a peripherally located recovery chamber. These are all connected by a series of channels (**Figure 4-2**). This architecture produced a flow pattern akin to other multilayered fluidic approaches in which a dissolvable film,²³ laser-valve,²⁴ or porous membrane^{8, 9} is oriented perpendicular to the axis of rotation and embedded between two otherwise open fluidic layers. Disc rotation provided the necessary force to drive fluid radially outward from the sample chamber and through a channel to the vertical flow (VF) port. Centrifugally generated hydraulic pressure caused the fluid to turn 90° and flow through the embedded membrane (transverse flow). Finally, the fluid again turned 90° to flow radially outward from the VF port and into the outlying recovery chamber. (**Figure 4-2**).

4.2.3 Centrifugally Driven Vertical Flow (proof-of-principle)

Prior to lamination, 5 mm diameter (\emptyset) membrane cut-outs were inserted into layer 3 of the VFI disc. Microfluidic architectures with 1- and 2-mm \emptyset VF ports were evaluated. To visually characterize flow, aqueous 10 mM erioglaucine dye solution (Sigma-Aldrich, St. Louis, MO, USA) was prepared in artificial blood plasma with bovine serum albumin (0.3341 mM). Artificial

blood plasma (ABP, pH = 8.13) was prepared according to Liu et al. and consisted of potassium chloride (0.0131 g KCl), sodium chloride (0.4030 g NaCl), disodium phosphate (0.0086 g Na_2HPO_4), sodium bicarbonate (0.0173 g NaHCO_3), magnesium chloride (0.1545 g $\text{MgCl}_2 \cdot 6\text{H}_2\text{O}$), and calcium chloride (0.0193 g CaCl_2) dissolved in 50 ml deionized water (diH_2O) (**Table 4-2**).²⁵ A 10 μl aliquot of the dye solution was added to each sample loading chamber. The disc was then subjected to sequential 30s spins ranging from 100 to 5500 rpm (500 rpm increments). Images of each disc were captured as described above.

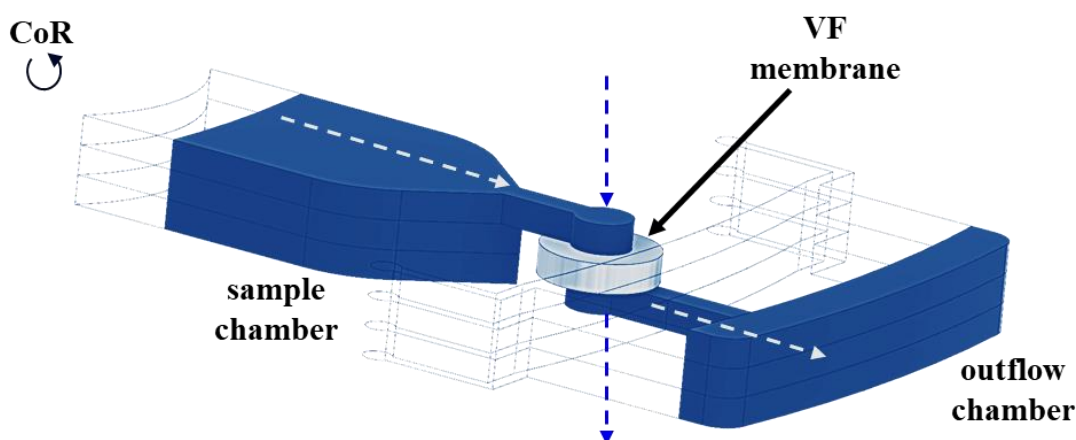


Figure 4-2. On-disc microfluidic layout and vertical flow pattern. Dashed white arrows denote flow direction in layers 2 and 4. Dashed blue arrows denote orthogonal flow direction through the VF port and membrane. Eight microfluidic testing domains were arranged radially around the center of rotation (CoR) (see **Figure 1**). Each testing domain was comprised of a sample loading chamber located nearer the CoR, a nanoporous membrane within the plane of the disc (oriented perpendicular to the axis of rotation) and between the disc layers 2 and 4, and a peripherally located outflow chamber. Disc rotation provided the force required to drive fluid radially outward from the sample chamber and through a short channel to the vertical flow (VF) port. Here, centrifugally generated hydraulic pressure caused the fluid to turn 90° and flow orthogonally through the membrane. Finally, the fluid turned 90° again to flow radially outward into the outlying recovery chamber.

4.2.4 Characterization of On-Disc Vertical Flow

Fluid samples included assay buffer, artificial urine, and artificial blood plasma. Assay buffer consisted of 0.1 M phosphate buffer (PB) containing 0.1% Triton X-100 and 0.1% bovine serum albumin (BSA, pH = 7.2) (Diagnostics Discovery Laboratory, School of Medicine, University of Nevada, Reno, USA). Artificial urine (AU, pH = 6.77) was prepared according to Liu et al.²⁶ The AU solution consisted of urea (1.25 g NH_2CONH_2), sodium chloride (0.45 g NaCl),

ammonium chloride (0.15 g NH_4Cl), creatinine (0.1 g $\text{C}_4\text{H}_7\text{N}_3\text{O}$), disodium phosphate (0.125 g Na_2HPO_4), monopotassium phosphate (0.125 g KH_2PO_4), and sodium sulfite (0.15 g Na_2SO_3) dissolved in 50 ml dH_2O (**Table 4-3**).

Table 4-2. Constituents and concentrations of artificial blood plasma body fluid simulant.

Artificial Blood Plasma (pH = 8.13)								
Name	Linear Formula	Mass (g)	Molecular Weight (g/mol)	Moles (mol)	Volume (ml)	Volume (l)	Concentration (M)	Concentration (mM)
Potassium chloride	KCl	0.0131	74.5513	0.0002	50	0.05	0.0035	3.51
Disodium phosphate	Na_2HPO_4	0.0086	141.96	0.0001	50	0.05	0.0012	1.21
Sodium bicarbonate	NaHCO_3	0.0173	84.007	0.0002	50	0.05	0.0041	4.12
Sodium chloride	NaCl	0.403	58.44	0.0069	50	0.05	0.14	137.92
Magnesium chloride hexahydrate	$\text{MgCl}_2 \cdot 6\text{H}_2\text{O}$	0.1545	203.3	0.0008	50	0.05	0.015	15.20
Calcium chloride	CaCl_2	0.0193	110.98	0.0002	50	0.05	0.0035	3.48

Table 4-3. Constituents and concentrations of artificial urine body fluid simulant.

Artificial Urine (pH = 6.77)								
Name	Linear Formula	Mass (g)	Molecular Weight (g/mol)	Moles (mol)	Volume (ml)	Volume (l)	Concentration (M)	Concentration (mM)
Urea	NH_2CONH_2	1.25	60.06	0.0208	50	0.05	0.42	416.25
Sodium chloride	NaCl	0.45	58.44	0.0077	50	0.05	0.15	154.00
Ammonium chloride	NH_4Cl	0.15	53.491	0.0028	50	0.05	0.056	56.08
Creatinine	$\text{C}_4\text{H}_7\text{N}_3\text{O}$	0.1	113.12	0.0009	50	0.05	0.018	17.68
Disodium phosphate	Na_2HPO_4	0.125	141.96	0.0009	50	0.05	0.018	17.61
Monopotassium phosphate	KH_2PO_4	0.125	136.086	0.0009	50	0.05	0.018	18.37
Sodium sulfite	Na_2SO_3	0.15	126.043	0.0012	50	0.05	0.024	23.80

Pietryzyska et al. described these aqueous simulants as the most stable body fluid analogs.²⁷ A 200 μl aliquot of the sample solution was pipetted into a single loading chamber. To visualize the fluid meniscus during this fluid drainage study, the disc was mounted onto a high-speed stroboscopic video system (HSVS) (described below). To centrifugally pump the liquid through the VF membrane, the disc was spun at a single rotational frequency (range = 750 – 2000 rpm in 250 rpm increments). Total time to drainage for each 1mm graduation was recorded. Data

exploration, statistical analysis, and visualization were performed in R Studio with the aid of the ggplot2 package (R v.3.5.1 and RStudio v.1.1.456).²⁸⁻³⁰ Drainage profiles for six unbacked nitrocellulose membranes were characterized (n = 4 at ea. rotational frequency): BioRad precut nitrocellulose sheets (0.2 μm , BioRad, Hercules, CA, USA), Amersham Protran® and Whatman Protran® BA83/BA85 (0.2 μm and 0.45 μm , GE Healthcare, Little Chalfont, UK), and UniSart® CN140 (0.45 μm , Sartorius, Göttingen, DE).

The HSVS was comprised of five major components: a MotionBLITZ EoSens® mini high-speed CMOS recording camera (Mikrotron-GmbH, Unterschleißheim, DE), MotionBLITZDirector software v.2 1.4.0.1 (Mikrotron-GmbH), a TV ZOOM LENS G6X16 16-100 mm 1:1.9 1” macro (Mikrotron-GmbH), a Nova-Strobe PBL LED portable stroboscope (Monarch Instrument, Amherst, NH, USA), and a custom-built mechatronic spin system that governed disc rotational frequency and strobe rate. The mechatronic spin system consisted of a stepper motor (Sanmotion series, SANYO DENKI, Moriguchi, Japan), stepper motor driver (drv8801), photointerrupting optical switch (TT Electronics/Optek Technology, Woking, UK), and an 8-core microcontroller (Propeller P8X32A-M44; Propeller Inc., Rockland, CA, USA).

4.3 Results and Discussion

Few published articles exist that describe using embedded membranes in centrifugal microfluidic discs. These publications demonstrate flow through porous media and allude to some hypothetical impact of sample composition, sample chamber position, and inlet channel length. However, none provide a clear empirical characterization of these variables and the effect on fluid transport through the embedded porous materials. Section **4.3.1** provides evidence that porous membranes can be embedded within and bonded to PCL fabricated devices. This section describes the initial proof-of-principle dye studies demonstrating a three-dimensional orthogonal flow path

through an inserted membrane. Subsequent preliminary on-disc flow studies suggested dramatic changes in fluid flow behavior when changing sample type and matrix, e.g., fluid flow would slow and eventually stop when using artificial blood plasma with high concentrations of bovine serum albumin. To better understand this phenomenon, sections 4.3.2 and 4.3.3 describe highspeed videography studies that elucidate the effects of membrane pore size, rotational frequency, and sample composition on flow behavior. Section 4.3.4 offers good faith attempts to perform on-disc blood separation and large volume sample handling of whole blood, serum, and urine.

4.3.1 On-Disc Vertical Flow

Initial on-disc experiments were conducted to assess the leak-free tightness of the HSA-membrane bond within the microdevice and to demonstrate proof-of-principle continuous, centrifugally driven, vertical (orthogonal) flow on a PCL fabricated device (**Figure 4-3**). Cellulosic materials offered relatively low resistance to flow, i.e., flow was observed when the rotational frequency was only slightly above 500 rpm ($14 \times g$ with radial distance from CoR = 5.0 cm). No leaking or bypass flow (seen as dye flow along the perimeter of the membranes) was observed.

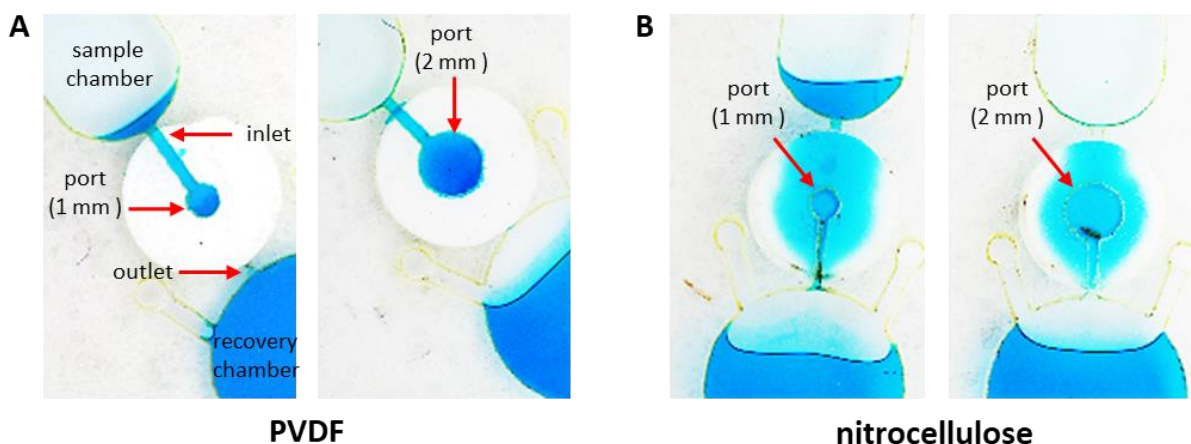


Figure 4-3. Proof-of-principle dye studies to demonstrate feasibility of disc-based vertical flow through porous membranes. Small aliquots (13 μ l) of eriochlorin-spiked artificial blood plasma (ABP) were added to each sample chamber to permit visualization of flow pattern through the membrane. Rotational forces were used to pump the fluid aliquots through membranes comprised of (A) PVDF and (B) nitrocellulose. Fluid intrusion and flowthrough began

at 500 rpm and 4,000 rpm, as shown in A and B, respectively. Complete flowthrough was observed in 30-45 s. This figure features representative AFTER images of the nitrocellulose (A) and PVDF (B) membranes.

As hypothesized, the heat lamination step of the PCL protocol activates HSA that encompasses layers 2 and 4 of the disc, anchoring and sealing the porous membranes into position - coplanar to layer 3. However, this permanent bond between the membrane and adjoining disc layers did not prevent lateral wicking away from the microchannel and VF port (**Figure 4-3 B**). We hypothesized that radial capillary penetration in the cVF system was inducing fluid movement away from the VF port and that these regions of lateral flow were secondary to the primary vertical flow path defined by the microfluidic architecture.

In LFI systems, fluid wicking via capillary forces can be understood by considering the Lucas-Washburn equation (**Eq. 8**) and Darcy's law (**Eq. 9**), which describe the extent of radial penetration and volumetric rate of capillary flow, respectively.³¹⁻³⁵ Within an LFI system, as the leading edge of the advancing fluid front crosses the dry region of the porous media, persistent unidirectional capillary flow is sustained via fluid removal by the wicking pad at the distal end of the strip.^{11, 15} In the context of our disc-based system, it stands to reason that capillary wicking away from the VF port can occur when fluid encounters a dry embedded VF membrane, i.e., the liquid is transported away from the primary flow path and into the dry fibrous media via capillary forces.

Interestingly, the Lucas-Washburn equation presumes relatively dry conditions at the leading edge of the advancing fluid front and does not consider conditions where the system is partially or fully saturated.^{31, 32, 35, 36} We believe that these partially- and fully saturated states contribute to LFI flow variability and significantly limit total allowable LFI sample volume. In contrast and in the context of the on-disc VF system, we believe that priming (pre-saturating) cellulosic membranes can be employed as a means of limiting radial capillary penetration.

To further assess the disc-membrane seal and to evaluate the extent of radial capillary penetration, the same experiment was repeated using hydrophobic membranes (e.g., PVDF), which showed a dye flow path that was clearly defined by the shape and geometry of the microfluidic architecture (**Figure 4-3 A**). No net flow was noted at rotational frequencies $\leq 4,000$ rpm (894*g), suggesting that porous hydrophobic materials offered greater resistance to flow than cellulosic media - requiring higher entry pressures for membrane wetting and initiation of flow.^{37, 38} No lateral diffusion or capillary penetration away from the primary flow path, leaking along the perimeter of the membranes, or fluid bypass of the membrane were observed.⁷

These preliminary studies showcase several key findings. Porous membranes can be laminated into and sealed within PCL fabricated discs, which creates an effective HSA-membrane bond to prevent fluid bypass and delineate the primary flow path. Vertical (orthogonal) flow through these embedded porous membranes (hydrophilic and hydrophobic) can be readily controlled via centrifugo-pneumatic pressure generation via disc rotation. Each membrane functions as a pressure-sensitive valve, permitting flow only when a sufficient pressure head is achieved.^{37, 38} Although flow is primarily radially outward as dictated by centrifugal forces, some radial capillary penetration is to be expected when using dry cellulosic membranes. However, this phenomenon may be limited via pre-saturation or priming of the membrane.

4.3.2 *Effect of Membrane Pore Size and Rotational Frequency*

The dye studies discussed above indicate relationships between rotational frequency, membrane type, and fluid entry pressure.^{37, 38} With this in mind, high-speed video capture was utilized to better understand and characterize the relationships between rotational frequency, the total time to drainage, membrane manufacturer, and pore size. Overall, the volumetric flow rate, hereafter referred to as the discharge, was consistently higher with greater rotational frequencies

and larger membrane pore sizes. The equation for discharge (Q) is given as the volume of fluid (V) passing a point in space per unit time (t)

$$Q = \frac{V}{t} = A \frac{\text{(distance)}}{t} = \bar{v}A$$

Eq. 13

where Q is proportional to mean fluid velocity (\bar{v}) and cross-sectional area of the microfluidic channel (A).⁵

Plotting the height of the remaining fluid column (Δr) as a function of elapsed time at a constant rotational frequency revealed a nonlinear decay in the rate of fluid discharge (**Figure 4-4**). This nonlinear decay can be understood when considering **Eq. 11** and **12**. When rotational frequency (ω) and fluid mass density (ρ) are held constant, fluid drains from the sample chamber (lower values for in Δr and \bar{r}). This decrease in fluid level compels corresponding decreases in the hydraulic pressure (Δp_ω) applied at the fluid-membrane interface, mean fluid velocity (\bar{v}), and fluid discharge (Q) (**Eq. 11, 12, & 13**). For example, in **Figure 4-5 B**, if the rotational frequency is held constant at 750 rpm (black dots), changes in hydraulic pressure (blue dots) are anticipated as the mean radial extent of the fluid plug in the sample chamber (Δr) decreases. These findings are not unlike those observed in classical burette model experiments used to empirically determine the value of Euler's number.³⁹

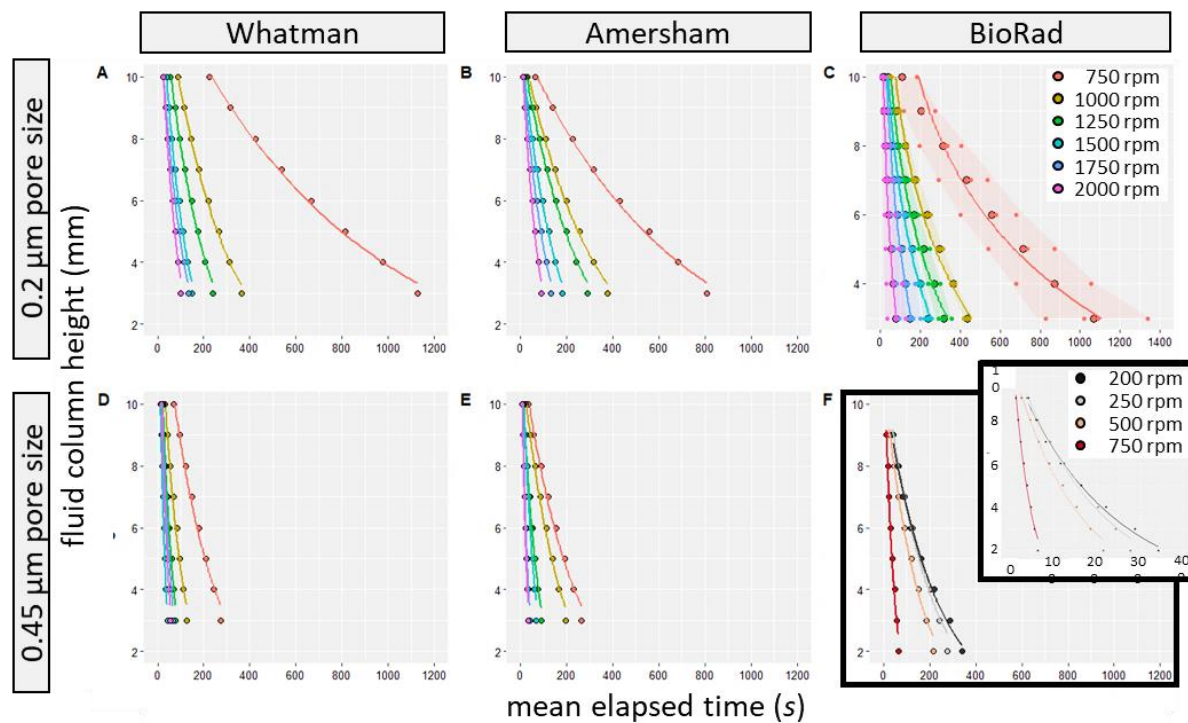


Figure 4-4. Exponential decay curves depicting the remaining fluid column height in the sample chamber (Δr) as a function of elapsed time. Assay buffer (200 μ l) was loaded into each sample chamber (Fig. 2A inset). Rotational frequency (rpm) was held constant for each fluid drainage trial ($n = 4$ for each membrane type-rpm pairing). A high-speed, stroboscopic video system was used to visualize incremental changes in the height of the fluid column over time. Small colored points (3-C only) represent elapsed time for individual trials at each rotational frequency. Larger colored points with dark borders correspond to mean elapsed time. Solid colored lines represent exponential best-fit curves for mean elapsed time values. Lighter, colored traces (4-C only) are 90% confidence intervals (CI) for each rotational frequency.

That is, the cVF system follows a first-order kinetics model in which the rate of fluid drainage is proportional to the amount of fluid remaining in the sample loading chamber; the relationship between total elapsed time and fluid discharge produces continuous curves that take the form of an exponential decay function

$$y = y_0 e^{-kt}$$

Eq. 14

where y is the ending height for the remaining fluid column in the sample chamber, y_0 is the initial value for the height of the fluid column in the sample chamber, e is Euler's number, k is the continuous proportionality rate constant, and t is the total elapsed time. The magnitude of these k

values describe the behavior of the fluid columns undergoing continuous, progressive drainage and is indicative of the rapidity with which that fluid column recedes. Here, the instantaneous rate of change in the height of the fluid column, with respect to time, is proportional to the height of the fluid column itself.

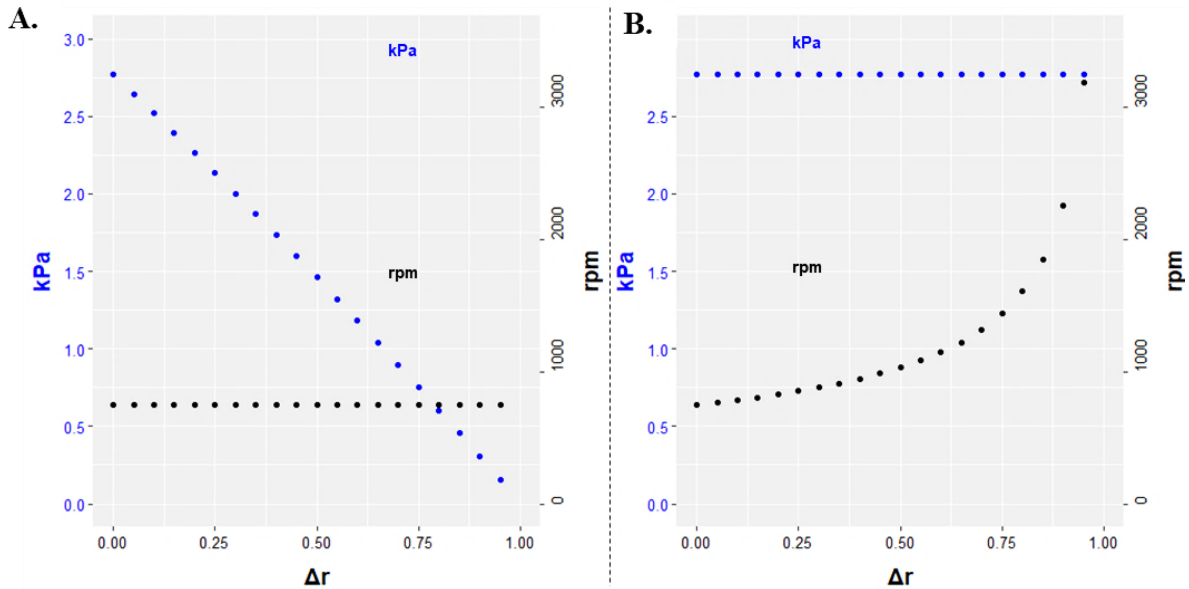


Figure 4-5. Predicted changes in hydraulic pressure head (kPa) as a function of changing fluid column height (Δr). (A) When rotational frequency is held constant, a linear decrease in hydraulic pressure is predicted with decreasing fluid column height. (B) To achieve constant hydraulic pressure an exponential increase in rotational frequency is required throughout the fluid drainage process.

Semi-log transformation of the y-axis linearizes the decay curves, revealing the proportionality constant (k) for each relationship. Plots of $\ln(\Delta r)$ as a function of elapsed time are described by the linear equation

$$\ln(\Delta r) = -kt + \ln\Delta r_0$$

Eq. 15

where Δr is the height of the fluid column at time t , Δr_0 is the height of the column at $t = 0$, and k is the proportionality constant for the draining fluid column (exemplar semi-log transformation

shown in **Figure 4-6 B**). A strong, negative correlation between mean elapsed time and $\ln(\Delta r)$ was observed for all membranes and rotational frequencies (all R^2 values exceeded 0.97).

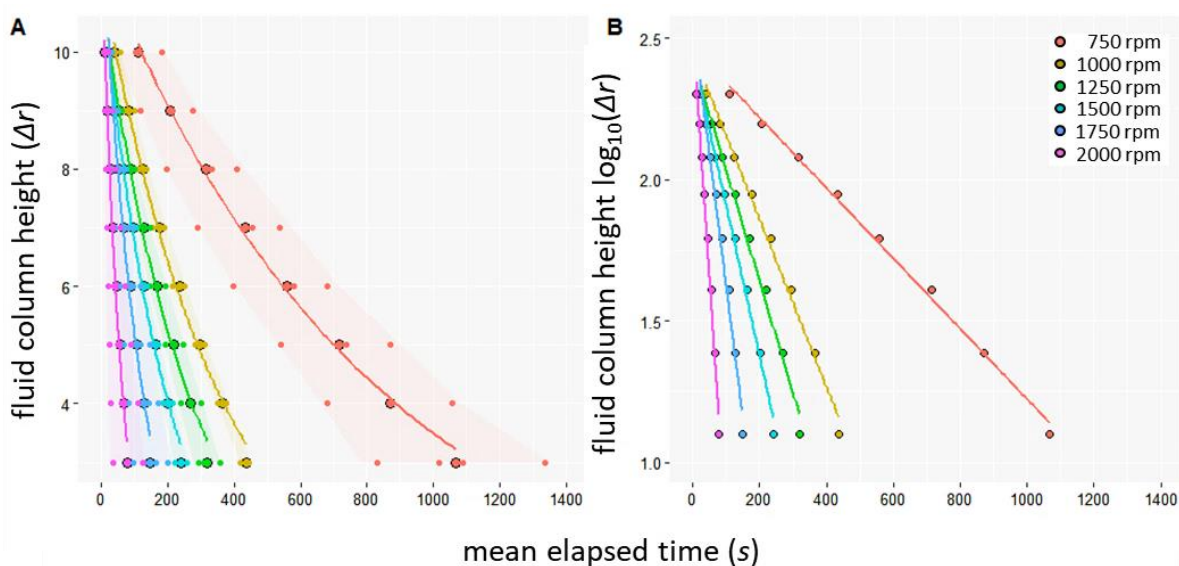


Figure 4-6. Semi-log transformation of drainage data for BioRAD 0.2 μm pore size membrane cut-outs when experiencing differing rotational frequencies. **(A)** Exponential decay curve depicting the remaining fluid column height in the sample chamber (Δr) as a function of elapsed time. These curves take the form of the general equation $\ln(h) = -kt + \ln h_o$ where h is the height of the fluid column at time t and h_o is the height of the column at $t = 0$. Lighter, colored traces (panel A only) represent 90% confidence intervals (CI) for each rotational frequency. **(B)** Semi-log plot of the $\log_{10}\Delta r$ as a function of elapsed time. The slopes of these semi-log plots represent decay constants (k) for the draining fluid column.

Therefore, as the fluid column drains, hydraulic pressure diminishes, and fluid discharge slows. Across all membrane types, larger k values corresponded to higher rotational frequencies and larger pore sizes (**Figure 4-4** and **Figure 4-6**), signifying conditions where the fluid column drains more swiftly. Variable fluid drainage rates would adversely impact assays requiring continuous flow to measure reaction progress or assay performance. We believe that it is possible to remedy issues associated with varying flow speed (drainage rate) by employing a spin protocol that exponentially increases disc rotational frequency throughout the fluid drainage process, thereby maintaining constant hydraulic pressure and flow (**Figure 4-5 B**).

Some variation in membrane performance was noted between manufacturers (**Figure 4-4**) and between replicate cuttings from within the same lot of NC membranes (**Figure 4-6 A**), i.e.,

variation between replicates, raw data points at the same level of fluid drainage (Δr) and at the same rotational frequency were observed. These variations appeared more pronounced at lower rotational frequencies and as the total elapsed time increased (**Figure 4-4 A**). We believe that this variability in the data is best explained by the complex, non-uniform nature of the interconnected three-dimensional (3D) pore networks of the NC membrane cut-outs.^{37, 38, 40, 41} The size, number, distribution, arrangement, connectedness, and hydrodynamic interaction of pore radii impact hydrodynamic resistance to flow, making some variation in fluidic behavior unavoidable.⁴² Simply stated, we do not believe that pore size, as reported by the manufacturer, accurately describes the permeability of these NC membranes, e.g., the permeability of the membrane might be different than expected given the reported pore size (**Eq. 9**);^{40, 43, 44} it is unlikely that models describing NC membranes as simple bundles of uniformly arranged microtubules adequately characterize membrane complexity or predict fluidic behavior through these cellulosic materials.^{17, 40, 45, 46}

4.3.3 *Effect of Sample Composition*

To assess the potential impact of sample composition on fluid discharge, a second HSVS study was performed. For this study, nitrocellulose (**NC**) membrane cut-outs were taken from a single source (unbacked Whatman BA83 0.2 μm pore size). To reduce the number of contributing variables in this study, we utilized three body fluid simulants with viscosities (η) similar to water at room temperature ($\cong 1.0005$ cP at 20°C), namely artificial urine, assay buffer, and artificial blood plasma (**Figure 4-7**).

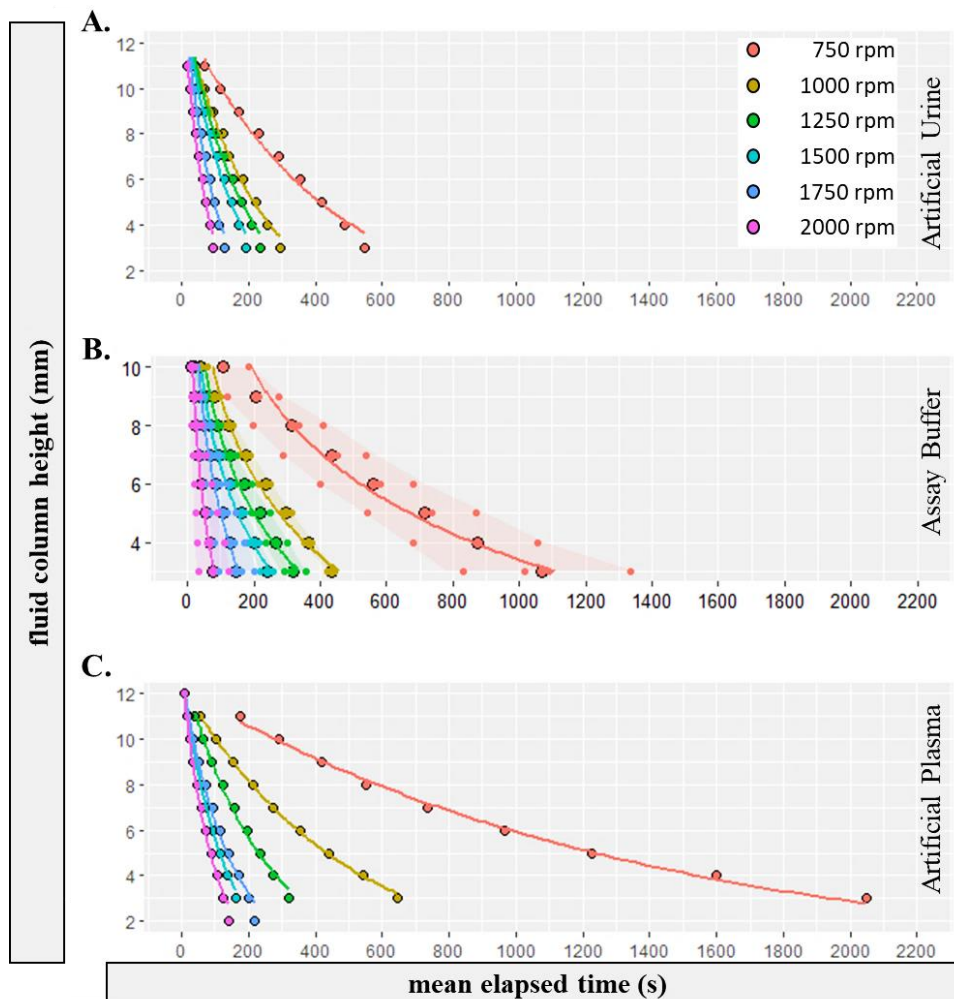


Figure 4-7. Exponential decay curves depicting the remaining fluid column height in the sample chamber (Δr) as a function of elapsed time. To assess the impact of differing aqueous sample matrices, 4 mm cut-outs of BioRAD 0.2 μm pore size membranes were embedded into each cVF disc. Aliquots of each sample solution (200 μl volumes of artificial urine, assay buffer, and artificial blood plasma) were loaded into the sample chambers (Fig. 2A inset). Rotational frequency (rpm) was held constant for each fluid drainage trial ($n=4$ for each fluid type-rpm pairing).

Like the HSVS study described in the previous section, plotting the height of the remaining fluid column (Δr) as a function of elapsed time discloses exponential decay curves, which showed that the composition of the aqueous system flowing through the porous cVF membranes had a considerable impact on fluid discharge. The fluid discharge was greatest when artificial urine was used and least when artificial plasma was used (**Figure 4-7** and **Figure 4-8**). We hypothesized that these differences resulted from NC fiber swelling; greater fiber swelling would restrict flow through the porous network.⁴⁰

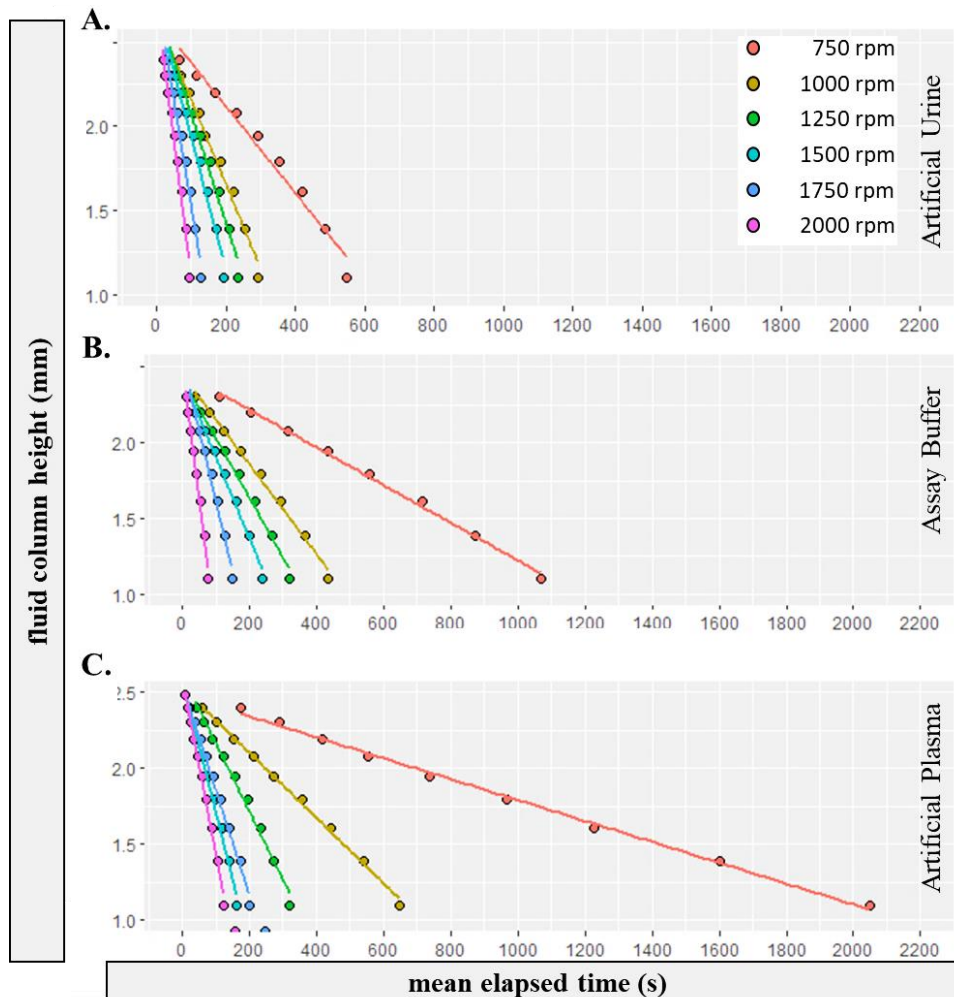


Figure 4-8. Semi-log plots of the $\log_{10}\Delta r$ as a function of elapsed time. The slopes of these semi-log plots represent decay constants (k) for the draining fluid column. Cut-outs of BioRAD 0.2 μm pore size membranes were embedded into each cVF disc and exposed to 200 μl of different body fluid simulants, i.e., artificial urine, assay buffer, and artificial blood plasma ($n= 4$ for each fluid type-rpm pairing).

To elaborate, the fluid drainage profiles presented in **Figure 4-7** and **Figure 4-8** suggest that the NC fibers may have been most swollen when in contact with the artificial plasma solution and least swollen when in contact with the artificial urine solution. This observed influence of solution composition on fluid drainage rates and its potential connection to NC fiber swelling can be rationalized by considering the influence of the solutes on the thermodynamic activity of the solvent (water) in the solutions. In general, polymer swelling is restricted as the solute concentration and osmotic pressure of the solution increases, which simultaneously reduces the

thermodynamic activity of the solvent.⁴⁷⁻⁴⁹ This phenomenon, often called ‘osmotic deswelling’, could induce increased flow through a fibrous network. Stated another way, fiber swelling or deswelling due to differences in solute concentration alters the microstructure of the porous 3D network and, as described in **Eq. 9**, these changes to membrane permeability (K) influence fluid flow (Q).^{7, 40} This description is consistent with the greater fluid discharge observed with artificial urine compared to artificial plasma (**Figure 4-7** and **Figure 4-8**). Since artificial urine had a greater concentration of solutes than artificial plasma, we would expect less pronounced NC fiber swelling in artificial urine compared to artificial plasma. Moreover, the artificial plasma solution contains sodium bicarbonate – known to promote polymer swelling due to its kosmotropic nature.^{50, 51} This effect, while perhaps secondary relative to osmotic deswelling effects, may also contribute to lessened fluid discharge observed when analyzing artificial plasma.

Minimally, the videography findings presented here are consistent with the notions that fluid discharge rate is not constant throughout the course of sample processing and that sample composition influences membrane behavior.^{42, 52, 53} While these simulants were not entirely representative of the analogous body fluids, they did provide clear evidence regarding the impact of sample matrix on membrane behavior and flow patterns.

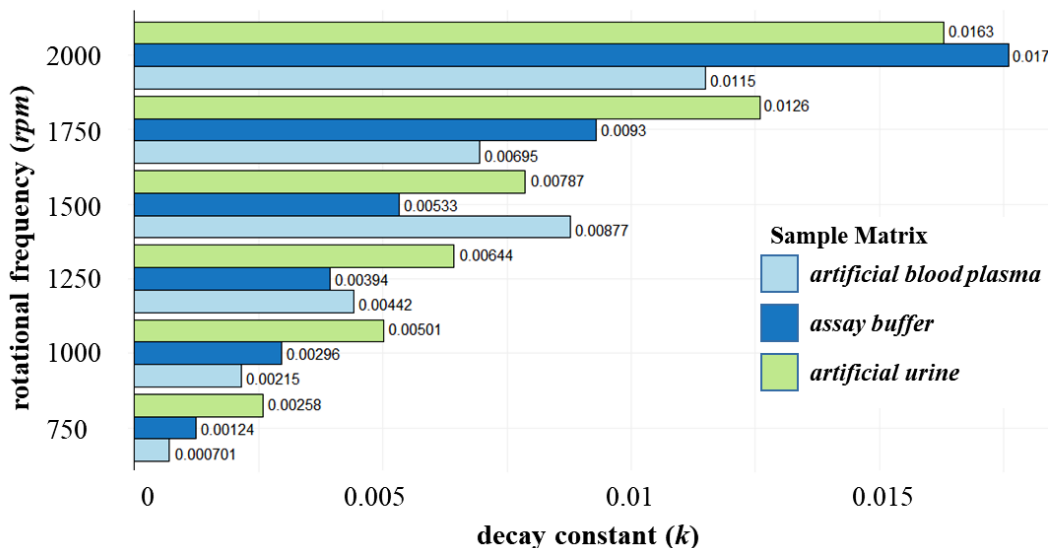


Figure 4-9. Changes in decay constant with differing sample composition and decreasing rotational frequency. To assess the impact of differing aqueous sample matrices, 4 mm cut-outs of BioRAD 0.2 μm pore size membranes were embedded into each cVF disc. Aliquots of each sample solution (200 μl volumes of artificial urine, assay buffer, and artificial blood plasma) were loaded into the sample chambers (Fig. 2A inset). Rotational frequency (rpm) was held constant for each fluid drainage trial ($n= 4$ for each fluid type-rpm pairing).

4.3.4 Logical Extensions and Ongoing Efforts

Our lab has previously published work detailing on-disc analysis of whole blood samples.⁵⁴⁻⁵⁶ Those approaches to microfluidic blood testing described therein required on-disc separation of plasma from the whole blood sample. In those studies, plasma was separated from small volumes of whole blood ($\sim 3 \mu\text{l}$) via centrifugally induced cell sedimentation at $> 3,000 \text{ rpm}$ for $>7 \text{ min}$; those chambers were located approximately 5 cm from the CoR, occupying a significant portion of the architectural real estate in this region (**Figure 4-10 A and B**). Accordingly, the studies detailed herein were designed to address differences in fluid flow and sample chamber drainage when the embedded VF membrane is placed downstream of, but near to, the sample preparation chamber.

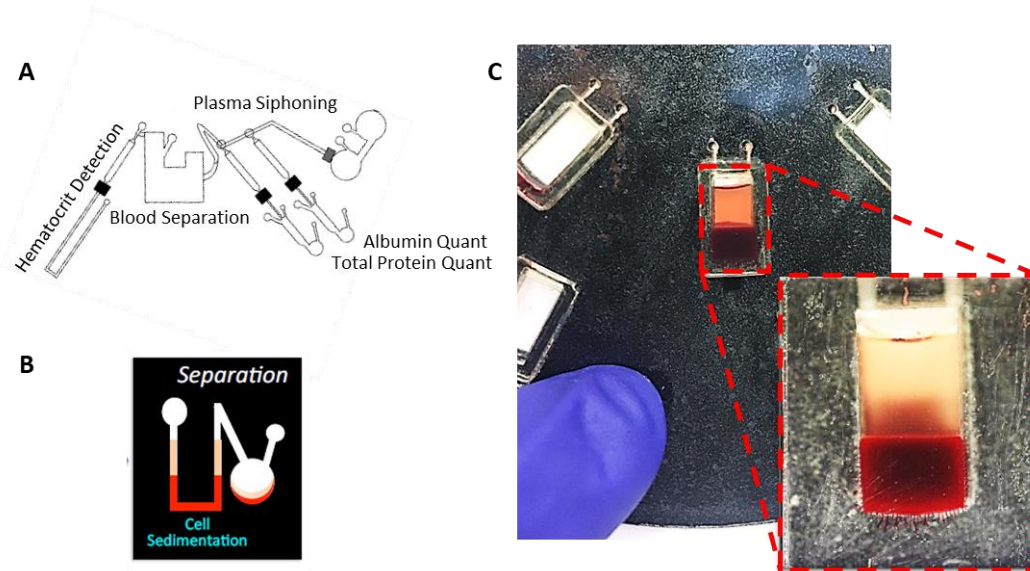


Figure 4-10. On-disc whole blood sample preparation. On-disc plasma separation from $\sim 3 \mu\text{l}$ of neat human blood. Adapted from (A) Thompson et al. 2014 and (B) Thompson et al. 2016.^{54, 55} (C) Demonstration of on-disc plasma separation from $\sim 200 \mu\text{l}$ of neat human blood.

As currently designed, the cVF system can handle fluid volumes $>200 \mu\text{l}$ – a stark contrast to the small whole blood volumes ($\sim 3 \mu\text{l}$) used and reported elsewhere.^{54, 55} As a good-faith demonstration, we have performed preliminary studies showing that it is possible to separate plasma from larger whole blood volumes via on-disc centrifugation (**Figure 4-10**). Here, we demonstrate that plasma can be separated from $>200 \mu\text{l}$ of whole blood in ≤ 3 min (chamber located at 5 cm from CoR, 6,000 rpm, 180 s). Efforts to increase liquid volume handling capabilities are also ongoing (**Figure 4-10**). To date, we have shown that large volumes of other neat body fluids can be passed through these embedded membranes (**Figure 4-11** and **Figure 4-12**).

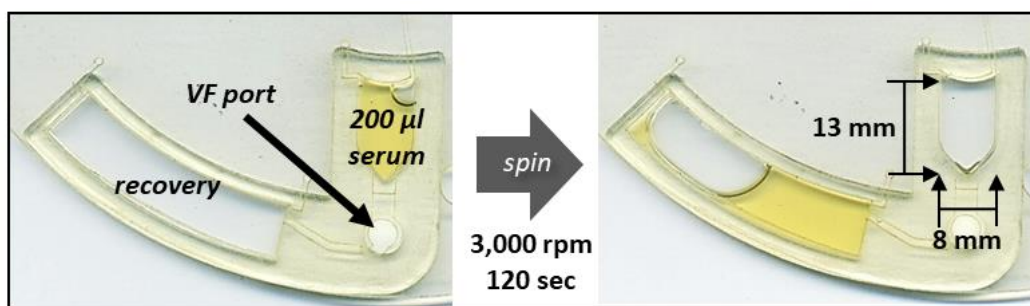


Figure 4-11. On-disc flowthrough of large volume body fluid samples (human serum). At 3,000 rpm, this cVF design processed $200 \mu\text{l}$ of human serum in ~ 120 s. Three additional aliquots of serum ($200 \mu\text{l}$ ea.) were passed through the same membrane (total serum volume = $800 \mu\text{l}$).

Initial efforts to process larger volumes focused on the sequential addition and drainage of smaller fluid volumes (**Figure 4-11**). For example, we have demonstrated that 200-800 μl of human serum can be passed through the VF membrane with no appreciable indication of membrane fouling or excessive deswelling, i.e., four 200 μl aliquots of human serum were sequentially added to and drained from the sample chamber. The approximate time to drainage for each 200 μl aliquot was ~ 120 s at 3,000 rpm (**Figure 4-11**). Preliminary studies have also shown that embedded VF membranes can process larger sample volumes in a non-sequential manner, e.g., ≥ 1.5 ml of urine and ≥ 800 μl of serum (**Figure 4-12**). Further experimentation is needed to reduce the footprint of these large volume sample loading chambers, e.g., the sample loading chamber design for the large volume urine handling disc was 12 mm wide and 30 mm long (disc diameter = 70 mm).

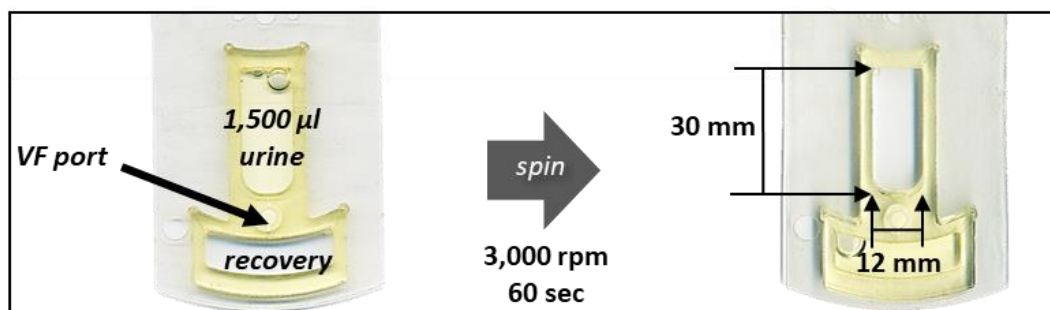


Figure 4-12. On-disc flowthrough of large volume body fluid samples (human urine). The cVF disc was redesigned with a 4 mm VF port (same radial distance from CoR) and larger chambers, i.e., thicker 1.5 mm PMMA accessory pieces were affixed to the top and bottom of the disc. At 3,000 rpm, this cVF design was able to process 1.2 ml of assay buffer (~ 3 min). Likewise, at 3,000 rpm, this design processed 1.5 ml of neat urine (< 60 sec). The bulk fluid was removed from the recovery chamber, and two additional 1.5 ml aliquots of urine were passed through the same cVF membrane (total urine volume = 4.5 ml).

4.4 Conclusions

We have demonstrated the feasibility of on-disc vertical flow through unbacked porous membranes, characterized flow decay patterns and membrane behavior within the cVF format, and highlighted the impact of sample composition on transverse flow through the membrane. However, *Sample in – Answer out* μTAS devices often require on-disc, upstream sample preparation steps,

e.g., separation of plasma from whole blood. In those cases, it may be necessary to locate the sample chamber in a more radially outward position, i.e., farther from the CoR and closer to the detection window and porous membrane, which, in turn, increases the potential for significant changes in hydraulic pressure and flow rate. Our high-speed videography studies show that, under such conditions, changes in drainage rate due to the diminishing height of the inlet fluid column (\bar{r} and Δr) are quite substantial and take the form of predictable exponential decay curves; in part, these changes are predicted by **Equations 11, 12, and 13**. We describe an embedded membrane system in which the porous media is permanently bonded to the disc via heat lamination to preclude bypass flow. This PCL-based approach to membrane integration creates a seal between the disc and membrane and directs flow tangentially through the porous media; This style of embedding membranes offers an alternative to other disc-membrane bonding methods and produces a multilayered flow path akin to those described elsewhere.^{8, 9, 23, 24}

Highspeed videography studies confirm that sample composition has a remarkable impact on flow through cellulosic membranes; the presence of soluble ionic compounds significantly influences membrane behavior and flow patterns. Membrane behavior was impacted by changes in solute concentration, osmotic pressure, the thermodynamic activity of the solvent (e.g., water), and the kosmotropic effect of bicarbonate.⁴⁷⁻⁵¹ We have hypothesized that osmotic swelling or deswelling of the membrane altered the microstructure of porous NC networks, which, in turn, influenced both membrane permeability and influenced fluid discharge rates.^{7, 40}

Taken together, the findings reported herein suggest that future endeavors to design and optimize any VF platform should consider membranes that are less sensitive to osmotic swelling, e.g., non-cellulosic. Fortunately, this cVF platform is amenable to a variety of nanoporous substrates, e.g., PVDF, cellulosic, glass microfiber, etc. We believe that these proof-of-principle

studies highlight critical aspects of on-disc VF prototype development and are the first step toward the development of a portable, enclosed, fully integrated system for multiplexed sample processing, including for filtration or immunoassay.

4.5 Acknowledgments

I wish to thank Lindsay A. L. Bazydlo, Ph.D. and the UVa Department of Pathology for providing the deidentified fluid samples.³ Dr. David L. Green (UVa Department of Engineering: Materials Science, Chemical, and Mechanical Engineering) for his patience related to the discussion of sample viscosity and insights regarding potential membrane swelling.

³ All human body fluid samples used for these studies were scheduled for discard and were deidentified prior to the authors receipt, thus exempting Institution Review Board (IRB) oversight and approval.

4.6 References

1. D. R. Reyes, D. Iossifidis, P.-A. Auroux and A. Manz, *Analytical chemistry*, 2002, **74**, 2623-2636.
2. A. Manz, N. Graber and H. á. Widmer, *Sensors and actuators B: Chemical*, 1990, **1**, 244-248.
3. J. Ducrée, S. Haeberle, S. Lutz, S. Pausch, F. Von Stetten and R. Zengerle, *Journal of Micromechanics and Microengineering*, 2007, **17**, S103.
4. R. Gorkin, J. Park, J. Siegrist, M. Amasia, B. S. Lee, J.-M. Park, J. Kim, H. Kim, M. Madou and Y.-K. Cho, *Lab on a Chip*, 2010, **10**, 1758-1773.
5. M. Madou, J. Zoval, G. Jia, H. Kido, J. Kim and N. Kim, *Annu. Rev. Biomed. Eng.*, 2006, **8**, 601-628.
6. S. Lai, S. Wang, J. Luo, L. J. Lee, S.-T. Yang and M. J. Madou, *Analytical chemistry*, 2004, **76**, 1832-1837.
7. D. M. Kainz, S. M. Früh, T. Hutzenlaub, R. Zengerle and N. Paust, *Lab on a Chip*, 2019, **19**, 2718-2727.
8. E. J. Templeton and E. D. Salin, *Microfluidics and nanofluidics*, 2014, **17**, 245-251.
9. M. Karle, J. Wöhrle, F. von Stetten, R. Zengerle and D. Mark, 2013.
10. V. Gubala, L. F. Harris, A. J. Ricco, M. X. Tan and D. E. Williams, *Analytical chemistry*, 2012, **84**, 487-515.
11. N. Jiang, R. Ahmed, M. Damayantharan, B. Ünal, H. Butt and A. K. Yetisen, *Advanced healthcare materials*, 2019, **8**, 1900244.
12. M. M. Gong and D. Sinton, *Chemical reviews*, 2017, **117**, 8447-8480.
13. E. Fu, S. A. Ramsey, P. Kauffman, B. Lutz and P. Yager, *Microfluidics and nanofluidics*, 2011, **10**, 29-35.
14. E. W. Washburn, *Physical review*, 1921, **17**, 273.
15. G. A. Posthuma-Trumpie, J. Korf and A. van Amerongen, *Analytical and bioanalytical chemistry*, 2009, **393**, 569-582.
16. H.-A. Joung, Z. S. Ballard, A. Ma, D. K. Tseng, H. Teshome, S. Burakowski, O. B. Garner, D. D. Carlo and A. Ozcan, *Lab on a Chip*, 2019, DOI: 10.1039/C9LC00011A.
17. P. Chen, M. Gates-Hollingsworth, S. Pandit, A. Park, D. Montgomery, D. AuCoin, J. Gu and F. Zenhausern, *Talanta*, 2019, **191**, 81-88.

18. D. Quesada-González and A. Merkoçi, *Biosensors and Bioelectronics*, 2015, **73**, 47-63.
19. N. G. Anderson, *Clinica Chimica Acta*, 1969, **25**, 321-330.
20. B. L. Thompson, Y. Ouyang, G. R. Duarte, E. Carrilho, S. T. Krauss and J. P. Landers, *Nature protocols*, 2015, **10**, 875.
21. B. L. Thompson, Y. Ouyang, G. R. Duarte, E. Carrilho, S. T. Krauss and J. P. Landers, *Nature protocols*, 2015, **10**, 875-886.
22. C. Birch, J. A. DuVall, D. Le Roux, B. L. Thompson, A.-C. Tsuei, J. Li, D. A. Nelson, D. L. Mills, J. P. Landers and B. E. Root, *Micromachines (Basel)*, 2017, **8**, 17.
23. R. Gorkin III, C. E. Nwankire, J. Gaughran, X. Zhang, G. G. Donohoe, M. Rook, R. O'Kennedy and J. Duce, *Lab on a Chip*, 2012, **12**, 2894-2902.
24. J. L. Garcia-Cordero, D. Kurzbuch, F. Benito-Lopez, D. Diamond, L. P. Lee and A. J. Ricco, *Lab on a Chip*, 2010, **10**, 2680-2687.
25. L. Liu, C. Qiu, Q. Chen and S. Zhang, *Journal of alloys and compounds*, 2006, **425**, 268-273.
26. L. Liu, L. Shou, H. Yu and J. Yao, *Journal of Macromolecular Science, Part B*, 2015, **54**, 962-974.
27. M. Pietrzyńska and A. Voelkel, *Microchemical Journal*, 2017, **134**, 197-201.
28. R Core Team, *Journal*, 2018.
29. RStudio Team, *Journal*, 2018.
30. H. Wickham, *ggplot2: elegant graphics for data analysis*, Springer, 2016.
31. M. Liu, J. Wu, Y. Gan, D. A. H. Hanaor and C. Q. Chen, *Langmuir*, 2016, **32**, 9899-9904.
32. M. Liu, J. Wu, Y. Gan, D. A. H. Hanaor and C. Q. Chen, *International Journal of Heat and Mass Transfer*, 2018, **123**, 239-250.
33. D. Danino and A. Marmur, *Journal of Colloid and Interface Science*, 1994, **166**, 245-250.
34. N. K. Palakurthi, S. Konangi, U. Ghia and K. Comer, *International Journal of Multiphase Flow*, 2015, **77**, 48-57.
35. H. Lim, A. T. Jafry and J. Lee, *Molecules*, 2019, **24**, 2869.
36. Y. V. Zaccardi, N. Alderete and N. De Belie, 2018.
37. B.-S. Kim and P. Harriott, *Journal of colloid and interface science*, 1987, **115**, 1-8.

38. M. d. C. García-Payo, M. A. Izquierdo-Gil and C. Fernández-Pineda, *Journal of colloid and interface science*, 2000, **230**, 420-431.
39. J. F. Yegge, *The Physics Teacher*, 1968, **6**, 41-41.
40. S. Sun, S. Feng, C. Ji, M. Shi, X. He, F. Xu and T. J. Lu, *Journal of Membrane Science*, 2020, **595**, 117502.
41. H. F. Pierce, *Journal of Biological Chemistry*, 1927, **75**, 795-815.
42. K. H. Jensen, A. X. Valente and H. A. Stone, *Physics of Fluids*, 2014, **26**, 052004.
43. J. R. Nimmo, *Encyclopedia of Soils in the Environment*, 2004, **3**, 295-303.
44. R. Liu, Y. Jiang, B. Li and L. Yu, *Microfluidics and Nanofluidics*, 2016, **20**, 1-13.
45. A. Gugliuzza, in *Encyclopedia of Membranes*, eds. E. Drioli and L. Giorno, Springer Berlin Heidelberg, Berlin, Heidelberg, 2016, DOI: 10.1007/978-3-662-44324-8_720, pp. 1251-1252.
46. A. Gugliuzza, in *Encyclopedia of Membranes*, eds. E. Drioli and L. Giorno, Springer Berlin Heidelberg, Berlin, Heidelberg, 2016, DOI: 10.1007/978-3-662-44324-8_1407, pp. 1801-1802.
47. G. M. Geise, B. D. Freeman and D. R. Paul, *J. Membr. Sci.*, 2013, **427**, 186-196.
48. G. M. Geise, D. R. Paul and B. D. Freeman, *Prog. Polym. Sci.*, 2014, **39**, 1-42.
49. A. R. Khare and N. Peppas, *Biomaterials*, 1995, **16**, 559-567.
50. G. M. Geise, M. A. Hickner and B. E. Logan, *ACS Macro Letters*, 2013, **2**, 814-817.
51. L. Liu, T. Wang, C. Liu, K. Lin, Y. Ding, G. Liu and G. Zhang, *J. Phys. Chem. B*, 2013, **117**, 2535-2544.
52. K. Glavatskiy and S. K. Bhatia, *Journal of Membrane Science*, 2017, **524**, 738-745.
53. K. Boomsma and D. Poulikakos, *J. Fluids Eng.*, 2002, **124**, 263-272.
54. B. L. Thompson, R. J. Gilbert, M. Mejia, N. Shukla, D. M. Haverstick, G. T. Garner and J. P. Landers, *Analytica chimica acta*, 2016, **924**, 1-8.
55. B. L. Thompson, Y. Ouyang, J. Li, S. T. Krauss, N. Shukla, B. G. Kessel, D. M. Haverstick, G. T. Garner and J. P. Landers, 2014.
56. B. L. Thompson, S. L. Wyckoff, D. M. Haverstick and J. P. Landers, *Analytical chemistry*, 2017, **89**, 3228-3234.

5.1 Introduction

5.1.1 *Lateral flow, Vertical flow, and Point-of-Care Diagnostics*

Infectious disease outbreaks occur frequently and naturally worldwide, wreaking havoc on human, animal, and plant populations – thus posing great threats to global economies, public health, and security.¹ The Centers for Disease Control and Prevention (CDC) Federal Select Agent Program lists a unique subset of nearly 70 agents and toxins that have tremendous potential for weaponization, biocrime, and bioterrorism – including Zaire Ebola virus and the *Y. pestis* bacterium. In cases of suspected exposure to these notable infectious agents, early identification and diagnosis is paramount to administering timely, appropriate medical treatment for improved patient outcomes, as well as informing emergency responses such as evacuation, containment, and decontamination. Current methods for detecting and identifying these agents rely upon microbiological cell culture and polymerase chain reaction (PCR)-based molecular diagnostics, both of which are complex and time-consuming, precluding utility as expedited emergency response systems.

Further, cell culture and PCR tests are generally not amenable to point-of-care (POC) diagnostics or deployment to resource limited areas, largely due to requirements for specialized equipment, dedicated laboratory workspace, and skilled analysts. Readily accessible clinical samples (e.g., blood plasma, serum, urine, pus, sputum, etc.) frequently exhibit low titer levels of many biological agents, which confound PCR-based diagnostic assays.^{2,3} For improved sensitivity with low titer samples, current methodologies require time intensive cell culture-PCR (CC-PCR), which often necessitates the development and validation of special laboratory techniques and cell culture guidelines for each novel organism.^{2,4} Efforts to provide CC-PCR diagnostics are often

thwarted by the fact that a large fraction of organisms are difficult or impossible to culture in a laboratory; it is estimated that less than 2% of all environmental organisms and roughly 50% of known human microflora are culturable.⁵ A 2016 report from the U.S. Army Research, Development and Engineering Command (ECBD-TR-1392) highlighted these gaps in pathogen detection capability and the significant associated dangers for public health and safety, national security, and military operations.⁶ Specifically, the report recommended increased focus on developing diagnostic technologies that support the detection of Tier 1 biothreats not readily amenable to PCR.

Affinity-based systems provide an effective orthogonal approach to diagnosis by detecting agents, agent-derived biomarkers, or host-derived biomarkers in biofluids. Among these, paper-based lateral flow immunoassays (LFI) represent the ‘gold standard’ technology and make up the overwhelming preponderance of reported methods for detection of Federal Select Agents (**Figure 5-1A**).⁷ LFIs offer a cost-efficient, simple, and rapid (15-20 min) solution for POC diagnostics that are amenable to in-theater use by nontechnical personnel.^{8,9} However, existing LFI systems suffer from notable operational limitations, largely stemming from dependence upon capillary-driven flow, which provides minimal control over sample incubation and mixing, and limited sampling volumes constrained by absorbent wicking pads that quickly saturate with fluid, preventing further flow.^{10, 11} Alternative approaches, such as vertical flow immunoassays (VFI), stand to supplant existing LFI systems by offering improved sensitivity, circumventing capillary-driven flow, avoiding system saturation, and providing greater flexibility regarding sample types and volumes.¹²⁻¹⁴

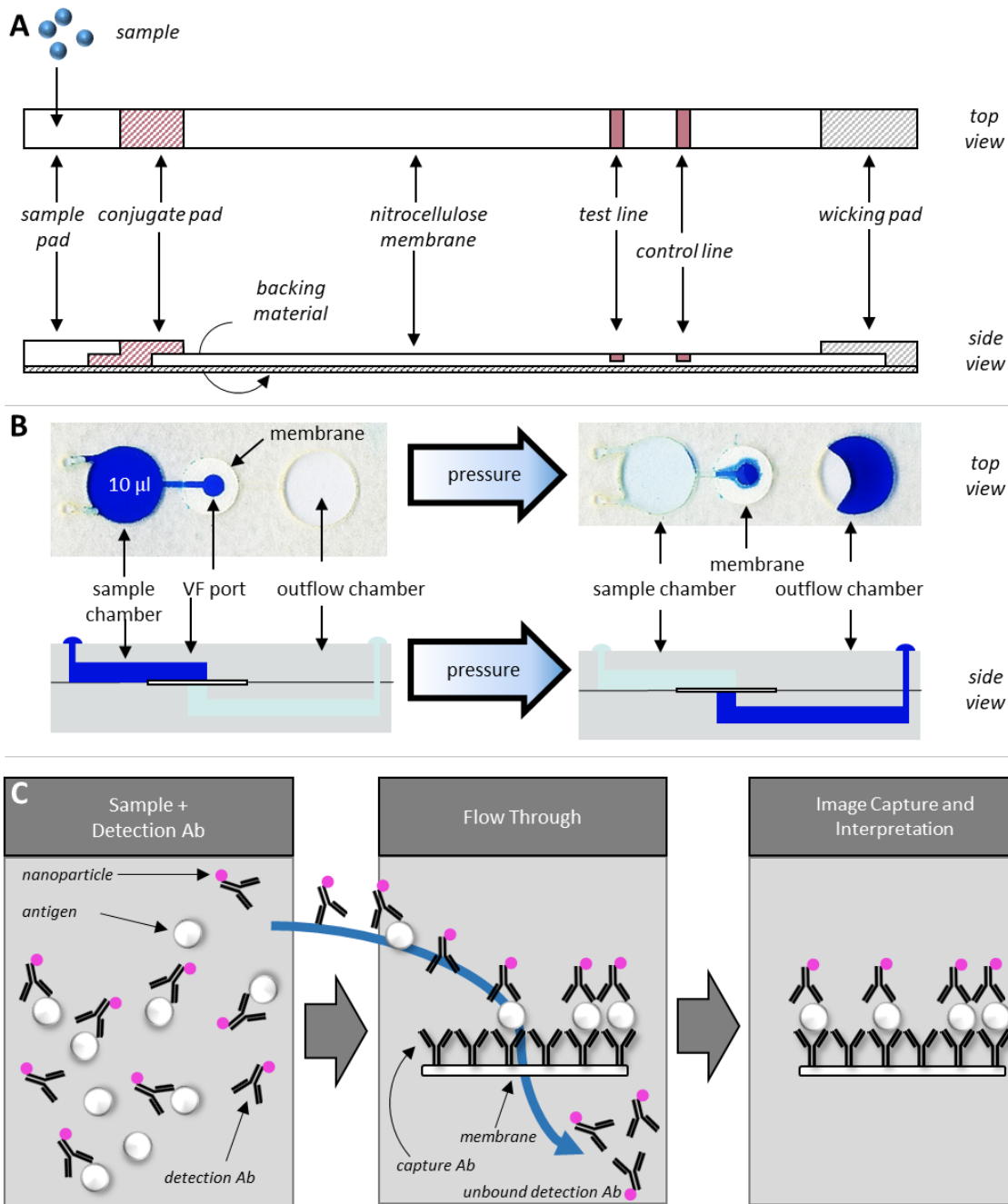


Figure 5-1. Schematic comparison between lateral and vertical flow immunoassays. **(A)** Diagrammatic representation of a typical lateral flow immunoassay (LFI) test strip in which sample traverses from the sample pad to the optical detection zone (test and control lines) via capillary action, parallel to the device surface. **(B)** Top view images of a centrifugally driven vertical flow microdevice with accompanying side-view schematics. Sample is flowed orthogonally through the detection zone (VF port) via centrifugally generated hydraulic pressure. **(C)** A schematic illustrating the principle of centrifugally driven vertical flow immunoassays.

Much like conventional strip-based LFIs, most capillary-driven VFI sensors are produced by vertically stacking LFI components (e.g., sample pad, conjugate pad, pre-functionalized porous

cellulosic membrane, etc.) (**Figure 5-1B**).^{12, 15} In contrast, pressure-driven VFI approaches dispense with many LFI components and differ from conventional LFIs in two fundamental ways; fluid is driven orthogonally through a porous membrane, rather than horizontally, and flow is pressure driven and thereby does not rely upon capillary wicking (**Figure 5-1C**).^{7, 12, 15} By circumventing capillary-driven flow, the pressure-driven VFI approach stands to supplant existing LFI systems by offering improved sensitivity, while avoiding system saturation and providing greater flexibility regarding sample types and volumes.¹²⁻¹⁴ However, in their current form, pressure-driven VFI systems require extensive off-device sample handling, user intervention for reagent loading steps due to poor amenability to onboard reagent storage, and the need for device disassembly/cleaning after each run. In essence, current pressure driven VFI systems remain tethered to a central laboratory.

The development of POC sensors has greatly leveraged the advantages of microfluidic devices, such as micro total analysis systems (μ TAS)^{16, 17} and lab-on-a-CD platforms.¹⁸⁻²¹ These devices offer attractive, portable approaches to standard sample handling techniques that directly address many of the limitations associated with existing VFI systems and eliminate the need for a laboratory environment.²² In a recently published manuscript, we demonstrated that sample volume, membrane pore size, and ionic composition of the sample matrix significantly impact fluid drainage profiles and membrane behavior. Here, we report a disc-based approach to vertical flow through porous media. Utilization of centrifugal force as the primary driving force to move fluids within a microfluidic architecture permits reduction of instrument size and cost by eliminating the need for peripheral hardware such as pneumatic syringe pumps, and the associated tubing networks.^{18, 19} Once fully developed, this device will offer clear solutions to on-disc reagent storage, full automation, and true portability and field-forward capabilities.

5.2 Experimental Section

5.2.1 Image Capture, Processing, and Data Analysis

Digital images of the cVFI discs (1200 dpi, TIFF) were captured before and after each assay with a Perfection V100 desktop scanner (Epson, Suwa, Nagano, JP). All images were cropped and rotated, as needed, with the Microsoft Windows 64-bit Fiji distribution of ImageJ v.1.52p (<https://imagej.net/Fiji/Downloads>), as detailed in Woolf et al.²³ For clarity, hereafter we use two acronyms to describe and distinguish two different image segmentation methods, explicitly AOI and ROI.

We define an ‘area of interest’ (AOI) as a section of a digital image that was selected by simple cropping, e.g., circular or rectangular (**Figure 5-2**). In this manuscript, these AOIs encompass either LFI test and control lines, or circular cVFI membranes. Images of LFI strips were cropped (rectangular) such that each AOI comprised a single test and control line (200 by 185 pixels). Images of individual cVFI membranes were manually cropped (circular) such that each circular AOI consisted of a single 4 mm NC biopsy punch with a diameter (\emptyset) of 200 pixels, which equates to 4 mm \emptyset (area $\cong 12.57 \text{ mm}^2$). Prior to measurement and analysis, the background surrounding these circular AOIs was removed (converted to black) using the ImageJ Edit > Clear Outside command path.²³ For all AOIs, area measurements and analysis were performed over the entire expanse of the selection, i.e., the entirety of a cVFI biopsy punch.

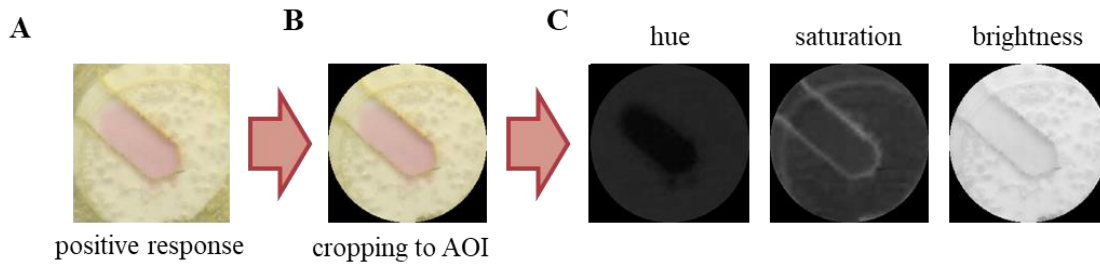


Figure 5-2. Overview of AOI generation via digital image cropping and color space conversion. (A) Images of each VF membrane are digitally captured. (B) Each digital image is cropped to the appropriate size. Removing the background surrounding these circular crops forms the area of interest (AOI) described in the narrative. (C) The AOIs are converted into a three-slice color space stack (HSB color space shown here).

We use the term ‘regions of interest’ (ROIs) to distinguish smaller sections within the AOI, usually a region of localized positive color response (**Figure 5-3**). For these studies, the ROIs were acquired via the $L^*a^*b^*$ color thresholding method described by Woolf et al. ($L^* = 0-230$, $a^* = 135-255$, and $b^* = 0-255$).²³ Segmenting or masking the image in this way allowed isolation, retention, and analysis of pixels associated with a positive immunoassay color response while excluding all other superfluous pixels (e.g., background). Prior to measurement and evaluation, the area outside the masked ROIs was removed (converted to black).

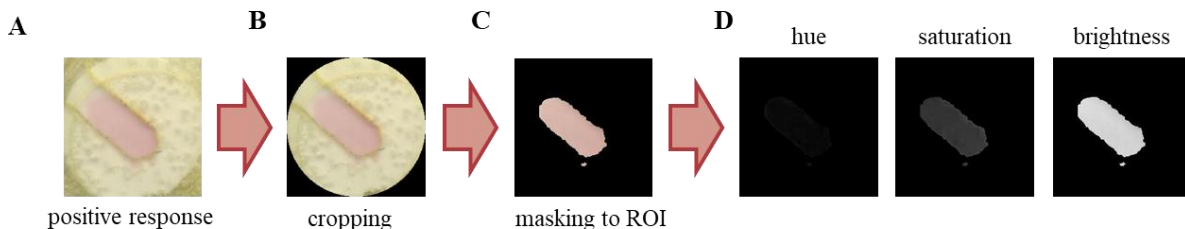


Figure 5-3. Overview of ROI generation via color thresholding and image masking. (A) Images of each VF membrane are digitally captured. (B) Each digital image is cropped to the appropriate size. The background surrounding each circular crop is removed. (C) The region of interest (ROI) is created by masking and selecting pixels corresponding to the color of interest. This is accomplished using native ImageJ color thresholding tools. (D) The masked ROIs are converted into a three-slice color space stack (HSB color space shown here).

Accordingly, each AOI and ROI was converted to weighted 8-bit grayscale using the Image > Type > 8-bit command path ($gray_{weighted} = 0.299 * R + 0.587 * G + 0.114 * B$). Grayscale intensity profiles were plotted with the native ImageJ Plot Profile tool. To obtain hue and saturation values, ImageJ was used to convert masked ROIs into HSB stacks. For reference, ImageJ reports

grayscale, hue, and saturation values on an 8-bit, 0 to 255 scale. On the grayscale, 0 is black and 255 is pure white. On the saturation scale 0 represents complete unsaturation of the color.

5.2.2 *VFI Microfluidic Disc Fabrication*

Each cVFI disc was constructed via the print-cut-laminate (PCL) fabrication method.^{24, 25} Each 5-layer disc consisted primarily of alternating sheets of polyethylene terephthalate film (PeT, 101.6 μm thickness, Film Source, Inc. Maryland Heights, MO, U.S.A.) and heat sensitive adhesive (HSA, 50.8 μm thickness, EL-7970-39, Adhesives Research, Inc. Glen Rock, PA, U.S.A.).²⁵ Disc layers, microfluidic architecture, and accessory pieces were designed in AutoCAD® 2019 (Autodesk Inc., San Rafael, CA, U.S.A.), then ablated into the appropriate layers with a 50 W CO₂ laser engraving system (VLS3.50, Universal® Laser Systems, Scottsdale, AZ, U.S.A.). Layers 2 and 4 served as the primary fluidic layers, layers 1 and 5 as capping layers, and layer 3 functioned as the flow-through or via layer. A disposable biopsy punch was used to obtain circular cutouts (4 or 5 mm \varnothing) of the porous membranes, which were then placed into corresponding laser ablated voids in layer 3. Layers 1-5 were heat bonded via a single pass through an office laminator (\sim 175-190°C) (UltraLam 250B, Akiles Products, Inc. Mira Loma, CA, U.S.A.). This heat lamination step activated the HSA that bounded layers 2 and 4, anchoring and sealing the porous membranes into position, while simultaneously forming a permanent bond between the adjoining PeT layers.

Polymethyl methacrylate (PMMA, 1.5 cm, McMaster-Carr, Elmhurst, IL, U.S.A.) accessory pieces provided additional chamber depth and volume. PMMA accessory pieces and the concomitant PeT coverlets were bonded to the 5-layer disc (Figure 2A), post-lamination, with pressure sensitive adhesive (PSA, 55.8 μm thickness, ARcare 7876, Adhesives Research, Inc. Glen Rock, PA, U.S.A.). To ensure consistent PSA adhesive bonding, fully assembled cVFI discs were pressed under a 10 lb. load for 1 hr. For easier visualization and estimation of fluid drainage,

horizontal, linear graduations were rastered into the PeT coverlets of each sample loading chamber (Figure 5-4).

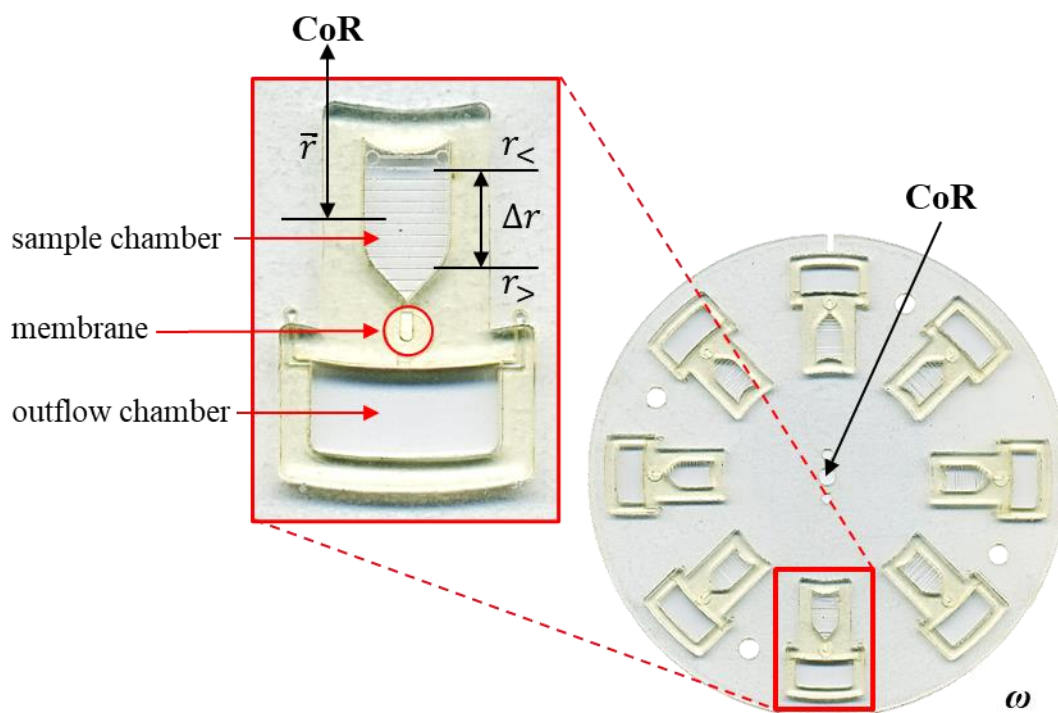


Figure 5-4. Scanned image of a fully assembled cVF disc (top view) and a close-up detailing a single cVFI testing domain. Location of the sample chamber, embedded cVF membrane, and outflow chamber are denoted by red arrows. CoR = center of rotation, $r_{<}$ and $r_{>}$ represent the inner and outer menisci of the fluid plug, Δr = radial extent (length) of the fluid plug, \bar{r} = mean radial distance of the fluid plug relative to the CoR

5.2.3 *On-disc, Vertical Flow, Immunocapture – proof of principle*

Mouse, whole molecule, IgG (Jackson ImmunoResearch Laboratories, Inc., West Grove, PA, U.S.A.) was immobilized on a 4 mm ($2.5 \mu\text{l}$ at 5.5 mg/ml), circular nitrocellulose (NC) membrane cutout ($0.2 \mu\text{m}$ pore size, Bio-Rad). Prior to lamination into the disc, each NC cutout was dried for 60 min at 37°C in a convection oven (Thermo Scientific™ PR305220G, Thermo Fisher Scientific Inc., Waltham, MA, U.S.A.). Detection membranes for negative controls were not spotted with capture antibody. Fully assembled discs were cured in foil moisture barrier bags (Dri-shield™, Uline, Pleasant Prairie, WI, U.S.A.) with two-three 3-gram silica gel moisture absorbent packets (S-3904, Uline) for ≥ 48 hrs.

Gold nanoparticle labelled goat anti-mouse monoclonal antibodies (AuNP-mAbs) served as the detection agents. The stock AuNP-mAb (4 nm colloidal AuNP, OD 2.0 at 520 nm, Jackson ImmunoResearch Laboratories, Inc., West Grove, PA, U.S.A.) was diluted 1:39 (5 μ L in 195 μ L total volume) with assay buffer, which consisted of 0.1 M phosphate buffer (PB) containing 0.1% Triton X-100 and 0.1% bovine serum albumin (BSA), pH = 7.2 (Diagnostics Discovery Laboratory, School of Medicine, University of Nevada, Reno, USA). The resultant sample solution was centrifugally pumped through the cVFI membrane via disc rotation at 2,000 rpm for 5 minutes (n = 4 ea).

5.2.4 *On-disc, Vertical Flow with Sandwich-type Immunocapture – proof of principle*

Zaire Ebola and *Y. pestis* reagents were prepared in the Diagnostics Discovery Laboratory as per the protocol described in DeMers et al. and Hau et al., respectively.²⁶ Monoclonal antibodies specific to Zaire Ebola virus-like particle (eVLP) or the *Y. pestis* antigen (YpF1) served as capture antibodies for this study; each 4 mm membrane punch was manually spotted with 2.5 μ L of 1HK7 (eVLP specific mAb at 5.1 mg/mL) or Yp11C7 0416 IgG1 (YpF1 specific mAb at 5.95 mg/mL). Fully assembled discs were dried cured as described above.

Prior to sample loading, all NC membranes were pre-wetted with 40 μ L of assay buffer (30 s at 3,000 rpm). Antigen dilutions (10.0 and 1.0 μ g/ml) were prepared by mixing stock eVLP and YpF1 solutions (eVLP = 10 μ g/ml and F1 = 430 μ g/mL) with assay buffer. The antigen dilutions (40 μ L of eVLP or YpF1) were premixed with 5 μ L of the appropriate AuNP-mAb (Yp3F2 or 1HK11 at OD 10). Negative controls consisted only of assay buffer (40 μ L) and AuNP-mAb (5 μ L), i.e., no antigen was present. Spiked samples and negative controls were pipetted into cVFI discs and centrifugal forces were used to drive the spiked samples through the cVFI detection membrane. No post-wash step was performed.

5.2.5 Comparison of on-disc cVFI with traditional LFI – dilution series

Ebola assay reagents (eVLP, 1HK7, and 1HK11) and prototype LFI strips were prepared in the Diagnostics Discovery Laboratory according to the protocol outlined in DeMers et al.²⁶ As described above, 2.5 µl of eVLP-specific antibodies (1HK7 at 5.1 mg/mL) was manually spotted onto a 4 mm NC membrane cutout (BioRad). Fully assembled discs were dried and cured as described above. Antigen dilutions were serially diluted (10X) by mixing stock eVLP samples (10 µg/ml) with assay buffer to yield concentrations between 0.001 and 10.0 µg/ml. Antigen dilutions (80 µl ea) were premixed with 5 µl of AuNP-mAb (1HK11 at OD 10). Negative controls consisted entirely of assay buffer (80 µl) and AuNP-mAb (5 µl), i.e., no antigen was added. Spiked samples of each dilution were split equally between concurrently executed LFI and cVFI tests. An aliquot of each spiked sample (40 µl) was manually pipetted onto the conjugate pad of an LFI test strip. These GP-specific LFIs were then placed vertically in individual 1.5 mL microcentrifuge tubes containing 150 µl assay buffer. LFIs were removed from the assay buffer after 15 min, dried at room temperature for 5 min, and imaged for downstream analysis and evaluation.

On-disc cVFI tests were performed in parallel with the LFI tests. Explicitly, all NC membranes were pre-wetted with 40 µl of assay buffer (30 s at 3,000 rpm) prior to loading spiked samples and negative controls into cVFI disc sample chambers. Centrifugal force was used to push the spiked samples through the cVFI detection membrane. The stepwise spin protocol consisted of the following sequential steps: 1,000 rpm 15 s, 1,500 rpm 15 s, 2,000 rpm 30 s, 2,500 rpm 30 s, 3,000 rpm 30 s, and 4,000 rpm 30 s. No post-wash step was performed.

5.3 Results and Discussion

Previous research by other groups has, in part, demonstrated either on-disc vertical flow through porous media or centrifugally assisted LFI. To the best of my knowledge, the work

described here is the first instance of on-disc vertical/orthogonal flow with sandwich-type immunocapture. To elaborate, Templeton et. al and Karle et. al provided valuable proof-of-principle for on-disc centrifugal vertical flow (cVF) through embedded porous membranes. However, rather than on-disc immunocapture and antigen detection, those cVF approaches centered on particulate filtration and pre-concentration of bacteria.^{27, 28} In contrast, others have performed on-disc centrifugally assisted LFI (cLFI); those approaches do not employ true vertical/orthogonal flow and either continue to rely upon cooperative capillary-centrifugal flow or are sensitive to bypass flow in which the sample flows around, rather than through, the membrane.²⁹⁻³¹ Hereafter we demonstrate full proof-of-principle for on-disc, centrifugally-driven vertical flow with immunocapture (cVFI) on pre-functionalized membranes.

The sections that follow detail the progressive stepwise process of demonstrating proof-of-principle for on-disc vertical flow with immunocapture. Sections **5.3.1** and **5.3.2** describe initial efforts to deconstruct an LFI and the transition to on-disc vertical flow. These two sections also highlight the initial problems relating to the size and shape of the color response. Section **5.3.3** focuses on positive and negative immunocapture trials (no antigen present), while section **5.3.4** focuses on full sandwich-type immunodetection with antigen present. Finally, Section **5.3.5** describes comparative analysis of LFI test strips and cVFI test spots; this section also emphasizes the potential importance of exploring multiple color variables and image analysis approaches during assay evaluation.

5.3.1 *Preliminary Studies – Centrifugally Assisted LFI*

Initial efforts to perform on-disc, centrifugally assisted LFI (cLFI) focused on deconstructing conventional LFIs, i.e., untethering the test strip from the conjugate and wicking pads (**Figure 5-5**). By and large, those experiments failed, highlighting key challenges to on-disc

LFI and exposing several logical flaws in the experimental design; these challenges to on-disc cLFI are also detailed in recently published works by Shen et al. and Kainz et al.²⁹⁻³¹ Early experimental designs envisioned an on-disc process in which recurring bouts of capillary flow through the test and control lines would improve assay sensitivity; in this ‘wick-spin-repeat’ system, capillary flow would serve as the primary driver for flow through the LFI strip and centrifugal force would serve as the primary driving force for fluid recovery from the test strip and wicking pad. Challenges to these experiments included bypass flow, diminished capillary flow after the first wick-spin cycle, and capillary retention forces. Bypass flow occurs when the liquid sample flows behind, around, or floods over the test strip rather than through the porous media; these aberrant flow patterns are a common problem in LFI cartridge design and are accentuated when LFI components are embedded in microfluidic discs.²⁹

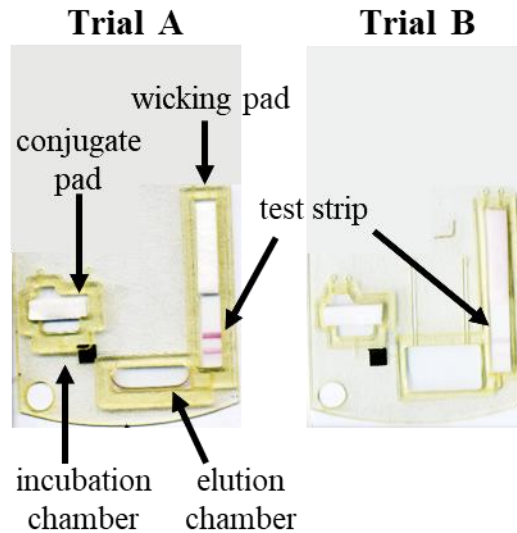


Figure 5-5. Initial efforts to perform on-disc centrifugally assisted LFI. A 40 ul aliquot of VLP sample was added to the incubation chamber and allowed to steep with the pad for 10 minutes at room temperature. Downstream laser valve actuation and centrifugation permitted release and flow of the incubated sample into the elution chamber. Fluid in the elution chamber fills a wicking channel that, in turn, leads to the test strip chamber. Capillary flow is the primary driver of flow in the test strip chamber.

Further, in the fully wetted state, capillary forces can be viewed as a retention force that opposes fluid flow or drainage from a porous medium.²⁹ In **Chapter 2**, these retention forces impacted the extent to which fluid was recovered from cotton swab cuttings. Here, capillary retention prevented effective recovery of fluid from the inserted LFI strip and wicking pad. This ineffective fluid recovery resulted in LFI materials that remained partially or completely wetted. In this wetted state, the conditions required for sustained capillary flow are diminished or removed. To elaborate, surface tension forces develop at the gas-liquid-solid interface; when the pores are sufficiently small to facilitate capillary condensation, that force (for contact angles < 90 degrees) provides the impetus for wicking fluid flow through the porous network. Saturating the porous medium dramatically reduces capillary action by eliminating the gas-liquid-solid interface and removing the surface tension force from the system.^{32, 33} Thus, it was unlikely that attempts to recover and re-expose the sample would prove fruitful. Shen et al. and Kainz et al. overcame these challenges, at least in part, by designing open microfluidic systems in which capillary flow was sustained via centrifugally assisted fluid removal, rather than a wicking pad.²⁹⁻³¹

In large part, the challenges outlined here led to a complete reassessment of the approach to this project. That reevaluation led me to focus on two ideas; sealing the membrane into the disc to prevent fluid bypass and directing the fluid sample orthogonally through the membrane, rather than laterally. Beyond these initial failures and shifting experimental approach, early on-disc trials suggested that untethering the conjugate pad from the LFI strip would allow for greater control of sample incubation with the gold conjugated monoclonal antibodies (Au-mAb); successful resuspension and elution of the Au-mAb with the sample was evidenced by no visible detection of pink residue on the inserted conjugate pad (**Figure 5-5B**).

5.3.2 *Transitioning to On-Disc Vertical Flow*

Results of the preliminary studies to perform on-disc vertical flowthrough were promising but variable (**Figure 5-6**). Prewetting the embedded membranes with a priming solution (20 μ l 1% TWEEN 20) served two purposes; reducing entry pressure (especially with trials using hydrophobic PVDF membranes) and limiting non-specific binding. Some residual fluid was retained at the tip of the VF port inlet and by the membrane (**Figure 5-6** -negatives). We suspected that this residual fluid could be removed via on-disc post-assay washing. Positive color responses exhibited irregular and unpredictable shapes. I developed several hypotheses that might explain these irregularities; those hypotheses included 1) issue related to the priming solution that could impact antibody-antigen behavior or interactions (e.g., TWEEN and Triton can interfere with hydrophobic bonding), 2) poor distribution of antibodies across the membrane surface during capture antibody spotting, 3) poor binding of the capture antibody to the porous membrane, 4) some abnormal flow that did not follow the primary flow path, and 5) preferential flow through portions of the membrane pore structure that offer less fluidic resistance.

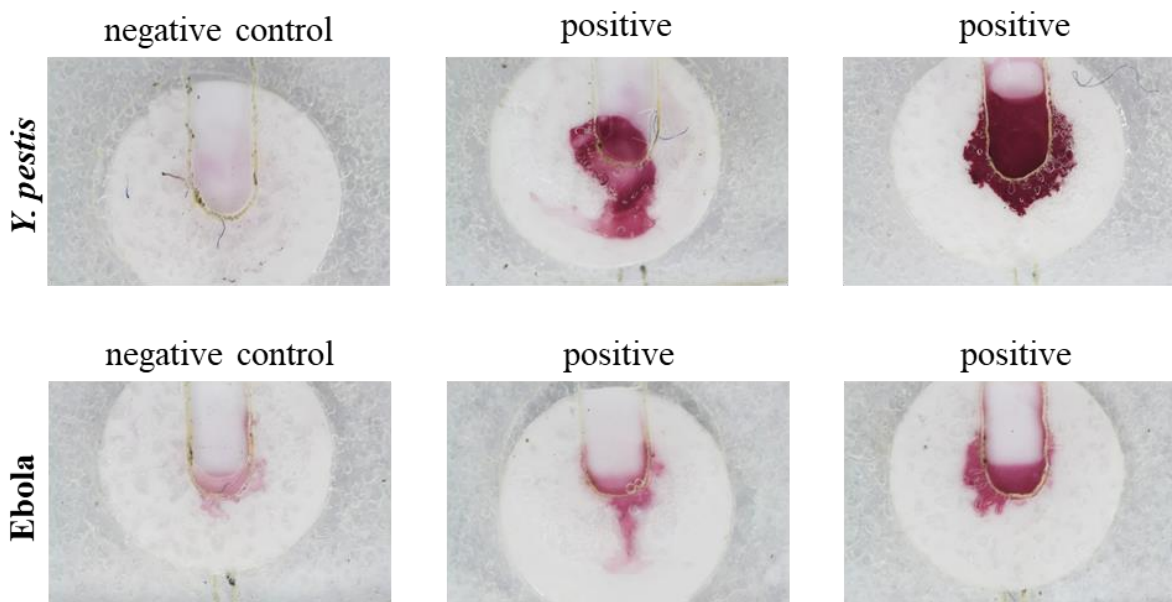


Figure 5-6. Preliminary evaluation of on-disc VF immunocapture of Ebola VLP and *Y. pestis* YPF1 antigens. Prior to embedding via lamination, each 4 mm biopsy punch was spotted with 2.5 μ l of the appropriate capture antibody [10 μ g/ mL]. Positive samples consisted of 20 μ l VLP or YPF1 [10 μ g/ml] and 2.5 μ l Au tagged mAb. Negative controls consisted of 20 μ l PBS and 2.5 μ l Au tagged mAb. All positive and negative samples were incubated in-tube

and at room temperature for 10 minutes prior to disc loading. Prior to loading and processing the samples, each embedded membrane was pretreated (primed) with 20 μ l 1% TWEEN 20.

Further preliminary studies and discussion with collaborators at the University of Nevada Reno suggested that adjusting our procedures following membrane spotting with capture antibody might help. Specifically, I found that drying each doped membrane cutout 60 min at 37°C in a convection oven (prior to disc assembly and lamination) and curing the assembled discs \geq 48 hrs in foil moisture barrier bags (with two-three 3-gram silica gel moisture absorbent packets) helped stabilize positive color responses tremendously. A cursory search of the literature suggests that drying steps following antibody spotting are common; the fundamental reasons underlying the need for these steps however are rarely discussed. It is likely, that as water is removed from the system that the membrane-antibody interactions shift from electrostatic to hydrophobic, with hydrophobic being the dominant interaction forming stable membrane-antibody bonds.⁸ The studies that follow were intended to further stabilize positive color response signal shape and size while demonstrating clear proof-of-principle for this on-disc cVFI approach. Unless otherwise stated, membranes were either unprimed or primed with assay buffer for the appropriate eVLP or YPF1 prototype LFI system. This decision, while perhaps less than ideal as a blocking step, was intended to minimize the potential for adverse effects on the antibody-antigen systems.

5.3.3 *On-Disc Immunocapture Studies – controls only, no antigen present*

Like conventional LFI strips, on-disc detection of specific immunocapture events leveraged gold nanoparticle aggregation, which induced a characteristic reddish-purple color response on the VF membrane. In instances that a target antigen was present, we expected positive responses to appear as a dark, reddish-purple color with consistent, uniform shapes defined by the primary microfluidic flow path, delineated by the microfluidic channel boundaries and VF port geometry. Primed positive control color responses were consistent with conventional LFI color

response and were visibly distinguishable from the negative controls (n=4 each), though objectively measuring and quantifying those differences proved challenging (**Figure 5-7**). Contrary to our hypothesis, most positive color responses exhibited appreciable irregularity and lack of uniformity along the boundaries of the primary flow path (**Figure 5-7**). Given that these aberrations were more pronounced in dry (unprimed) membranes (examples can be seen in **Figure 5-8**), we surmised that color response malformations along the edges of the VF channel and port were due, at least in part, to heterogeneity in the heat sensitive adhesive (HSA); fluid could penetrate the small voids or air pockets that unavoidably remain in the HSA after disc manufacture and lamination. Importantly, both the dry (unprimed) and pre-wetted (primed) negative controls appeared visually “clean”, with no observed nonspecific binding, indicated by the lack of appreciable color response (all membrane images seen in the **Figure 5-7** were primed). Although, not seen here, preliminary studies indicated that visible nonspecific binding occurs with some regularity and more frequently in dry, unprimed membranes. The impact of this non-specific binding, the relationship to radial capillary penetration, and implications for the cVFI system are discussed in the following section(s).

Hereafter, we distinguish two types of segmented images. Areas of interest (AOIs) are uniform sections of an image containing the entire footprint of the embedded VF membrane.²³ In contrast, regions of interest (ROIs) corresponded to irregular color response boundaries that were defined via color thresholding in an effort to skirt challenges associated with the AOI approach (e.g., pixel averaging of the background).²³ By applying predetermined color thresholds ($L^* = 0-230$, $a^* = 135-255$, and $b^* = 0-255$), pixels corresponding to nanoparticle aggregation and associated color formation were isolated, preserved, and analyzed, while pixels associated with the background of the digital images were removed (**Figure 5-7**). When comparing positive and

negative controls, circular AOIs (4 mm circular AOIs with area = 31,428 pixel²) exhibited comparable mean grayscale values (0 to 255 scale); positive mean = 206.29 ± 3.1 and negative mean = 212.68 ± 3.04 (**Figure 5-7-B**). Statistically, these mean values were different but only just so (Welch's t-test: p-value = 0.02576, α= 0.05), suggesting an under-estimation of the positive color response (due to a greater proportion of background pixels) by this AOI cropping approach. If unaddressed, the practical implication of this underestimation is poor discrimination between weak positive and negative color response results.

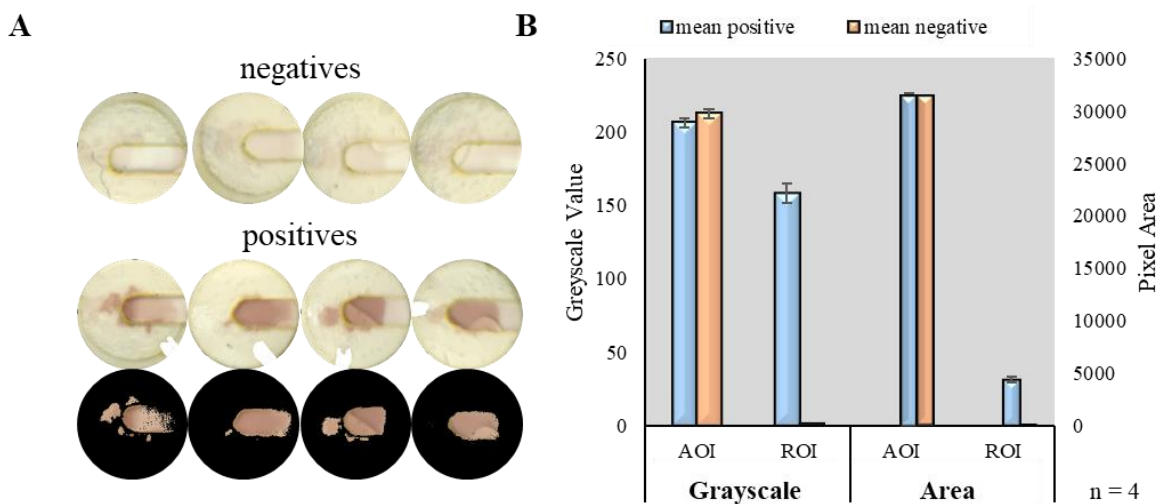


Figure 5-7. Proof-of-Principle for on-disc cVFI immunocapture using a mouse IgG and goat anti-mouse antibody pair. **(A)** Initial circular AOIs of the 4 mm Ø cVFI membranes (n = 4 ea negative and positive controls). Note: Black orientation marks were digitally removed prior to image segmentation (now appear as white marks along the edges of positive control membranes). Masked ROIs of the positive controls are featured immediately below the corresponding AOIs. **(B)** Mean grayscale and area values for the cropped AOIs and masked ROIs. No pixels were selected for the negative control ROIs. Accordingly, grayscale and area values are reported here as zero.

Comparatively, the threshold-based segmentation method effectively masked positive color responses (ROIs) and removed background pixels. The mean area of the positive color responses comprised only <10% of the total membrane surface area (ROIs with area = 4,331.25 ± 280.603 pixel² or 7.26% of the total 4 mm cVF membrane); corresponding mean grayscale value for these ROIs = 158.165 ± 6.71 (**Figure 5-7-B**). This ROI grayscale value was ~26% darker than the corresponding mean grayscale value for the positive AOIs in the previous

paragraph. Notably, when analyzing negative control ROIs, no pixels fell within the pre-established color threshold range (ROI area = 0.0 *pixel*²) (**Figure 5-7-B**); this result stands in stark contrast to the AOI result from the previous paragraph in which the entire area (31,428 *pixel*²) was assigned a mean grayscale value of 221.68. Our threshold-based ROI approach ameliorates complications associated with simple AOI analysis (e.g., >90% of the pixels included in the AOI analysis were associated with the background color of the membrane), permits more robust discrimination of positive and negative color responses, and provides a potential path for avoiding misclassification of weak positive results (e.g., false negative interpretation).

5.3.4 *On-Disc Immunocapture Studies –antigen present*

As observed in the above-described control studies, the color responses produced by successful immunocapture of either eVLP or YpF1 produced color responses that exhibit malformations along the edges of the inlet channel and VF port (**Figure 5-8-A & D**). Weighted grayscale values for these positive response ROIs ranged between 85 and 175 with pixel areas $\geq 5,000$ (**Figure 5-8-C**). Dry, un-primed negative controls exhibited a halo-like, annular ring of pink color, detectable both visually and using threshold-based color masking, that we again attributed to nonspecific binding following radial capillary penetration (**Figure 5-8-D & E**). Radial capillary penetration carries unbound detection antibody away from the primary flow path, which becomes trapped in the membrane (along the leading edge of the advancing fluid front) and is not easily removed with subsequent washing (**Figure 5-8-D**). This non-specific binding is significant and appears as a halo of color development outside the primary flow path; if unaddressed, this halo of color could confound threshold-based masking results. However, ‘priming’ the cellulosic VF membranes appears to induce a state of near saturation that minimizes radial capillary penetration (**Figure 5-8-A**); saturating the porous medium dramatically reduces capillary action by eliminating

the gas-liquid-solid interface and removing the surface tension force from the system.^{32, 33} Thus, in saturated cVF membranes, lateral transport (away from the primary flow path) would be dominated by diffusion or transient convective disturbances, which would be far less pronounced compared to the situation where surface tension forces drive convection through the membrane.³² Case in point, the primed negative controls in this study appeared ‘clean’ with no visually detectable chromogenesis due to non-specific binding (**Figure 5-8-A**). It should be noted that ROI image masking did isolate some extraneous pixels within the threshold ranges for the color of interest; these pixels were located along the edge of the VF port and appeared to correspond with residues (laser ablation products) that were not removed during the disc layer manufacture and assembly process) (**Figure 5-8-B**). Accordingly, we concluded that on-disc vertical flow sandwich-type immunocapture is a feasible option for pathogen detection and that, unlike traditional LFI strips, pre-saturating the porous medium is preferable. It is worth mentioning that this study, and those that follow, did not employ any methods for blocking the membrane surface. Blocking combined with membrane pre-saturation will further reduce the frequency and severity of non-specific binding of detection antibodies to the VF membrane.

Further, we believe the cVFI platform described here falls within the hypothetical bounds for a non-diffusion-limited immunoassay.⁷ An ideal LFI or VFI system allows the analyte to diffuse to the pore wall before being carried through the detection zone.^{7, 34-36} Membranes with smaller pore sizes enable efficient antigen capture at higher flow rates by reducing the distance an antigen-antibody complex must traverse to reach the membrane wall.^{7, 37} The Péclet number (Pe) is a unitless value that describes this relationship between analyte diffusion and fluid velocity through the detection zone. Hypothetically, a non-diffusion-limited immunoassay would exhibit (Pe) < 1 and antigen capture efficiency > 90%. We believe the cVFI platform described here falls

within these hypothetical bounds. Explicitly, at 1,000 rpm each 0.2 μm pore size cVF NC membrane processed 200 μl of assay buffer in roughly 400 s with an equivalent overall flow rate of 30 $\mu\text{l min}^{-1}$ (Chapter 4). This modest flow rate is significantly lower than flow speeds reported in Chen et al. where the authors explored flow speeds as high as 5 mL min^{-1} (1.06 mm s^{-1}).⁷

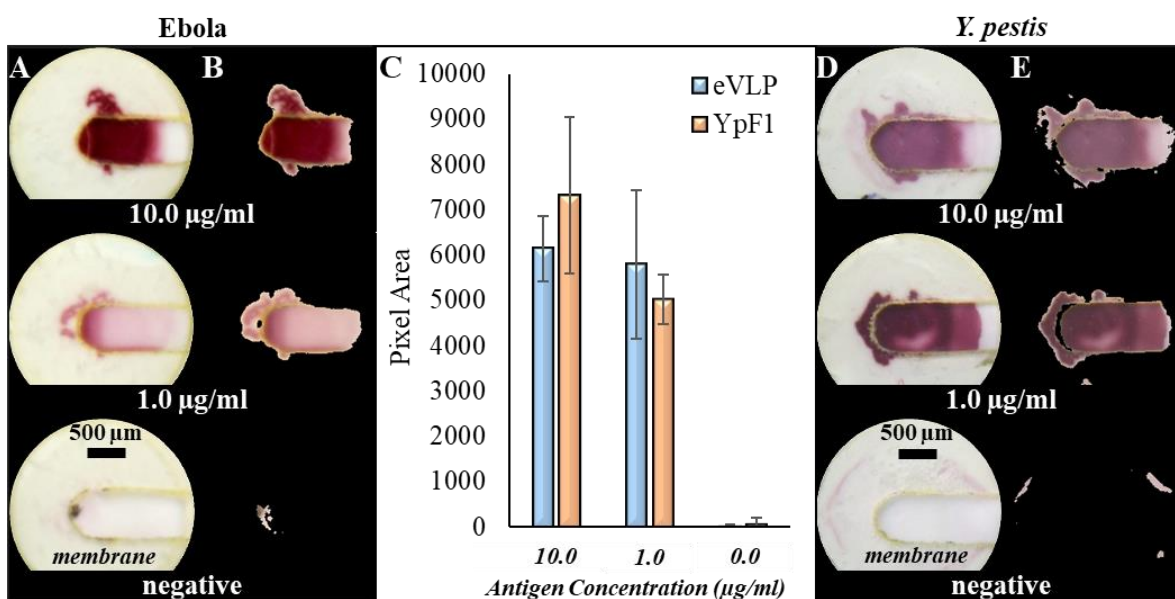


Figure 5-8. Proof-of-principle evaluation of an on-disc, sandwich-type, VFI for the detection of Ebola and *Y. pestis*. Representative cropped circular AOIs of Zaire Ebola VLP (A) and *Y. pestis* F1 color (D) responses ($n = 3$ ea). Corresponding masked ROIs of the images featured in columns A and D (B and E). Mean pixel area of the masked ROIs is reflected in the bar plot (C).

5.3.5 Comparison of on-disc cVFI with traditional LFI – dilution series

The primary goal of this study was to perform a direct, parallel comparison of color responses in the LFI and cVFI prototypes. Our cVFI system can handle sample volumes 5X larger than conventional LFI strips (200 vs 40 μl). However, to maintain the fidelity of this direct comparison, the sample volume for each trial in each system was held constant at 40 μl . All LFI and cVFI trials were performed simultaneously and using the same master dilution mixes. Collectively, grayscale values, intensity profiles (plot profiles), hue, saturation, and pixel area were measured and analyzed.

Visual Inspection

In both systems (LFI and cVFI), the intensity of the positive color response increased with antigen concentration and the negative controls appeared ‘clean’ with little to no nonspecific binding (**Figure 5-9-A** and **Figure 5-10-A**). However, at the lowest concentration (0.001 $\mu\text{g/ml}$, or 1 ng/ml), the cVFI system produced positive color responses that appeared visibly darker than the corresponding LFI results, i.e., LFI result at this concentration appeared equivocal, at best (**Figure 5-9-A**).

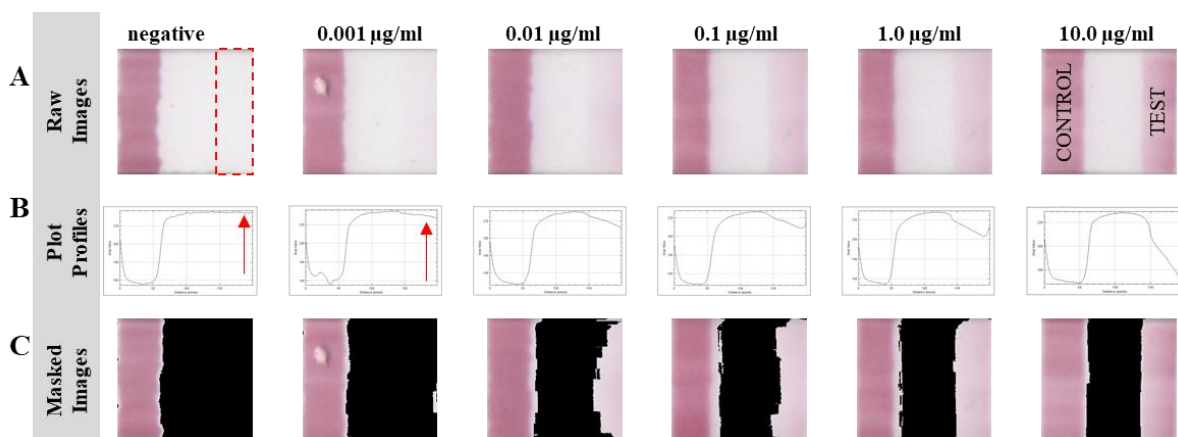


Figure 5-9. Detection of Zaire Ebola virus-like particles (VLP) using the LFI prototype system. A 10X eVLP dilution series (10 to 0.001 $\mu\text{g/ml}$) was prepared in chase buffer ($n = 1$ ea). Aliquots of each dilution (40 μl) were simultaneously tested on LFI (**A**) strips. Cropped AOIs of the detection zones (**A**), grayscale intensity profiles (**B**), and masked ROIs of each detection zone are featured here (**C**). For orientation purposes, LFI test and control line locations are noted in black text (**A**).

Grayscale Intensity Profiles

In our experience, visual interpretation of and discernment between weak positive results and true negative LFI results (e.g., 1 ng/ml) is challenging and often confounded by variable or poor lighting conditions and differences in analyst visual acuity and color perception.^{23, 38} Grayscale intensity profile analysis is a commonly employed, straightforward method that offers objective appraisal of weak color responses and evaluation of immunochromatographic results.^{7,}

³⁹⁻⁴² Grayscale intensity profiles of entire LFI strips are shown as column average plots (**Figure**

5-9-B), where the x-axis represents the horizontal distance through the rectangular AOI selection, and the y-axis represents vertically averaged pixel grayscale intensities (weighted). In this study, LFI intensity profiles indicated an inverse relationship between grayscale value and antigen concentration in which there was a clear loss of grayscale signal with increasing antigen concentration; lower grayscale values corresponded with darker color responses. These plot profiles also revealed uneven color response across the test and control lines, e.g., horizontally, a pronounced tapering effect was observed along the leading edge (relative to the direction of capillary flow) of the test lines. This tapering grayscale intensity rise with increasing distance along the x-axis is symptomatic of uneven capture antibody distribution across the width of the test line; this is attributable to diffusion away from the area of antibody deposition (e.g., test and control lines) during LFI strip spotting and fabrication. While this observation does offer some insight into antibody distribution across the LFI membrane, the practical implications are minimal and the impact on color response is not particularly concerning.

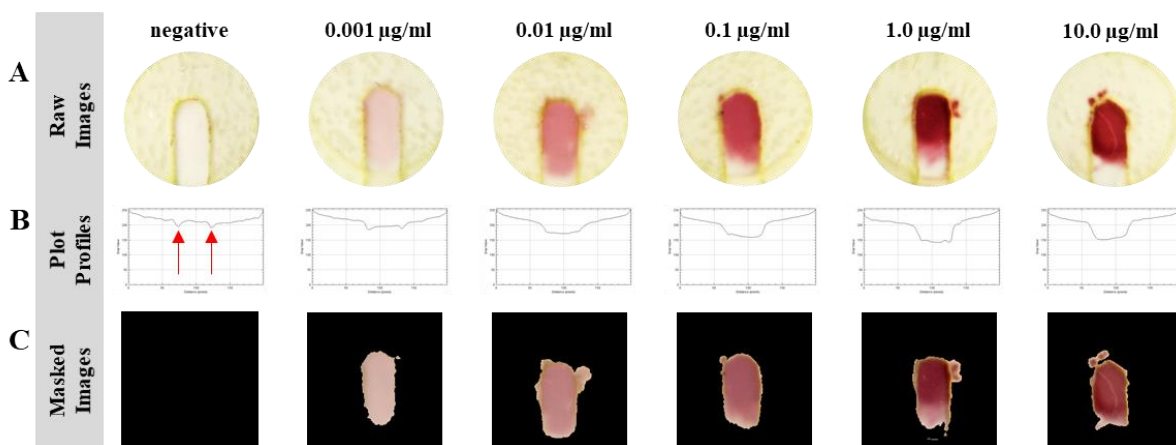


Figure 5-10. Detection of Zaire Ebola virus-like particles (VLP) using the cVFI prototype system. A 10X eVLP dilution series (10 to 0.001 µg/ml) was prepared in chase buffer (n = 1 ea). Aliquots of each dilution (40 µl) were simultaneously tested on on-disc (A). Cropped AOIs of the detection zones (A), grayscale intensity profiles (B), and masked ROIs of each detection zone are featured here (C).

Grayscale Values – Evaluation of LFI test lines

Rectangular AOIs corresponding to the test line of each LFI strip were cropped and analyzed (denoted by dashed red box in **Figure 5-9-A**).²³ As anticipated by the initial visual inspection, LFI test lines (55 by 185 pixels with total area = 10,175 *pixel*²) produced grayscale values that decreased with diminishing antigen concentration; in order, grayscale values of 187, 206.8, 211.6, 217.8, 228.5, 234.2 correspond to serially diluted (10X) eVLP solutions from 10.0 to 0.001 $\mu\text{g/ml}$. Threshold-based masks of each LFI test line were also evaluated. Grayscale values for these test line ROIs were like those produced via AOI analysis; 186, 206.8, 210, 215.1, 225.5, and null, respectively (**Figure 5-9-C**). However, threshold-based segmentation of the LFI test lines generated ROI masks that exhibited shapes and areas much smaller and more irregular than might be expected with simple visual inspection or rectangular AOI cropping; total area = 9731, 9726, 7893, 5792, 191, and null *pixels*² (**Figure 5-9-C**).

This ROI irregularity became more pronounced as antigen concentration decreased, which is suggestive of convex capillary flow profiles where slower flow dominates at the edges of the LFI membrane; this convex flow profile was likely due to membrane crush damage during the strip cutting process.⁸

Grayscale Values – Evaluation of cVFI test spots

Grayscale intensity profiles of the primed cVFI biopsy punches ($\emptyset = 200$ *pixels*, area = 31,428 *pixel*²) clearly defined the detection zone by revealing the location of microfluidic channel edges (red arrows in **Figure 5-10-B**) bracketing cVFI test spots, each with an approximate width of 50 pixels. Like the LFI test lines, intensity profiles of these cVFI test spots indicated a loss of grayscale signal with decreasing antigen concentration. Direct comparison of grayscale values for the masked test lines/spots for both systems (**Figure 5-9-B** and **Figure 5-10-B**)

supported the observation that the cVFI color responses were visibly darker than the LFI counterparts; cVFI grayscale values = 104.26, 104.02, 126.20, 154.209, 184.425, and null (from 10.0 $\mu\text{g/ml}$ to 0.001 $\mu\text{g/ml}$). For example, at the highest antigen concentration, the segmented cVFI grayscale signal was 43.8% darker than masked LFI equivalent. Likewise, at the lowest concentration, the segmented cVFI grayscale signal, which encompassed 4,596 pixel², was 18.2% darker and 24.06 times larger than the corresponding masked LFI test line (191 pixel²). It is noteworthy that the cVFI color response for the most dilute sample (0.001 $\mu\text{g/ml}$) was 1.37 % more intense than the LFI color response at the highest titer (10.0 $\mu\text{g/ml}$), 4 orders of magnitude more concentrated; grayscale values = 184.425 and 187, respectively. From a practical perspective, these findings suggest that the cVFI system enhances the color response signal for the prototype eVLP sandwich-type immunoassay, generating smaller, darker positive color responses at all antigen concentrations which likely enhances sensitivity.

HSB Analysis - Hue

Grayscale analysis provides only a single value representing light intensity, which can be problematic at low concentrations where the impact of background noise is more significant, e.g., background grayscale intensity values can shift due to membrane wetting or uneven penetration of liquid. As such, the components of HSB color space (Hue Saturation Brightness) can provide valuable insights into color response and assay performance that extend beyond conventional grayscale analysis. The saturation component is quite useful when evaluating colorless-to-colored responses (as featured herein), while the hue component is rather robust in terms of lighting variation.^{23, 43-47} Across the dilution series, hue values for the cVFI trials were variable with a red-to-blue shift that is consistent with increasing gold nanoparticle aggregation. (**Figure 5-11-A**), i.e., a hue shift from red at 0.001 $\mu\text{g/ml}$ to blue-purple region at 1.0 $\mu\text{g/ml}$.^{48, 49} Conversely, hue values

for the LFI test lines (55- by 185-pixel rectangular AOIs and threshold-based ROIs) were relatively stable regardless of antigen concentration, ranging from 219 at 0.001 $\mu\text{g/ml}$ to 235 at 10 $\mu\text{g/ml}$ (**Figure 5-11-A**). Minimally, these findings suggest that at higher antigen concentrations, the cVFI system produces greater gold nanoparticle aggregation in the detection zone. However, in this study, the hue parameter provides relatively poor discrimination between positive and negative LFI color responses, highlighting a characteristic challenge in applying hue analysis to monotonal, colorless-to-colored transitions on near-white backgrounds.^{23, 43} Simply stated, white does not appear in the hue palette of HSB color space. When analyzing negative or weak negative color responses, ImageJ assigns a hue value that best represents the overall color cast of the near-white background; in this case, ImageJ assigned a negative control hue value (195) that was remarkably close to that of the positive color responses. Despite this shortcoming, the hue parameter did provide some sense that the cVFI system can enhance gold nanoparticle aggregation in the detection zone of the membrane.

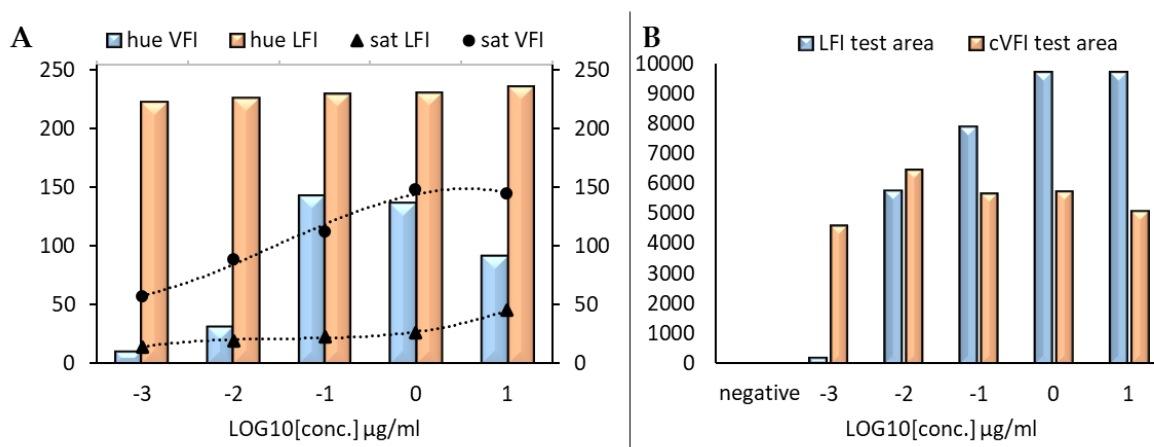


Figure 5-11. Detection of Zaire Ebola virus-like particles (VLP) using the LFI prototype system. (A) Hue and saturation values for the masked ROIs. (B) Comparison of total masked ROI areas (pixel area).

HSB Analysis - Saturation

Analysis of both rectangular AOIs and masked ROIs of the LFI test lines indicated that color saturation was relatively low and decayed with decreasing antigen concentration (saturation <50; **Figure 5-11-A**). Saturation of the cVFI color responses was significantly higher across the entire dilution series (saturation >50; **Figure 5-11-A**); 2.28 times more saturated at 10.0 µg/ml and 5.99 times at 0.001 µg/ml. We believe this is due, in part, to the decreased surface area of the cVFI detection zone relative to the LFI ($area_{LFI} \cong 10,000 \text{ pixel}^2$ and $area_{cVFI} \cong 5,000 \text{ pixel}^2$) (**Figure 5-11-B**). These LFI and cVFI saturation values are consistent with other reports of the sigmoidal relationship between saturation and LOG_{10} concentration (**Figure 5-11-A**).⁵⁰ It should be noted that the null saturation and area values reported for the negative controls signify that no pixels fell within the $L^*a^*b^*$ color threshold range for masking, thereby confirming that little to no appreciable nonspecific binding was present in the negative control. In general, the area of the masked positive color responses was more consistent across antigen concentrations in the cVFI system than in parallel LFI testing (**Figure 5-11-B**). At higher antigen concentrations (when the color response is darker and more intense), area of the masked detection zone favored the LFI system (**Figure 5-11-B**). This finding is not surprising given that the LFI detection area (test line) is significantly larger than the cVFI detection port; at higher concentrations it is expected that the LFI test strip will generate a large semi-rectangular color response. However, at the lowest antigen concentrations area of the masked color response favored the cVFI system (**Figure 5-11-B**). At the lowest concentration the cVFI signal was 24.06 times larger; $area_{cVFI} = 4,596 \text{ pixel}^2$ compared to $area_{LFI} = 191 \text{ pixel}^2$.

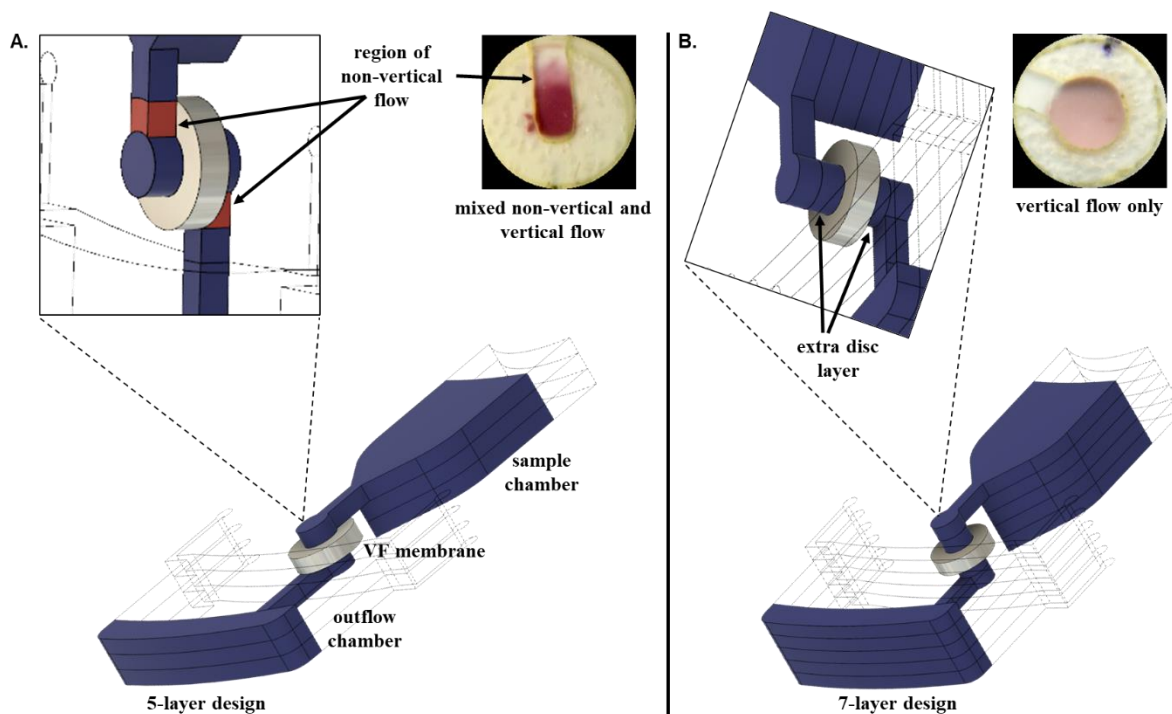


Figure 5-12. Redesigning the VF disc to eliminate regions of non-vertical flow. **(A)** In the original 5-layer design, regions of non-vertical flow often produced gradients of color response. **(B)** To address this issue, a 7-layer disc design was used to eliminate the regions of non-vertical flow and to force true orthogonal flow through the VF membrane (panel B inset photograph courtesy of Scott Karas).

5.3.6 Ongoing Efforts to Optimize the Flow Pattern

A prime focus for the studies discussed here was to stabilize positive color response shape and uniformity. Establishing a consistent process for drying and curing the doped membrane cutouts helped tremendously. Despite improvements resulting from membrane drying and curing, some irregularity persisted. Some of this irregularity was attributable to lateral capillary penetration and lack of homogeneity in the adhesive layers at the edges of the VF port and inlet channel. However, on occasion, some of the irregularity was more readily explainable by regions of non-vertical flow; a 1 mm long region where the inlet channel flows over the VF membrane before encountering the actual VF port (**Figure 5-12A**). Most often, irregularities in the color response within the region of non-vertical flow presented as a gradient of color (**Figure 5-12A** inset photograph). As such, the disc was redesigned with a 7-layer format. This design shifts the

primary fluidic channels to layers 2 and 6, while layers 3 and 5 serves as added via layers (**Figure 5-12B**). Testing of this new disc design are ongoing. But early results indicate that the 7-layer format eliminates the worrisome regions of non-vertical flow (**Figure 5-12B** inset photograph).

5.4 Conclusions

We established proof-of-principle for on-disc immunocapture (cVFI) and colorimetric detection via centrifugally driven orthogonal flow through unbacked porous membranes as applied to detection of two Tier 1 biological pathogens, namely Zaire Ebola virus-like particles and *Y. pestis* F1 antigen. By laminating and sealing the detection membranes into the cVFI disc, we prevented bypass flow, precluding the need for sensitive flow optimization studies and ‘design factor’ consideration.²⁹ The cVFI disc minimizes analyst exposure to biofluids and potential pathogens by offering a fully enclosed platform that does not require inclusion of post-assay membrane drying or device disassembly needed for other VFI techniques.⁷

The image analysis approach outlined herein offers insights beyond typical grayscale analysis and allows the user to employ inexpensive, ubiquitous image capture equipment (e.g., smart phone, flatbed scanner, Raspberry Pi, etc.) and freely available software (Fiji distribution of ImageJ) to access rich color data. By accessing digital image information in a variety of ways, this approach provided greater understanding of LFI and cVFI assay performance. Examples include isolating and measuring non-uniform color responses, identifying laser ablation products that were not removed during disc assembly and cleaning, measuring the extent of visible non-specific binding, visualizing the uneven distribution of color response at LFI test lines, and identifying anomalous flow patterns that suggest membrane damage during LFI manufacture. When comparing systems, the cVFI approach generated color responses that were demonstrably darker (at 10.0 $\mu\text{g/ml}$, 2.28 times more saturated and 43.8% darker grayscale signal: at 0.001 $\mu\text{g/ml}$, 5.99

times more saturated and 18.2% darker grayscale signal) and indicative of greater gold nanoparticle aggregation (red-to-blue hue shift). The cVFI color response for the most dilute sample (0.001 $\mu\text{g/ml}$) was 1.37 % more intense than the LFI color response at the highest titer (10.0 $\mu\text{g/ml}$, 4 orders of magnitude more concentrated); grayscale values = 184.425 and 187, respectively.

The cVFI system offers full customization and flexibility with regards to sample type (e.g., urine, blood products (plasma and serum), cellular lysates), sample volume (10 to 200 μl), membrane selection (e.g., nitrocellulose, PVDF), and flow rate (i.e., speed of disc rotation, chamber position). The current cVFI disc can process up to eight samples simultaneously and is amenable to integration of additional liquid handling steps (e.g., blocking, membrane priming, post-washing, etc.) and on-disc reagent storage. We believe that these proof-of-principle studies are the first step toward development of a portable, enclosed, fully integrated, immunoassay system for multiplexed biothreat detection. Once fully optimized, we believe that this cVFI system will extend the current limit of detection (LOD) for the prototype eVLP sandwich-type assay beyond 1 ng/ml.

5.5 Acknowledgements

The benchtop-safe reagents and test strips were graciously provided by our collaborators in the Diagnostics Discovery Laboratory at the University of Nevada, Reno. I wish to extend my gratitude to Haley DeMers, Derrick Hau, Marcie Gates-Hollingsworth, and Dr. Dave AuCoin for providing these reagents and for their ongoing support of this project.

5.6 References

1. Jansen, H.-J.; Breeveld, F. J.; Stijnis, C.; Grobusch, M. P., Biological warfare, bioterrorism, and biocrime. *Clinical Microbiology and Infection* **2014**, *20* (6), 488-496.
2. Hodinka, R. L., Point: is the era of viral culture over in the clinical microbiology laboratory? *Journal of clinical microbiology* **2013**, *51* (1), 2-4.
3. Yang, S.; Rothman, R. E., PCR-based diagnostics for infectious diseases: uses, limitations, and future applications in acute-care settings. *The Lancet infectious diseases* **2004**, *4* (6), 337-348.
4. Reynolds, K. A., Integrated cell culture/PCR for detection of enteric viruses in environmental samples. In *Public health microbiology*, Springer: 2004; pp 69-78.
5. Wade, W., Unculturable bacteria—the uncharacterized organisms that cause oral infections. *Journal of the Royal Society of Medicine* **2002**, *95* (2), 81-83.
6. Emanuel, P. A.; Hankla, L. W. *Recommendations on the Use of Diagnostic Devices in Far-Forward Military Operations*; ARMY EDGEWOOD CHEMICAL BIOLOGICAL CENTER APG MD ABERDEEN PROVING GROUND ...: 2016.
7. Chen, P.; Gates-Hollingsworth, M.; Pandit, S.; Park, A.; Montgomery, D.; AuCoin, D.; Gu, J.; Zenhausem, F., Paper-based Vertical Flow Immunoassay (VFI) for detection of bio-threat pathogens. *Talanta* **2019**, *191*, 81-88.
8. Wong, R.; Tse, H., *Lateral flow immunoassay*. Springer Science & Business Media: 2008.
9. Koczula, Katarzyna M.; Gallotta, A., Lateral flow assays. *Essays in Biochemistry* **2016**, *60* (1), 111-120.
10. Gong, M. M.; Sinton, D., Turning the page: advancing paper-based microfluidics for broad diagnostic application. *Chemical reviews* **2017**, *117* (12), 8447-8480.
11. Rattle, S.; Hofmann, O.; Price, C. P.; Kricka, L. J.; Wild, D., Lab-on-a-Chip, Micro-and Nanoscale Immunoassay Systems, and Microarrays. In *The Immunoassay Handbook*, Elsevier: 2013; pp 175-202.
12. Oh, Y. K.; Joung, H.-A.; Kim, S.; Kim, M.-G., Vertical flow immunoassay (VFA) biosensor for a rapid one-step immunoassay. *Lab on a Chip* **2013**, *13* (5), 768-772.
13. Joung, H.-A.; Ballard, Z. S.; Ma, A.; Tseng, D. K.; Teshome, H.; Burakowski, S.; Garner, O. B.; Carlo, D. D.; Ozcan, A., Paper-based multiplexed vertical flow assay for point-of-care testing. *Lab on a Chip* **2019**.
14. Clarke, O.; Goodall, B.; Hui, H.; Vats, N.; Brosseau, C., Development of a SERS-based rapid vertical flow assay for point-of-care diagnostics. *Analytical chemistry* **2017**, *89* (3), 1405-1410.

15. Jiang, N.; Ahmed, R.; Damayantharan, M.; Ünal, B.; Butt, H.; Yetisen, A. K., Lateral and Vertical Flow Assays for Point-of-Care Diagnostics. *Advanced healthcare materials* **2019**, *8* (14), 1900244.
16. Reyes, D. R.; Iossifidis, D.; Auroux, P.-A.; Manz, A., Micro total analysis systems. 1. Introduction, theory, and technology. *Analytical chemistry* **2002**, *74* (12), 2623-2636.
17. Manz, A.; Graber, N.; Widmer, H. á., Miniaturized total chemical analysis systems: a novel concept for chemical sensing. *Sensors and actuators B: Chemical* **1990**, *1* (1-6), 244-248.
18. Ducrée, J.; Haeberle, S.; Lutz, S.; Pausch, S.; Von Stetten, F.; Zengerle, R., The centrifugal microfluidic Bio-Disk platform. *Journal of Micromechanics and Microengineering* **2007**, *17* (7), S103.
19. Gorkin, R.; Park, J.; Siegrist, J.; Amasia, M.; Lee, B. S.; Park, J.-M.; Kim, J.; Kim, H.; Madou, M.; Cho, Y.-K., Centrifugal microfluidics for biomedical applications. *Lab on a Chip* **2010**, *10* (14), 1758-1773.
20. Madou, M.; Zoval, J.; Jia, G.; Kido, H.; Kim, J.; Kim, N., Lab on a CD. *Annu. Rev. Biomed. Eng.* **2006**, *8*, 601-628.
21. Lai, S.; Wang, S.; Luo, J.; Lee, L. J.; Yang, S.-T.; Madou, M. J., Design of a compact disk-like microfluidic platform for enzyme-linked immunosorbent assay. *Analytical chemistry* **2004**, *76* (7), 1832-1837.
22. Gubala, V.; Harris, L. F.; Ricco, A. J.; Tan, M. X.; Williams, D. E., Point of care diagnostics: status and future. *Analytical chemistry* **2012**, *84* (2), 487-515.
23. Woolf, M. S.; Dignan, L. M.; Scott, A. T.; Landers, J. P., Digital postprocessing and image segmentation for objective analysis of colorimetric reactions. *Nature Protocols* **2020**.
24. Thompson, B. L.; Ouyang, Y.; Duarte, G. R.; Carrilho, E.; Krauss, S. T.; Landers, J. P., Inexpensive, rapid prototyping of microfluidic devices using overhead transparencies and a laser print, cut and laminate fabrication method. *Nature protocols* **2015**, *10* (6), 875-86.
25. Birch, C.; DuVall, J. A.; Le Roux, D.; Thompson, B. L.; Tsuei, A.-C.; Li, J.; Nelson, D. A.; Mills, D. L.; Landers, J. P.; Root, B. E., Rapid Fabrication of Electrophoretic Microfluidic Devices from Polyester, Adhesives and Gold Leaf. *Micromachines (Basel)* **2017**, *8* (1), 17.
26. DeMers, H. L.; He, S.; Pandit, S. G.; Hannah, E. E.; Zhang, Z.; Yan, F.; Green, H. R.; Reyes, D. F.; Hau, D.; McLarty, M. E., Development of an antigen detection assay for early point-of-care diagnosis of Zaire ebolavirus. *PLoS neglected tropical diseases* **2020**, *14* (11), e0008817.
27. Templeton, E. J.; Salin, E. D., A novel filtration method integrated on centrifugal microfluidic devices. *Microfluidics and nanofluidics* **2014**, *17* (1), 245-251.
28. Karle, M.; Wöhrle, J.; von Stetten, F.; Zengerle, R.; Mark, D. In *Axial centrifugal filtration—a novel approach for rapid bacterial concentration from a large volume*, 2013

Transducers & Eurosensors XXVII: The 17th International Conference on Solid-State Sensors, Actuators and Microsystems (TRANSDUCERS & EUROSENSORS XXVII), IEEE: 2013; pp 1235-1238.

29. Kainz, D. M.; Früh, S. M.; Hutzenlaub, T.; Zengerle, R.; Paust, N., Flow control for lateral flow strips with centrifugal microfluidics. *Lab on a Chip* **2019**, *19* (16), 2718-2727.

30. Shen, M.; Chen, Y.; Zhu, Y.; Zhao, M.; Xu, Y., Enhancing the sensitivity of lateral flow immunoassay by centrifugation-assisted flow control. *Analytical chemistry* **2019**, *91* (7), 4814-4820.

31. Shen, M.; Li, N.; Lu, Y.; Cheng, J.; Xu, Y., An enhanced centrifugation-assisted lateral flow immunoassay for the point-of-care detection of protein biomarkers. *Lab on a Chip* **2020**, *20* (15), 2626-2634.

32. Deen, W. M., *Analysis of Transport Phenomena*. 2nd ed.; Oxford University Press: New York, 2012.

33. Lim, H.; Jafry, A. T.; Lee, J., Fabrication, flow control, and applications of microfluidic paper-based analytical devices. *Molecules* **2019**, *24* (16), 2869.

34. Schlappi, T. S.; McCalla, S. E.; Schoepp, N. G.; Ismagilov, R. F., Flow-through capture and in situ amplification can enable rapid detection of a few single molecules of nucleic acids from several milliliters of solution. *Analytical chemistry* **2016**, *88* (15), 7647-7653.

35. Zimmermann, M.; Delamarche, E.; Wolf, M.; Hunziker, P., Modeling and optimization of high-sensitivity, low-volume microfluidic-based surface immunoassays. *Biomedical microdevices* **2005**, *7* (2), 99-110.

36. Squires, T. M.; Messinger, R. J.; Manalis, S. R., Making it stick: convection, reaction and diffusion in surface-based biosensors. *Nature biotechnology* **2008**, *26* (4), 417-426.

37. Yahaya, M.; Zakaria, N.; Noordin, R.; Razak, K., The effect of nitrocellulose membrane pore size of lateral flow immunoassay on sensitivity for detection of shigella sp. in milk sample. *Materials Today: Proceedings* **2019**, *17*, 878-883.

38. Krauss, S. T.; Remcho, T. P.; Lipes, S. M.; Aranda IV, R.; Maynard III, H. P.; Shukla, N.; Li, J.; Tontarski Jr, R. E.; Landers, J. P., Objective method for presumptive field-testing of illicit drug possession using centrifugal microdevices and smartphone analysis. *Analytical chemistry* **2016**, *88* (17), 8689-8697.

39. Saisin, L.; Amarit, R.; Somboonkaew, A.; Gajanandana, O.; Himananto, O.; Sutapun, B., Significant Sensitivity Improvement for Camera-Based Lateral Flow Immunoassay Readers. *Sensors* **2018**, *18* (11), 4026.

40. Chinnasamy, T.; Segerink, L. I.; Nystrand, M.; Gantelius, J.; Svahn, H. A., Point-of-care vertical flow allergen microarray assay: proof of concept. *Clinical chemistry* **2014**, *60* (9), 1209-1216.

41. Liu, C.; Ma, W.; Gao, Z.; Huang, J.; Hou, Y.; Xu, C.; Yang, W.; Gao, M., Upconversion luminescence nanoparticles-based lateral flow immunochromatographic assay for cephalixin detection. *Journal of Materials Chemistry C* **2014**, 2 (45), 9637-9642.
42. Lee, S.; Kim, G.; Moon, J., Performance improvement of the one-dot lateral flow immunoassay for aflatoxin B1 by using a smartphone-based reading system. *Sensors* **2013**, 13 (4), 5109-5116.
43. Krauss, S. T.; Nauman, A. Q.; Garner, G. T.; Landers, J. P., Color manipulation through microchip tinting for colorimetric detection using hue image analysis. *Lab on a Chip* **2017**, 17 (23), 4089-4096.
44. Cantrell, K.; Erenas, M.; de Orbe-Payá, I.; Capitán-Vallvey, L., Use of the hue parameter of the hue, saturation, value color space as a quantitative analytical parameter for bitonal optical sensors. *Analytical chemistry* **2010**, 82 (2), 531-542.
45. Capitan-Vallvey, L. F.; Lopez-Ruiz, N.; Martinez-Olmos, A.; Erenas, M. M.; Palma, A. J., Recent developments in computer vision-based analytical chemistry: A tutorial review. *Analytica Chimica Acta* **2015**, 899, 23-56.
46. Cao, S.; Huang, D.; Wang, Y.; Li, G., Phenolphthalein Alkalinity Testing Research Based on Computer Vision Technology and Electronic Technology. In *Advances in Mechanical and Electronic Engineering*, Springer: 2012; pp 381-386.
47. Krauss, S. T.; Holt, V. C.; Landers, J. P., Simple reagent storage in polyester-paper hybrid microdevices for colorimetric detection. *Sensors and Actuators B: Chemical* **2017**, 246, 740-747.
48. Yeh, Y.-C.; Creran, B.; Rotello, V. M., Gold nanoparticles: preparation, properties, and applications in bionanotechnology. *Nanoscale* **2012**, 4 (6), 1871-1880.
49. Su, K.-H.; Wei, Q.-H.; Zhang, X.; Mock, J.; Smith, D. R.; Schultz, S., Interparticle coupling effects on plasmon resonances of nanogold particles. *Nano letters* **2003**, 3 (8), 1087-1090.
50. Woolf, M. S.; Dignan, L. M.; Lewis, H. M.; Nauman, A. Q.; Tomley, C. J.; Landers, J., Optically-Controlled Closable Microvalves for Polymeric Centrifugal Microfluidic Devices. *Lab on a Chip* **2020**, (20), 1426 - 1440.

Chapter 6 . Final Remarks

6.1 Conclusions

The projects described in this dissertation were focused on the development of centrifugal microfluidic platforms to address unmet needs and technology gaps in the forensic, biomedical, and National Defense communities. Given the complex nature of these assays, a large portion of the work on these projects was necessarily dedicated to describing, characterizing, and integrating novel or improved microfluidic unit operations that enhance on-disc functionality by expanding our ‘microfluidic toolbox.’

Chapter 2 detailed the development of a centrifugal print, cut, and laminate (PCL) microdevice capable of automating a full forensic differential extraction (DE) with three intermediate wash steps, which is normally a highly laborious, manual process. To meet this goal, the proposed centrifugal differential extraction (**CDx**) platform must minimally provide for timed reagent release, temperature control for sequential enzymatic reactions, and fluidic fractionation that yields discrete sperm (SF), non-sperm (NSF), and waste fractions from sexual assault evidence collection kit (SAECK) samples. Early iterations of the **CDx** disc leveraged a hybrid active-passive valving approach in which the main fluidic challenges were centered on preferential fluid diversion into discrete fractions downstream of the sample chamber. Preliminary testing indicated that it was possible to recover and isolate up to three discrete fractions by manipulating resistance to flow via a combination of microchannel asymmetry (width and length) and tilt angle relative to the radial axis. However, that flow control strategy added considerable design complexity and was susceptible to failure under several sets of external conditions, including perturbation during disc handling and changing reagent/sample composition. Ultimately, these challenges forced a shift in

the approach to on-disc fluidic control, i.e., development and characterization of active laser-based closable valving method (**Chapter 2** and **3**), which served as the linchpin for the current **CDx** system by enhancing on-disc flow control and ultimately providing the robust, reliable fractionation capabilities essential for DE. With this integrated laser valving method, I demonstrated effective removal of e-cell DNA from cotton swab cuttings within the **CDx** central sample chamber where the preponderance of the e-cell DNA was recovered in the NSF and first wash fraction; e-cell DNA was virtually undetectable in the SF using the PicoGreen® dsDNA assay. Further, **Chapter 2** highlights how fractionation permits retrieval of each discrete fraction allowed for a thorough assessment of sperm cell retention, loss, and recovery, in turn, allowing for improved evaluation of the disc architecture and transparency in data reporting.

Chapter 3 is devoted to a detailed discussion of the development, characterization, and optimization of the laser-based microvalve closure method implemented in the **CDx** device, above, as well as a nonlaser-based contact heating strategy. In this chapter, I explore and present a method for evaluating and visualizing binary outcome data (logistic regression with main effects modeling), as applied to microvalve closure success rates. With standard 5-layer PCL disc fabrication, the optimized contact heating method achieved >93% success rate when $rcf \leq 982.3$ *g; rcf (relative centrifugal field) is the centrifugal force acting on the fluid at the interface of the fluid and valve closure, $rcf = g = (1.118 * 10^{-5}) r s^2$ where r is the radial distance from the center of rotation in cm and s is the speed of the disc in revolutions per minute (rpm). The laser-based method achieved >96% success at $rcf \leq 970$ *g and >84% success when $rcf \leq 4,908$ *g. When reinforcing layers were added to the disc, laser-based success rates improved to >99% and >94, respectively ($n = 90$ ea). As mentioned previously, each of the chapters in this dissertation were guided by clear unmet needs and technology gaps. The primary motivator for the research

described in the previous paragraphs (and in **Chapters 2** and **3**) was an unmet forensic science need. Equally, the chief inspiration for Chapters 4 and 5 was enhanced capabilities to address technology gaps related to National Defense and preparedness.

The work presented in **Chapter 4** describes visualization and characterization of on-disc flow and fluid drainage patterns, achieved largely through high-speed videography. These studies highlight critical observations impacting ongoing centrifugal vertical flow (*cVF*) experiments and endeavours, including changes in drainage profiles with differing sample matrix composition and the loss of hydraulic pressure with changes in fluid filling height during continued flow. The results outlined in **Chapter 4** will inform future decisions regarding centrifugally-driven vertical flow immunoassay design, including sample chamber position, port position and inlet channel length, membrane composition, and spin protocol optimization.

Finally, the work presented in **Chapter 5** describes crucial pilot and proof-of-principal studies for on-disc pathogen detection via *cVF* sandwich-type immunocapture. Direct juxtaposition of parallel centrifugal vertical flow immunoassay and lateral flow immunoassay (*cVFI* and *LFI*, respectively) results demonstrated that the on-disc approach generated positive color responses that were visibly darker and more saturated than the corresponding LFI results; using the *cVFI* system, the positive color response at the lowest antigen concentration was more visually apparent and intense than the LFI test result at the highest concentration, suggesting that a fully optimized *cVFI* system is capable of outperforming the existing LFI counterpart scheme. Additional pilot studies (beyond those described in **Chapter 5**) to extend *cVF* sensitivity suggested that it is possible to detect positive responses below 0.1 ng/ μ l.

6.2 Ongoing Studies, Persistent Challenges, and Future Work

Many of the studies presented throughout this dissertation are centered on the development of centrifugal PCL microfluidic discs that incorporate a variety of assays and unit operations with utility in clinical, biomedical, and forensic applications. Although I have provided critical foundational work to enable increasingly complex on-disc processing, additional research and development is required to bring these systems to a fully functional state for point-of-care (POC) testing.

6.2.1 *The CDx Project*

The proof-of-principle work described in **Chapter 2** showcased how integrating novel active laser-based valving with PCL microdevices can be used to automate the forensic DE process. To realize the long-term goal of developing and building prototype **CDx** instruments for external, forensic laboratory evaluation, the microfluidic architecture and workflow will require significant improvement. Anticipated modifications include incorporation of reinforcing layers to reduce probability of laser valve failure (**Chapter 3**), optimization of the sample chamber and elution architecture for maximized sperm cell retention, design and integration of a fully enclosed sample chamber, and exploitation of novel enzyme-based chemistry to simplify the workflow and associated architectural footprint.

Maximizing Sperm Cell Retention

As described in **Chapter 2**, the intermediate wash fractions for a forensic DE typically contain high concentrations of e-cell DNA from the victim, non-sperm round cell (RC) DNA, and a variable number of intact sperm cells and nuclei. Preliminary studies suggest that thoughtful redesign of the sample chamber elution architecture can dramatically improve sperm cell and sperm cell nuclei retention in the swab chamber during on-disc DE, demonstrated using both 6 μm

particles and stained sperm cells (**Figure 6-1**). Specifically, the sample chamber bottom was modified to form a shallow triangular depression (5° down angles) and the outlet channel was moved inward relative to the sample chamber bottom (immediately above the triangular depression with $\cong 230 \mu\text{m}$ offset from the previous position) (**Figure 6-1A** and **B**). The combination of those features was intended to centrifugally trap larger proportions of the yellow green (YG) beads or fluorescently stained sperm cells than the original design with minimal fluid carryover between fractions.

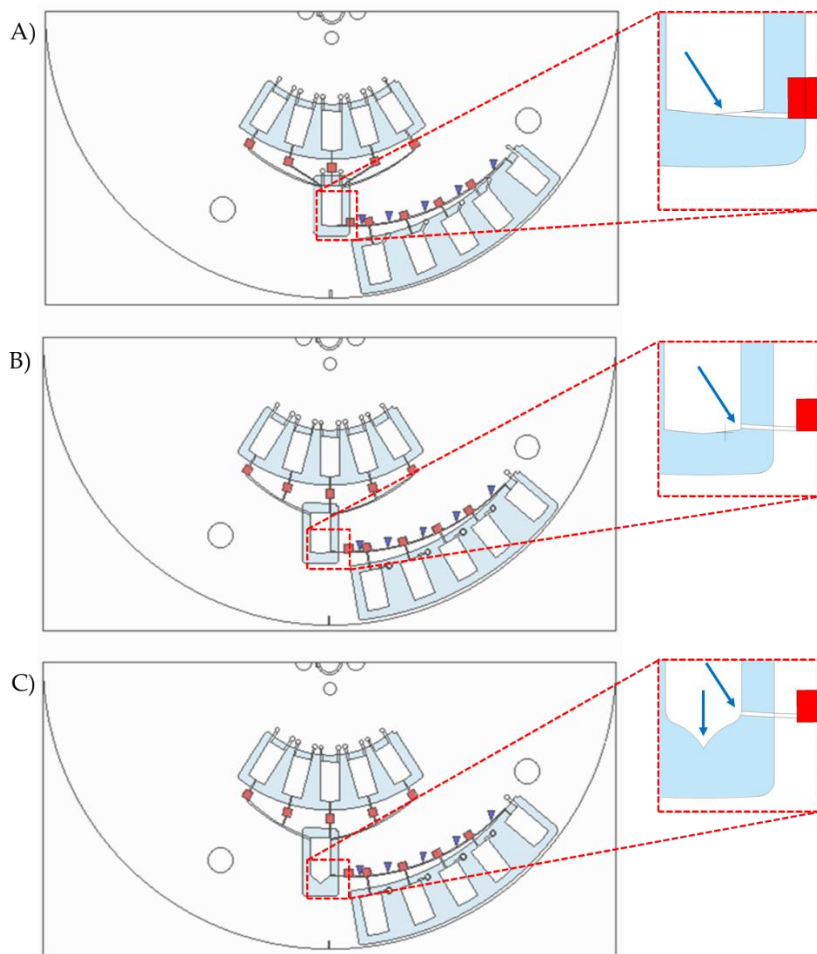


Figure 6-1. Schematic overview of modifications to the CDx sample chamber vertex and outlet channel (top view). (A and B) The sample chamber outlet was moved inward relative to the shallow depression at the outer edge of the sample chamber. (C) Elongation of the sample chamber at the outer edge (farthest from CoR) to form an inverted, teardrop-shaped retention vertex.

Despite some apparent bead loss using the modified architecture, nearly all perceivable sperm cells were retained in the sample chamber. We believe this disparity was largely due to particle concentration. Where some non-specific binding between YG beads and PeT coverlets was noted (**Figure 6-2A**), no such adhesion between stained sperm cells and polymeric disc materials (**Figure 6-2B**) was observed, suggesting that YG beads are not always suitable surrogates for sperm cells, e.g., in the SONIC ADE project YG beads are used for their similarity in size and compressibility when compared to sperm cells. More recent design changes to address undesirable particle migration have focused on increasing the depth and concavity of the depression at the sample chamber vertex (**Figure 6-2C**); pilot bead studies indicate that this modified chamber shape effectively mitigates unwanted bead migration into the downstream architecture. Minimally, these preliminary findings indicate that thoughtful architectural design changes can dramatically enhance sperm cell retention. Studies to quantify the degree to which sperm cells and sperm cell nuclei are retained (or lost) are ongoing. To date, all DNA quantification has used PicoGreen® chemistry; using commercially available qPCR and STR kits in the future will align *CDx* workflow with accepted forensic casework protocols. Should it prove necessary, embedding a non-cellulosic membrane with pore size <6 µm (as described in **Chapter 4**) could ensure retention of all intact sperm cells and sperm cell nuclei. In fact, Lenz et al. recently described a centrifugal microfluidic filtration platform that combines embedded membranes, vertical flow, and cross-flow to separate serum from whole blood.¹

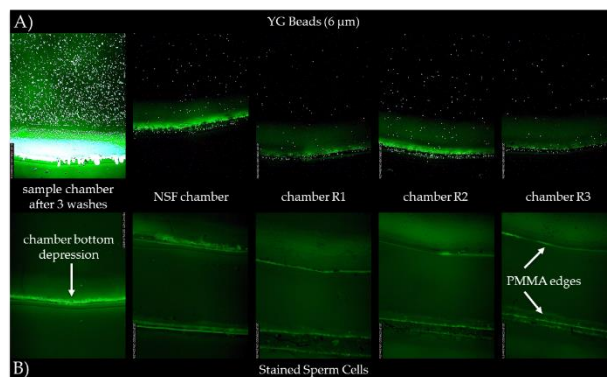


Figure 6-2. On-disc bead tracking studies. The original *CDx* architecture was modified such that each sample chamber bottom was no longer concentrically flat but rather possessed a small, convex depression just below the outlet channel. This depression was intended to retain a small fluid volume and to trap beads in the sample chamber. **(A)** Fluorescent yellow-green (YG) beads were used as a visual surrogate for sperm cells (Fluoresbrite® 6 μm YG polystyrene microspheres, 2.5% aqueous suspension, 2.10×10^8 particles/ml or 210,000 beads/μl, excitation max. = 441 nm, emission max. = 486 nm, Polysciences, Inc., Warrington, PA, U.S.A.). The stock microsphere solution was diluted to 4,200 beads/μl; 100 μl of this bead solution was added directly to each *CDx* sample chamber. Images of each chamber were captured with a Zeiss Axio Scope A1 (Carl-Zeiss AG, Oberkochen, Germany) at 5X magnification (Plan-Neofluar EC 5X/0.16 M27 objective, Zeiss) with a 120W mercury vapor short arc external light source (X-Cite Series 120Q, Excelitas Technologies, Waltham, MA, U.S.A.), a 60N-C 2/3" 0.63x camera adapter (Zeiss), and μScope software v.3.6 (Pixelink, Ottawa, Ontario, Canada). **(B)** This experiment was repeated with fluorescently stained sperm cells (SYTO™ 11 green, fluorescent nucleic acid stain, ThermoFisher).

Addressing Fluid Loss During Incubation

Pilot studies related to on-disc incubation during enzymatic lysis steps highlighted potential material issues related to microdevice composition, namely adhesive softening and subsequent fluid loss. During incubation cycles, a visible depression formed in the disc layers directly compressed by the Peltier thermoelectric coolers. This ‘footprint’ formation was most notable in shallow on-disc chambers without PMMA accessory pieces. In the absence of PMMA accessory pieces, visible fluid ‘evacuation’ into the surrounding channels, inlets, and vents was noted. I concluded that this phenomenon resulted from a combination of excessive clamping pressure, which caused a significant reduction in effective chamber volume (e.g., chamber collapse), and prolonged heating at or near the softening/activation temperature of the adhesives. During lengthy temperature hold times (3-5 min at 70-95 °C) two fluid loss failure modes were noted. First, fluid egress through

open inlets and vents was driven by chamber collapse combined with rising sample temperature; resulting fluid pressure was sufficient to overcome capillary valves at chamber-channel or chamber-vent junctions. Second, during on-disc incubation, Peltier thermoelectric heaters are brought into direct contact with the upper- and lower-disc surfaces (e.g., clamping). On numerous occasions, visible changes in the disc materials immediately surrounding the area of clamping and incubation were observed. Specifically, the heat sensitive adhesive layers within the disc appeared cloudy and less translucent. In the absence of fluid within the incubation chamber, this cloudiness was not noted; I attributed that cloudiness to fluid permeation into the HSA layers.

To address the above issues associated with on-disc heating, I have begun collaborating with another Ph.D. candidate (Scott Karas) to design and fabricate fully enclosed sample chambers that interface with PCL microdevices (**Figure 6-3**).

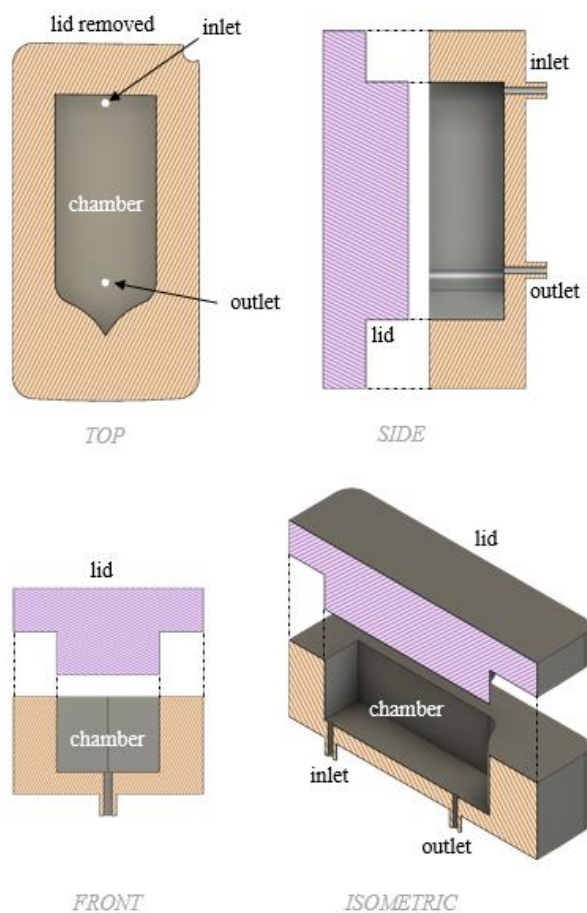


Figure 6-3. Multidimensional orthographic projection of the proposed 3D printed sample chamber.

As currently designed, this fully enclosed, 3D printed chamber offers several advantages over the previous PMMA design, namely, elimination of fluid contact with adhesives during incubation (e.g., reduce or eliminate the potential for chemical leaching from the adhesives), mechanical resistance to deformation during prolonged temperature hold times, and possession of a removable lid (like a plastic test tube). Efforts to evaluate and improve upon this design are ongoing, e.g., a snap-on lid will minimize the potential for lid release during high frequency spin steps.

Simplifying the On-disc Workflow

Simplification of the on-disc DE workflow will permit compressed microfluidic architectures that will ultimately allow for the simultaneous, automated processing of multiple evidence samples on a single *CDx* disc (**Figure 6-4**). In large part this simplification will rely upon “out-of-the-box” enzyme-based chemistry developed in the Cotton Lab at Boston University (**Table 6-1**). The temperature-controlled, “enzyme stacking” DE (TCDE) chemistry employs enzymes in a more sophisticated manner than conventional DE, eliminating physical washing of the sample, as well as required use of reducing agents and concentrated surfactants/detergents. The TCDE process relies on three key enzymes, namely EA1 protease, *Acrosolv*, and Benzonase. Each TCDE enzyme is activated at its optimal temperature and is then inactivated in one of two ways, digestion by another TCDE enzyme that is active in a different temperature range (e.g., Benzonase and *Acrosolv* are digested by EA1) or heat-killed (e.g., EA1 is irreversibly inactivated at 95 °C; order of enzyme addition and precise temperature control are critical for successful TCDE. To elaborate, much like the traditional Gill method of forensic DE, the first and most important enzyme is a proteolytic enzyme that preferentially lyses e-cells. Here, we leverage the EA1 protease (available as *forensicGEM* and *prepGEM* from MicroGEM PLC, Hamilton, NZ) isolated from the thermophilic bacteria *Bacillus sp.* strain EA1, which offers key advantages over existing proteases (e.g., ProK) used for forensic DE. First, EA1 does not require the assistance of concentrated detergents, which are known to adversely affect downstream PCR assays. Second, EA1 is inactive below 70 °C but extremely active at 75 °C, a critical feature for the enzyme stacking TCDE process. Within that active temperature range, EA1 will rapidly and preferentially lyse e-cells, as well as other proteins in the TCDE

cocktail, e.g., Benzonase and *Acrosolv* must be inactivated, via numerous known cut sites for the EA1 enzyme, prior to downstream, PCR-based assays. Third, EA1 can be irreversibly inactivated at 95 °C. Thus, temperature not only acts as an “ON/OFF” switch, but it also serves as the final “kill switch” for EA1. Finally, an added benefit of sourcing EA1 from an extremophile is that it is stable in solution at room temperature for 2 years with a loss of <2% activity, making on-disc storage a viable possibility.

Table 6-1. Critical features and optimal working temperatures for each of the enzyme components used in the TCDE process.

Reaction Component	Optimal Temperature	Presence of EA1 Cleavage Sites	Method of Inactivation	Presence of Protamine Cleavage Sites
EA1	75°C	NA	Heat (95°C)	2
Benzonase® Nuclease	37°C	Multiple	EA1	NA
Acrosolv	52°C	Multiple	EA1	Multiple

Benzonase (EMD Millipore), the second key, commercially available nuclease is commonly used in large-scale biochemical processes to digest DNA and RNA. In recent years, nucleases have garnered favor in some forensic laboratories as a means of eliminating residual e-cell DNA from forensic DE samples. Since benzonase has both endonuclease and exonuclease activity, this enzyme is a better choice for TCDE than the DNase I used in other “nuclease-based” DE protocols, i.e., this genetically engineered nuclease swiftly digests nucleic acids to 5'- monophosphate terminated oligonucleotides 3 to 5 bases in length and is ideal for removal of residual non-sperm DNA in the DE workflow. During the TCDE process, Benzonase is used to ‘*cleanup*’ residual e-cell DNA prior to lysis of the sperm cells to provides more favorable ratios of male:autosomal DNA and eliminate the need for intermediate washing steps; as described in **Chapter 2**, these wash steps are a major source of sperm cell loss.

The final, key reagent in the TCDE process is commercially available *Acrosolv*, a mixture of proteases designed to release DNA from sperm nuclei without the need for reducing agents. **Figure 6-4** shows the overall workflow for the TCDE process.

As planned, the two-year goal for the CDx project is to design, develop, and manufacture two prototype instruments for testing in accredited forensic laboratories. Specifically, we have established relationships with Miami-Dade Police Department and DNA Labs International (Deerfield Beach, FL) to perform onsite testing and evaluation with mock and previously adjudicated SAECK samples. To realize this two-year goal, key experimental milestones need to be reached. As discussed here, those milestones include maximizing sperm cell retention, eliminating fluid loss during on-disc incubation, and simplifying the *CDx* workflow via TCDE chemistry.

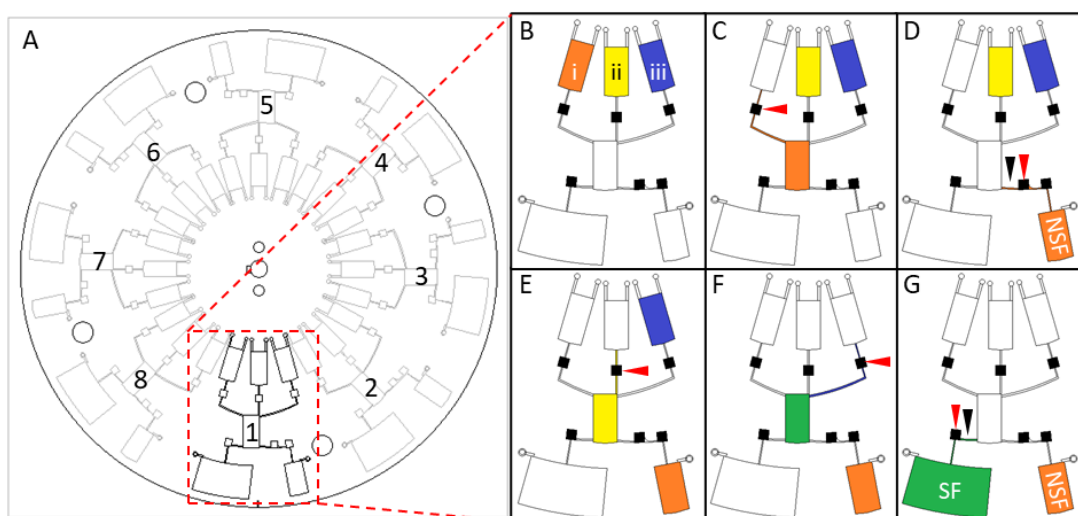


Figure 6-4. Schematic overview of the CDx disc (A) and the integrated TCDE workflow (B-G). All laser valving events are indicated by red or black arrowheads - opening and closing, respectively. (B) Reagents located near the center of rotation (CoR); B.i) EA1 (orange), B.ii) Benzonase (yellow), and B.iii) Acrosolv (blue). (C) The first laser valve is irradiated, and rotational forces are used to drive the e-cell lysis cocktail into the swab chamber. (D) Following an incubation period, the second laser valve is opened permitting access to the NSF chamber. Rotational force is used to drive the e-cell lysate into that NSF chamber. A laser is used to close that access channel, effectively isolating the NSF from subsequent fractions. (E) Similarly, the benzonase “cleanup” cocktail is released to the swab chamber and incubated accordingly. Benzonase is killed via EA1 activity. (F) Acrosolv is released and added to the swab chamber. Incubation of the Acrosolv liberates DNA from sperm cells. Appropriate temperature escalation permits EA1 digestion of the Acrosolv. At 95°C the EA1 is irreversibly inactivated. (G) The sperm cell lysate is eluted to and isolated within the terminal SF chamber.

6.2.2 *The VFI Project*

The proof-of-principle work described in **Chapters 4** and **5** showcased how embedded membranes could be used to facilitate and regulate vertical flow for on-disc immunocapture, while also highlighting enduring challenges. With modification and further investigation, a fully functional, field forward cVFI pathogen detection platform can be wholly realized and stands to supplant existing LFI technology. Key modifications and research paths include improving on-disc membrane and assay performance, stabilizing flow (drainage) profiles, augmenting on-disc liquid handling capabilities, addressing adhesives failures, and exploring options for alternative detection methods.

Enhancing On-Disc Assay Performance

Supplementary pilot testing with the current cVF system suggests that it is possible to extend on-disc assay sensitivity beyond 1.0 ng/ μ l with gold nanoparticle detection, even at the low input sample volumes dictated by LFI systems, e.g., ≤ 40 μ l of sample (**Figure 6-5A**). Although discrimination between negative and weak positive results at 0.1 ng/ μ l appears possible via the image segmentation process described in **Chapter 5** (**Figure 6-5B** and **Figure 6-6**), these low antigen concentration tests also highlight a lingering problem with non-specific binding in the cVF disc.

To elaborate, almost all LFI and VFI systems rely upon visible color development via gold nanoparticle aggregation. In those systems, as antigen concentration decreases, it becomes progressively more difficult to distinguish between the color response and the background, i.e., the color response becomes increasingly faint and less saturated. Accordingly, robust results discrimination at or near the limit of detection is most often dependent upon minimizing or eliminating visible non-specific binding of the detection antibody to the porous substrate. Pre-

assay washing steps are commonplace in LFI and plate-based ELISA systems and are intended to fulfill this role.

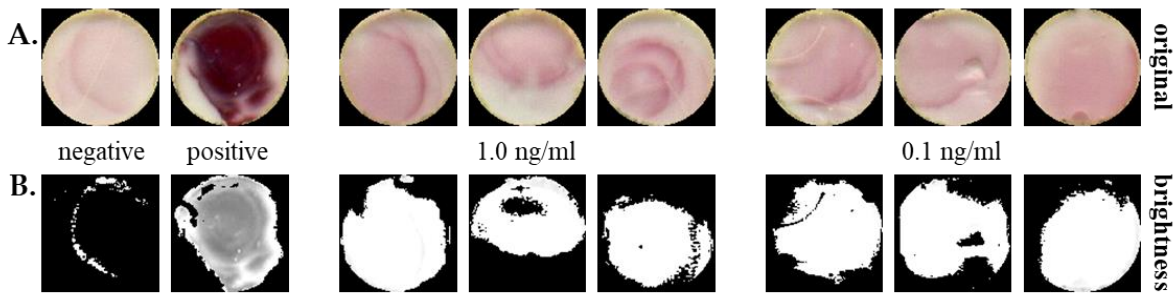


Figure 6-5. Pilot study results attempting to extend on-disc assay sensitivity beyond 1 ng/ μ l. Nitrocellulose (BioRad 0.2 μ m pore size) VF membranes were spotted with 2.5 μ l of capture antibody prior to drying and lamination into VF discs. Positive samples consisted of 40 μ l eVLP dilution (10.0 (positive control), 1.0 or 0.1 ng/ μ l) and 5.0 μ l Au tagged mAb. The negative control consisted of 40 μ l assay buffer and 5.0 μ l Au tagged mAb. Images were cropped, digitally tinted (blue = -126 to 128), and masked via color thresholding ($Y'UV = 0-200, 115-255, \text{ and } 135-255$, respectively). The ROI mask was applied to the original (untinted image) prior to color space conversion (3-slice HSB stack) and analysis. Image tinting, masking, and analysis were performed in ImageJ.

As described in **Chapter 5**, pilot studies for the VF project suggested that an on-disc priming step can limit non-specific binding and can be used to minimize radial capillary penetration of fluid in the membrane. Those same studies also raised concerns regarding the impact of priming/blocking on immunoaffinity binding events, resulting in inconsistent, irregular color responses. Although subsequent proof-of-principle experiments shifted away from membrane priming and blocking, recent success towards stabilizing on-disc color response shape and homogeneity (**Chapter 5**) suggest revisiting incorporation of pre-assay blocking/priming treatments, as well as post-assay washing as logical next steps. I believe that future efforts to improve on-disc assay performance and to extend sensitivity of the system beyond 1.0 ng/ μ l will hinge upon minimizing non-specific binding, radial capillary penetration, and the presence of unbound detection antibody that remains trapped in the VF port and/or membrane, i.e., without post-washing, some fluid will be trapped/retained by the porous media (this is not the same as nonspecific binding). In turn, those improvements will alleviate concerns surrounding discrimination of negative and weak positive results at lower antigen concentrations.

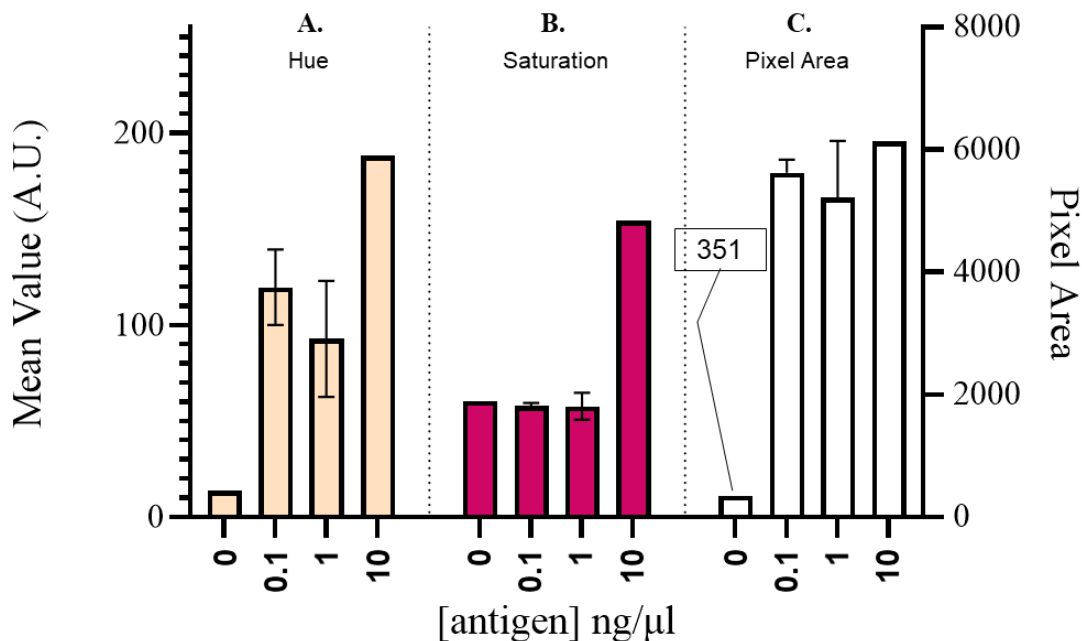


Figure 6-6. Image analysis of on-disc cVFI color responses at low eVLP concentrations (n= 3 ea at 1.0 and 0.1 ng/μl, n = 1 ea for positive and negative controls). The experimental setup and digital masking process that generated these data are described in figure **Figure 6-5**. As described in **Figure 6-5**, the ROI mask was applied to the original (untinted image) prior to color space conversion (3-slice HSB stack) and measurement of the total pixel area. **(A)** The hue parameter provides modest discernment of results. **(B)** As antigen concentration decreases the color response becomes progressively fainter; in turn, the saturation color space channel becomes less useful as metrics for distinguishing weak positives and negatives. Hue value may still provide some power of discrimination. **(C)** Total pixel area of the masked ROI provides clear discrimination of weak positives from negatives. Like the other color parameters, I suspect that pixel area will less stable and more variable as antigen concentration continues to decrease. Grayscale analysis (not shown) is another promising metric for assessment.

Stabilizing Flow/Drainage Profiles

Most LFI systems are only intended to function as qualitative, yes-no diagnostic tests. However, recent work in the field suggests that a transition to semi-quantitative analysis is possible via image analysis and stabilization of flow, i.e., reducing or eliminating variation generated by capillary pumping. Moving forward, I believe that three critical modifications to the cVF approach will improve flow/drainage profiles and will, at least in part, help minimize the impact of sample matrix on flow (**Chapter 4**), namely embedding non-cellulosic membranes, increasing the length of the inlet channel leading to the VF port, and utilizing a spin system capable of performing a

continuous spin ramping protocol. Nanoporous cellulosic membranes are standard fare for lateral flow immunoassays and other paper-based microfluidic devices. However, as described in **Chapter 4**, cellulosic membranes exhibit highly irregular, nonuniform pore structures, are susceptible to membrane swelling-deswelling, and are sensitive to changes in sample matrix composition. Minimally, future endeavours on this cVF project should consider using non-cellulosic membranes with more uniform pore structures and that are less sensitive to changes in sample composition (**Chapter 4**). Experiments to investigate the following candidate membrane materials are imminent: glass microfiber (Whatman GF/a and GF/F), fused silica (Whatman Fusion 5), polyethersulfone (PES), polyacrylonitrile (PAN), polyvinylidene difluoride (PVDF, Bio-RAD), and polytetrafluoroethylene (PTFE, Sterlitech).

As discussed in **Chapter 4 (Eq. 4 and Eq. 5)**, centrifugally generated hydraulic pressure (Δp_ω) and fluid velocity within the microfluidic channel (\bar{v}) are governed, in part, by the radial extent of the fluid plug (Δr) and mean radial distance of the plug from the CoR (\bar{r}). In the current cVF system, the fluid filling height within the sample chamber (~13 mm) and the inlet channel (~2.7 mm) determine \bar{r} and Δr . As seen in **Figure 6-7A and D**, the fluid column height determining hydraulic pressure, fluid velocity, and discharge are primarily dictated by the length of the fluid column within the sample chamber. Moving the sample chamber to a more radially inward position increases inlet channel length ($l = 26 \text{ mm}$) (**Figure 6-7B and E**) such that sample chamber filling height has less impact on the values for \bar{r} and Δr . Reorienting the sample chamber within the xy plane such that the longest dimension is parallel to the axis of rotation (**Figure 6-7C**) further reduces the impact of sample chamber filling height on \bar{r} and Δr . Together, these design changes allow for increased hydraulic pressure at lower rotational frequencies and for sustained inlet

channel filling throughout sample processing and drainage, i.e., changes in flow rate are diminished.

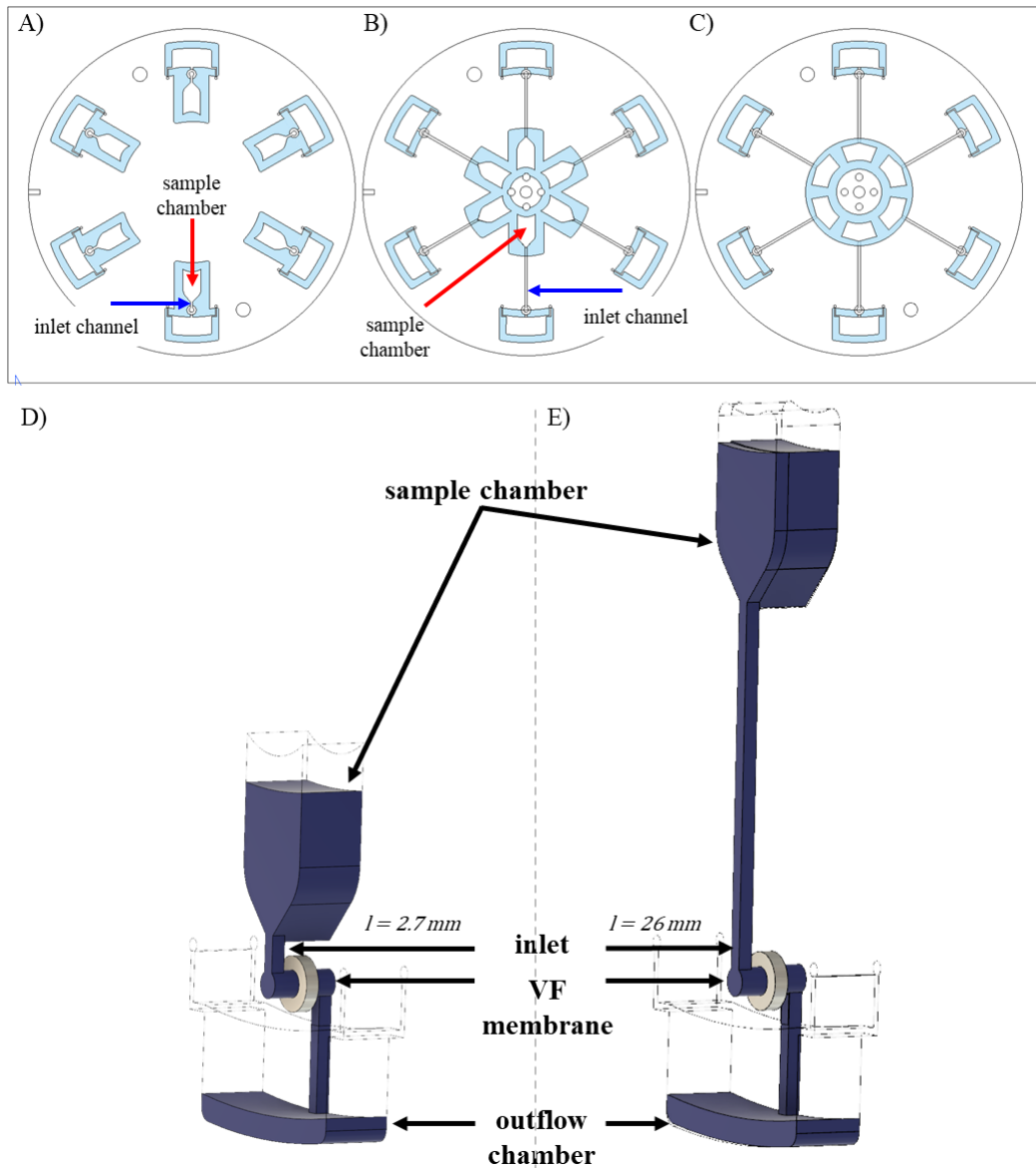


Figure 6-7. Schematic top view of three cVFI disc designs and isometric projections of two 7-layer cVF microfluidic architectures. (A and D) Placing the sample chamber and the VF port in proximity dictates that the inlet channel be very short ($l = 2.7 \text{ mm}$). (B and E) Conversely, placing the sample chamber nearer the center of rotation and farther away from the VF port allows for a much longer inlet channel ($l = 26 \text{ mm}$). (C) Reorienting the sample chamber within the xy plane such that the longest dimension is parallel to the axis of rotation, contrast with panel A and B where the longest dimension is perpendicular to the axis of rotation.

Finally, as discussed in **Chapter 4**, rebuilding and/or recoding an existing spin system to perform a continuous spin frequency ramping protocol will mitigate any residual loss of hydraulic

pressure, allowing for continuous sample drainage with no loss in flow rate. Given that sample drainage profiles follow an exponential decay curve, it stands to reason that a spin protocol following an exponential growth curve could mitigate any changes in flow rate due to diminishing fluid column filling height. Minimally, the modifications suggested in this section will stabilize flow, reducing signal variation induced by capillary pumping and easing assay optimization by offering greater control over flow rate and analyte transport through the detection zone.

Meso-scale Liquid Handling and Addressing Adhesive Failures

Given that increasing sample volume can extend VFI limits of detection well beyond existing LFI technology, the liquid handling capabilities of the existing cVF system will need to expand from 200 μ l to 1-5 ml. Volumes in the milliliter range present several challenges to the current PCL fabrication methods, chiefly, adhesive failures, chamber deformation (e.g., sagging), and excessive sample chamber footprint. Currently, the pressure sensitive adhesive (PSA) used to affix PMMA accessory pieces is the primary culprit implicated in adhesive failure. PSA failures are most often attributable to fluid infiltration with high fluidic pressures that result from: increasing chamber distance from CoR, increased fluid column length, and/or sustained spin cycles at high rotational frequencies.

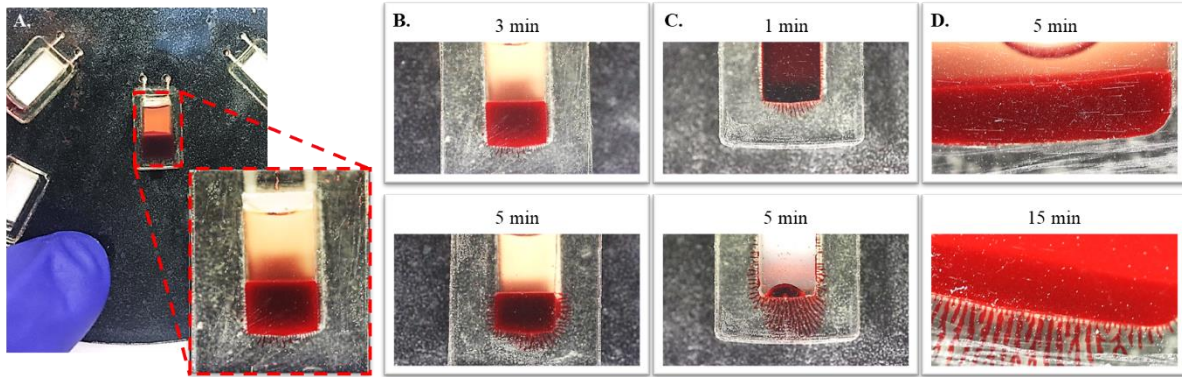


Figure 6-8. Visualizing on-disc pressure sensitive adhesive (PSA) failures. **(A and B)** On-disc separation of 100 μ l whole blood via centrifugation; 180 sec at 6,000 rpm (B-top) followed by an additional 120 sec at 6,000 rpm (B-bottom). **(C)** Similar fluid infiltration and PSA failure were observed with 100 μ l of 96 mM Allura Red AC (Sigma-Aldrich) dye solution; 60 sec at 5,000 rpm (C-top). Complete fluid loss was observed with additional 120 sec at 6,000 rpm and 120 sec at 7,000 rpm (C-bottom). **(D)** Reorienting the sample chamber in the xy plane allowed for sustained spin cycles; 80 μ l whole blood for 300 sec at 5,000 rpm (D-top) and 900 sec at 6,000 rpm (D-bottom).

I first observed pressure sensitive adhesive failures when performing pilot studies for on-disc whole blood separation. Although possible to perform on-disc whole blood fractionation in 3-5 minutes (**Figure 6-8**), fluid intrusion into the PSA binding the PeT coverlet to the PMMA chamber wall is observed by 3 minute and becomes more pronounced with continued high-frequency rotation (**Figure 6-8B-top and B-bottom**, respectively) and the resultant centrifugal forces (6,000 rpm, $*g = 2,012$) experienced at the outer edge of the sample chamber (5 cm from CoR). Similar patterns of fluid ingress and adhesive de-bonding were observed with dye studies (**Figure 6-8C**). Minimal fluid intrusion was noted at 5,000 rpm ($*g = 1,398$) for 50 sec (**Figure 6-8C-top**), whereas complete materials failure and fluid loss was noted at 6,000-7,000 rpm ($*g = 2,012$ to 2,739) for an additional 240 sec (**Figure 6-8C-bottom**). As discussed in 6.2.2.b, reorienting the sample chamber within the xy plane such that the longest dimension is parallel to the axis of rotation reduces the effective fluid filling height (\bar{r} and Δr), which in turn reduces the hydraulic pressure experienced by the adhesives along the bottom of the chamber. With blood volumes $\leq 100 \mu$ l, sample chamber reorientation partially remedied the adhesive failure issue, slowing the progression of fluid intrusion and allowing for longer sustained spin cycles; 300 sec

at 5,000 rpm (D-top) and 900 sec at 6,000 rpm (D-bottom). However, with larger volumes (≥ 850 μ l) PSA failures occurred more frequently ($\sim 75\%$), more rapidly (≤ 180 sec), and at lower rotational frequencies ($\leq 3,000$ rpm) (**Figure 6-9**). Placing fully fabricated discs under a 10 lb weight overnight did improve the PeT-PSA-PMMA bonds ($\sim 50\%$ failure rate). Chamber reorientation further reduced the failure rate but only just so ($\sim 40\%$) (**Figure 6-9B**).

Accordingly, studies to evaluate other options for PeT-PMMA bonding methods were undertaken. Bonding methods and adhesives have included surface functionalization via plasma oxidation (Plasma Etch PE-75), loctite® supergel (Henkel Corp.), 2-part epoxy (Bob Smith Industries), J-B KwikWeld 2-part epoxy (Dynamix), Dymax 9481-E dual cure (Dymax), model cement (3512A and 3521X, Testors), silicone windshield glass sealer (81730, Permatex), and ambient curable 2-part epoxy (120 hr 25°C or 1 hr 150°C, EG8020, AI Technology Inc.). To date, none of these methods have performed as well or better than the PeT-PSA-PMMA methods. Until a more effective adhesive is identified, other approaches to this issue of fluid intrusion and adhesive failure must be explored.

In the absence of a more effective candidate adhesive, two cVFI disc modifications are recommended. First, fabricating the sample chambers as a single, complete piece (e.g., injection molded or 3D printed) will eliminate or reduce adhesive-polymer seams that are exposed to fluid (**Section 6.2.1.b**). Incorporation of short fluidic nipples that extend outward from the chamber outlet will further reduce fluid-adhesive contact (**Figure 6-3**); these nipple fittings should reach through the adhesive layer(s) and into the underlying microfluidic channel. Fabricating sample chambers as entire pieces may also provide a path to reservoir footprint reduction, e.g., larger chamber volumes that consume less microfluidic real-estate in the xy plane. Second, as discussed in 6.2.2.b, moving the sample reservoirs closer to the CoR creates a longer VF port inlet channel

(Figure 6-7), which in-turn allows for simultaneous heightened hydraulic pressure at the membrane-fluid interface and diminished pressure on the sample reservoir walls and seams (Ch 4 Eq. 4). In conjunction with chamber reorientation (Figure 6-7C, Figure 6-8D, and Figure 6-9B).

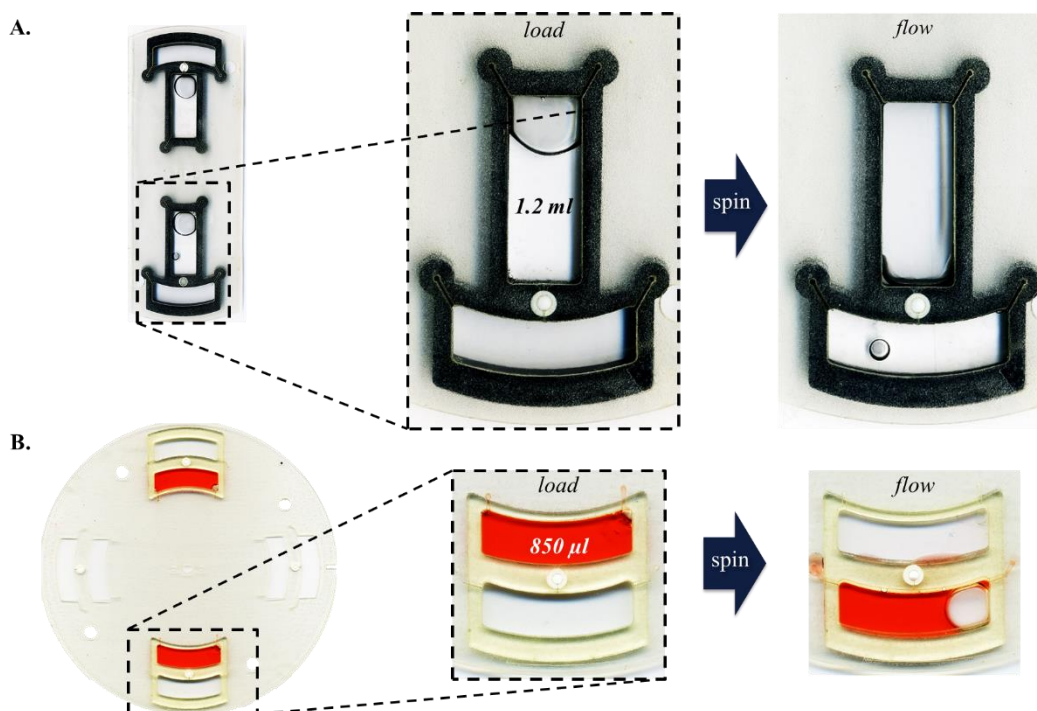


Figure 6-9. Meso-scale liquid handling and flow through. Sample chamber depth and volume were boosted by expanding the chamber footprint in the xy plane and by increasing PMMA accessory piece thickness ($t = 3.0 \text{ mm}$). (A) Successful flow through of 1.2 ml assay buffer. With this design, PeT-PSA-PMMA adhesive failure was $> 50\%$. (B) Successful flow through of dyed 850 μl assay buffer. With this reoriented chamber design, PeT-PSA-PMMA adhesive failure was reduced to $< 50\%$.

Detection Method – Improving Sensitivity

It has been suggested that the limit of detection for the cVFI system could be improved by changing from colorimetric gold nanoparticles to fluorescence detection. However, ubiquitous polymeric plastics that are commonly used in microfluidic systems are known to exhibit significant autofluorescence under laser irradiation, such as that required for fluorophore excitation. As expected, preliminary studies revealed significant background autofluorescence signals from plastics and adhesives employed in the PCL disc fabrication process, including PeT, PSA, and

PMMA. If unconsidered and unaddressed, this background autofluorescence would be a detriment to efforts towards on-disc cVFI fluorescence detection.

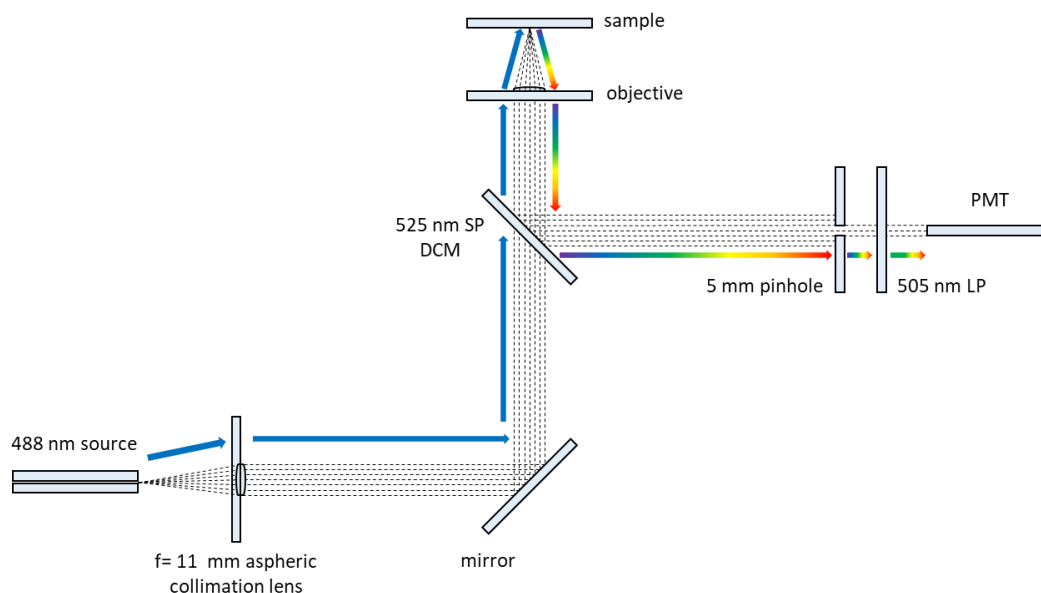


Figure 6-10. Schematic overview of the current fluorescence detection system.

Disc fabrication materials were further evaluated using a fluorescence detection system with a 488 nm laser for excitation (**Figure 6-10**). Response curves for three different PeT films are featured in **Figure 6-11**; CG 5000 (3M), T60 (Toray Industries, Inc.), and clear laser transparency film (Film Source, Inc.). In general, each of the PeT films exhibited an autofluorescence response (logarithmic decay) with peak fluorescence occurring immediately upon laser irradiation. Under continuous laser irradiation, the autofluorescence response decreased by > 65% at 60 s and by > 77% at 120 s.

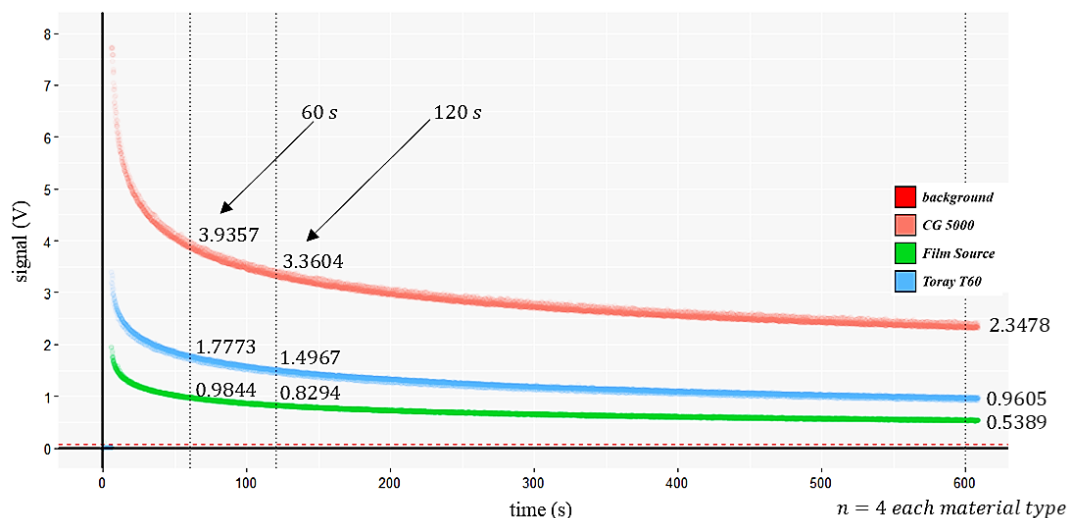


Figure 6-11. Autofluorescence and photobleaching response curves for three different PeT films ($n = 4$ ea). Peak autofluorescence signals were 7.7173, 3.2949, and 1.8964 V (CG 5000, T60, and Film source, respectively). PMT gain = 3.75

Published studies on these responses indicated that photobleaching is persistent but not permanent.² For similar plastics, autofluorescence recovery after 12 hrs of dark storage immediately following 10 min irradiation was >20%. Thus, it may be possible to reduce disc autofluorescence by simply pre-irradiating the cVF detection window. It has also been suggested that longer excitation wavelengths yield autofluorescence of significantly lower magnitude. In tandem, photobleaching and shifting to longer excitation wavelengths present workable solutions to the potential challenges associated with on-disc fluorescence detection. Thus, when considering fluorophore tags, it is advisable to consider dyes with longer excitation wavelengths, e.g., Alexa Fluor 555 **absorption_{max} = 555** (ThermoFisher Scientific).

Similarly, autofluorescence of candidate membranes is an important selection criterion, as discussed in section 6.2.2.b. For example, a panel of aspirant nitrocellulose membranes demonstrated lower peak and steady state autofluorescence responses than observed in polymeric materials (**Figure 6-12**). Despite the manufacturer claims that premium nitrocellulose membranes should exhibit lower autofluorescence, this study indicated little to no difference in

autofluorescence response under continuous irradiation at 488 nm. Importantly, unbacked PVDF exhibited an autofluorescence response of significantly higher magnitude than all nitrocellulose analogs.

The long-range goal for the cVF project is to design and develop a multiplex disc (6-8 domains) that can either screen multiple samples for a single target pathogen or screen a single sample for a panel of potential pathogens. Prior to the eventual development of an accompanying portable, field-deployable instrument, several key experimental questions must be answered and addressed, including minimizing non-specific binding (especially in negative controls), stabilizing flow rate (e.g., move chamber closer to CoR, longer VF port inlet channel, non-cellulosic membranes, etc.), increasing liquid handling capabilities (e.g., eliminate adhesives failures, move samples chambers closer to the CoR, sample chamber reorientation in the *xy* plane, fabricate entire sample chambers, integrating fluidic nipples at the sample chamber outlet, etc.), and exploring other methods of visualization and detection (e.g., fluorescence and/or catalytic ELISA).

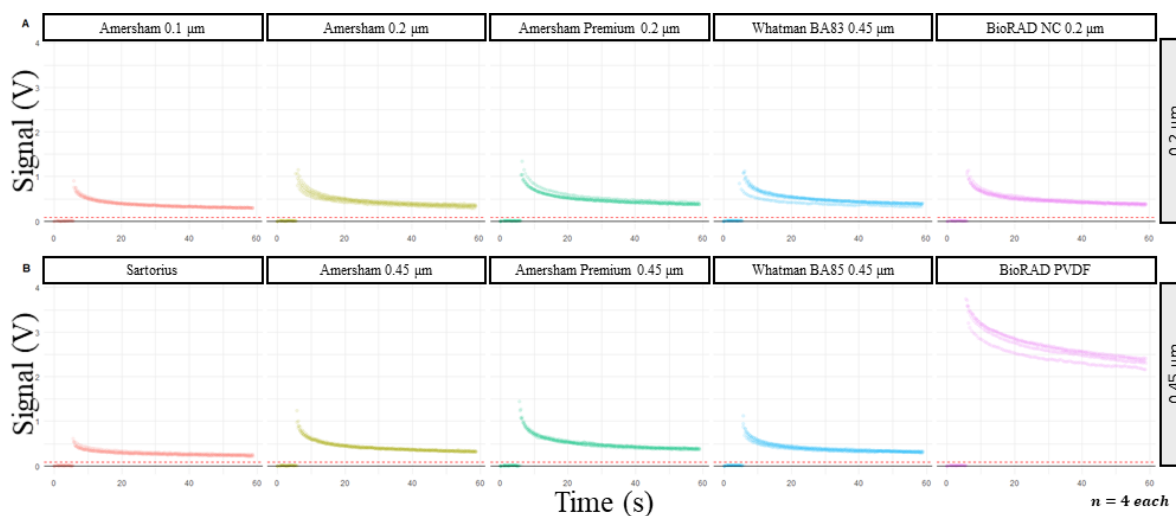


Figure 6-12. Autofluorescence and photobleaching response curves for different unbacked nitrocellulose membranes and unbacked, hydrophobic PVDF.

6.3 Summation

Centrifugal microfluidic approaches offer solutions to a variety of sample handling and analytical problems, spanning numerous fields that include forensics, National Defense and Security, environmental, clinical, and biomedical. Each of the projects outlined in this dissertation is driven by a clear unmet need. The *CDx* project is aimed at automating the manually intensive, time-consuming sample preparation workflow associated with SAECK samples, while the *cVF* project is targeting a portable, field deployable device capable of supplanting existing LFI technology and untethering pathogen detection from central laboratories. In tandem, these projects provided the impetus for laser-based closable valve development and characterization of embedded nitrocellulose membrane behavior. At present, the laser-based closable valving method is being integrated into several other Landers Lab projects. Substantial work on the parent projects (*CDx* and *cVF*) remains, yet the exploratory studies outlined here bode well for the future of the ventures.

6.4 References

1. K. D. Lenz, S. Jakhar, J. W. Chen, A. S. Anderson, D. C. Purcell, M. O. Ishak, J. F. Harris, L. E. Akhadov, J. Z. Kubicek-Sutherland and P. Nath, *Scientific reports*, 2021, **11**, 1-8.
2. A. Piruska, I. Nikcevic, S. H. Lee, C. Ahn, W. R. Heineman, P. A. Limbach and C. J. Seliskar, *Lab on a Chip*, 2005, **5**, 1348-1354.

